LAPPEENRANTA
UNIVERSITY OF TECHNOLOGY

Janne Kinnunen

DIRECT-ON-LINE AXIAL FLUX PERMANENT MAGNET SYNCHRONOUS GENERATOR STATIC AND DYNAMIC PERFORMANCE

Thesis for the degree of Doctor of Science (Technology) to be presented with due permission for public examination and criticism in the Auditorium 1382 at Lappeenranta University of Technology, Lappeenranta, Finland on the 29th of November, 2007, at noon.

Acta Universitatis
Lappeenrantaensis
284

Supervisor Professor Juha Pyrhönen
Department of Electrical Engineering
Lappeenranta University of Technology
Finland

Reviewers Professor Ewen Ritchie
Institute of Energy Technology
Aalborg University
Denmark

Professor Valeria Hrabovcova
Faculty of Electrical Engineering
University of Žilina
Slovakia

Opponents Professor Ewen Ritchie
Institute of Energy Technology
Aalborg University
Denmark

Professor Valeria Hrabovcova
Faculty of Electrical Engineering
University of Žilina
Slovakia

ISBN 978-952-214-470-6
ISBN 978-952-214-471-3 (PDF)
ISSN1456-4491

Lappeenrannan teknillinen yliopisto
Digipaino 2007

Abstract

Janne Kinnunen

Direct-On-Line Axial Flux Permanent Magnet Synchronous Generator Static and Dynamic Performance

Lappeenranta, 2007
167 p.
Acta Universitatis Lappeenrantaensis 284
Diss. Lappeenranta University of Technology

ISBN 978-952-214-470-6; ISBN 978-952-214-471-3 (PDF)
ISSN 1456-4491

In distributed energy production, permanent magnet synchronous generators (PMSG) are often connected to the grid via frequency converters, such as voltage source line converters. The price of the converter may constitute a large part of the costs of a generating set. Some of the permanent magnet synchronous generators with converters and traditional separately excited synchronous generators could be replaced by direct-on-line (DOL) non-controlled PMSGs. Small directly network-connected generators are likely to have large markets in the area of distributed electric energy generation. Typical prime movers could be windmills, watermills and internal combustion engines. DOL PMSGs could also be applied in island networks, such as ships and oil platforms. Also various back-up power generating systems could be carried out with DOL PMSGs. The benefits would be a lower price of the generating set and the robustness and easy use of the system.

The performance of DOL PMSGs is analyzed. The electricity distribution companies have regulations that constrain the design of the generators being connected to the grid. The general guidelines and recommendations are applied in the analysis. By analyzing the results produced by the simulation model for the permanent magnet machine, the guidelines for efficient damper winding parameters for DOL PMSGs are presented. The simulation model is used to simulate grid connections and load transients. The damper winding parameters are calculated by the finite element method (FEM) and determined from experimental measurements. Three-dimensional finite element analysis (3D FEA) is carried out. The results from the simulation model and 3D FEA are compared with practical measurements from two prototype axial flux permanent magnet generators provided with damper windings.

The dimensioning of the damper winding parameters is case specific. The damper winding should be dimensioned based on the moment of inertia of the generating set. It is shown that the damper winding has optimal values to reach synchronous operation in the shortest period of time after transient operation. With optimal dimensioning, interference on the grid is minimized.

Keywords: axial flux, damper winding, direct-on-line, permanent magnet synchronous generator
UDC 621.313.8 : 621.313.322

Acknowledgements

This research work has been carried out during the years 2005–2007 in the Laboratory of Electric Drives Technology, Department of Electrical Engineering, Lappeenranta University of Technology, where I have been working as a student of The Graduate School of Electrical Engineering.

I wish to thank all the people and parties who have promoted this thesis. Especially, I would like to express my gratitude to the supervisor of this thesis, Professor Juha Pyrhönen, who inspired me over the years in the field of electrical machines. I also wish to thank D.Sc. Markku Niemelä for his fruitful guidance and comments on the thesis. I am also grateful to the laboratory personnel Martti Lindh, Harri Loisa and Jouni Ryhänen for the practical arrangements.

I am grateful to the preliminary examiners of the thesis, Professor Ewen Ritchie and Professor Valeria Hrabovcova for their valuable comments to improve the manuscript.

Many thanks are due to PhD Hanna Niemelä for making a huge effort to improve the English language of this work.

In particular, I would like to thank The Switch Oy for material and technical support.

The financial support by Ulla Tuominen Foundation, Walter Ahlström Foundation, the South Carelia Regional Fund of the Finnish Cultural Foundation and the City of Lappeenranta is highly appreciated. Many thanks are directed to The Graduate School of Electrical Engineering and its leader, Professor Jarmo Partanen for financially supporting my post graduate studies.

And finally, I am grateful to my loving wife Eve for patience and understanding during the busy years. My family, with a special mention to our children Sarah and Angeliina, has given me the energy to carry on and motivate myself to cross the finish line.

Lappeenranta, November 2007 *Janne Kinnunen*

Contents

Nomenclature

Roman letters

B	flux density
d	diameter
$\boldsymbol{e}$	electromotive force space vector
E	electromotive force
E_k	kinetic energy
E_r	rotational energy
f	frequency
g	gravitation constant 9.81 m/s^2
h	height
H	magnetic field strength
i_f	equivalent excitation current for permanent magnet flux linkage
$\boldsymbol{i}$	current space vector
I	current
I, i	current matrix
J	moment of inertia
k	coefficient
k_w	winding factor
k_sq	skew factor
K_con	connection factor
l	length
L	inductance
L	inductance matrix
L''	subtransient inductance
m	mass, number of phases
n	rotation speed
N	number of turns
M	number of discrete measuring points
p	number of pole pairs
R	resistance
R_in	stator stack inner radius
R_out	stator stack outer radius
P	power
S	apparent power
t	time
T	torque
T_pu	per unit torque
$\boldsymbol{u}$	voltage space vector
U	voltage
v	velocity
w	width
V	volume
$\dot{V}$	volume flow

X	reactance
X''	subtransient reactance
Z	impedance
$\underline{U}$	underlined symbols are RMS phasors

Greek letters

α_p	pole angle
δ	load angle, depth of penetration
δ_{ag}	air gap length
ϕ	flux
η	efficiency
φ	phase angle
φ_t	phase angle between the test voltage and the induced current
μ	permeability
ν	ordinal of stator harmonic
θ	angle
ρ	density
ρ_ν	referring factor
σ	conductivity
τ	time constant, per unit time, pitch
ω	electric angular velocity
Ω	mechanical angular velocity
ψ_{pu}	per unit flux linkage
$\boldsymbol{\psi}$	flux linkage space vector
Ψ	flux linkage, RMS
$\mathbf{\Psi}$, $\boldsymbol{\psi}$	flux linkage matrix

Subscripts

0	initial value
a	stator bore
b	base value
bar	damper bar
c	coercivity
ci	intrinsic coercivity
d	direct-axis
D	damper winding direct-axis
e	electro-magnetic
er,in	end ring, inner radius
er,out	end ring, outer radius
Fe	iron losses
J	mechanical
lead	leading power factor

lag	lagging power factor
m	magnetizing
max	maximum
mc	measuring coil
md	direct-axis magnetizing
mq	quadrature-axis magnetizing
n	nominal value
p	pole
PM	permanent magnet, phase
pu	per unit
pull-out	maximum
q	quadrature-axis
Q	damper winding quadrature-axis
r	rotor, remanence
s	stator phase
sc	short-circuit
ssc	sustained short-circuit
start	starting
tot	total value
u	slot
δ	air gap
σ	leakage

Acronyms

2D	Two-dimensional
3D	Three-dimensional
AFPMSG	Axial Flux Permanent Magnet Synchronous Generator
cosφ	fundamental power factor
DOL	Direct-on-line
EMF	Electromotive force
FEA	Finite Element Analysis
FEM	Finite Element Method
IM	Induction Machine
LSPMSM	Line-Start Permanent Magnet Synchronous Motor
NdFeB	Neodymium-Iron-Boron
PM	Permanent Magnet
PMSM	Permanent Magnet Synchronous Motor
PMSG	Permanent Magnet Synchronous Generator
pu	per unit
SM	Synchronous Machine
RMS	Root Mean Square

1 Introduction

In general, electrical machines play an extremely important role in industry and in our every day life. Electrical machines generate electrical power in power plants and convert electric power to mechanical power in industrial and consumer applications. If the conversion is from electrical power to mechanical power, the machine is called a motor, while in the conversion from mechanical to electrical, the machine is called a generator. Conversion of energy is based on two electromagnetic phenomena. First, if a conductor is in a magnetic field and there occurs any change in the magnetic field or the conductor moves, a voltage is induced in the conductor. This phenomenon is generally known as Faraday's Law. Second, if a charged item, such as a current-carrying conductor, is placed in a magnetic field, the conductor experiences mechanical force. This is known as the Lorentz force. The DC machine, induction machine, and synchronous machine are the common rotating electrical machines. All the other electrical machines – except, maybe, the switched reluctance machine – may be derived from these three constructions.

In rotating electrical machines the magnetic circuits are formed by ferromagnetic materials in conjunction with air as a medium. The magnetic field is typically produced by feeding electric current through coils that are wound around ferromagnetic materials. In permanent magnet synchronous machines the permanent magnets are the major source of magnetic flux. A permanent magnet is capable of maintaining a magnetic field without any excitation current linkage provided to it. The first commercial versions of industrial permanent magnet synchronous machines emerged in the early 1980s. The development of high energy-product NdFeB (Neodymium-Iron-Boron) magnets accelerated the era of modern permanent magnet machines. Nowadays, even in mass production, the energy products over 400 kJ/m^3 can be achieved while the remanent flux density of the permanent magnets can be over 1.4 T. On the demagnetization curve, there is a single point at which the maximum value for $-BH$ product may be found. In modern magnet materials, for which the demagnetization curve may even be a straight line from the remanent flux density B_r to the coercive force H_c the maximum energy product is directly proportional to these values and is $-B_\mathrm{r}H_\mathrm{c}/4$. The larger the energy product the less permanent magnet material is required (in principle), and the smaller the electrical machine can be made. The maximum energy product is not usually utilized in machine design, because the magnetic circuit of an electrical machine can seldom be designed in such a way that the operating point of the permanent magnet material would be at the maximum energy product. In theory, a permanent magnet can produce its characteristic remanent flux density inside itself only if the ends of the magnet are short-circuited with a material of zero reluctance. The remanent flux density B_r of the permanent magnet affects the electromotive force produced by the generator. The permanent magnets should have a large remanent flux density in order to reduce the required volume of the actual magnets. This enables a high air gap flux density and high torque. The coercivity H_c defines the ability of a permanent magnet material to tolerate demagnetization. The permanent demagnetization occurs if the external demagnetising magnetic field strength reaches the intrinsic coercivity field strength H_ci. Modern motor control methods use large demagnetizing negative direct-axis currents, for example, in the field weakening. In direct-on-line applications, the

permanent magnets have to tolerate large demagnetizing currents during grid connection, during asynchronous operation and under possible fault conditions. Deshpande (2003) has presented the historical development of permanent magnets in detail. Examples of the development of the energy product of the permanent magnet materials are presented in Table 1.1.

Table 1.1 Development of permanent magnets. Today, energy products over 400 kJ/m^3 can be reached.

Year	Energy product [kJ/m^3]	Summary
1966	143	Dr. Karl J. Strnat discovers the high energy product of the Samarium-Cobalt (Sm-Co) compound. (U.S. Patent 4063971, 1966)
1972	239	Dr. Karl J. Strnat and Dr. Alden Ray develop a higher energy product Samarium-Cobalt (Sm-Co) compound.
1983	279	General Motors, Sumitomo Special Metals and the Chinese Academy of Sciences develop a high energy product Neodymium-Iron-Boron (Nd-Fe-B) compound (U.S. Patent 4601875, 1986). 290 kJ/ m^3 was discovered by Sagawa et al in 1984.
1993	308	A rubber isostatic processing was developed, including apparatus to implement this technology (Sagawa et. al. 1993). 308 kJ/m^3 for Nd-Fe-B compound was found.
2000	400	Kaneko (2000) devised high energy product magnets in the laboratory conditions. 444 kJ/m^3 was obtained, which started the mass production of 400 kJ/m^3 Nd-Fe-B magnets.
2001	409	Tokoro et al. (2001) studied wet compacting process. As a result, Nd-Fe-B magnets with 409 kJ/m^3 were obtained in mass production.
2007	415	Nd-Fe-B compound, commercial name BM 53 (Bakkermagnetics 2007).

In a typical three-phase synchronous machine, the rotor carries the field winding and the stator carries the armature windings. In a permanent magnet synchronous machine, the rotor DC fed field windings are replaced by permanent magnets. The field windings or permanent magnets are used to produce flux in the air gap. When the excited rotor is rotating at no load, voltages are induced in the stator windings. On load the stator also creates its own current linkage and field component in the air gap. The rotor and the stator fields tend to align to synchronous operation when the electromagnets or permanent magnets rotate with the same speed as the stator field.

Synchronous generators are the primary energy conversion devices of electric power systems. When a synchronous machine is network connected and producing power, the power factor of the synchronous machine may be controlled by changing the DC current in the field windings. In permanent magnet synchronous machines, however, the excitation is permanent and lacks practical control possibilities. Controlling the permanent magnet excitation is, in principle, possible only by mechanical means. In a radial flux machine the relative position of the rotor and the stator could be adjusted, whereas in single-sided axial flux machines, the air gap length could be altered, and in double-sided axial flux machines, the angle of the two (series connected) stators could be changed. Mechanical means of controlling the PM

excitation are rather impractical and expensive solutions and applications of that kind are therefore apparently not used in practice.

Slight undesirable changes of the PM field excitation come from the temperature dependence of the permanent magnets. The load conditions also affect the terminal voltage of PMSGs. Therefore, PMSGs are often connected to the grid via frequency converters such as voltage source line converters. However, some traditional separately excited synchronous generators might be replaced by carefully designed direct-on-line (DOL) uncontrolled permanent magnet synchronous generators. Small, directly network-connected, generators are likely to find large markets especially in the area of distributed electric energy generation, in small power plants (below 10 MW). Typical prime movers could be windmills, watermills and internal combustion engines. DOL PMSGs could also be applied in island networks, such as ships, submarines and oil platforms. Various back-up power generating systems could also be considered. In distributed generation system, bidirectional power flow and complicated behaviour of the reactive power may cause problems if the control systems are not suitably designed. It is, however, possible to control the voltage of an island PM generator by a power electronic reactive power controller (Kinnunen et al. 2007). In such a case, the frequency converter sizing is remarkably smaller than in cases where all the power is transmitted via the frequency converter.

In general, permanent magnet technology provides several advantages over conventional solutions. The separately excited synchronous machine produces additional losses in the excitation winding that the PMSM does not generate. Additional energy is not needed in the PMSM excitation and higher efficiencies can be achieved. The power required by the field winding is dissipated as heat. In a small machine, the power needed for the rotor excitation may be of order 5 % of the machine rating. Even in large traditional synchronous generators the power needed for the rotor excitation is 0.5–2% of the machine rated power (Slemon 1992). PMSGs are often vector-controlled and indirectly connected to the network via power electronic converters. In many power generating applications, the power electronic converter combined with a synchronous generator is not needed and could well be replaced with a cheaper and simpler system that consists of only a permanent magnet synchronous generator provided with damper windings. This could mean remarkable savings and typically a 2 to 3 %-unit increase in the system efficiency resulting from the absence of the frequency converter.

In a DOL PMSG, a careful design of the damper winding is needed to achieve stable operation. The price of the machine must also remain competitive with traditional generators. This may limit the practical applications of some damper winding structures with expensive materials. Modern neodymium-based magnets have a relative low resistivity, in the range of $150–250\times10^{-8}$ Ωm (International Magnetics Association, MMPA standard No 0100-00) and hence eddy currents in the permanent magnets produce losses and increase the temperature of the permanent magnets. This must be taken into account particularly in rotor constructions with a poor or average thermal conductivity. If the cooling of the rotor is not sufficient, permanent demagnetization of the magnets can take place. The demagnetization is far easier if the temperature of the magnets rises higher, as it is shown in Fig 1.1. Despite the

relatively high electric conductivity of NdFeB magnets, their thermal conductivity is poor, in the range of 9 W/Km (K&J Magnetics 2007). As a comparison, the thermal conductivity is about 5 times larger for common steels, 9 times larger for iron and 25 times larger for aluminium. The losses in the magnets are, however, by no means comparable with the losses of field windings, and in a properly designed machine, the PM losses do not affect the efficiency in practice.

Therefore, either the generators can be smaller or higher output levels can be achieved without the need to increase the size of the generator. Separate excitation is not required. There are no wearing parts that would require intensive service or maintenance and that are prone to faults; such components are for instance slip rings or brushes. This results in high reliability and low maintenance requirements. In particular, these properties are important for generators, which may be located in remote or isolated areas, where their service and repair can be problematic.

However, there are drawbacks in DOL PMSGs. They might also have quite high initial costs because of the high price of the permanent magnets. The cost of the permanent magnets seems to be rising at the moment. The price of the several lanthanides used in NdFeB magnets have raised. The price of the neodymium and dysprosium in 2007 has risen by about a factor of three to four compared with its price in 2003–2004 (Neorem Magnets Oy 2007a, Shin-Etsu Chemical Co., LTD 2007). China, which is the main supplier of the rare earth materials, began to limit the export of these materials (Shin-Etsu Chemical Co., LTD 2007). The global demand for rare earth materials is growing rapidly. In future, a large fraction of the demand for rare earth materials is expected to come from hybrid electric vehicle applications.

The dimensioning of a permanent magnet pole is challenging because of the limited dimensions of a single unit. This has to be taken into account especially in large machines. One magnetic pole may consist of several permanent magnet units with unidirectional magnetization. The manufacturing tolerances of the permanent magnet material properties are also a challenge for the designer of the DOL PMSGs. Two magnets with identical dimensions can have different magnetic properties, even if they come from the same manufacturer. Reported manufacturing tolerances for remanent flux densities in NdFeB magnets are about 5% (Neorem 2007, K&J Magnetics 2007). The characteristics of a NdFeB permanent magnet material are illustrated in Fig. 1.1.

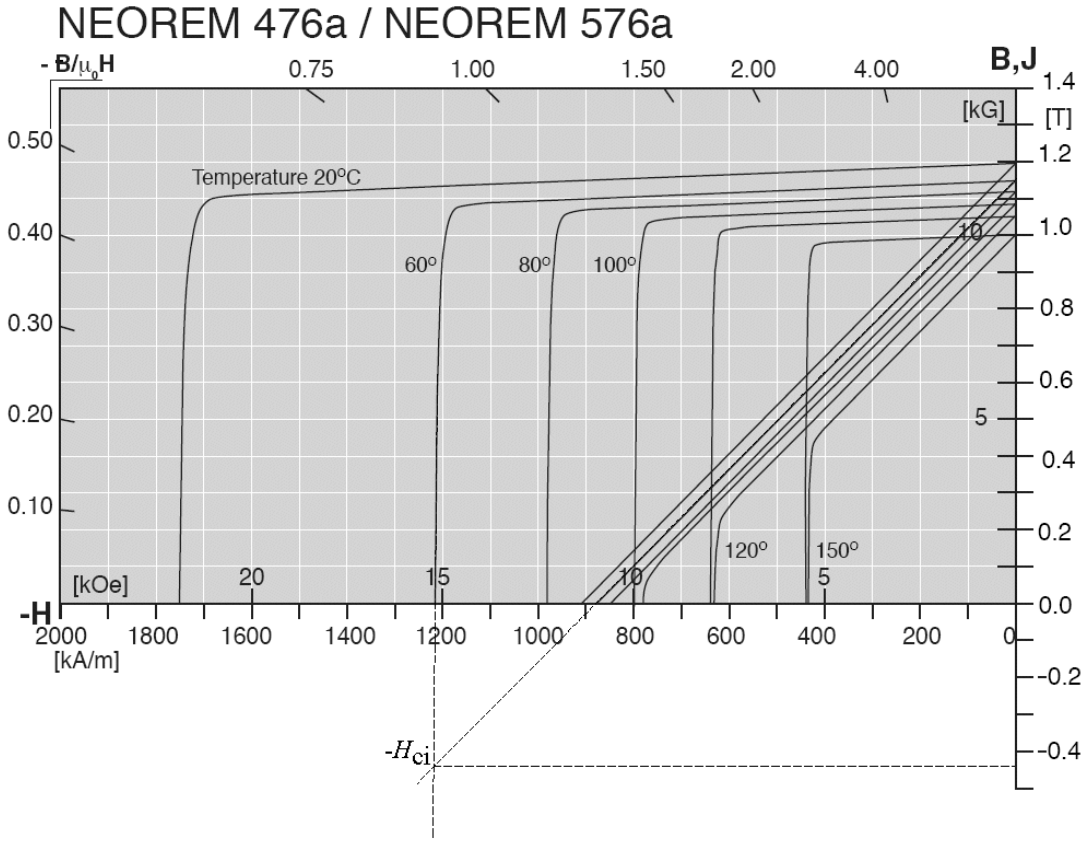

Fig. 1.1 Polarization $J(H)$ and demagnetization $B(H)$ curves of the NdFeB permanent magnet materials Neorem 476a and Neorem 576a (Neorem Magnets Oy, 2006). At 20ºC the remanent flux density $B_r = 1.2$T. At 60ºC $B_r = 1.15$T. As the temperature rises, the permanent magnet material is far more easily demagnetized. The permanent demagnetization occurs at the intrinsic coercivity field strength H_{ci}. As can be seen, the polarization J is lost at dramatically smaller demagnetizing field strengths as the temperature increases from 20 °C to 150 °C.

It can be seen in Fig. 1.1 that the temperature rise drops the knee of the demagnetization of the permanent magnet material. The remanent flux density varies by about 10% depending on the manufacturing tolerances and the temperature variations. This means that the electromotive force (EMF) of the generator may vary by about 10%.

1.1 Evolution of synchronous machines

Michael Faraday made a wire revolve around a magnet, and a magnet revolve around a wire in September 1821 (Laithwaite 1991). The fundamental induction law was invented in 1831 by Faraday. In America, Thomas Davenport developed a four-pole motor in 1834, and received both U.S. and British patents in 1837 (Davenport, 1837). In the long run, the fundamental principles became better understood and modern, efficient motors were developed.

The commercial birth of the alternator (synchronous generator) can be dated back to August 24, 1891. The first large-scale demonstration of transmission of AC power was carried out. The transmission line was a 25kV AC line and extended from Lauffen, Germany, to Frankfurt, about a distance of 175 kilometres. This major step

was taken by C.E.L. Brown. The demonstration was carried out during an international technical exposition in Frankfurt. This demonstration convinced the city of Frankfurt to adopt AC transmission for their first power plant, commissioned in 1894. The same technology was used by New York's Niagara Falls power plant. The Niagara Falls power plant became operational in 1895. After that, the development was rapid, a 40 kV line from Gromo to Nembro of 1903 was followed by others, rated between 50 kV and 66 kV in Germany, France, and Spain, all operating by 1910. After that, in North America in 1912, lines for 140 kV were built in Michigan. In Europe, the first three-phase alternating current power transmission at 110 kV took place in 1912 between Lauchhammer and Riesa, Germany (Klempner 2004, Olivera 2003).

Because of its simple construction and good starting ability, Tesla's induction motor replaced the synchronous motor as the choice for electric motor applications, but the synchronous generators remained dominant in the generation of electric power. The most common frequencies used in the electric networks is divided between countries generating their power at 50 Hz and others (e.g., the United States) at 60 Hz. 60 Hz frequency covers 90 % of the electricity systems of transporting ships (Wärtsilä 2005). The reason for this is probably that the size of 60 Hz machines is, because of a lower torque, slightly lower than that of 50 Hz machines for the same power. However, some commercial electrical machines have the same machine classified to operate at both 50 Hz and 60 Hz frequency (in the name-plate). Additional frequencies (e.g., 25 Hz) can still be found in some locations, but they are rare exceptions. Also historic $16^2/_3$ Hz single-phase railway electricity transmission still exists. The size and the power of the synchronous generators have continuously grown over the years. This can be explained by economical reasons. The output power of the machine per unit of weight increases with the unit size. Hence, it is not uncommon to see machines with ratings reaching up to 1500 MVA. The world's largest H_2/H_2O-cooled generator (1715 MW) is made by Alstom. In Olkiluoto, a 1600 MW generator manufactured by Siemens will be erected in near future. The largest units are typically used in nuclear power stations.

Permanent magnet generator drives with frequency converters rated up to 5 MW and more are emerging in wind power plants. For instance, the Finland-based electrical consortium of Rotatek Finland Ltd, Verteco Ltd (nowadays The Switch) and Vaasa Engineering Ltd has successfully supplied electrical systems for the Norwegian ScanWind AS for their 3 MW wind turbines. The turbines have gearless PMSGs. Also General Electric has successfully tested a 2.5 MW permanent magnet wind turbine, and the company will be manufacturing both 2.5 MW and 3 MW wind turbine designs in the future (General Electric 2005). Siemens also reports that they are able to manufacture PMSGs up to 5 MW (Siemens 2006b). Multibrid has also 5 MW offshore wind generators in the production (Multibrid 2006). These are some of the largest wind turbine units in the world when measured by the generated electricity. An example of a gearless permanent magnet generator by Siemens for wind turbines is shown in Fig. 1.2.

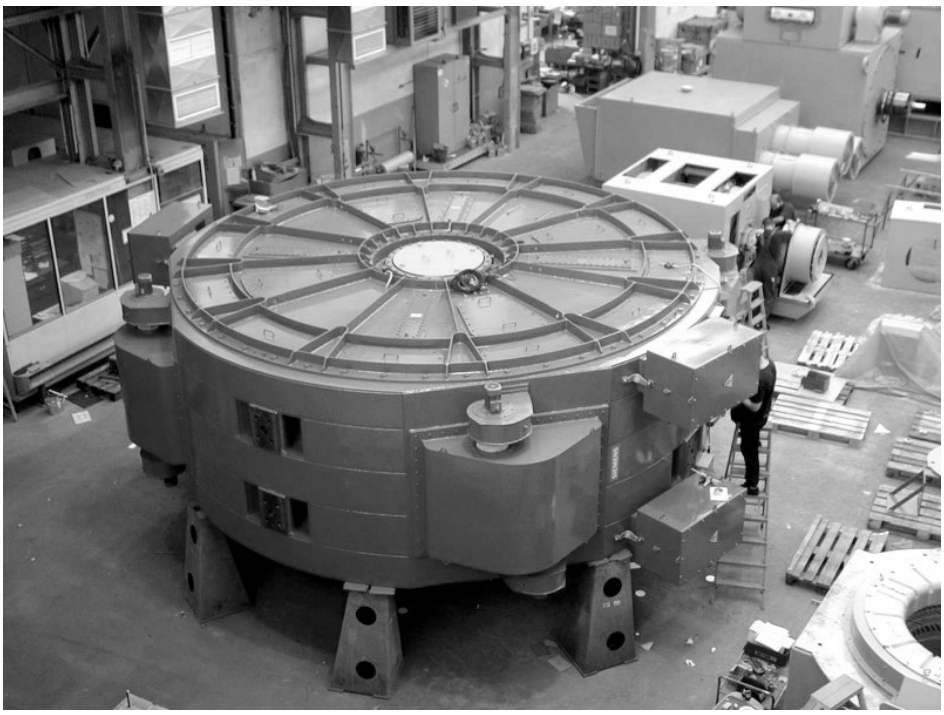

Fig. 1.2 Gearless 3 MW permanent magnet synchronous generator for wind turbine (Siemens 2004).

Another direction of development is towards smaller generating units in distributed generation. The constructions of electrical distribution networks are constantly changing. Traditional networks have been somewhat passive with unidirectional power flow. Nowadays, distributed electric energy production is becoming more popular. As one of the benefits, important loads can be protected against power loss if local isolated operation is based on local energy production. As a disadvantage, the network safety devices must be replaced by more intelligent relays and devices as the amount of distributed energy production increases. In order to find energy production solutions with lower investments, direct-on-line permanent magnet synchronous generators (DOL PMSG) could be used in the distributed electricity generation. A frequency converter is no longer needed, which reduces the costs of the generating set. The small generating units could be used to harness energy from minor energy sources, such as small waterfalls and small wind turbines.

1.2 Outline of the thesis

This research focuses on direct-on-line permanent magnet synchronous generators (DOL PMSG) provided with damper windings. The objective of the thesis is to analyze and define suitable parameters and dimensioning methods for permanent magnet synchronous generators operating in directly network-connected applications. In particular, the electrical parameters of the damper windings are studied in detail. Permanent magnet synchronous generators have two main requirements in directly network-connected operation. First, the generator must be capable of synchronization after grid connection and second, the generator has to maintain synchronous running during electric load variation and other transients. The generator characteristics vary depending on the strength of the electric network.

Therefore, both infinite bus network and isolated microgrid operations are processed in the analysis.

With these targets in mind, the study first introduces the topic of synchronous generators and the simulation model used in the analysis (Chapters 1 to 3). Secondly, the study discusses in detail the design of damper windings for permanent magnet synchronous machines (Chapter 4) and presents the experimental results and comparison of the prototype machines (Chapter 5). Finally, the conclusions are presented (Chapter 6). Below, the contents of each chapter are introduced in brief:

Chapter 1 gives an introduction to the topic.

Chapter 2 introduces the general constructions of both radial flux and axial flux permanent magnet machines. The basic differences of these two machine types are shown. A brief glance is taken to the evolution of the synchronous generators. Various constructions of the permanent magnet synchronous machines with damper windings are described. Analytical analysis of PMSGs in rigid network and island network operation is discussed. The methods used in this study to determine the electrical parameters of the DOL PMSG from practical measurements are explained.

Chapter 3 introduces the simulation model used in the analysis. The simulation model is the base for the damper winding parameter analysis. The simulation model is applied to simulate the performance of the permanent magnet machines with different electrical parameters. The target is to find the optimal design parameters for the damper windings. Some of the simulation results are illustrated.

Chapter 4 addresses in detail the asynchronous performance of the direct-on-line permanent magnet synchronous machines. The different torque components of the asynchronous operation are described. The effects of the different electrical parameters of the permanent magnet synchronous machine on the damping features are analyzed. The construction topologies of the two prototype AFPMSGs provided with damper windings are introduced. The damper winding parameters are calculated by the three-dimensional finite element method, which is explained in detail.

Chapter 5 focuses on the practical measurements. The test setups and measured results are analyzed. The theoretical results from the finite element analysis, simulation model, and analytical calculations are compared with the experimental measurements. Two prototype axial flux permanent magnet generators with damper windings, introduced in Chapter 4, are tested for verification.

Chapter 6 includes the conclusions and summarizes the most relevant results.

1.3 Scientific contribution of the work

DOL PMSGs are an interesting alternative for example in microgrid operation and in small hydro power generation. The most critical design question in directly network connected generators is their stability and thereby the design of the damping of the permanent magnet machine. The traditional literature on electrical machine design does not usually provide a detailed analysis of the damper winding design, but

typically only very general guidelines for the damper winding design of synchronous machines are given. Usually, no direct design information of the damper winding is presented (Vogt 1996, Richter 1963). This work concentrates on the permanent magnet synchronous generator stability and the damper winding design. Line-start permanent magnet motors are widely studied and published, yet there is limited public information available on the DOL permanent magnet generators.

The scientific contributions arising from the research are:

1. Analyzing the performance of a network-connected permanent magnet generator static and dynamic performance. In the static performance analysis, the inductance ratio and its effects on the machine performance are studied. In the dynamic analysis, the synchronization and load variation situations are analyzed by simulations. As a result, graphs for the transient stability are produced.

2. Selecting the damper winding parameter values for direct-on-line permanent magnet synchronous generators. The damper winding resistance in particular seems to be an important factor, and selecting a correct value for the damper is highly dependent on the system inertia. Also the effects of the magnetizing inductance and the damper winding leakage inductance are studied.

3. Dimensioning of the damper winding for disc rotor construction according to the selected values. One of the main problems in the thesis was to find practical design rules for the damper winding. What are the constructions that realize the parameters found in the dynamic simulations? The modelling of the damper windings accurately is complicated; however, the modern finite element method calculation softwares enable the study of accurate modelling of the magnetic fields.

4. Verifying the design results with two axial flux prototype machines. Intensive laboratory tests were run to evaluate the selected design criteria.

In the analysis of the damper windings and the performance of the DOL PMSGs, new and useful information on the performance characteristics was found for the axial flux permanent magnet synchronous generators with the type of damper windings that were constructed in the two prototype machines.

The most relevant publications related to the thesis are:

1. Kinnunen J., Pyrhönen J., Liukkonen O., Kurronen P. 2007. Design of Damper Windings for Permanent Magnet Synchronous Machines, paper no. 02-48 on the *International Review of Electrical Engineering, IREE*, issue March 2007. Vol.2. N.2. pp.260-272

2. Kinnunen, J., Pyrhönen, J., Liukkonen, O. and Kurronen, P. 2006. Design parameters for directly network connected non-salient permanent magnet synchronous generator. In *Proc. International Conference on Electrical Machines, ICEM2006*, 2–5 September 2006, Chania, Greece. Proceedings CD.

3. Kinnunen, J., Pyrhönen, J., Liukkonen, O. and Kurronen, P. 2006. Analysis of directly network connected non-salient pole permanent magnet synchronous machines. In *Proc. International Symposium on Industrial Electronics, ISIE 2006*, 9–13 July 2006, Montreal, Canada. pp. 2217–2222.

This thesis provides an extended approach to the issues addressed in the above publications and adds to the knowledge in the field of permanent magnet synchronous machine design. The topics of Publication 1 are discussed in more detail in Chapter 4. Publication 2 discusses the simulation model explained in Chapter 3 and presents the comparisons between the results from the simulation model and experimental results. The topics of Publication 3 include the damper winding parameters measurements, which can be found in Chapter 5.

This chapter began with an introduction to the topic. It included the outline of the thesis and scientific contribution of the work, including the publications by the author arising from the research.

2 Characteristics of permanent magnet synchronous generators

This chapter gives an overview of both radial flux and axial flux permanent magnet machines. Steady-state performances of DOL PMSGs in a rigid network and island network operation are explained by analytical equations and illustrating figures. Finally, the methods used in this study to determine the electrical parameters are explained.

According to IEC 50(411), the armature winding is a winding in a synchronous machine, which, in service, receives active power from or delivers active power to the external electrical system. The air gap field component caused by the armature current linkage is called the armature reaction. The armature reaction of the permanent magnet synchronous generator depends on the values of the synchronous inductances. Traditional separately excited salient pole synchronous machines have large direct-axis inductances, typically in the range of 1–2 per unit, because of the short air gaps and non-saturating magnetic circuit. Because of the salient pole construction, quadrature-axis inductances are smaller. In permanent magnet machines the values of the synchronous inductances are typically lower compared with the traditional synchronous machines. The relative permeability of the NdFeB permanent magnets is close to unity ($\mu_r \approx 1.05–1.1$), which equals the relative permeability of air (Neorem 2007b, Bakkermagnetics 2007). Most commonly, permanent magnet machines have rotor-surface-mounted permanent magnets. Such machines are, in principle, magnetically non-salient and have a large equivalent air gap producing low magnetizing inductance values, Fig. 2.1.

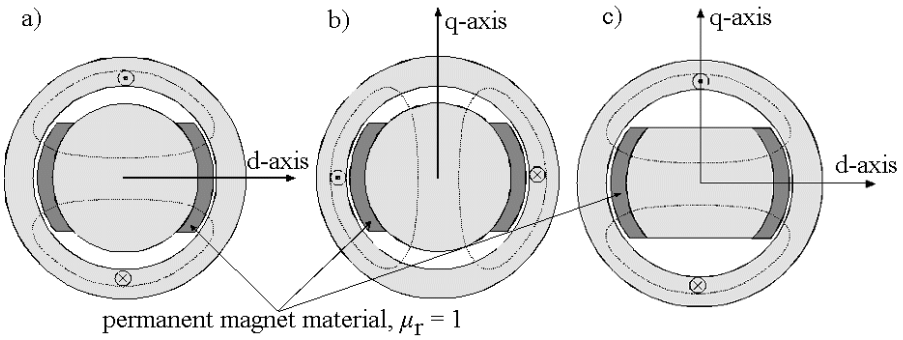

Fig. 2.1 Non-salient pole machine (a and b) and salient pole machine (c). The permeance of both d- and q-axes is equal in a) and b). c) Magnetically asymmetrical rotor produces different d-and q-axis permeances.

It might be beneficial to have some permeance differences in the d- and q-axes in order to produce some reluctance torque. The machine responds better to the torque changes if the d-axis reluctance is smaller than the q-axis reluctance. This could be achieved by cutting some ferromagnetic material from the q-axis areas of the rotor. In a rotor surface magnet motor it is, however, difficult to have large differences in the inductances, since the magnet itself forms a large air gap for the armature reaction. A magnetically asymmetrical rotor produces different d-and q-axes permeances. Such a rotor produces, in addition to the torque caused by the permanent magnet, also some reluctance torque, which depends on the RMS stator flux linkage

$\Psi_s = U_s/\omega_s$ (where U_s is the phase voltage) the quadrature-axis inductance L_q and the inductance ratio (L_q/L_d) between the axes as

$$T_r = 3p\Psi_s^2 \frac{1}{L_q}\left(1 - \frac{L_q}{L_d}\right). \tag{2.1}$$

In practice, the direct-axis inductance of a non-salient pole machine may be somewhat lower because of the slight saturation of the d-axis. On the other hand, the direct-axis inductance naturally depends on the direct-axis current, which is usually opposing the field winding current under operation. The current components and their definitions are discussed in more detail in the following sections. In particular, the d-axis current may relieve the saturation. Due to small synchronous inductances, the armature reaction is rather small. However, with inset magnet rotors, the quadrature-axis inductance can be larger than the direct-axis inductance. This is due to the placement of the permanent magnets and the flux barriers. The saliency of the rotor brings some additional features to the performance of the PMSG that are analyzed in the following sections.

2.1 Radial flux machines

The first commercial radial flux permanent magnet synchronous machines were made to increase efficiency. The induction motors were used as a starting point and the squirrel cage rotor was replaced with a rotor provided with permanent magnets. The permanent magnet machines are divided into two categories; the ones with the line-start capability and the ones that were designed to operate only in synchronous mode. Usually, the latter ones are driven by frequency converters. The common permanent magnet synchronous machines driven by frequency converters have the permanent magnets attached on the rotor surface, Fig. 2.2.

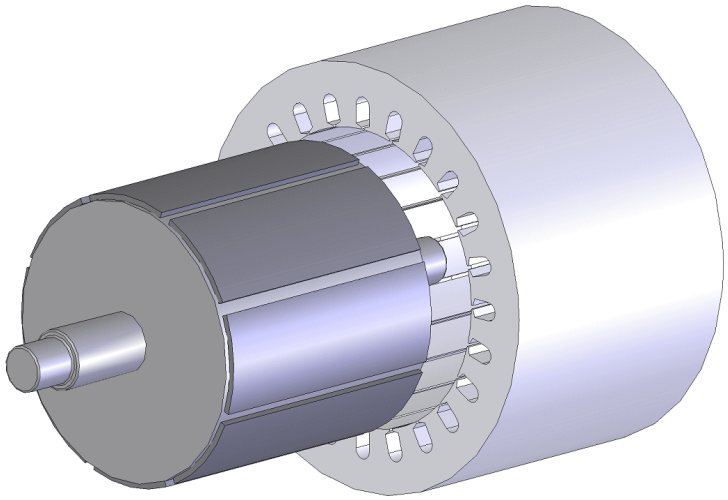

Fig. 2.2 Radial flux permanent magnet synchronous machine provided with magnets on the surface of the rotor. The rotor core can in some cases be made of solid cast iron. A laminated construction, however guarantees less eddy current losses and may thus be a safer choice.

There are also various alternatives to install permanent magnets inside the rotor. In the case of inset magnets, a laminated rotor construction is usually required to enable the manufacturing of the rotor. The stator stack of the radial flux permanent magnet machine consists of shape-cut laminations shown in Fig. 2.3.

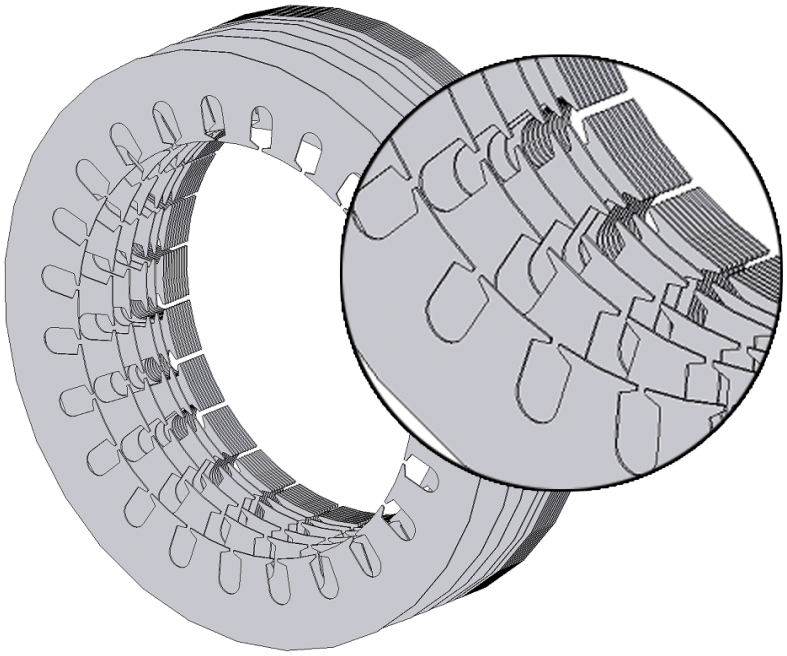

Fig.2.3 Stator stack laminations of a radial flux permanent magnet machine.

The stack of laminations easily enables for instance the skewing of the stator slots.

2.2 Axial flux machines

Axial flux machines can typically be found in applications, in which the axial length of the machine is limited, such as fans. The best power density can be reached by the one-rotor-two-stators topology (Parviainen 2005). An example of the axial flux permanent magnet synchronous generator (AFPMSG) with this kind of a topology is illustrated in Fig. 2.4.

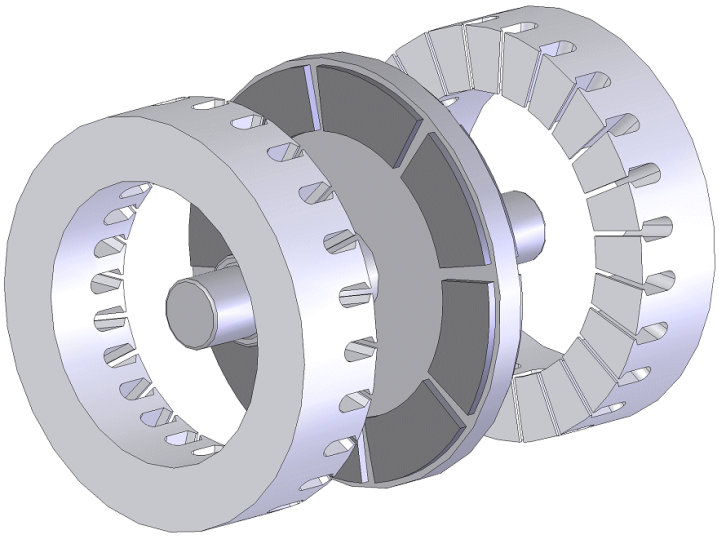

Fig. 2.4 Magnetic circuit parts of an axial flux permanent magnet synchronous generator with a one-rotor-two-stators topology. Magnets are, in this case, installed on both sides of the disc rotor so that the flux of a pole travels through both magnets associated with the pole.

One stator of the AFPMSG consists only of one long lamination rolled in circular form illustrated in Fig. 2.5. This means that the stator slot pitch shortens towards the inner radius of the stator stack. Therefore the manufacturing of the stator is somewhat more difficult than of the stators in the radial flux machines. On the other hand the rotor is usually very simple and the flat shape of the permanent magnets is easy to manufacture.

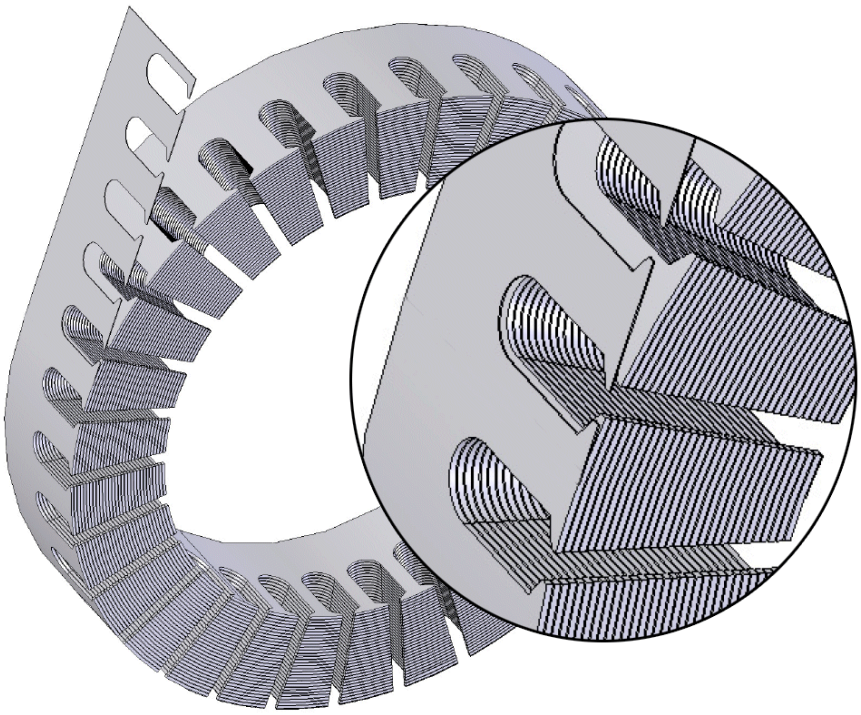

Fig. 2.5 Stator lamination of an axial flux machine made of a single long electric steel band. The stator lamination is rolled into a circular form.

Axial flux permanent magnet machines have both benefits and drawbacks compared with the radial flux permanent magnet machines. The space for the end windings at the inner radius is limited. The head of the end windings comes close to the rotor shaft. This can be problematic especially in small-scale axial flux machines and may limit the use of small pole pair numbers p. For instance, $p = 1$ is practically impossible if a lap winding is used. The stator tooth width is narrowing towards the inner radius of the stator and high flux densities may occur at the inner radius of the tooth. The tooth gets wider towards the outer radius and allows more flux to flow through that area. This causes a higher flux density in the stator yoke at the outer radius. These higher flux densities can cause excessive yoke saturation and thermal hot spots. The stator is more difficult to manufacture as the distance between the stator slots along the rolled lamination vary. Also the stator teeth of the steel sheet are more difficult to bend, especially in the stators with small diameters. Instead, the stator in radial flux machines is a stack of metal sheets, in which the slots are usually stamped. The slots in an axial flux stator are also cut using a stamping tool and a controllable distribution head. After having stamped a slot, the distribution head drives the stator lamination with a suitable angle before the next stamping.

If the axial flux machine has only one stator and one rotor, a remarkable axial loading is exerted on the bearings. With two stators the attracting forces may cancel each other. Axial flux machines have the advantage if a short axial length is needed. Also a small rotor moment of inertia is possible with the short disc rotor, the core of which can be manufactured of low density materials such as aluminium.

In axial flux machines it is possible to adjust the terminal voltage to the correct value in a specific temperature. This can be carried out by adjusting the air gap or the air gaps until the desired back-EMF and terminal voltage is reached. In radial flux machines the adjustment is not reasonable. Mechanical adjustment is a very expensive solution due to high attracting forces between the rotor and the stator. The remaining challenges in both of the topologies are the effects of the temperature alterations, especially in extreme conditions. Therefore, the operating temperature range must be known when a PMSG is designed.

2.3 Permanent magnet machines with damper windings

The first permanent magnet synchronous machines were used in motor applications. In the 1940s, H. Johnson came up with an infinite motion machine powered by permanent magnets. He received a US patent in 1979 (Johnson 1979). The principle of the motion was based on an idea that a constant imbalance is created between the rotor and the stator. One of the earliest designs of an operational permanent magnet machine was the “Permasyn motor” (Merrill 1950, 1952, Abdelaziz 1982) shown in Fig. 2.6a. A further version of the same construction included also damper cage bars at the outer circumference of the rotor. One of the earliest commercial permanent magnet synchronous motors with line-start capability was introduced by Siemens, Fig. 2.6b. Permanent magnets were added inside the rotor of an induction machine to improve the power factor and the efficiency of the machine and to enable synchronous operation. Some of the first experimental upgrades from induction motors to line-start permanent magnet synchronous motors (LSPMSM) were

implemented by replacing the old induction machine rotors by new PM rotors with damper windings.

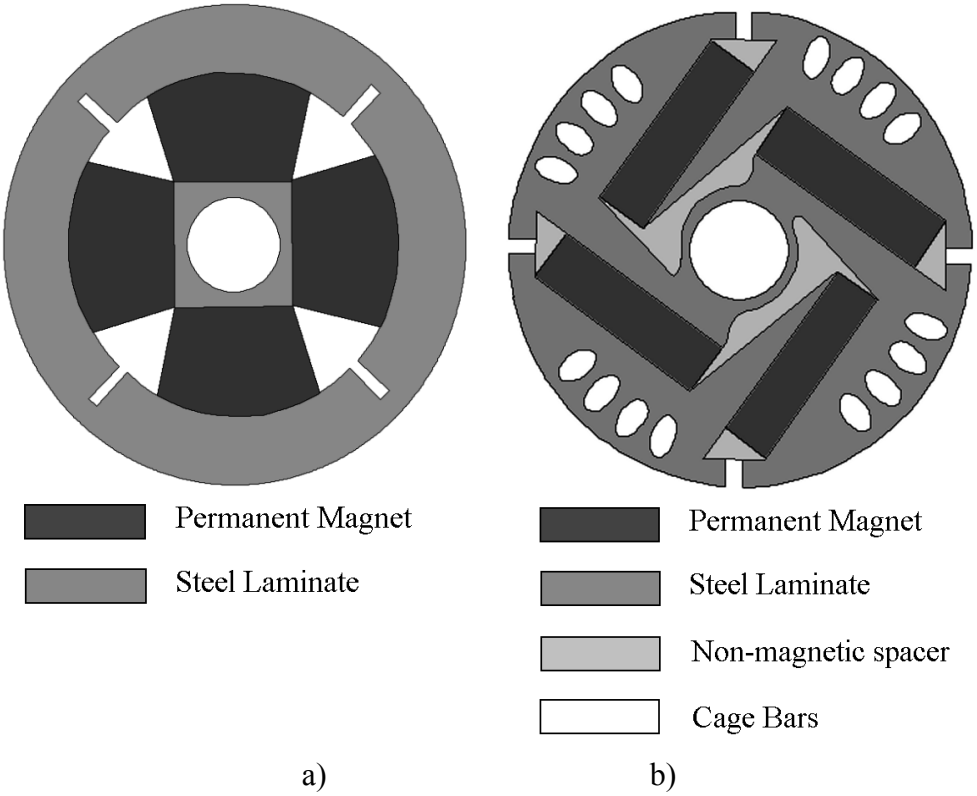

Fig. 2.6 a) Permasyn motor (Abdelaziz 1982, Merrill 1950). The permanent magnets are surrounded by an iron ring. Additional slots in the ring reduce the leakage flux but degrade the asynchronous performance. Further version included also a squirrel cage at the outer radius of the rotor. b) Commercial self-starting Siemosyn motor by Siemens (Abdelaziz 1982). The rotor has a die cast cage.

There are still commercial line-start permanent magnet motors (LSPMSM) with inset magnets and squirrel cage from few kilowatts to 1 MW (Siemens 2006a, Zhao 2001, 2003). Most of the LSPMSMs have similarities with the induction motors with a squirrel cage. In addition, inset magnets are added to achieve synchronous operation. In the literature, various constructions for line-start permanent magnet synchronous motors have been given (Binns et al. 1992, Rahman 1994, 1996, Smith 2006, Soulard 2000, 2002, Miller 1984, Zhao 2003, Knight 2000). Some of these structures are described in Figs. 2.7-2.9.

The asynchronous and the steady-state operation of LSPMSMs have been widely studied. The pull-in criterion for line-start permanent magnet synchronous motors were studied by Soulard et. al (2000) by using a Lyapunov function defined by Lagrange-Charpit method. This criterion proved to give underestimations for the critical synchronization conditions.

Binns et al. have studied the electromagnetic performance of the rotors provided with cage bars. Inset magnets are held in place by nonmagnetic material and the flow of the flux is controlled by flux guides and flux barriers. Two of the rotor constructions

are shown in Fig. 2.7a and Fig. 2.7b. The study (Binns et al. 1992) focused on the steady-state performance. In addition, the cylindrical rotors were surrounded by nonmagnetic cans. In Binns (1995), the damper winding parameters as a function of direct and quadrature-axis current were studied with the assumption that the damper winding parameters do not depend on the frequency. Both of these rotor constructions have line-start capability and they are able to synchronize. The conditions for line-start were not mentioned. However, these are very small-scale machines with a low efficiency and power factor compared with the power-scale used in the electric power generation.

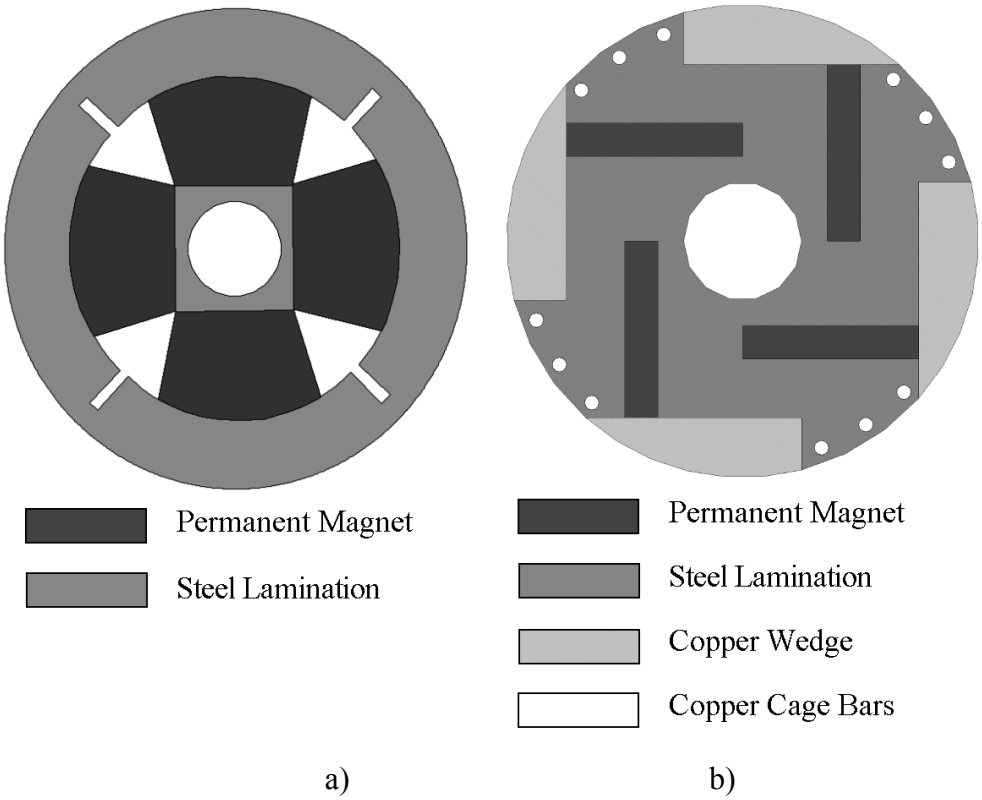

Fig. 2.7. Construction topologies of line-start permanent magnet synchronous machines. a) Modified hybrid construction (Binns et al. 1992) Some of the squirrel cage bars are extended to the edges of the permanent magnets to prevent excessive leakage flux. b) High air gap flux density construction (Binns et al. 1992).

Libert et al. (2002) presented a design procedure for a four-pole LSPMSM shown in Fig. 2.8a. The permanent magnets are embedded in U-shape. The effects of the cage bar and the magnet dimensions on start-up and synchronization were simulated. Also the effect of the system inertia on the starting capability was analyzed. A similar design with pole shoes producing a sinusoidal flux density has been illustrated in Fig. 2.8b. The most common structures of the LSPMSM presented in the literature have cage windings and I-, U-, V- or W-positioned inset magnets.

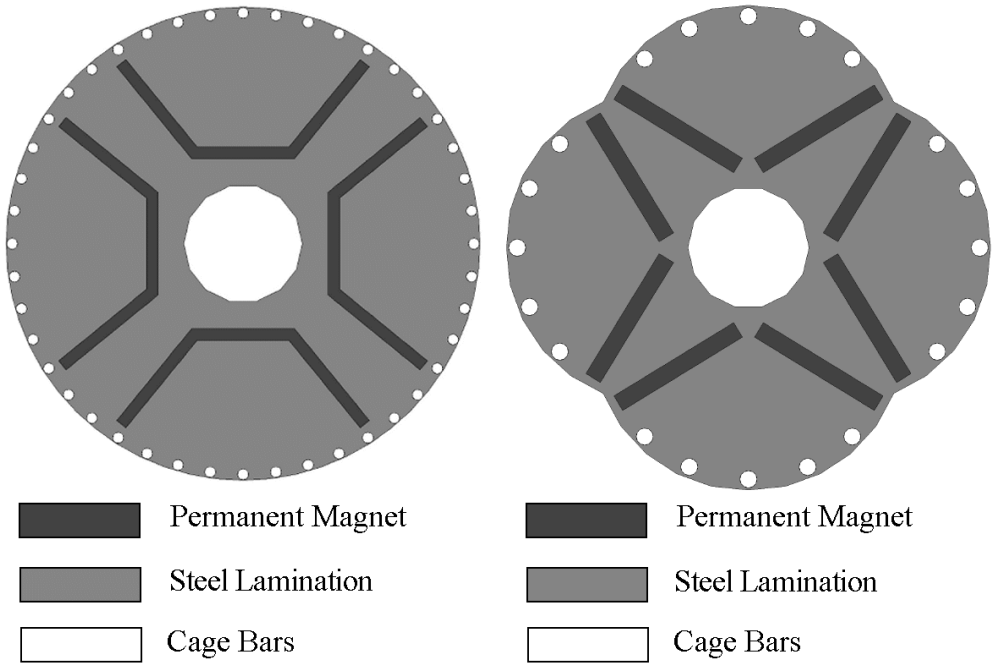

a) b)

Fig. 2.8. Construction topologies of line-start permanent magnet synchronous machines. a) U-shaped magnets (Libert et al. 2002). b) V-shaped magnets and poles producing about 1/cosine-shaped air gap length.

Rahman et al. (1994, 1996) studied a construction with extended rotor conducting cages in a straight rotor magnets assembly shown in Fig. 2.9a. Adaptive parameters for a two-axis simulation model were obtained by Finite Element Method solutions (FEM). A simpler construction of LSPMSM for chemical pumps was introduced by Smith (2006) shown in Fig. 2.9b. It is a surface-magnet rotor surrounded by a conducting can. There is no separate cage winding with conducting bars. A similar rotor construction for axial flux permanent magnet generators was analyzed by Kinnunen et al. (2006a, 2006b).

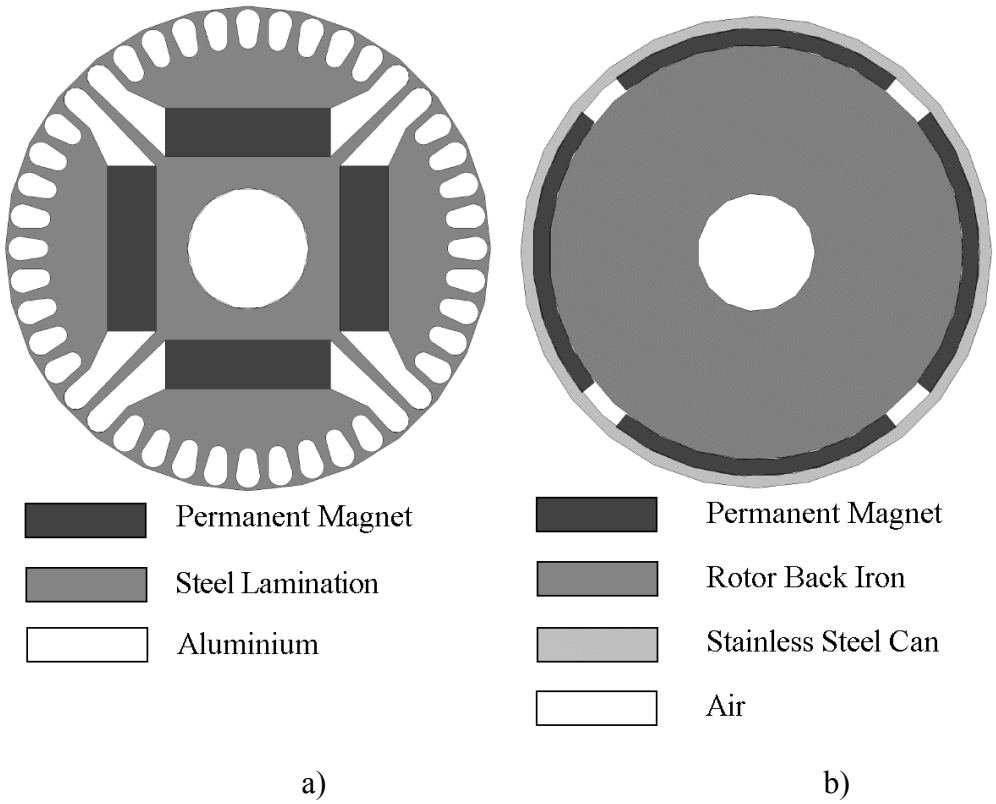

Fig. 2.9. Construction topologies of line-start permanent magnet synchronous machines. a) Inset magnets and extended rotor bars (Rahman 1994, 1996). b) Non-salient rotor and a conducting can on the surface (Smith 2006).

An alternative approach for the damper windings in a wind turbine application was presented by Westlake (1996), who analyzed an arrangement, in which the stator of a permanent magnet synchronous generator was supported on a flexible mounting consisting of springs and dampers; this mounting is dissipative. A setup of this kind can provide the damping by restricting oscillations caused by both electrical disturbances and wind gusting. The damping of oscillations takes place as the stator moves in response to torque fluctuations and energy is dissipated. The advantage in a solution of this kind is that the damping losses take place outside of the machine itself.

At present, there are commercial DOL PMSGs for water power plants in ECOBulbs^{TM} manufactured by Va Tech Hydro. The first 310 kW unit was put in operation in Aubas, France, 2002. In 2006, two 4 MW units were commissioned in Canada (Va Tech Hydro 2007a, 2007b). The rotor of the 310 kW permanent magnet generator is shown in Fig. 2.10.

Fig. 2.10. Rotor of the 310 kW direct-on-line permanent magnet synchronous generator provided with damper windings around the permanent magnets (Va Tech Hydro 2007).

Commonly used vector controlled permanent magnet machines do not, necessarily, have damper windings. However, the rotor construction and materials form paths of some kind for eddy currents. The damping eddy currents can flow in the permanent magnets and in the rotor yoke if it is made of solid material. Depending on the rotor structure the damper winding currents in equivalent circuits consist of eddy currents and possibly occurring currents in the damper winding bars.

When a changing flux penetrates the conductive damper winding, an opposing flux is produced by the damper winding according to Lenz's Law. The opposing flux tries to keep the flux constant. The damper winding can absorb the harmonics of the magnetic flux by ohmic losses and by the generation of induced currents that form opposite flux components against the flux harmonics. This phenomenon is utilized when damping rotor speed oscillations and also reducing the noise and the vibration. The use of a frequency converter along with the PMSM with damper windings may be problematic due to the high harmonic content of the PWM supply voltage. The damper winding may heat excessively. In vector-controlled machines, the original primary function of a separate damper winding is not needed, and the winding may be left out if it does not have another important function such as protecting the permanent magnets. In DOL generators, however, the damper winding is essential in stabilizing the running of the machine.

In this work, two different notation systems are used depending on the applicability of the system. Normal effective value phase voltage, flux linkage and current phasors and their components are used in phasor diagrams. The space-vector theory notation introduced originally by Kovacs and Racz (1959) is used during transients, and one

frozen space vector diagram is shown in Fig 2.11. The space vector theory is used in all the simulations. The main principles of the space vectors are introduced in Appendix D.

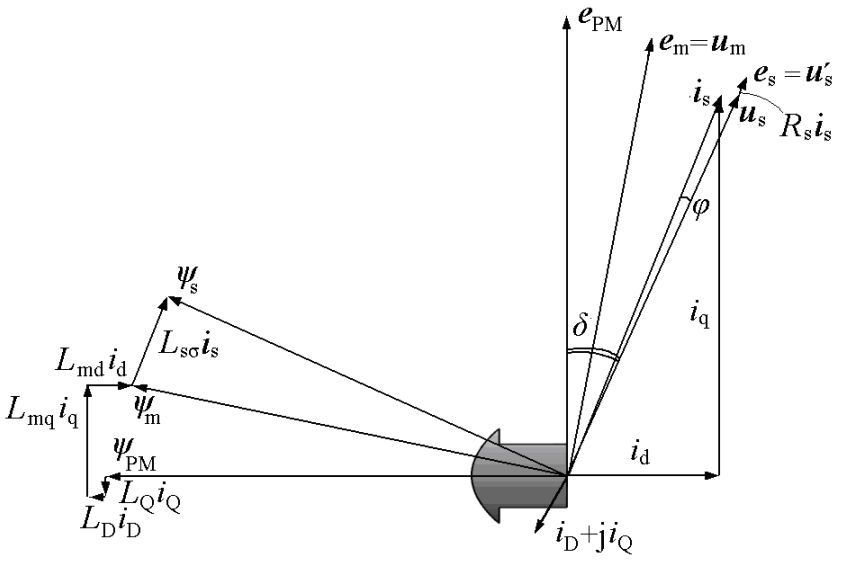

Fig. 2.11 Permanent magnet synchronous generator space vector diagram in a transient state. In the transient state, the rotor speed or load angle is not correct and the generator tries to reach equilibrium. The change in the flux flowing through the damper windings induces damper winding currents that try to keep the flux constant. The rotor is rotating counter-clockwise. $\boldsymbol{\psi}_{PM}$, permanent magnet flux linkage space vector, $\boldsymbol{\psi}_m$, air gap flux linkage, $\boldsymbol{\psi}_s$, stator flux linkage, $L_D i_Q$, quadrature axis damper reaction, $L_D i_D$, quadrature axis damper reaction, $L_{mq} i_q$, quadrature axis armature reaction, $L_{md} i_d$, direct axis armature reaction, $L_{s\sigma} \boldsymbol{i}_s$, stator leakage flux linkage, $\boldsymbol{e}_{PM}$, electromotive force induced by $\boldsymbol{\psi}_{PM}$, $\boldsymbol{e}_m$, air gap electromotive force, $\boldsymbol{e}_s$, stator electromotive force, R_s, stator resistance, $\boldsymbol{i}_s$, stator current space vector, δ, load angle, φ, power factor angle.

The rotor permanent magnet flux linkage $\boldsymbol{\psi}_{PM}$ induces the main electromotive force of the machine $\boldsymbol{e}_{PM}$. The stator flux linkage $\boldsymbol{\psi}_s$ is formed starting from the $\boldsymbol{\psi}_{PM}$ by adding first the damper winding flux linkages $i_D L_D$ and $i_Q L_Q$. The stator armature reaction components $i_q L_{mq}$ and $i_d L_{md}$ are added. We have now reached the air gap flux linkage $\boldsymbol{\psi}_m$. After adding the stator leakage $L_{s\sigma} \boldsymbol{i}_s$ we end up to the stator flux linkage $\boldsymbol{\psi}_s$. The damper winding and armature reaction flux linkages create corresponding voltage components in the voltage phasor diagram. Hence, starting from the internal electromotive force $\boldsymbol{e}_{PM}$ and adding the voltage components one by one, we end up to the air gap voltage $\boldsymbol{u}_m$ and the stator voltage $\boldsymbol{u}_s$. Between $\boldsymbol{u}_m$ and $\boldsymbol{u}_s$ there are the stator leakage inductance $L_{s\sigma}$ and resistance R_s caused voltage components. At this instant, the current space vector is $\boldsymbol{i}_s$ slightly leading the voltage $\boldsymbol{u}_s$ with phase angle φ. The load angle is denoted by δ. The space vector diagram shows the current and flux linkage space vectors during a transient at a time instant when the damper winding carries damping currents. The damper winding is cut by the air gap flux $\boldsymbol{\phi}_m$ forming the air gap flux linkage $\boldsymbol{\psi}_m$. The torque produced by the damper at the moment according to the space vector theory is

$$\boldsymbol{T}_{\mathrm{c}} = \frac{3}{2} p\left(\boldsymbol{\psi}_{\mathrm{m}} \times \left(i_{\mathrm{D}} + \mathrm{j} i_{\mathrm{Q}}\right)\right). \tag{2.2}$$

It may be noticed that at the moment the damper torque is opposite to the torque produced by the stator current

$$\boldsymbol{T}_{\mathrm{e}} = \frac{3}{2} p\left(\boldsymbol{\psi}_{\mathrm{m}} \times \boldsymbol{i}_{\mathrm{s}}\right) \tag{2.3}$$

In order to make the DOL PMSG competitive with present-day generators, it has to be easy to manufacture. The electromotive force of the DOL PMSG should be dimensioned within the defined tolerances taking into account the tolerances from the material aspect. The price of the generator cannot be high or the efficiency should be remarkably higher to overcome the additional costs in the long run. There are some advantageous solutions in the rotor structure of line-start PMSMs, yet they still have some major disadvantages considering the generator operation. The rotors are quite complicated to design and manufacture, and some of the rotors seem to have a large amount of permanent magnet material because of the large leakage flux of the magnets, which in turn increases the price. The synchronous pull-out torque has to be rather low compared with the cage-produced torque in order to achieve line-start capability. For example, the synchronous pull-out torque of the commercial LSPMSM Siemosyn 1FU8 by Siemens is only 35% higher than the nominal torque (Siemens 2003). Also the level of the electromotive force in LSPMSMs is generally far too low for the generators. All the line-start PMSMs the author found in the literature are radial flux machines. Therefore, the rotor structures have to be modified for axial flux DOL generator applications.

A permanent magnet synchronous machine has only one damper winding time constant, which comes from the subtransient state. Traditional separately excited synchronous machines have damper windings and also field windings that form another transient time constant. Even additional sub subtransient time constants have been introduced in the literature to take into account the skin effect in the damper bars (Nabeta et al. 1997, Simon et al. 2003) The PMSG damper winding time constants for short-circuited stator windings and for open stator windings are given in Fig. 2.12. In practice, the damper winding time constant lies somewhere between these two extreme values. The value of the damper winding time constant depends on the impedance of the electric network. During transient asynchronous operation, the damper winding sees the stator short-circuited via the network, and at a synchronous speed, the electric network voltage space vector is rotating synchronously with the back-EMF of the machine. It is worth remembering that the damper winding operates only when the flux through the damper windings is changing. In practice, some flux disturbance is present all the time during operation since the air gap permeance harmonics cause variations in the air gap flux.

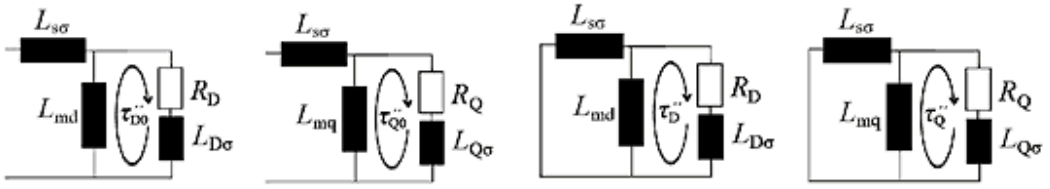

a) b)

Fig. 2.12 a) The open stator damper winding time constants $\tau''_{D0,Q0}$. b) Short circuited stator damper winding time constants $\tau''_{D,Q}$ (In the equivalent circuits in d-axis also parameters of field winding or PM should be included). There are no equivalent parameters in PMSG for field winding leakage inductance $L_{F\sigma}$ or field winding resistance R_F.

The time constants according to Fig. 1.12 are

$$\begin{aligned}
\tau''_{D} &= \frac{1}{R_D}\left(\frac{L_{md}L_{s\sigma}}{L_{md}+L_{s\sigma}}+L_{D\sigma}\right)\\
\tau''_{Q} &= \frac{1}{R_Q}\left(\frac{L_{mq}L_{s\sigma}}{L_{mq}+L_{s\sigma}}+L_{Q\sigma}\right)\\
\tau''_{D0} &= \frac{1}{R_D}\left(L_{md}+L_{D\sigma}\right)\\
\tau''_{Q0} &= \frac{1}{R_Q}\left(L_{mq}+L_{Q\sigma}\right)
\end{aligned} \tag{2.4}$$

2.4 Per-unit values

Per unit (pu) system has special importance in the area of power systems, machines and drives. The per-unit values are based on the base values that usually come from the rated values of the machines. All quantities are specified as multiples of selected base values. Different electrical parameters become dimensionless. The per-unit values are sometimes expressed as percent values. Consequently, calculations now become simpler because quantities expressed in per-unit values are the same regardless of the voltage level, and the comparison between different individual machines is straightforward. The per-unit values are defined by the quotient of the selected values and the base values. The designers of the synchronous generators consider the rated apparent output power as the base power, while for the synchronous motors, the rated apparent input power is considered as the base power. According to IEEE standard 86-1987 for synchronous generators, induction generators and synchronous motors, the base apparent power should be the total apparent electrical power at rated voltage and rated current. In induction motors the rated power output is also used as a base value. Due to the case-specific definition of the per unit values, it is essential to know the base values on which the pu values are based.

The following equations have been used in the determination of the per unit values in this study. The base values of the current and voltage are defined as the peak values of the nominal phase quantities. The mechanical angular velocity is determined from the nominal rotational speed. The base values for the selected current I_b, voltage U_b, impedance Z_b, apparent power S_b, torque T_b, angular frequency ω_b, inductance L_b and flux linkage Ψ_b are:

$$
\begin{aligned}
&I_b = \hat{I}_n = \sqrt{2} I_n \\
&U_b = \hat{U}_{n,s} = \sqrt{2} U_{n,s} \text{ (phase voltage)} \\
&Z_b = \frac{\hat{U}_{n,s}}{\hat{I}_n} = \frac{U_{n,s}}{I_n} \\
&S_b = \frac{3}{2} \hat{I}_n \hat{U}_{n,s} = 3 U_{n,s} I_n \\
&\omega_b = \omega_n = 2\pi f_n \\
&L_b = \frac{\hat{U}_n}{\omega_n \hat{I}_n} = \frac{Z_b}{\omega_b} \\
&\Psi_b = \frac{\hat{U}_{n.s}}{\omega_n} \\
&T_b = \frac{S_b}{\omega_b}
\end{aligned}
\tag{2.5}
$$

Per-unit values for the current I_{pu}, voltage U_{pu}, resistance R_{pu}, impedance Z_{pu}, torque T_{pu}, angular frequency ω_{pu}, inductance L_{pu} and flux linkage Ψ_{pu} are

$$
\begin{aligned}
&U_{pu} = \frac{U}{U_b} \\
&I_{pu} = \frac{I}{I_b} \\
&R_{pu} = R \frac{I_b}{U_b} = \frac{R}{Z_b} \\
&Z_{pu} = \frac{Z}{Z_b} \\
&T_{pu} = \frac{T}{T_b} \\
&\Psi_{pu} = \frac{\omega_n \Psi}{U_b} = \frac{\Psi}{\Psi_b} \\
&\omega_{pu} = \frac{\omega}{\omega_n} \\
&\tau_{pu} = \omega_n t \\
&L_{pu} = \frac{\omega_n L}{Z_b} = \frac{L}{L_b}
\end{aligned}
\tag{2.6}
$$

It is important to note that also the physical time t has per unit scaling. If the physical time is used in the per unit valued equations instead of per unit time τ_{pu}, it has to be multiplied with the base value of the angular frequency.

2.5 Permanent magnet generator electric network operation

National and international regulations and classifications limit the design procedure of the DOL PMSGs. They define the limits for the voltage and current quality in steady-state operation, transients and fault conditions (e.g. standard EN 50160). Also the network companies have set their own requirements and conditions to guarantee the good voltage quality of the electric network.

The DOL PMSG characteristics in the steady-state depend on the strength of the electric network. The stiffness of the grid must be taken into account in the design parameters. The largest generator power that can be connected into the mains is limited by the rigidity requirements of the grid connection point. The grid voltage is allowed to change by a certain magnitude during the grid connection transient. The required short-circuit power S_{sc} of the grid interface for the generator of the apparent power S_n is

$$S_{sc} = \frac{U_n}{\Delta U_n} \cdot S_n \frac{I_{start}}{I_n}. \tag{2.7}$$

If the allowed deviation in the grid voltage is $\Delta U_n = 5\%$ and the starting current I_{start} of the generator is twice the nominal value I_n, the short-circuit power of the grid connection point has to be 40 times larger than the nominal power of the connected generator.

In the grid connection of DOL PMSG, large current pulses may occur if there is a phase, frequency or amplitude difference between the grid voltage and the generator electromotive force. Large current pulses cause large voltage sags if the network is weak. Large current pulses cause also large torque components to the generator that have to be taken into account in the mechanical design. After transients, the generator must reach synchronous operation in a limited time sequence to avoid excessive disturbances to the electric grid.

There can also be a requirement to produce a certain amount of short-circuit current in fault conditions. The proper operation of the network safety devices requires a sufficient short circuit current from the generator. This is the case if the network is weak or has an option to operate in island conditions. In island operation the required short-circuit current is typically two to three times the nominal current of the generator. All these features and limitations must be taken into account in the design procedure.

The conditions in the grid connection and present standards for separately excited synchronous generators and their applicability for permanent magnet generators have been studied. Nordel (1995) gives recommendations for grid operation of generators below 25 MW. Nordel is a collaboration organisation of the Transmission Systems Operators of Denmark, Finland, Iceland, Norway and Sweden. Synchronization of direct-on-line synchronous generators onto grid operation is defined e.g. in VDE (2004). The standard is valid for generators larger than 50 MW and may be suitably

applied to other generators. The synchronization takes place at a minimum speed difference, at a correct phase sequence and a correct voltage phase, i.e. the voltages of the grid and the generator should be the same before connection. The voltage amplitudes may differ by 10 %. In the case of permanent magnet generators, the back electromotive force E_{PM} may not be controlled but it has to be slightly higher than the rated grid voltage in order to get an adequate power factor at the rated power. Usually the $E_{PM} = 1.1U_n$. The voltage level fluctuation during synchronization is restricted in the EU primarily by the EN 50160 and secondarily by the standards and engineering recommendations that normally restrict the voltage fluctuation at the connection point during synchronization to 3-5 % (Engineering recommendation G59/1).

Limits for voltage fluctuations in public low-voltage (230/400V) systems for equipment with rated current ≤ 16 A, are defined in standards IEC 6000-3-2 (2001) and IEC 61000-3-3 (2002). Standard EN 50438 (2005) has been established by CENELEC and is currently in draft format. It is to be published in 2008. It outlines the requirements for the connection of micro-scale generators in parallel with public low voltage distribution. Micro generation is defined by the standard as a source of electrical energy and all associated equipment, rated up to and including:

-25A at low voltage (230V), when the network connection is single phase

-16A at low voltage (230/400V), when the network connection is three phase, and, designed to operate in parallel with the low voltage system.

In some countries, there is a national deviation to extend the scope of this standard for equipment rated above 16 A. For instance in Finland, the scope of this standard is extended to a rated power of up to 30 kVA for three-phase equipment. For micro-generation, the conditions proposed in the EN 50438 draft are shown in Table 2.1.

Table 2.1 Recommendations for micro generation (EN 50438).

Default interface protection settings		
Parameter (phase values)	Trip setting	Max clearance time
Over voltage - stage 1	230 +10 % V	1.5 s
Over voltage - stage 2	230 +15 % V	0.2 s
Under voltage	230 –15 % V	1.5 s
Over frequency	51 Hz	0.5 s
Under frequency	47 Hz	0.5 s
cos φ	± 0.95 at three voltage levels; 210 V, 230 V and 250 V	

Maximum voltage fluctuations and flicker		
	Starting	Stopping
Limit	3.3 % V	3.3 % V

In EN 50438, the generalities of synchronization are defined only so that the synchronization must be fully automatic. Several electrical distribution companies have proposed similar conditions and regulations defined for the grid connection of the generators. The conditions for the grid connection have been obtained from the electrical distribution company Helsinki Energy. The conditions that have to be fulfilled when a synchronous generator is connected to the 50 Hz mains are shown in Table 2.2.

Table 2.2 Conditions for the grid connection of synchronous generators.

Grid connection conditions by Helsinki Energy	
Parameter	Condition
Voltage difference	$\Delta U < \pm 8\ \%\ U_n$
Frequency difference	$\Delta f < \pm 0.5$ Hz
Phase difference	$\Delta\varphi < \pm 10°$

For comparison, asynchronous grid connection for asynchronous machines is allowed when $\Delta n \leq \pm 5\ \%\ n_n$. A single voltage level is calculated from the average value of the 10-minute sequence. Fast voltage transients can be 10% of the nominal value a couple of times a day. This may cause visible flickering.

The prime mover should control the speed of the PMSG up to the synchronous speed. If the prime mover is not capable of exactly controlling the speed, as it might be the case in small water power plants, the generator is connected to the grid at a speed slightly smaller than the synchronous speed, and the damper winding has to synchronize the machine to the network.

These recommendations and conditions were used as guidelines in the further analysis.

2.5.1 Rigid network operation

In the following, the static performances of DOL PMSGs are studied by two-axis analysis. The effects of saliency in a rigid network and an island network on power and the power factor are analyzed.

The direct- and quadrature-axis current components may be solved from the corresponding voltage equations in the steady-state generator operation. A phasor diagram showing two-axis components are shown in Fig. 2.13. The RMS phase voltage components are

$$\begin{aligned} U_d &= I_q \omega_s L_q - I_d R_s = U_s \sin\delta \\ U_q &= E_{PM} - I_d \omega_s L_d - I_q R_s = U_s \cos\delta \end{aligned} \tag{2.8}$$

where the RMS current components are defined as

$$\begin{aligned} I_\mathrm{d} &= I_\mathrm{s}\sin(\delta+\varphi) \\ I_\mathrm{q} &= I_\mathrm{s}\cos(\delta+\varphi) \end{aligned} \quad . \tag{2.9}$$

The sign of phase angle φ between current and voltage is defined positive if the power factor is lagging and negative for leading power factors when following the generator logic in the phasor diagrams.

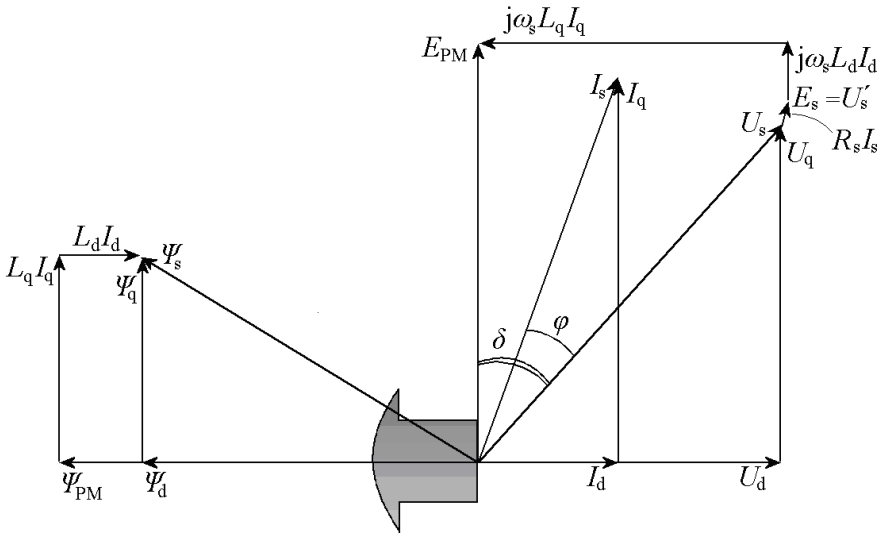

Fig. 2.13 Phasor diagram of a permanent magnet synchronous generator corresponding to Eq. (2.8) with leading power factor.

By solving the current components from Eq. (2.8), we obtain a system of equations

$$\begin{cases} I_\mathrm{d} = \dfrac{E_{PM} - U_\mathrm{s}\cos\delta - R_\mathrm{s} I_\mathrm{q}}{\omega_\mathrm{s} L_\mathrm{d}} \\ I_\mathrm{q} = \dfrac{U_\mathrm{s}\sin\delta + R_\mathrm{s} I_\mathrm{d}}{\omega_\mathrm{s} L_\mathrm{q}} \end{cases} . \tag{2.10}$$

There are two unknown variables and two equations. Therefore, the current components can be solved (Appendix B.3):

$$\begin{cases} I_\mathrm{d} = \dfrac{\omega_\mathrm{s} L_\mathrm{q}\left(E_{PM} - U_\mathrm{s}\cos\delta\right) - R_\mathrm{s} U_\mathrm{s}\sin\delta}{R_\mathrm{s}^2 + \omega_\mathrm{s}^2 L_\mathrm{d} L_\mathrm{q}} \\ I_\mathrm{q} = \dfrac{R_\mathrm{s}\left(E_{PM} - U_\mathrm{s}\cos\delta\right) + \omega_\mathrm{s} L_\mathrm{d} U_\mathrm{s}\sin\delta}{R_\mathrm{s}^2 + \omega_\mathrm{s}^2 L_\mathrm{d} L_\mathrm{q}} \end{cases} . \tag{2.11}$$

The power factor cosφ can be determined from the phase angle between the phase voltage $\underline{U}_s$ and current $\underline{I}_s$. The flux linkages interact with the currents producing torque by the cross product of the orthogonal components of the current and the flux. In addition, the rotor saliency produces some reluctance torque. The electromagnetic time dependent torque $T_e(t)$ written using to the two-axis space vector rotor co-ordinate components is

$$T_e(t) = \frac{3}{2} p\left[\psi_{PM} i_q(t) - \left(L_q - L_d\right) i_d(t) i_q(t) + L_{md} i_D(t) i_q(t) + L_{mq} i_Q(t) i_d(t)\right]. \quad (2.12)$$

In steady-state operation, the damper winding currents are ideally zero. Equation (2.12) may now be written in steady state using the RMS phase current and flux linkage components as

$$T_e = 3p\left[\Psi_{PM} I_q - \left(L_q - L_d\right) I_d I_q\right], \quad (2.13)$$

where

$$\Psi_{PM} = \frac{E_{PM}}{\omega_s} \quad (2.14)$$

By substituting Eq. (2.14) and the current component solutions from Eq. (2.11) into the steady-state Eq. (2.13), the electromagnetic torque is

$$\begin{aligned} T_e = 3p & \left(\frac{R_s\left(E_{PM} - U_s \cos\delta\right) + \omega_s L_d U_s \sin\delta}{R_s^2 + \omega_s^2 L_d L_q} \right) \cdot \\ & \left[\frac{E_{PM}}{\omega_s} + \left(L_d - L_q\right) \left(\frac{\omega_s L_q \left(E_{PM} - U_s \cos\delta\right) - R_s U_s \sin\delta}{R_s^2 + \omega_s^2 L_d L_q} \right) \right] \end{aligned} \quad (2.15)$$

For a non-salient pole PMSG where $L_d = L_q$, Eq. (2.15) can be written in a simpler form:

$$T_e = 3p \left(\frac{E_{PM}}{\omega_s} \frac{R_s\left(E_{PM} - U_s \cos\delta\right) + \omega_s L_d U_s \sin\delta}{R_s^2 + \omega_s^2 L_d^2} \right). \quad (2.16)$$

In a rigid network the amplitude of the grid voltage remains nearly constant. The same procedure may be carried out also in the motor mode. The torque equation including the stator resistance for motor applications according to Gieras (1997) and Parviainen (2005) is

$$T_e = 3p\left\{\frac{U_s E_{PM}\left(R_s\cos(\delta)+\omega_s L_d\sin(\delta)\right)}{\left(\omega_s^2 L_d L_q + R_s{}^2\right)^2}\left\{\left[R_s^2-\omega_s^2 L_q^2\right]-\right.\right.$$
$$U_s E_{PM} R_s\left(\omega_s L_q\cos(\delta)-R_s\sin(\delta)\right)\left(\omega_s L_d-\omega_s L_q\right)+$$
$$U_s^2\left(R_s\cos(\delta)+\omega_s L_d\sin(\delta)\right)\left(\omega_s L_q\cos(\delta)-R_s\sin(\delta)\right)\left(\omega_s L_d-\omega_s L_q\right)-$$
$$\left.\left.E_{PM}^2 R_s\left[\left(\omega_s L_d\omega_s L_q-R_s{}^2\right)-\omega_s L_q\left(\omega_s L_d-\omega_s L_q\right)\right]\right\}\right\} \quad (2.17)$$

When the steady-state electrical parameters of the PMSG are known, the load angle δ can be calculated from Eq. (2.15).

The diagrams of the following figures Figs. 2.14–2.17 illustrate the infinite bus operation of the PMSG having various inductance ratios with saliency ($L_d > L_q$), non-saliency ($L_d \equiv L_q$) and inverse saliency ($L_d < L_q$) in the steady-state. All the figures are drawn by using per unit values given in the figure text but the pu-subscripts have not been shown in the figures for the sake of convenience. In rigid networks the power factor and the load angle of a synchronous generator vary as a function of the load current and the field winding current. PMSGs lack the field windings and the flux produced by permanent magnets can be considered as a fictional fixed field winding current. The grid voltage level is assumed to remain constant.

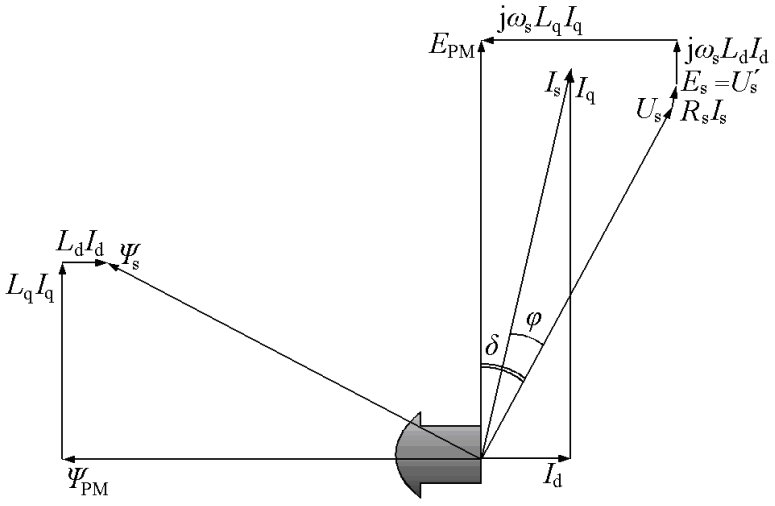

Fig. 2.14 Phasor diagram of a small non-salient pole (the pole in the figure just shows the direction) permanent magnet synchronous generator (L_d/L_q =1) in rigid network operation. The leading power factor is cosφ = 0.96 and the load current is the nominal value of the current. $L_{d,pu}$ = 0.5, $L_{q,pu}$ = 0.5, δ = 28.5°, φ = 15.5°, $E_{PM,pu}$ = 1.04, $U_{s,pu}$ = 1,$I_{s,pu}$ = 1, $R_{s,pu}$ = 0.05.

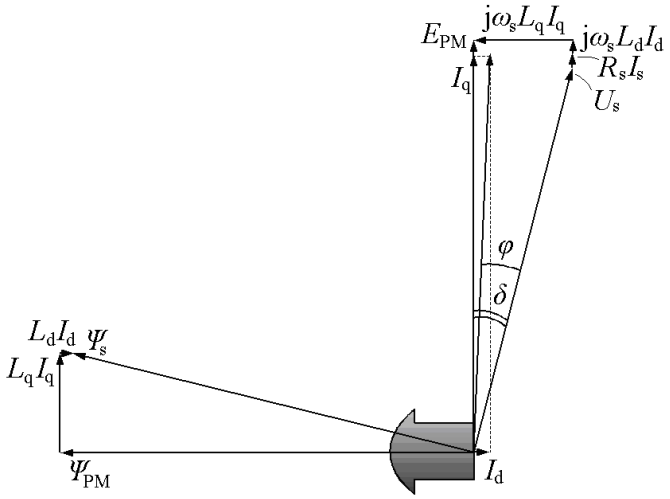

Fig. 2.15 Phasor diagram of a small salient pole permanent magnet synchronous generator ($L_d/L_q = 2$) in rigid network operation. The leading power factor is $\cos\varphi = 0.98$ and the load current is the nominal value of the current. $L_{d,pu} = 0.5$, $L_{q,pu} = 0.25$, $\delta = 14.4°$, $\varphi = 11.9°$, $E_{PM,pu} = 1.04$, $U_{s,pu} = 1$ pu, $I_{s,pu} = 1$, $R_{s,pu} = 0.05$.

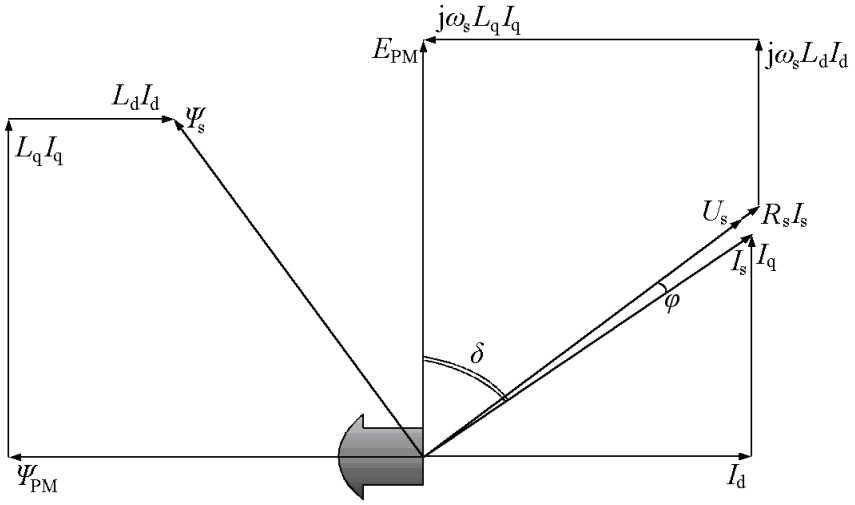

Fig. 2.16 Phasor diagram of a small salient pole permanent magnet synchronous generator with inverse saliency ($L_d/L_q = 1/3$) in rigid network operation. The lagging power factor is $\cos\varphi = 0.999$ and the load current is the nominal value of the current. $L_{d,pu} = 0.5$,$L_{q,pu} = 1.5$, $\delta = 53.3°$,$\varphi = 2.5°$, $E_{PM,pu} = 1.04$, $U_{s,pu} = 1$, $I_{s,pu} = 1$, $R_{s,pu} = 0.05$.

In a rigid network the nominal operating point of the DOL PMSG should be designed for a certain power factor. An acceptable power factor at nominal operation for a DOL PMSG should be selected based on the recommendations of the grid area. Also the load characteristics have to be considered. The generator should have an acceptable power factor in a wide range of power supplied by the generator. Typically, PMSGs produce the inductive current for inductive loads, such as induction motors, solenoids and relays. The effect of the system current on the power factor is illustrated in Fig. 2.17. The results are based on Eqs. (2.8)–(2.15). The effect of the rotor saliency on the power factor is also shown.

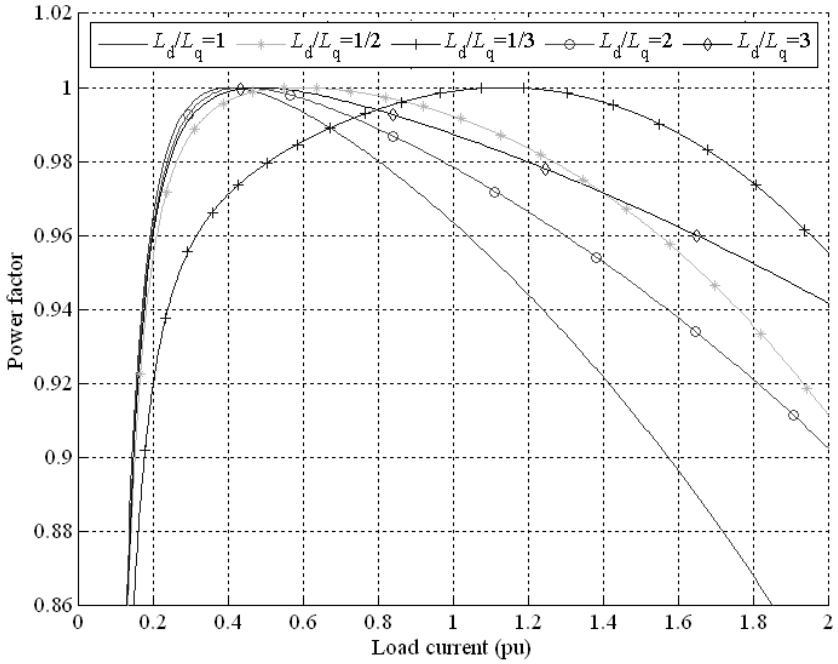

Fig. 2.17 Power factor as a function of the load current when the generator is supplying an infinite bus at $U_{s,pu} = 1.0$ with $E_{PM,pu} = 1.04$ and $R_{s,pu} = 0.05$. The direct-axis synchronous inductance is fixed to $L_d = 0.5$ and the inductance ratio is altered. The inverse saliency seems to improve the generator power factor at higher loads in this case.

When the electromotive force of the generator is larger than 1 pu, the power factor is lagging at low loads. At no-load, the generator is feeding only negative I_d current to the grid. At higher loads, the power factor eventually becomes leading. The back-emf of the generator can be dimensioned in order to gain a certain power factor at some operating point. The phase RMS back-EMF of the PMSG is

$$E_{PM} = U_s \cos\delta + I_d \omega_s L_d + I_q R_s \,. \tag{2.18}$$

If the power factor is fixed, the current components are known from Eq. (2.9). Terminal voltage U_s is defined by Eq. (2.8). The back-emf from Eq. (2.18) is calculated and the corresponding current components are obtained from Eq. (2.11). After the selection of the power factor, the load angle δ is iterated until the length of the current space vector defined by the current components shown in Eq. (2.11) is 1 pu.

The dependence of the electrical parameters and the power factor in a rigid network at a nominal load current for non-salient pole machines, using Eqs. (2.8), (2.9), (2.11), and (2.18), is illustrated in Fig. 2.18. The acceptable values for the DOL PMSG, with the defined limitations and requirements, can be found in the shaded areas.

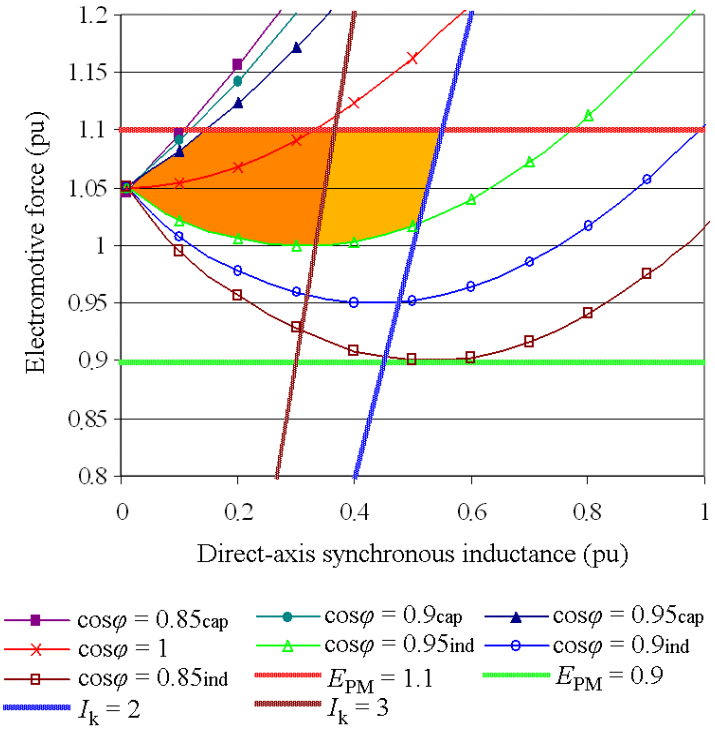

Fig. 2.18. Requirement for the electromotive force of the non-salient pole permanent magnet generator as a function of synchronous inductance with power factor as a variable at nominal load current $I_s = 1$ when $R_{s,pu} = 0.05$. In the figure, the leading and lagging power factors are denoted by the terms ”cap” and ”ind”, respectively. The required short-circuit current condition is fulfilled with the synchronous inductance values lower than the plotted lines $I_{k,pu} = 2$ and $I_{k,pu} = 3$. All the general guidelines are met in the shaded areas.

It was mentioned previously that the saliency of the rotor depends on the rotor structure. The rotors with the pole shoes have saliency. Rotors with magnets assembled on the surface of the rotor are somewhat non-salient, and the direct-axis synchronous inductance is smaller than the quadrature-axis synchronous inductance that can be achieved by the inset magnets. The static power curves based on Eq. (2.15) are shown in Fig. 2.19.

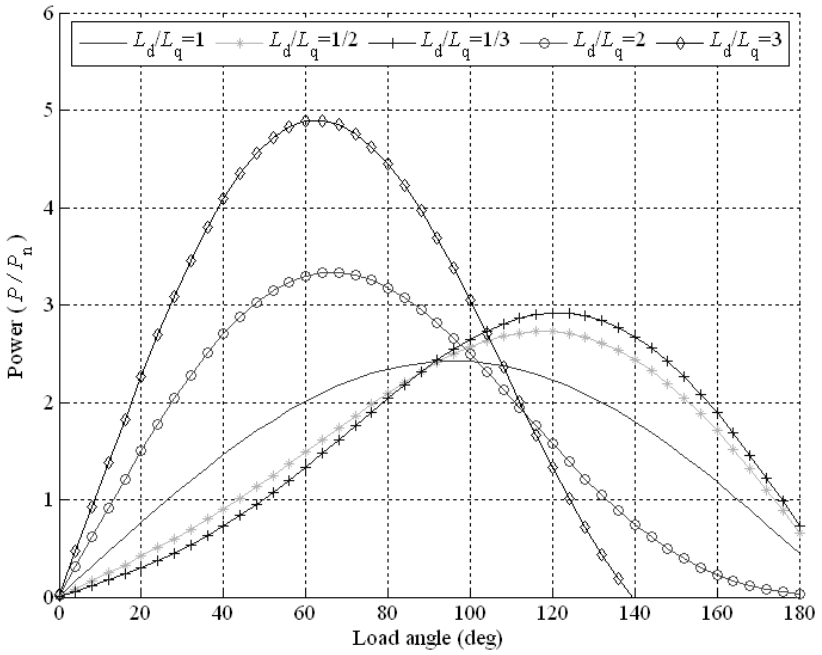

Fig. 2.19. Effect of the saliency ratio on the power versus load angle of the rigid network operated generator. $E_{PM,pu}$ = 1.04, $R_{s,pu}$ = 0.05 and $L_{d,pu}$ = 0.5. The maximum power P/P_n = 2.4 for non-salient pole PMSG is found in this case at δ = 96°. The maximum torque load angle deviates from 90° because of the resistive stator losses.

The non-salient pole PMSG in infinite bus operation has a power ratio $P_{pull\text{-}out}/P_n$ = 2.4. Reluctance torque moves the load angle value of the maximum power.

2.5.2 Island operation

The operation of the PMSG differs in the island operation. In island operation, the grid is weak and its voltage level depends on the generator characteristics. The power factor is determined by the load power factor. The following equations can be written for single isolated generator operation with a lagging power factor of the load. The direct and the quadrature-axis parts of the terminal voltage and current are shown in Eqs. (2.8) and (2.9), see Fig. 2.13.

The terminal phase voltage is dependent on the load characteristics:

$$\underline{U}_s = \underline{Z}\underline{I}_s, \underline{Z} = Z\angle\varphi \ . \tag{2.19}$$

By substituting Eqs. (2.19) and (2.9) into Eq. (2.8):

$$U_d = U_s \sin\delta = \omega_s L_q I_s \cos(\delta+\varphi) - R_s I_s \sin(\delta+\varphi) \ . \tag{2.20}$$

By substituting Eq. (2.19) into Eq. (2.20) and converting the sums of the sine and cosine functions:

$$
\begin{aligned}
ZI_\mathrm{s}\sin\delta &= \omega_\mathrm{s}L_\mathrm{q}I_\mathrm{s}\left(\cos\delta\cos\varphi-\sin\delta\sin\varphi\right)-R_\mathrm{s}I_\mathrm{s}\left(\sin\delta\cos\varphi+\cos\delta\sin\varphi\right)\\
Z\sin\delta &= \omega_\mathrm{s}L_\mathrm{q}\left(\cos\delta\cos\varphi-\sin\delta\sin\varphi\right)-R_\mathrm{s}\left(\sin\delta\cos\varphi+\cos\delta\sin\varphi\right)\\
Z\tan\delta &= \omega_\mathrm{s}L_\mathrm{q}\cos\varphi-\omega L_\mathrm{q}\tan\delta\sin\varphi-R_\mathrm{s}\tan\delta\cos\varphi-R_\mathrm{s}\sin\varphi
\end{aligned}
\qquad (2.21)
$$

The load angle can be calculated:

$$
\begin{aligned}
&\tan\delta\left(Z+\omega_\mathrm{s}L_\mathrm{q}\sin\varphi+R_\mathrm{s}\cos\varphi\right)=\omega_\mathrm{s}L_\mathrm{q}\cos\varphi-R_\mathrm{s}\sin\varphi\\
&\delta=\tan^{-1}\left(\frac{\omega_\mathrm{s}L_\mathrm{q}\cos\varphi-R_\mathrm{s}\sin\varphi}{Z+\omega_\mathrm{s}L_\mathrm{q}\sin\varphi+R_\mathrm{s}\cos\varphi}\right)
\end{aligned}
\quad . \qquad (2.22)
$$

When the load power factor is known, the load current and the terminal phase voltage can be calculated (Appendix B1).

$$
U_\mathrm{s}=\frac{E_\mathrm{PM}Z}{\dfrac{Z^2\sin\delta+Z\sin\delta(\omega_\mathrm{s}L_\mathrm{q}\sin\varphi+R_\mathrm{s}\cos\varphi)}{\omega_\mathrm{s}L_\mathrm{q}\cos\varphi-R_\mathrm{s}\sin\varphi}+X_\mathrm{d}\sin\left(\delta+\varphi\right)+R_\mathrm{s}\cos\left(\delta+\varphi\right)} \qquad (2.23)
$$

The corresponding load current is solved from Eq. (2.19).

$$
\underline{I}_\mathrm{s}=\frac{\underline{U}_\mathrm{s}}{\underline{Z}} \quad . \qquad (2.24)
$$

The following four figures, Figs. 2.20–2.23 illustrate the island operation of permanent magnet generators with saliency, non-saliency and inverse saliency. The stator leakage inductance, electromotive force, stator resistance, and the direct-axis synchronous inductance have been kept constants.

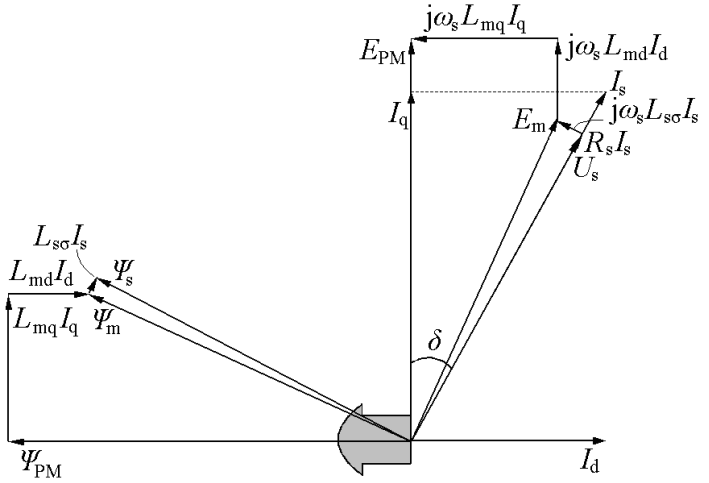

Fig. 2.20 Phasor diagram of a small non-salient pole permanent magnet synchronous generator ($L_\mathrm{q}/L_\mathrm{d}$ = 1) in isolated network operation. The power factor is cosφ = 1 and the load current is the nominal value of the current. $L_\mathrm{d,pu}$ = 0.5, $L_\mathrm{q,pu}$ = 0.5, δ = 28.8°, φ = 0°, $E_\mathrm{PM,pu}$ = 1.04, $U_\mathrm{s,pu}$ = 0.86, $I_\mathrm{s,pu}$ = 1, $R_\mathrm{s,pu}$ = 0.05. The terminal voltage U_s is clearly below the rated value (U_s < 1).

.

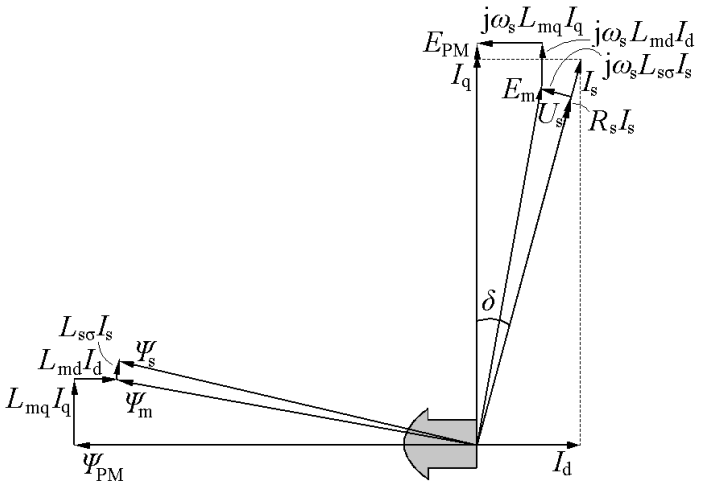

Fig. 2.21 Phasor diagram of a small salient pole permanent magnet synchronous generator. The saliency ratio L_d/L_q=2, cosφ = 1, $L_{d,pu}$ = 0.5, $L_{q,pu}$ = 0.25, δ = 14.9°,φ = 0°, $E_{PM,pu}$ = 1.04, $U_{s,pu}$ = 0.89, I_s = 1 and $R_{s,pu}$ = 0.05. The armature reaction is smaller compared with the non-salient pole machine. Therefore, the load angle δ is also smaller. Nevertheless, the terminal voltage $U_{s,pu}$ is still below the rated value.

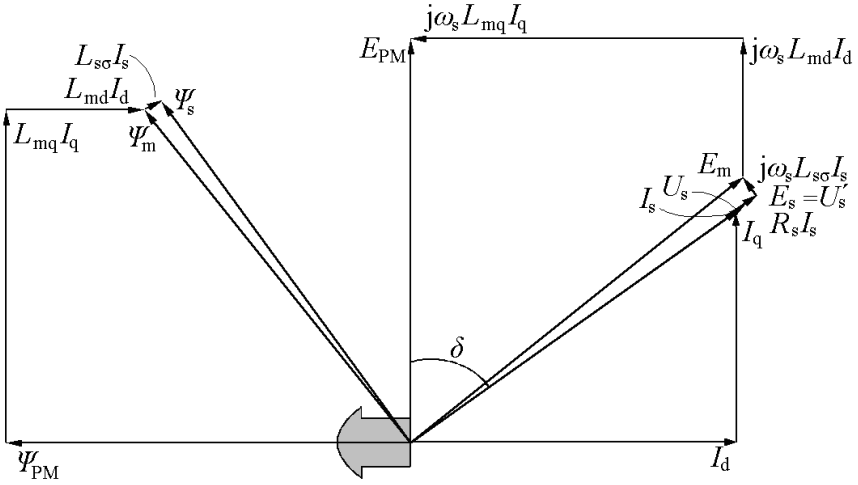

Fig. 2.22 Phasor diagram of a small salient pole permanent magnet synchronous generator with the saliency ratio L_d/L_q = 1/3. cosφ = 1, $L_{d,pu}$ = 0.5, $L_{q,pu}$ = 1.5, δ = 54.2°, φ = 0°, $E_{PM,pu}$ = 1.04, U_s = 1.03, I_s = 1 and $R_{s,pu}$ = 0.05. The terminal voltage can reach the rated line voltage at certain loads despite the armature reaction.

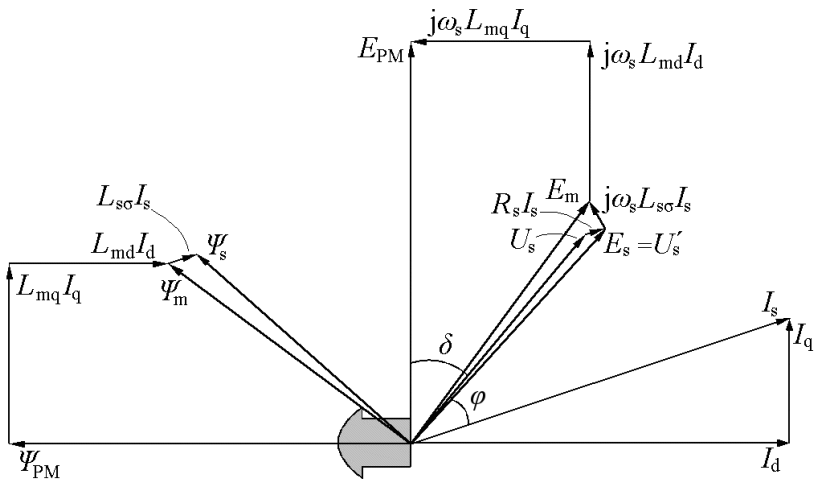

Fig. 2.23 Phasor diagram of a small permanent magnet synchronous generator with the saliency ratio L_d/L_q =1/3 and inductive load power factor cosφ = 0.85$_{ind}$. φ = 31.8°, $L_{d,pu}$ = 0.5, $L_{q,pu}$ = 1.5, δ = 39.0°, $E_{PM,pu}$ = 1.04, $U_{s,pu}$ = 0.71, $I_{s,pu}$ = 1 and $R_{s,pu}$ = 0.05. Inductive load has a remarkable effect on the terminal voltage level. Despite of the inverse saliency of the rotor the terminal voltage is very low compared with the rated value $U_{n,s,pu}$ = 1.

The effect of the saliency on the output power of the PMSG in island operation with resistive load is illustrated in Fig. 2.24, where the load power factor cosφ = 1, $R_{s,pu}$ = 0.05 and $L_{d,pu}$ = 0.5 have been fixed. The equation used for the output power in the island operation is written (Appendix B.2)

$$P = \frac{3E_{PM}^2 Z\cos\varphi}{\left(\dfrac{Z^2\sin\delta + Z\sin\delta(\omega_s L_q\sin\varphi + R_s\cos\varphi)}{\omega_s L_q\cos\varphi - R_s\sin\varphi} + \omega_s L_d\sin(\delta+\varphi) + R_s\cos(\delta+\varphi)\right)^2} \tag{2.25}$$

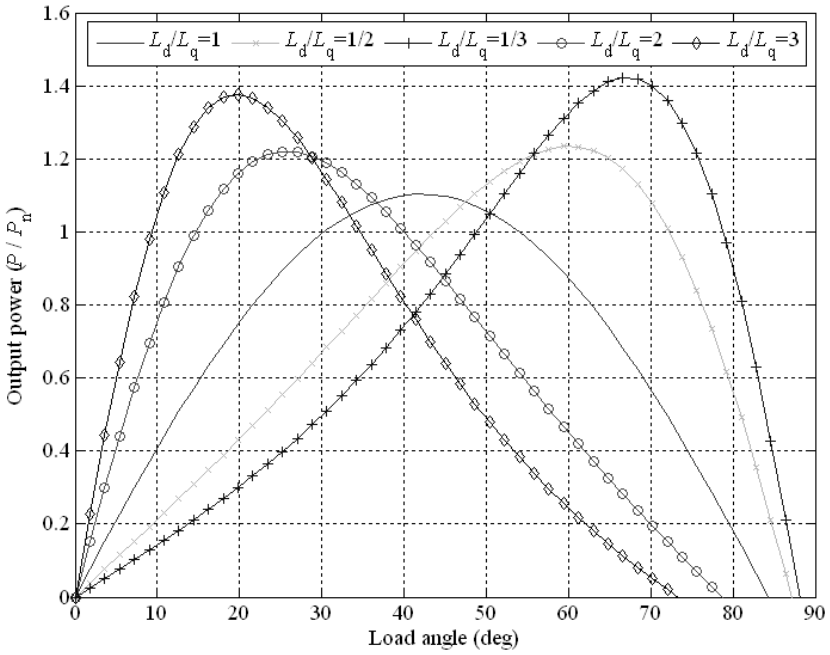

Fig. 2.24 Effect of the saliency ratio on the power versus load angle of the island operated generator at resistive load. The load power factor $\cos\varphi = 1$, $E_{PM,pu} = 1.04$, $R_{s,pu} = 0.05$ and $L_{d,pu} = 0.5$. The maximum output power of non-salient PMSG is much less than in DOL operation ($P_{max}/P_n = 1.1$ in island operation compared with $P_{max}/P_n = 2.42$ in DOL) and the maximum power is found in this case at $\delta = 43°$. By increasing the saliency ratio either way, the pull-out torque is increased. By increasing the inverse saliency ratio the pull-out torque is increased but also the load angle of the partial loads increase significantly.

When $L_d > L_q$ the load angle increases slowly as more output power is required. If $L_d < L_q$ the load angle variation is large at partial loads. With loads having a lagging power factor, the output power characteristics of the PMSG in island operation are different. The effect of the saliency on the output power of the PMSG driving at a lagging power factor load is illustrated in Fig. 2.25.

Increasing the load current continuously drops the terminal voltage. Finally, short circuit current is reached and the terminal voltage is zero. The terminal voltage and power of non-salient pole PMSG in island operation is illustrated in Fig. 2.26.

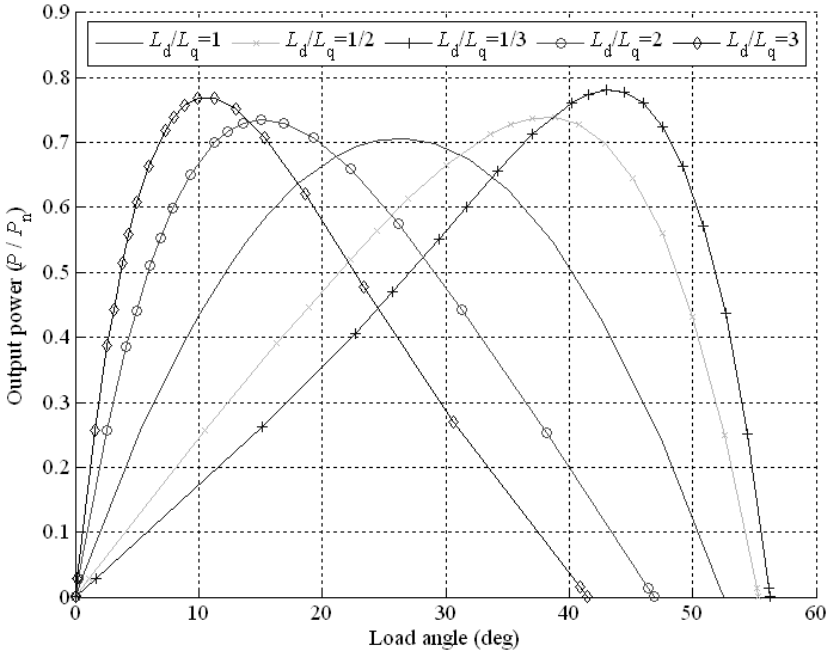

Fig. 2.25 Effect of the saliency ratio on the power versus the load angle of the island generator. The power factor of the inductive load is cosφ = 0.85, $E_{PM,pu,}$ = 1.04, $R_{s,pu}$ = 0.05 and $L_{d,pu}$ = 0.5 have been fixed. When the load is inductive, the effect of saliency is not so significant. The pull-out load angle is less than in the case of the resistive load because of the inductive load.

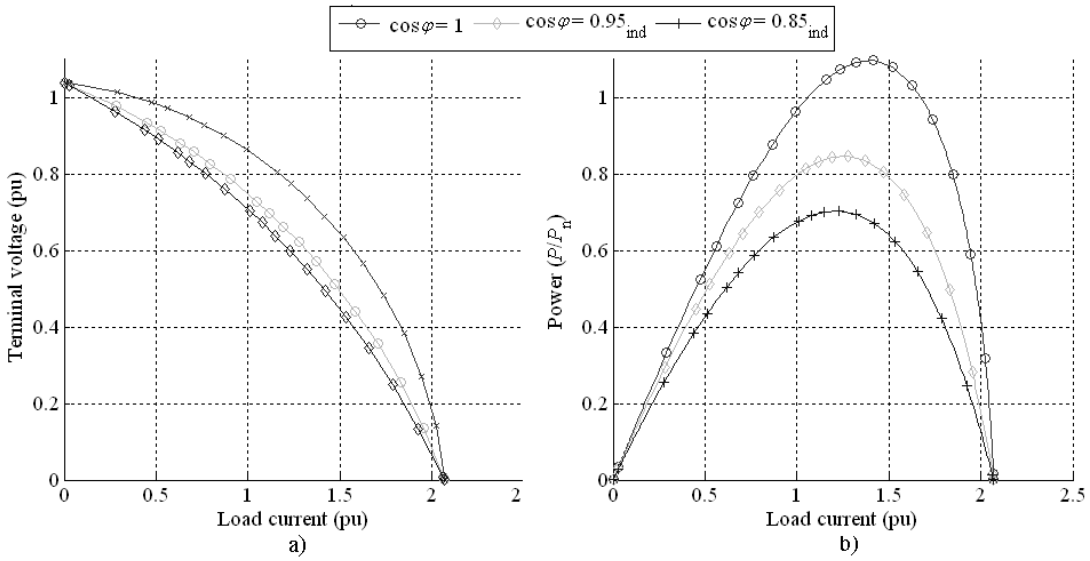

Fig. 2.26 Terminal voltage and power of a non-salient pole PMSG in island operation. a) The terminal voltage drops as the load current increases. The voltage drop is dependent on the load power factor. Sustained short-circuit power may be found from zero terminal voltage. b) Voltage drop affects dramatically the produced power. For resistive loads, the power reaches maximum value of P/P_n = 1.1 when the load current $I_{load,pu}$ = 1.4 .

The synchronous generators drive both leading and lagging power factor loads. In the industry, the induction motors are common lagging power factor loads. If a small

load is fed via long transmission lines, the load seen by the generator can become leading.

Figures 2.19 and 2.24 show the notable difference in the power production when operating with an active load or when supplying only a passive load. The grid acts as an active load, which is capable of maintaining the terminal voltage U_s of the generator independent of the power supplied. If the load is a passive one, the armature reaction caused voltage drop is directly visible in the terminal voltage U_s, and the voltage drops dramatically compared with the active load supply. Fig. 2.27 shows different operation points of a non-salient pole PMSG in island operation supplying resistive load.

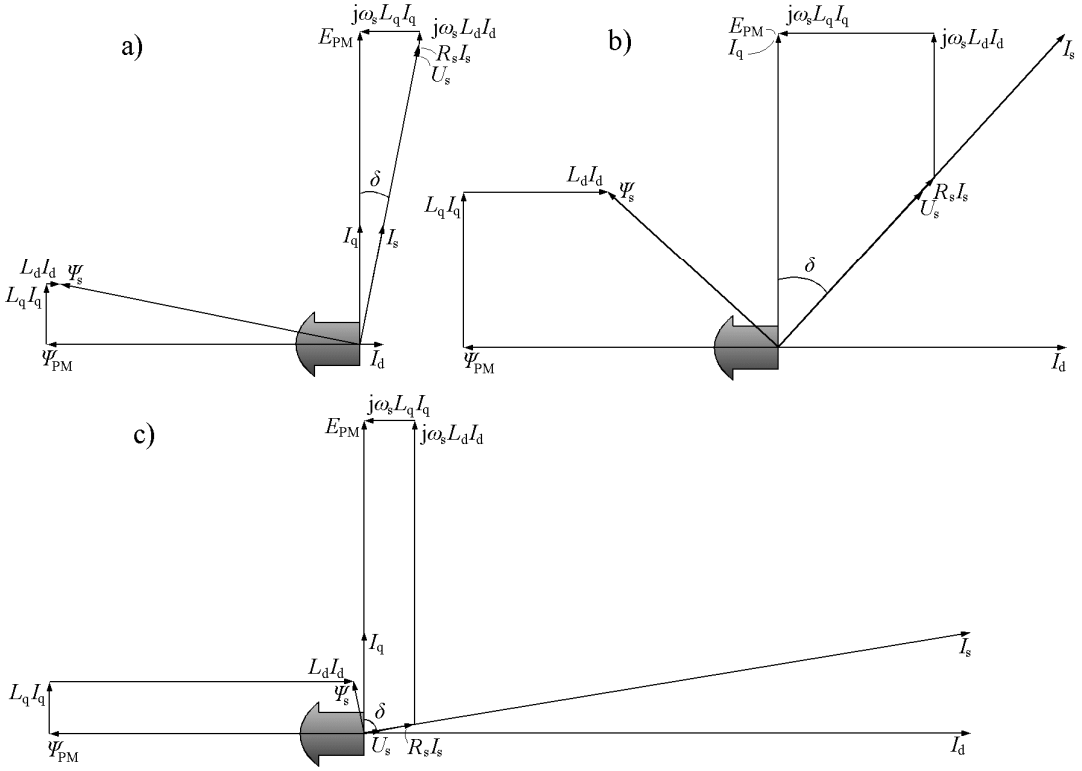

Fig. 2.27. Operation points of a non-salient pole PMSG in island network supplying resistive loads ($\cos\varphi = 1$). a) $I_{load,pu} = 0.40$, $\delta = 11.4°$, $U_{s,pu} = 1$. b) $I_{load,pu} = 1.4$, $\delta = 42.3°$, $U_{s,pu} = 0.70$. c) $I_{load,pu} = 2.05$, $\delta = 80.4°$, $U_{s,pu} = 0.07$.

The nominal operation points of the phasor diagrams illustrated in this chapter for a rigid network and island network operation are summarized in Table 2.3.

Table 2.3 Comparison between a rigid network and isolated network operation.

Rigid network operation				Isolated network operation				
parameter	Fig. 2.14	Fig. 2.15	Fig. 2.16	parameter	Fig. 2.20	Fig. 2.21	Fig. 2.22	Fig. 2.23
$L_{d,pu}$	0.5	0.5	0.5	$L_{d,pu}$	0.5	0.5	0.5	0.5
$L_{q,pu}$	0.5	0.25	1.5	$L_{q,pu}$	0.5	0.25	1.5	1.5
L_d/L_q	1	2	1/3	L_d/L_q	1	2	1/3	1/3
E_{PM}	1.04	1.04	1.04	$E_{PM,pu}$	1.04	1.04	1.04	1.04
$\cos\varphi$	0.96_{lead}	0.98_{lead}	0.999_{lag}	$\cos\varphi$	1	1	1	0.85_{lag}
$I_{s,pu}$	1	1	1	$I_{s,pu}$	1	1	1	1
δ	28.5	14.4	53.3	δ	28.8	14.9	54.2	39.0
$U_{s,pu}$	1	1	1	$U_{s,pu}$	0.86	0.89	1.03	0.71
$R_{s,pu}$	0.05	0.05	0.05	$R_{s,pu}$	0.05	0.05	0.05	0.05
$P_{pull\text{-}out}/P_n$	2.42	3.33	2.91	$P_{pull\text{-}out}/P_n$	1.1	1.22	1.42	0.7

Voltage drop has to be taken into account if the generator is designed for the island operation. For instance, the synchronous pull-out power for the non-salient pole PMSG with given electrical parameters is approximately 64 % of the nominal power in the rigid network, when $\cos\varphi = 0.85$ (see Fig. 2.25). In practice, this means that the permanent magnet generator must be larger in island operation than in network operation if the same output power is desired. When using a synchronous generator with a field winding, the armature reaction effects may be compensated if the field winding thermal design is aimed for island operation or for highly inductive loads. In a permanent magnet machine, this option is not present, and the only possibility is to diminish the stator inductances, which in practice means that the machine size must be larger. This indicates that the permanent magnet synchronous generator is not very suitable for island operation without a static VAr compensator.

Kinnunen et al. (2007b) reported that in island network, it is possible to control the reactive power by an active compensator in parallel with generator to maintain the nominal terminal voltage. The system consisting of a permanent magnet generator equipped with an active compensator that controls the generator voltage is electrically simple because we may assume that the reactive power control is carried out by the power electronic converter. The size of the compensator is smaller than the frequency converter in series with the generator, because the whole power produced by the generator is not fed through the compensator. In addition, in island networks, the frequency converter connected in serial, has to be dimensioned according to the short circuit current of the generator. An example of a PMSG with an active reactive power compensator is shown in Fig. 2.28.

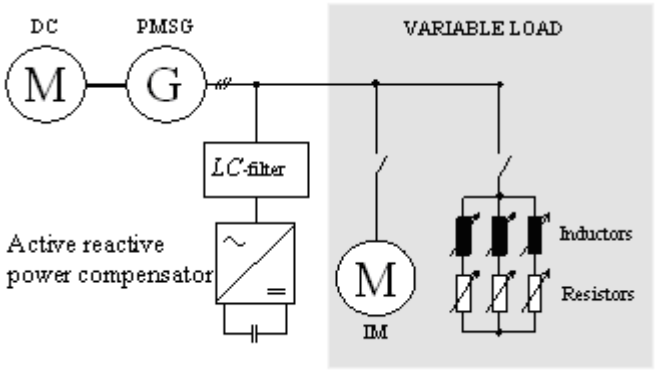

Fig. 2.28. Test setup diagram of the permanent magnet synchronous generator with an active reactive power controller in island operation. The induction motor and the series of passive components are switched on by manually controlled contactors. *LC* filter is added to the system to filter the current harmonics of the compensating current.

There are several possible applications for the DOL PMSGs. One potential alternative is a water power plant. This is a challenging environment for the DOL PMSG designer. The flowing water has an effect on the kinetic energy of the system. Also the water flow rate is not constant. Hydroelectric facilities often depend on a dam to raise the level of the water in the reservoir. Water from this reservoir is allowed to fall through pipes to water-driven turbines. The potential energy of water converted to kinetic energy of the falling water spins the turbines. The turbines are connected to generators that make electricity as they turn. The power that can be harnessed from the falling water through the pipes can be estimated by calculations. An example of a single water power plant pipe diameter dimensioning and the effects of the flowing water on the kinetic energy of the system is proposed by the author in the following equations. The power from the water flow through the pipe is

$$P = \eta \rho g h \dot{V} , \tag{2.26}$$

where η is the efficiency of the turbine (typically 70–90 % depending on the size of the turbine), ρ is the density of the flowing water (1000 kg/m^3), h is the height of the water column and $\dot{V}$ is the volume flow of the water. The volume flow in a cylindrical tube is

$$\dot{V} = \frac{\pi d^2}{4} v \tag{2.27}$$

where d is the tube diameter and v is the velocity of the flowing water. The required diameter for the tube is

$$d = \sqrt{\frac{4P}{\eta \rho g h \pi v}} = 2\sqrt{\frac{P}{\eta \rho g h \pi v}} . \tag{2.28}$$

For example, if we need 50kW power with 85% efficiency when the water column height is 10 meters and the velocity of the flowing water is 3 m/s, the diameter of the tube should be at least 0.50 m.

The kinetic energy of the water column E_k can be converted to mechanical rotational energy. The efficiency in the conversion is around 85% which corresponds to the turbine efficiency. The flowing water column has a kinetic energy

$$E_k = \frac{1}{2}mv^2 = \frac{1}{2}\rho V v^2, \tag{2.29}$$

where V is the volume of the water column. The equation for rotational energy E_r is

$$E_r = \frac{1}{2}J\Omega^2, \tag{2.30}$$

where Ω is the mechanical angular velocity. The equivalent moment of inertia for the water column can be calculated

$$\begin{aligned} &\eta E_k = E_r \Leftrightarrow \eta\frac{1}{2}mv^2 = \frac{1}{2}J\Omega^2 \Leftrightarrow \eta\frac{1}{2}\rho V v^2 = \frac{1}{2}J\Omega^2 \\ &\Rightarrow \eta\rho V v^2 = J\Omega^2 \Rightarrow J = \eta\rho V\left(\frac{v}{\Omega}\right)^2 \end{aligned} \tag{2.31}$$

The extra moment of inertia from the water column for the example presented above for an eight-pole machine rotating 750 rpm is $J = 2.48\text{kgm}^2$. The moment of the rotor inertia of the 50kW permanent magnet generator could be $J_{rotor} = 6\ \text{kgm}^2$. In this example, the water column increases the moment of inertia by about 50%. This extra inertia provided by the flowing water has to be taken into account in the water power applications of the DOL PMSG.

2.6 Methods for determining permanent magnet synchronous machine parameters

Methods to determine the electrical parameters of the machine are based on the international standard IEC 60034-4 with some modifications resulting from permanent magnet excitation. Some analytical methods have also been proposed for parameter calculations. All the presented methods that define the parameters in the direct-axis and the quadrature-axis phasor equivalent circuits can also be performed in practice. The measurement methods selected in this study are described in Fig. 2.29; it illustrates the order of the measurements being performed. First, the stator leakage inductance $L_{s\sigma}$ is measured with the rotor removed. Also the stator resistance R_s can be measured at this point. After the assembly of the rotor, the no-load saturation and the three-phase short-circuit tests are performed in the generator mode. The PMSG is rotated by some prime mover. The electromotive force E_{PM} is determined at no-load conditions. The result of L_d'' from the three-phase short-circuit test can be compared with the value obtained from the variable frequency test with a

locked rotor. Since a permanent magnet machine is not carrying a field winding at all and the corresponding leakage inductance is missing, we define only the sub-transient inductances. The sub-transient inductances are selected, since in the sub-transient inductances of synchronous machines the damper leakage inductances are the dominating ones.

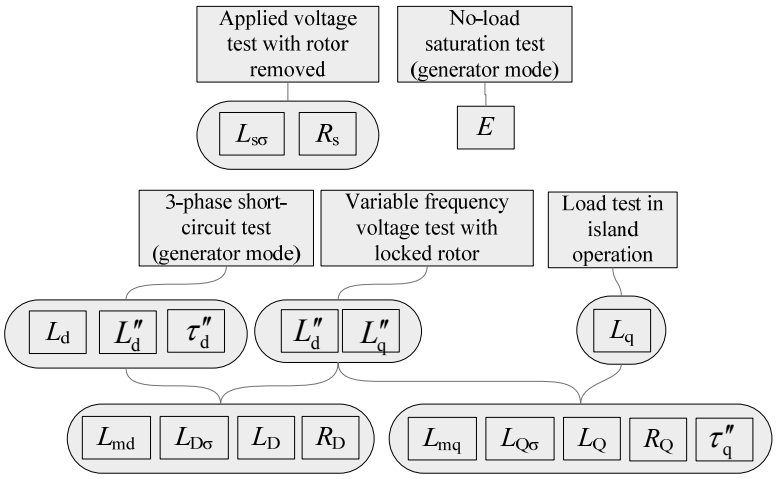

Fig. 2.29 Test methods for determining permanent magnet synchronous machine parameters. The test methods and the corresponding parameters of the generator that can be obtained are presented in the first and second rows. The same parameters can be obtained from different tests, which can be used as a comparison to verify the results. The third row shows the rest of the parameters of the permanent magnet synchronous generator that are calculated based on the results from the first and the second row. The measurements are mainly based on the standard IEC 60034-4.

These tests will be discussed in detail in the following.

2.6.1 Leakage inductance

The stator leakage inductance $L_{s\sigma}$ should be measured at the beginning or at the end of the no-load and load tests, because the rotor has to be removed during the accurate leakage inductance measurements. The stator is supplied from a controllable three-phase voltage source. By controlling the voltage, the stator current is set to its rated value if possible. Despite the missing rotor, the three phase currents create a rotating field in the air gap. The stator represents an impedance $\underline{Z}$. This impedance corresponds to the stator resistance and the stator leakage inductance but also to the air gap field. To extract the effect of the air gap field, a search coil is placed over the teeth. The width of the measuring coil is equal to the pole pitch. The length of the coil equals the stator stack length. The turn number of the measuring coil N_{mc} is known. The larger the number of turns is, the larger the induced voltage in the measuring coil will be. This coil indicates the air gap flux during the measurement. The measuring coil in an axial flux machine is shown in Fig. 2.30.

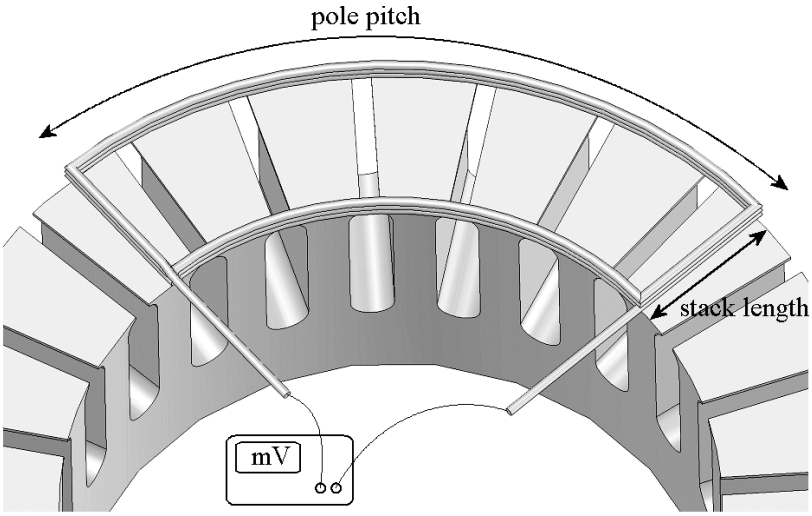

Fig. 2.30 Leakage inductance measurement. The measuring coil is placed over pole pitch to determine the air gap field.

When the armature windings are connected to the three-phase voltage source the phase voltage U_s, the phase current $I_{s,}$ and the phase power P_{ph} are measured. The induced voltage U_{mc} in the measurement coil should be measured accurately, because in small machines, the voltage level of the measurement coil is typically in the range of mV.

$L_{s\sigma}$ can be determined as:

$$L_{s\sigma} = L_s - L_a, \tag{2.32}$$

where

$$\begin{aligned} L_s &= \frac{\sqrt{Z^2 - R_s^2}}{\omega}, \\ Z &= \frac{U_s}{I_s}, \\ R_s &\approx \frac{P}{3I_s^2} = \frac{P_{ph}}{I_s^2} \end{aligned} \tag{2.33}$$

The inductance of the stator bore without the rotor L_a can be written as:

$$L_a = \frac{U_{mc} N_s k_w}{\omega_s I_s N_{mc}}. \tag{2.34}$$

$N_s k_w$ is the effective number of turns in the stator. According to the standard IEC 60034-4, without the measurement coil, the inductance of the stator bore without the rotor can be estimated as

$$L_{\mathrm{a}} \approx \frac{15\left(N_{\mathrm{s}} k_{\mathrm{w}}\right)^2 f_{\mathrm{s}} L'}{\omega_{\mathrm{s}} p} 10^{-8}, \tag{2.35}$$

where f_{s} is the supply frequency, p the number of pole pairs and L' is the effective length of the stator stack.

2.6.2 Synchronous inductances

Direct-axis synchronous inductance is determined from the no-load saturation test and the three-phase short-circuit test. In the no-load saturation test, the tested PMSM operates as a generator by some prime mover with a constant rotation speed. The armature winding is open-circuited and the terminal voltages are measured. The short-circuit test is made from the no-load saturation test by short-circuiting the terminals of the tested PMSG. After short-circuiting the terminals, the subtransient terminal currents stabilize into the sustained values of short-circuit currents. An example of the combination of the no-load saturation test and the short-circuit test is illustrated in Fig. 2.31.

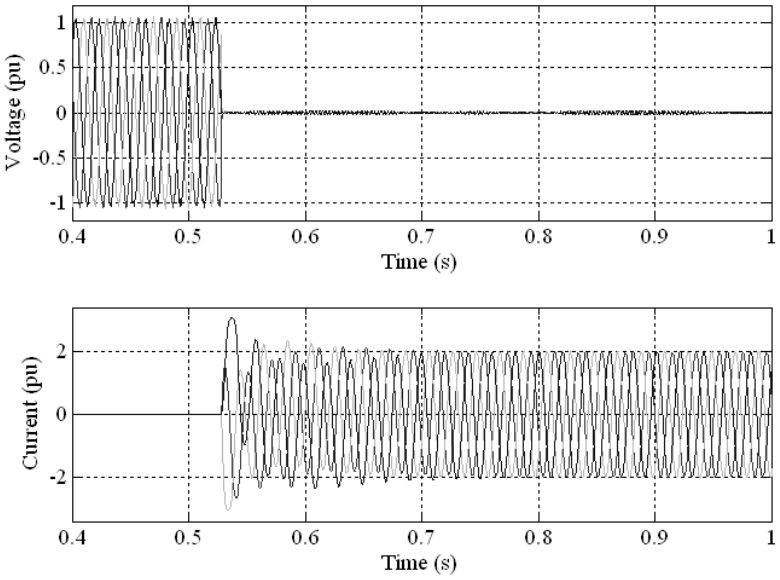

Fig. 2.31 Short-circuit test after no-load saturation test at 50 Hz. The permanent magnet machine is operating at no-load, rotating with constant speed. At time t = 0.52s a sudden three-phase short-circuit is applied. The subtransient currents dampen into the sustained short-circuit current values.

The direct-axis synchronous inductance is determined by the quotient of the open-circuit phase $U_{\mathrm{s,oc}}$ voltage and the sustained short-circuit current $I_{\mathrm{s,ssc}}$.

$$L_{\mathrm{d}} = \frac{U_{\mathrm{s,oc}}}{\omega_{\mathrm{s}} I_{\mathrm{s,ssc}}} \tag{2.36}$$

The quadrature-axis synchronous inductance L_{q} can now be calculated from the steady-state load test. The calculation is based on the dq-axis phasor diagram. The

condition is that the L_d is known from the previous short-circuit test. The permanent magnet machine can be operated either in the motor mode or generator mode. The quadrature-axis synchronous inductance can also be calculated from the measurements in the island operation of a PMSG by using the phasor diagram.

The following equations are given for the test procedure in the generator mode with lagging power factor load. The direct and the quadrature-axis parts of the terminal voltage are shown in Eq. (2.8). The current components are shown in Eq. (2.9)
By substituting Eq. (2.9) into Eq. (2.8)

$$U_s \cos\delta = E_{PM} - I\sin(\delta+\varphi)\omega_s L_d - I\cos(\delta+\varphi)R_s \tag{2.37}$$

Knowing that

$$\begin{aligned}\sin(\delta+\varphi) &= \sin\delta\cos\varphi + \cos\delta\sin\varphi \\ \cos(\delta+\varphi) &= \cos\delta\cos\varphi - \sin\delta\sin\varphi\end{aligned} \tag{2.38}$$

$$\begin{aligned}&E_{PM} - \omega_s L_d I(\sin\delta\cos\varphi + \cos\delta\sin\varphi) - R_s I(\cos\delta\cos\varphi - \sin\delta\sin\varphi) = U_s\cos\delta \\ &E_{PM} + \sin\delta(-\omega L_d I\cos\varphi + R_s I\sin\varphi) + \cos\delta(-\omega_s L_d I\sin\varphi - R_s I\cos\varphi - U_s) = 0 \\ &E_{PM} + A\sin\delta + B\cos\delta = 0, \\ &A = -\omega_s L_d I\cos\varphi + R_s I\sin\varphi, \\ &B = -\omega_s L_d I\sin\varphi - R_s I\cos\varphi - U_s\end{aligned} \tag{2.39}$$

By inserting

$$\sin\delta = \sqrt{1-\cos^2\delta} \tag{2.40}$$

into Eq. (2.39), Eq. (2.39) can be rewritten as

$$\begin{aligned}&E_{PM} + A\sqrt{1-\cos^2\delta} + B\cos\delta = 0 \Leftrightarrow \\ &(A^2+B^2)\cos^2\delta + 2E_{PM}B\cos\delta + (E_{PM}^2 - A^2) = 0\end{aligned} \tag{2.41}$$

The load angle is

$$\delta = \arccos\left(\frac{-2E_{PM}B \pm \sqrt{(E_{PM}B)^2 - 4(A^2+B^2)(E_{PM}^2 - A^2)}}{2(A^2+B^2)}\right) \tag{2.42}$$

The quadrature-axis synchronous inductance is solved by substituting Eq. (2.42) into Eq. (2.20):

$$U_{\mathrm{d}} = -U_{\mathrm{s}} \sin\delta = \omega_{\mathrm{s}} L_{\mathrm{q}} I \cos(\delta+\varphi) - R_{\mathrm{s}} I \sin(\delta+\varphi) \Rightarrow$$

$$L_{\mathrm{q}} = \frac{-U_{\mathrm{s}} \sin\delta + I \sin(\delta+\varphi) R_{\mathrm{s}}}{\omega_{\mathrm{s}} I \cos(\delta+\varphi)}, \qquad . \qquad (2.43)$$

$$\delta = \arccos\left(\frac{-2E_{\mathrm{PM}} B \pm \sqrt{(E_{\mathrm{PM}} B)^2 - 4(A^2+B^2)(E_{\mathrm{PM}}^2 - A^2)}}{2(A^2+B^2)} \right)$$

Now that the synchronous inductances and the stator leakage inductance are known, the magnetizing inductances can be estimated by subtracting the leakage inductance from the synchronous inductances.

2.6.3 Subtransient inductances

Because of their simplicity, this section focuses on the methods in the standard IEC 60034-4. It describes the applied voltage test with the rotor locked in direct- and quadrature-axis positions and the same test with the locked rotor in any arbitrary position. This method is used to determine the damper winding parameters.

First, the direct-axis and quadrature-axis positions of the rotor are determined. Fixed rotor positions are defined by applying DC current into any two line terminals of the armature winding. It is also possible to connect one phase coil branch in series with the parallel connection of the other two phase coil branches and let a DC current run in the windings. The rotor aligns with the flux created by the DC-current-fed phase coils. If the polarity of the DC current is changed, the rotor should align accordingly. These positions are determined as d-axis positions, and the q-axis position is in the middle of these two d-axis positions.

To determine the subtransient inductances, instead of DC current, AC voltage with different frequencies is applied to the same configuration. Possible configurations of the tests are presented in Fig. 2.32.

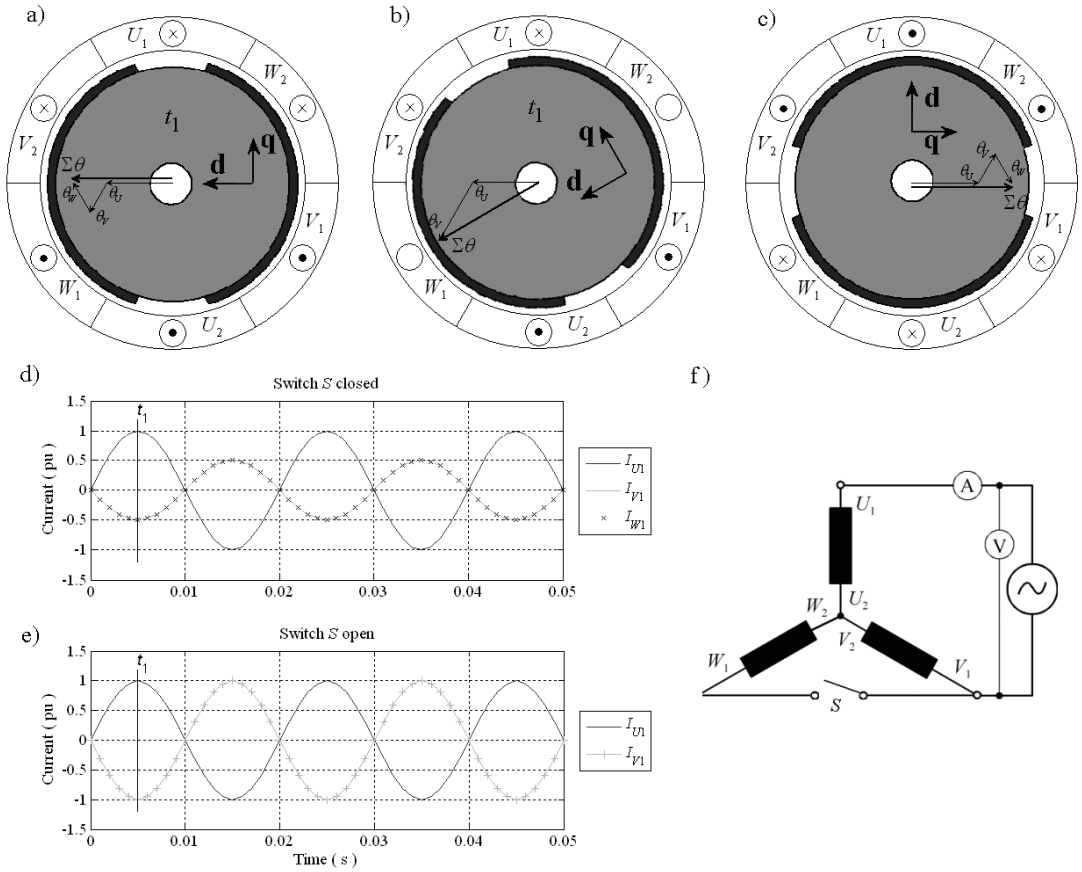

Fig. 2.32 Configuration alternatives of the tests at standstill. Single-phase fed coils produce pulsating flux. a) At time t_1, when the switch S is closed, the rotor is aligned with the resulting pulsating flux of the phase coils into d-axis position. b) At time t_1, when the switch S is open, the rotor aligns into another position of the resulting flux of the phase coils. c) At time t_1, when the switch S is closed, the rotor may be fixed into q-axis position, where flux from the magnets is normal to the resulting flux of the phase coils. d) If the switch S is open, at time t_1, one phase has maximum current amplitude, the second ones have half of the negative maximum current. e) If the switch S is closed, at time t_1, one phase has maximum current amplitude, the second one has negative maximum current. f) The connection factor $K_{con} = 2/3$ if the switch S is closed and $K_{con} = ½$ if the switch S is open.

In this test, the equivalent circuits are similar to the equivalent circuits of the transformer. The total resistance consists of the stator resistance in series with the parallel connection of the damper winding resistance and iron loss resistance. The total inductance consists of the stator leakage inductance in series with the parallel connection of the damper winding leakage inductance and magnetizing inductance. The stator field does not rotate, but it pulsates. Therefore, there are no additional voltage terms because of the rotation of the rotor. The equivalent circuits at standstill are presented in Fig. 2.33.

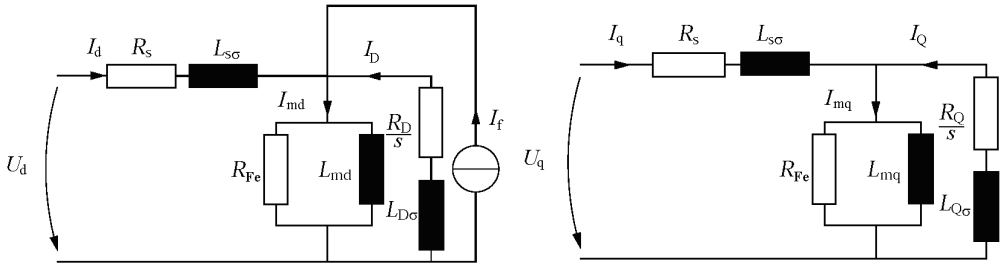

Fig. 2.33 Equivalent circuits of the PMSM during the applied voltage test with a locked rotor. a) Direct-axis. b) Quadrature-axis.

The direct-axis subtransient inductance in the first test with the rotor fixed in the direct-axis position is determined by the formula

$$L_{\mathrm{d}}'' = \frac{\sqrt{Z_{\mathrm{d}}''^2 - R_{\mathrm{d}}''^2}}{\omega_{\mathrm{s}}}. \tag{2.44}$$

If the voltage is applied to two line terminals

$$L_{\mathrm{d}}'' \approx \frac{U_{\mathrm{s}}}{2I\omega_{\mathrm{s}}}, R_{\mathrm{d}}'' = \frac{P}{2I_{\mathrm{s}}^2} \quad , \tag{2.45}$$

or if one phase coil branch is in series with the parallel connection of the other two phase coil branches

$$L_{\mathrm{d}}'' \approx \frac{2U_{\mathrm{s}}}{\omega_{\mathrm{s}} 3I_{\mathrm{s}}}, R_{\mathrm{d}}'' = \frac{2P_{\mathrm{ph}}}{3I_{\mathrm{s}}^2} \ . \tag{2.46}$$

The values of the voltage, current and input power or power factor are measured. The quadrature-axis subtransient inductance is measured in the same way with the rotor fixed in the quadrature-axis position.

If the determination of the direct and quadrature-axis positions is problematic, the same configuration can be used with the rotor fixed in any arbitrary position. The inductance between each pair of the line terminals of the armature winding is calculated with Eq. (2.44). Note that the rotor is fixed in the same position when the test voltage is applied to the three different pairs of the terminals. The subscripts are selected according to the terminals to which the voltage is applied. The direct and quadrature-axis subtransient inductances are:

$$L''_{\mathrm{d}} = \frac{L_{\mathrm{UV}} + L_{\mathrm{VW}} + L_{\mathrm{WU}}}{3} \pm \Delta L$$
$$, \qquad (2.47)$$
$$L''_{\mathrm{q}} = \frac{L_{\mathrm{UV}} + L_{\mathrm{VW}} + L_{\mathrm{WU}}}{3} \mp \Delta L$$

where

$$\Delta L = \frac{2}{3}\sqrt{L_{\mathrm{UV}}\left(L_{\mathrm{UV}} - L_{\mathrm{VW}}\right) + L_{\mathrm{VW}}\left(L_{\mathrm{VW}} - L_{\mathrm{WU}}\right) + L_{\mathrm{WU}}\left(L_{\mathrm{WU}} - L_{\mathrm{UV}}\right)}. \qquad (2.48)$$

The sign of Eq. (2.47) is determined from the rotor structure. Usually in surface magnet permanent magnet machines the permanent magnets slightly saturate the stator. Therefore the minus sign is selected for the direct-axis subtransient inductance. If the permanent magnet machine rotor has some saliency, the rotor construction has to be known and the ± sign is selected accordingly. In permanent magnet machines the saliency ratio $L_{\mathrm{d}}/L_{\mathrm{q}}$ may vary around 1 in both directions. In machines with embedded magnets $L_{\mathrm{d}}/L_{\mathrm{q}} < 1$. With surface magnets, depending on the rotor magnetic circuit construction $L_{\mathrm{d}}/L_{\mathrm{q}}$ may vary from slightly below 1 to slightly above 1.

2.6.4 Damper winding parameters

Damper winding leakage inductances can be determined from the equations based on the equivalent circuits of the PMSM. It is worth bearing in mind that if the frequency of the flux in the rotor is high, the flux may not penetrate the entire rotor because of the eddy currents. Therefore the skin depth of the materials used in the rotor must be calculated. The subtransient inductances are defined by a connection of the stator leakage inductance $L_{\mathrm{s}\sigma}$ in series with the parallel connection of the damper winding leakage inductance and the magnetizing inductance (Vas 1998; see Figs. 2.12 and 2.33):

$$L''_{\mathrm{d}} = L_{\mathrm{s}\sigma} + \frac{L_{\mathrm{md}} L_{\mathrm{D}\sigma}}{L_{\mathrm{md}} + L_{\mathrm{D}\sigma}},$$
$$\qquad (2.49)$$
$$L''_{\mathrm{q}} = L_{\mathrm{s}\sigma} + \frac{L_{\mathrm{mq}} L_{\mathrm{Q}\sigma}}{L_{\mathrm{mq}} + L_{\mathrm{Q}\sigma}}.$$

In the case of classical field winding in the expression for L''_{d} there is also leakage inductance of field winding. There are no equivalent parameters in PMSG for field winding leakage inductance $L_{\mathrm{F}\sigma}$ or field winding resistance R_{F}. The direct- and quadrature-axis leakage inductances solved from Eq. (2.49) are:

$$L_{\mathrm{D}\sigma} = \frac{L_{\mathrm{md}}\left(L''_{\mathrm{d}} - L_{\mathrm{s}\sigma}\right)}{L_{\mathrm{md}} - L''_{\mathrm{d}} + L_{\mathrm{s}\sigma}},$$
$$L_{\mathrm{Q}\sigma} = \frac{L_{\mathrm{mq}}\left(L''_{\mathrm{q}} - L_{\mathrm{s}\sigma}\right)}{L_{\mathrm{mq}} - L''_{\mathrm{q}} + L_{\mathrm{s}\sigma}}. \tag{2.50}$$

The characteristics of the damper winding parameters are highly dependent on the frequency. In DOL PMSGs various load transients and grid connections produce varying flux components into the damper windings with a large range of frequencies. Also the harmonics in the flux through the damper windings have an effect on the damper winding parameters. Therefore, frequencies other than the nominal frequency of the generator should also be tested. The frequency response characteristics and damper winding parameters are determined with the applied variable frequency voltage test at standstill. Testing is obtained for both direct and quadrature-axis positions. The impedance of the circuit at standstill is:

$$\underline{Z} = \frac{\underline{U}}{\underline{I}} K_{\mathrm{con}} \quad , \tag{2.51}$$

where K_{con} depends on the connections of the armature windings. K_{con} is used in the scaling of the damper winding parameter results. Two possible connections are given in Fig. 2.32 with the connection factors.

The values of the inductances and resistances were determined by the phase angle φ_{t} between the test voltage and the induced current:

$$L''_{\mathrm{d,q}} = \frac{\mathrm{Im}\left(Z_{\mathrm{d,q}}\right)}{\omega_{\mathrm{s}}} = \frac{Z_{\mathrm{d,q}} \sin\varphi_{\mathrm{t}}}{\omega_{\mathrm{s}}}, \tag{2.52}$$

$$R_{\mathrm{d,q}} = \mathrm{Re}\left(Z_{\mathrm{d,q}}\right) = Z_{\mathrm{d,q}} \cos\varphi_{\mathrm{t}}. \tag{2.53}$$

The values for the damper winding leakage inductance and damper winding resistance can now be calculated. The damper winding resistance seen by the stator is:

$$R_{\mathrm{D,Q}} = R_{\mathrm{d,q}} - R_{\mathrm{s}} \tag{2.54}$$

If the iron losses are taken into account (see Fig. 2.33), the damper winding resistance seen by the stator becomes:

$$R_{\mathrm{D,Q}} = \frac{R_{\mathrm{Fe}}\left(R_{\mathrm{d,q}} - R_{\mathrm{s}}\right)}{R_{\mathrm{s}} + R_{\mathrm{s}} - R_{\mathrm{d,q}}} \tag{2.55}$$

The slip of the rotor must be taken into account when the damper winding resistances are determined. When the slip is taken into account, the damper winding resistances are:

$$R_{\mathrm{D,Q}}(s) = R_{\mathrm{D,Q}} + \frac{R_{\mathrm{D,Q}}(1-s)}{s} = \frac{R_{\mathrm{D,Q}}}{s}. \tag{2.56}$$

2.6.5 Time constants

Permanent magnet synchronous machines do not include excitation windings. Therefore PMSM has only one time constant from the subtransient state to the sustained state. The subtransient time constant may be determined for the open-circuit and short-circuit states in both direct- and quadrature-axis positions. In reality, the time constant of the permanent magnet synchronous generator is somewhere between these extremes depending on the load impedance, as discussed in section 2.3.

The direct-axis subtransient short-circuit time constant τ_{d}'' may be determined from the three-phase short-circuit test presented in section 2.6.2. τ_{d}'' is the time required for the subtransient currents to decay to 1/e ≈ 0.368 of its initial value. In the determination of τ_{d}'' the envelope curves of the short-circuit current are utilized. The subtransient current component may be separated from the envelope curves of the short-circuit currents by subtracting the sustained short-circuit current component. The remaining part is plotted on a semi-log scale, from which the direct-axis subtransient short-circuit time constant may be determined. The determination of the τ_{d}'' is shown in Figs. 2.34 and 2.35.

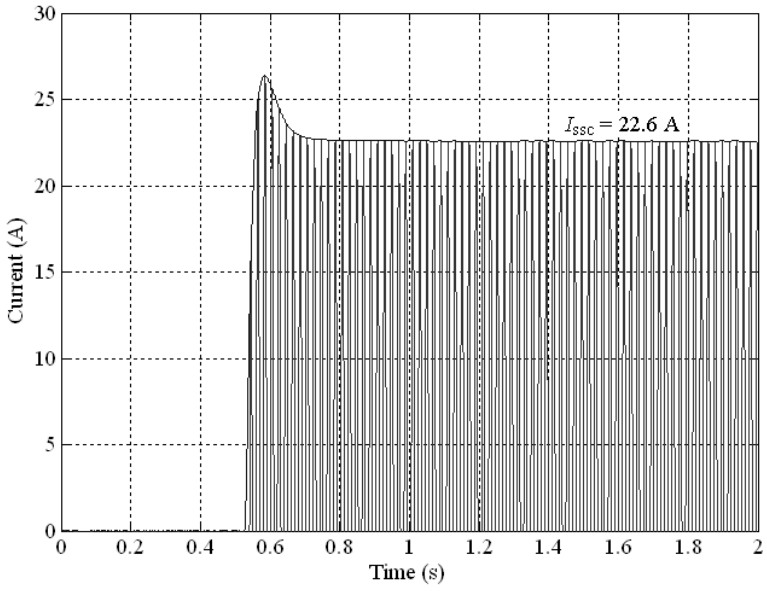

Fig. 2.34 Short-circuit current and the upper envelope curve. Sustained short-circuit current amplitude is 22.6A.

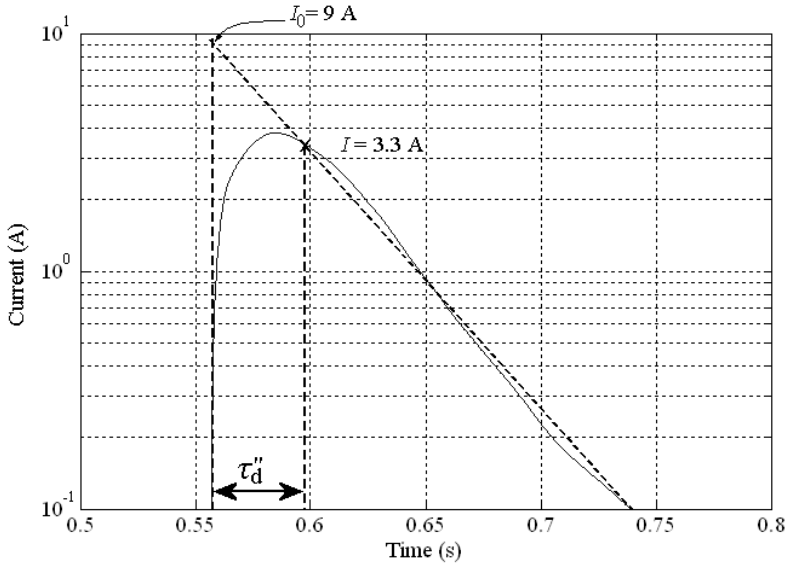

Fig. 2.35 Subtransient current component extracted from the previous figure. The sub-transient component has to start from zero value but it soon reaches its maximum and starts decaying at the rate defined by the appropriate time constant. The initial value for the decaying current I_0 is defined by extrapolating the curve plotted on the logarithmic scale. τ''_d = 0.035s is the time required for the subtransient current component to decay to 1/e ≈ 0.368 of its initial value from I_0 = 9A to I = 3.3A.

The maximum extrapolated current is 9 A. Now the direct-axis subtransient short-circuit time constant is the time τ''_d = 0.035s.

The quadrature-axis subtransient short-circuit time constant may be found from the parameters determined so far; the same can be done for the direct-axis subtransient short-circuit time constant.

$$\tau''_Q = \frac{1}{R_Q}\left(\frac{L_{mq}L_{s\sigma}}{L_{mq}+L_{s\sigma}} + L_{Q\sigma}\right)$$
$$\tau''_D = \frac{1}{R_D}\left(\frac{L_{mq}L_{s\sigma}}{L_{mq}+L_{s\sigma}} + L_{D\sigma}\right) \qquad (2.57)$$

The subtransient parameters determined from the three-phase short-circuit test should be defined with an experiment in which the rotation speed remains as constant as possible. A high torque component exists at the beginning of the three-phase short-circuit. This may rapidly decrease the rotation speed and distort the results.

The result of the direct-axis subtransient inductance L''_d from section 2.6.3 can be compared with the value obtained from the three-phase short circuit test shown in Fig. 2.35. The L''_d can be calculated by applying the quotient of the phase electromotive force E_{PM} and the subtransient short-circuit current I''. I'' is sum of the initial value of the decaying current and sustained short-circuit current.

$$I'' = I_0 + I_{ssc}$$
$$L_d'' = \frac{E_{PM}}{\omega_s I''} \tag{2.58}$$

2.7 Summary

The main characteristics of radial flux and axial flux machines were introduced. Some construction topologies of permanent magnet synchronous machines with damper windings were shown to give the reader a better understanding of the subject. Standards together with general regulations and recommendations concerning grid connections and micro-scale distributed generation were briefly discussed. PMSG performance in a rigid network and island operation was discussed and shown by figures and equations. Comparison showed that the size of the PMSG must be larger in island operation to produce the same power as in rigid network operation because of the passive load. The determination of PMSG electrical parameters by practical measurements was based on standards. Now that the static performance is analyzed, it is important for DOL PMSGs to analyze the dynamic performance, which is investigated by a simulation model in Chapter 3.

3 Simulation model for the permanent magnet synchronous generator

In the following chapter, a simulation model of PM machine is introduced. The model is based on generally known equations. By analyzing the results given by the two-axis space vector equivalent circuit based simulation model of the PM machine, it is possible to generate the guidelines for efficient damper winding parameters for DOL PMSGs. The simulation model is used to simulate grid connections and load transients. The effects of the electrical parameters, especially the damper winding parameters, on the performance are simulated and examined.

The simulation model employs some simplifications compared with the real situation. This is useful when the basic characteristics of different torque components are analyzed. The simulation model does not include the effects of saturation or the effects of temperature variation. Therefore the inductance and the resistance values are fixed. The electric grid is assumed to have infinite capacity and the network impedance seen by the generator is zero. The grid voltage amplitude remains constant. The grid produces purely sinusoidal signals. Also the induced EMF is sinusoidal.

3.1 Two-axis theory

The simulation model lays the foundations for an extensive parameter survey for damper winding parameters. The simulation model operates with space vector quantities on the rotor-oriented dq-coordinates. The derivation of the dq-components from three phase stator-oriented coordinates are demonstrated in Appendix D.1. The direct-axis (d) and quadrature-axis (q) equivalent circuits are shown in Fig. 3.1. The main parts of the simulation model are given in Fig. 3.2. The directions of the currents are selected based on the motor logic, and therefore the signs of currents are opposite compared with for instance the dq-currents shown in Eq. (2.10).

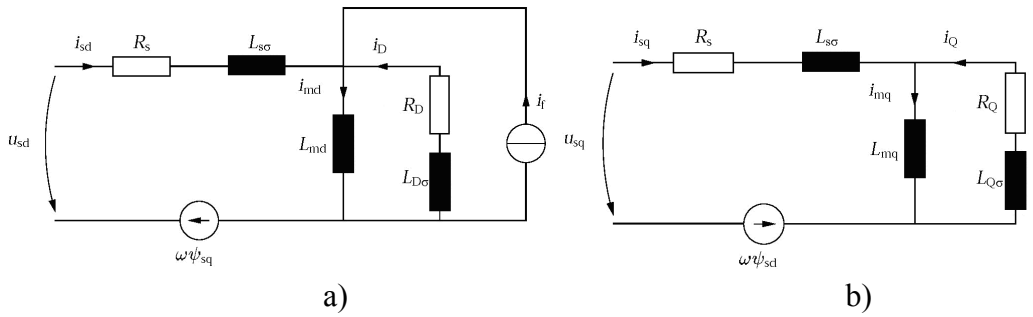

Fig. 3.1. Equivalent circuits of permanent magnet synchronous machines provided with damper windings. a) Direct-axis quantities. b) Quadrature-axis quantities.

$i_{d,q}$ are stator currents, $i_{md,q}$ are magnetizing currents, $i_{D,Q}$ are damper winding currents, i_f is the equivalent current for flux linkage $L_{md,q}$ are magnetizing inductances, $L_{s\sigma}$ is the stator leakage inductance, $L_{D,Q\sigma}$ are damper winding leakage inductances, ψ_{PM} caused by the permanent magnets as a product of virtual excitation current i_f and direct-axis magnetizing inductance L_{md} ($\psi_{PM} = L_{md}i_f$), R_s is the stator

resistance, $R_{D,Q}$ are damper winding resistances, ω is the rotor electrical angular frequency and $\psi_{d,q}$ are stator flux linkages.

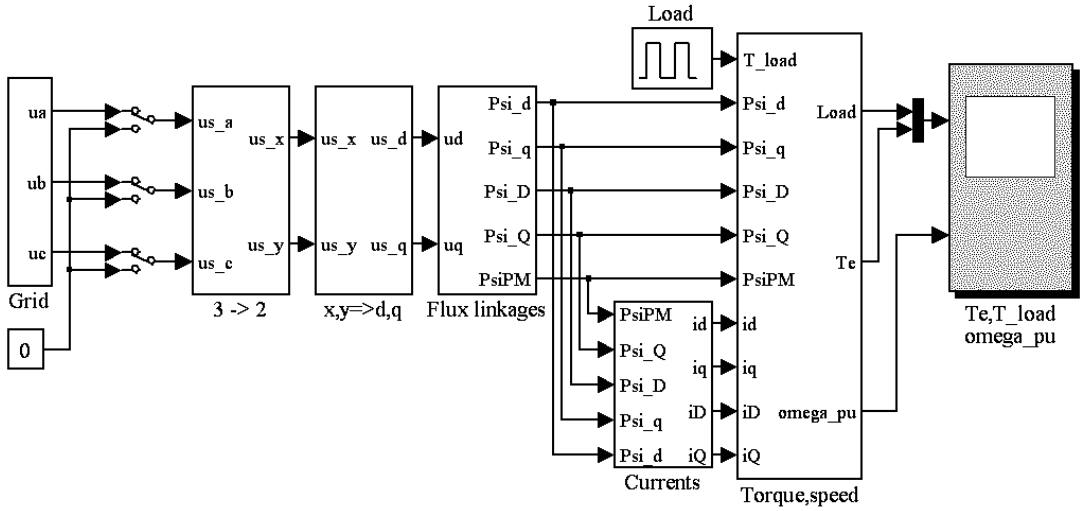

Fig. 3.2. Main parts of the simulation model. The grid on the left is rigid. The three-phase quantities are transformed into rotor-oriented dq-coordinates. The simulation model operates on per unit values.

According to Park's (1929) equations, the voltage equations for the stator in dq-coordinates are (Vas 1998, p.186)

$$u_{\mathrm{d}} = R_{\mathrm{s}} i_{\mathrm{d}} + \frac{\mathrm{d}\psi_{\mathrm{d}}}{\mathrm{d}t} - \omega\psi_{\mathrm{q}} \tag{3.1}$$

$$u_{\mathrm{q}} = R_{\mathrm{s}} i_{\mathrm{q}} + \frac{\mathrm{d}\psi_{\mathrm{q}}}{\mathrm{d}t} + \omega\psi_{\mathrm{d}}\,. \tag{3.2}$$

When using the per unit values in the equations, we first also have the per unit time τ in use. Per unit time is a result of the mathematical process employing the base values. The emergence of the per unit time is seen in the following. It is, however, more convenient to use the normal time instead of the pu time. Per unit time may be replaced by the real time in the equations when we know that $\omega_{\mathrm{n}} t = \tau$. In pu values, the voltage equations become

$$u_{\mathrm{d,pu}} = r_{\mathrm{s,pu}} i_{\mathrm{d,pu}} + \frac{\mathrm{d}\psi_{\mathrm{d,pu}}}{\mathrm{d}\tau} - \omega_{\mathrm{pu}}\psi_{\mathrm{q,pu}} = r_{\mathrm{s,pu}} i_{\mathrm{d,pu}} + \frac{1}{\omega_{\mathrm{n}}}\frac{\mathrm{d}\psi_{\mathrm{d,pu}}}{\mathrm{d}t} - \omega_{\mathrm{pu}}\psi_{\mathrm{q,pu}} \tag{3.3}$$

and

$$u_{\mathrm{q,pu}} = r_{\mathrm{s,pu}} i_{\mathrm{q,pu}} + \frac{\mathrm{d}\psi_{\mathrm{q,pu}}}{\mathrm{d}\tau} + \omega_{\mathrm{pu}}\psi_{\mathrm{q,pu}} = r_{\mathrm{s}} i_{\mathrm{q,pu}} + \frac{1}{\omega_{\mathrm{n}}}\frac{\mathrm{d}\psi_{\mathrm{q,pu}}}{\mathrm{d}t} + \omega_{\mathrm{pu}}\psi_{\mathrm{q,pu}} \tag{3.4}$$

The rotor circuit is short-circuited and the voltages are zero:

$$0 = R_{\mathrm{D}} i_{\mathrm{D}} + \frac{\mathrm{d}\psi_D}{\mathrm{d}t} \tag{3.5}$$

$$0 = R_{\mathrm{Q}} i_{\mathrm{Q}} + \frac{\mathrm{d}\psi_{\mathrm{Q}}}{\mathrm{d}t}. \tag{3.6}$$

In pu values

$$\begin{aligned} 0 &= r_{\mathrm{D,pu}} i_{\mathrm{D,pu}} + \frac{\mathrm{d}\psi_{\mathrm{D,pu}}}{\mathrm{d}\tau} = r_{\mathrm{D,pu}} i_{\mathrm{D,pu}} + \frac{1}{\omega_{\mathrm{s,n}}} \frac{\mathrm{d}\psi_{\mathrm{D,pu}}}{\mathrm{d}t} \\ 0 &= r_{\mathrm{Q,pu}} i_{\mathrm{Q,pu}} + \frac{\mathrm{d}\psi_{\mathrm{Q,pu}}}{\mathrm{d}\tau} = r_{\mathrm{Q,pu}} i_{\mathrm{Q,pu}} + \frac{1}{\omega_{\mathrm{s,n}}} \frac{\mathrm{d}\psi_{\mathrm{Q,pu}}}{\mathrm{d}t} \end{aligned} \tag{3.7}$$

The flux linkages ψ may be presented in a matrix form $\boldsymbol{\psi}$ by the product of inductance matrix $\mathbf{L}$ and current matrix $\mathbf{i}$.

$$\boldsymbol{\psi} = \mathbf{L}\mathbf{i} = \begin{bmatrix} \psi_{\mathrm{d}} \\ \psi_{\mathrm{q}} \\ \psi_{\mathrm{D}} \\ \psi_{\mathrm{Q}} \end{bmatrix} = \begin{bmatrix} L_{\mathrm{d}} & 0 & L_{\mathrm{md}} & 0 \\ 0 & L_{\mathrm{q}} & 0 & L_{\mathrm{mq}} \\ L_{\mathrm{md}} & 0 & L_{\mathrm{D}} & 0 \\ 0 & L_{\mathrm{mq}} & 0 & L_{\mathrm{Q}} \end{bmatrix} \begin{bmatrix} i_{\mathrm{d}} \\ i_{\mathrm{q}} \\ i_{\mathrm{D}} \\ i_{\mathrm{Q}} \end{bmatrix} + \begin{bmatrix} \psi_{\mathrm{PM}} \\ 0 \\ \psi_{\mathrm{PM}} \\ 0 \end{bmatrix} \tag{3.8}$$

The current components may be calculated using the inverse value of $\mathbf{L}$.

$$\begin{bmatrix} i_{\mathrm{d}} \\ i_{\mathrm{q}} \\ i_{\mathrm{D}} \\ i_{\mathrm{Q}} \end{bmatrix} = \frac{1}{\det(\mathbf{L})} \mathrm{adj}(\mathbf{L}) \left(\begin{bmatrix} \psi_{\mathrm{d}} \\ \psi_{\mathrm{q}} \\ \psi_{\mathrm{D}} \\ \psi_{\mathrm{Q}} \end{bmatrix} - \begin{bmatrix} \psi_{\mathrm{PM}} \\ 0 \\ \psi_{\mathrm{PM}} \\ 0 \end{bmatrix} \right) = \frac{1}{k_1} \begin{bmatrix} k_2 & 0 & k_3 & 0 \\ 0 & k_4 & 0 & k_5 \\ k_3 & 0 & k_6 & 0 \\ 0 & k_5 & 0 & k_7 \end{bmatrix} \left(\begin{bmatrix} \psi_{\mathrm{d}} \\ \psi_{\mathrm{q}} \\ \psi_{\mathrm{D}} \\ \psi_{\mathrm{Q}} \end{bmatrix} - \begin{bmatrix} \psi_{\mathrm{PM}} \\ 0 \\ \psi_{\mathrm{PM}} \\ 0 \end{bmatrix} \right) \tag{3.9}$$

From Eq. (3.9) we obtain four separate current components.

$$\begin{aligned} i_{\mathrm{d}} &= \frac{1}{k_1} \left[k_2 \left(\psi_{\mathrm{d}} - \psi_{\mathrm{PM}} \right) + k_3 \left(\psi_{\mathrm{D}} - \psi_{\mathrm{PM}} \right) \right] \\ i_{\mathrm{q}} &= \frac{1}{k_1} \left(k_4 \psi_{\mathrm{q}} + k_5 \psi_{\mathrm{Q}} \right) \\ i_{\mathrm{D}} &= \frac{1}{k_1} \left[k_5 \left(\psi_{\mathrm{d}} - \psi_{\mathrm{PM}} \right) + k_6 \left(\psi_{\mathrm{D}} - \psi_{\mathrm{PM}} \right) \right] \\ i_{\mathrm{Q}} &= \frac{1}{k_1} \left(k_5 \psi_{\mathrm{q}} + k_7 \psi_{\mathrm{Q}} \right) \end{aligned} \tag{3.10}$$

k_1 is the determinant of $\boldsymbol{L}$ and coefficients k_2, k_3, k_4, k_5, k_6 and k_7 are:

$$
\begin{aligned}
k_1 &= L_{\mathrm{sd}}L_{\mathrm{D}}\left(L_{\mathrm{sq}}L_{\mathrm{Q}} - {L_{\mathrm{mq}}}^2\right) - L_{\mathrm{md}}^2\left(L_{\mathrm{sq}}L_{\mathrm{Q}} - {L_{\mathrm{mq}}}^2\right) \\
k_2 &= L_{\mathrm{D}}\left(L_{\mathrm{sq}}L_{\mathrm{Q}} - {L_{\mathrm{mq}}}^2\right) \\
k_3 &= -L_{\mathrm{md}}\left(L_{\mathrm{sq}}L_{\mathrm{Q}} - {L_{\mathrm{mq}}}^2\right) \\
k_4 &= L_{\mathrm{Q}}\left(L_{\mathrm{sd}}L_{\mathrm{D}} - {L_{\mathrm{md}}}^2\right) \\
k_5 &= -L_{\mathrm{mq}}\left(L_{\mathrm{sd}}L_{\mathrm{D}} - {L_{\mathrm{md}}}^2\right) \\
k_6 &= L_{\mathrm{sd}}\left(L_{\mathrm{sq}}L_{\mathrm{Q}} - {L_{\mathrm{mq}}}^2\right) \\
k_7 &= L_{\mathrm{sq}}\left(L_{\mathrm{sd}}L_{\mathrm{D}} - {L_{\mathrm{md}}}^2\right)
\end{aligned}
\tag{3.11}
$$

The derivatives of the flux linkages are solved by substituting Eq. (3.10) into Eqs. (3.3), (3.4), (3.5) and (3.6).

$$
\begin{aligned}
\frac{\mathrm{d}\psi_{\mathrm{d}}}{\mathrm{d}t} &= U_{\mathrm{d}} - \frac{R_{\mathrm{s}}}{k_1}\left[k_2\left(\psi_{\mathrm{d}} - \psi_{\mathrm{PM}}\right) + k_3\left(\psi_{\mathrm{D}} - \psi_{\mathrm{PM}}\right)\right] + \omega\psi_{\mathrm{q}} \\
\frac{\mathrm{d}\psi_{\mathrm{q}}}{\mathrm{d}t} &= U_{\mathrm{q}} - \frac{R_{\mathrm{s}}}{k_1}\left(k_4\psi_{\mathrm{q}} + k_5\psi_{\mathrm{Q}}\right) - \omega\psi_{\mathrm{d}} \\
\frac{\mathrm{d}\psi_{\mathrm{D}}}{\mathrm{d}t} &= -\frac{R_{\mathrm{D}}}{k_1}\left[k_5\left(\psi_{\mathrm{d}} - \psi_{\mathrm{PM}}\right) + k_6\left(\psi_{\mathrm{D}} - \psi_{\mathrm{PM}}\right)\right] \\
\frac{\mathrm{d}\psi_{\mathrm{Q}}}{\mathrm{d}t} &= -\frac{R_{\mathrm{Q}}}{k_1}\left(k_5\psi_{\mathrm{q}} + k_7\psi_{\mathrm{Q}}\right)
\end{aligned}
\tag{3.12}
$$

The flux linkages are solved by integrating the equations in Eq. (3.12). The electromagnetic torque can be expressed as

$$
\boldsymbol{T}_{\mathrm{e}} = \frac{3}{2}p\left(\psi_{\mathrm{d}}i_{\mathrm{q}} - \psi_{\mathrm{q}}i_{\mathrm{d}}\right) \tag{3.13}
$$

The electromagnetic torque interacts with the mechanical shaft torque and the dynamic torque caused by the inertia of the rotating parts. The equation of motion in per unit (pu) values is

$$
\boldsymbol{T}_{\mathrm{e,pu}} = \boldsymbol{\psi}_{\mathrm{s,pu}} \times \boldsymbol{i}_{\mathrm{s,pu}} = \tau_{\mathrm{J}}\frac{\mathrm{d}^2\theta}{\mathrm{d}\tau^2} + T_{\mathrm{Load,pu}} = \tau_{\mathrm{J}}\frac{1}{\omega_{\mathrm{n}}}\frac{\mathrm{d}\omega_{\mathrm{pu}}}{\mathrm{d}t} + T_{\mathrm{Load,pu}} \tag{3.14}
$$

where $\boldsymbol{\psi}_{\mathrm{s,pu}}$ is the stator flux linkage, θ is the rotor angular position, τ is per unit time, T_{Load} is the mechanical torque and τ_{J} is a dimensionless mechanical time constant that replaces the moment of inertia J in per unit equations. τ_{J} describes the ratio of the rotor kinetic energy to the electrical machine apparent power:

$$
\tau_{\mathrm{J}} = \omega_{\mathrm{n}}\left(\frac{\omega_{\mathrm{n}}}{p}\right)^2\frac{J}{S_{\mathrm{b}}} \ . \tag{3.15}
$$

3.2 Simulation results

An extensive survey was made by varying the parameters of the non-salient pole PM machine. All the simulations were made in per unit values, because the comparison of pu values is straightforward. The PM machine was connected to a rigid network. To simplify the simulation, the torque of the machine was altered instead of the electric loading of the generator (T_load in Fig. 3.2). The mechanical connection was modelled ideal, which means that the shaft does not flex. The torque steps and grid connections were made to excite transients. If there is no damper winding resistance, the transients never attenuate and the synchronous operation speed is not achieved. By increasing the damper winding resistance, the speed oscillation starts to attenuate. At some point, the synchronization time reaches its minimum value. After that point, the increase of damper winding resistance increases the synchronization time. It was found that the damper winding resistance has an optimum value to reach the stable operation conditions at the shortest possible period of time. The parameters of the simulated PMSG are shown in Table 3.1

Table 3.1 Parameters of the simulated PMSG

Simulated PMSG			
Parameter	Value	Parameter	Value
$U_{s,pu}$	1	$L_{d,pu}$	0.5
$E_{PM,pu}$	1.04	$L_{q,pu}$	0.5
$R_{s,pu}$	0.05	$L_{s\sigma,pu}$	0.25
$R_{D,pu}$	0.15	$L_{D\sigma,pu}$	0.05
$R_{Q,pu}$	0.15	$L_{Q\sigma,pu}$	0.05
J_{rotor}	0.03 kgm^2		

In the following studies the stator direct and quadrature axes per unit inductances $L_{d,pu}$ and $L_{q,pu}$ are kept as constant values $L_{d,pu} = L_{q,pu} = 0.5$. This is a suitable compromise for permanent magnet generators in order to get a large enough peak torque for the machines and also a large enough magnetic coupling between the stator and the damper winding. If the magnetising inductance of the machine were smaller the damper winding effects should be weaker and a lower damper winding resistance should be needed.

The values of the damper winding parameters, electromotive force and the moment of inertia are varied during the simulations. The synchronization time is determined from the attenuation of the speed oscillation. Generator is considered to be operating in synchronous mode when the speed is 1 pu ± 0.2 %. An example is shown in Fig. 3.3.

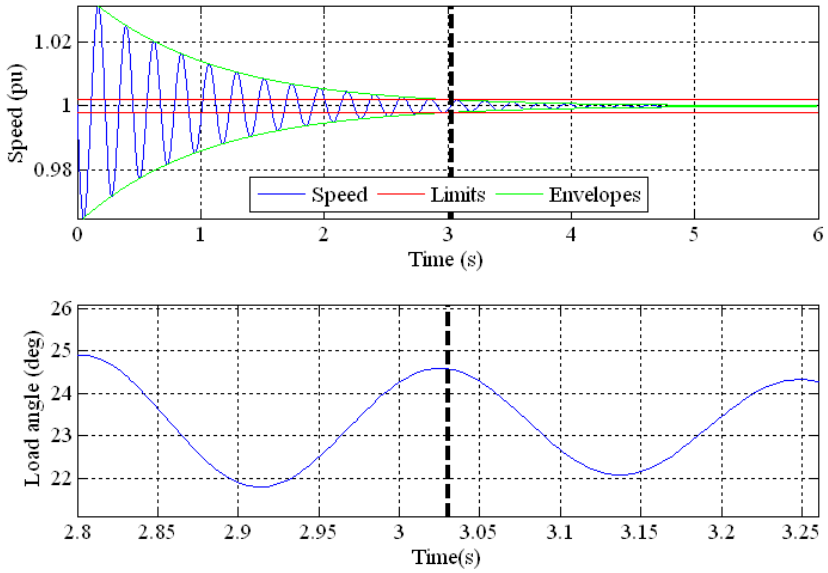

Fig. 3.3 Determination of the synchronization time. The generator is considered to operate in synchronism when the speed is 1 pu ± 0.2%. At that time, the load angle is alternating by only 2 degrees.

The rotor moment of inertia has a significant effect on the optimum damper winding resistance value. Also the damper winding leakage inductance has an effect. The generator is connected to the grid at 99% of the nominal operating speed while the phase difference between the grid and the generator voltages are 10 degrees. The synchronization times after grid connection as a function of damper winding leakage inductances and the moment of inertia are shown in Fig. 3.4. The synchronization times after grid connection as a function of damper winding resistances and the moment of inertia are shown in Fig. 3.5. The damper winding has to operate efficiently also in load transients. A similar test was performed by analyzing the synchronization time in the 60 % load torque step.

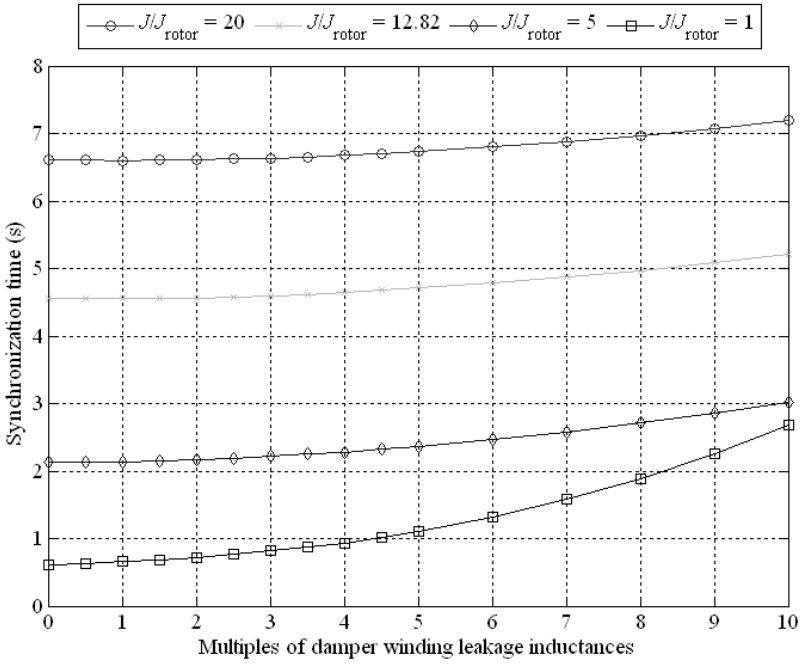

Fig. 3.4. Synchronization time in grid connection as a function of damper winding leakage inductance with different values of the rotating moment of inertia. The moment of the system inertia J is compared with the rotor inertia J_{rotor} of the PMSG 1 in Table 3.1. The actual damper winding leakage inductance values $L_{D\sigma,pu}$ and $L_{Q\sigma,pu}$ are multiplied by the values shown in the figure. The generator is connected to the grid at 99% of the nominal operating speed while the phase difference between the grid and the generator voltages are 10 degrees.

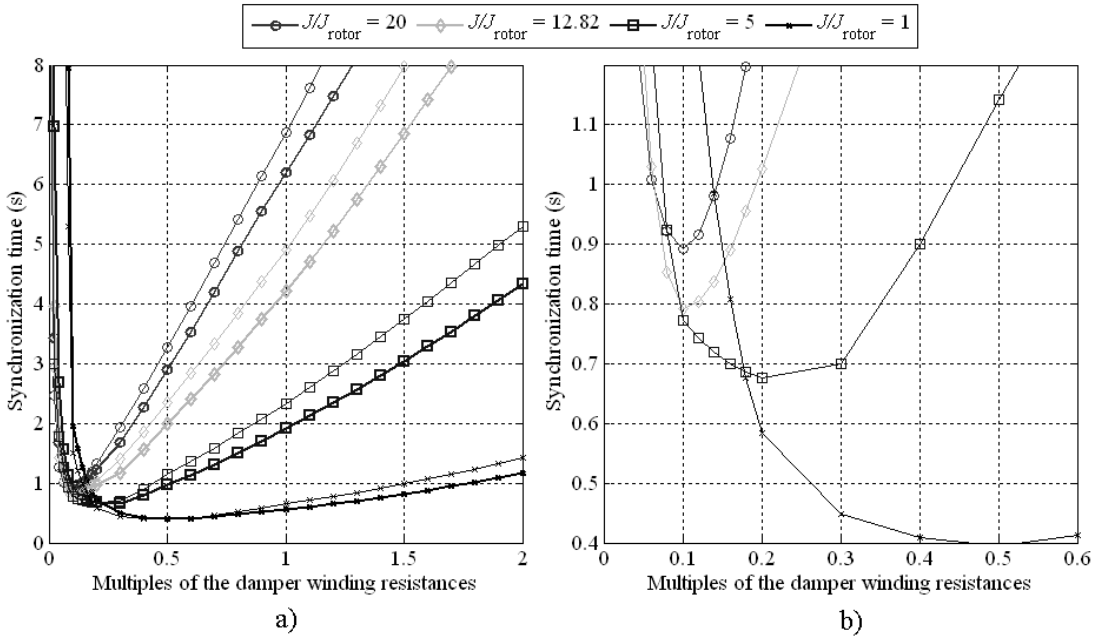

Fig. 3.5 Synchronization time as a function of damper winding resistance with different values of the rotating moment of inertia. a) 60 % load torque step is applied at no load (thinner plotted lines). The results are compared with the grid connection case. The generator is connected to the grid when f = 0.99 pu and the back-EMF of the generator is 10 degrees behind the grid voltage (thicker plotted lines). b) close-up of grid connection –detail of a). As it may be seen the damper winding resistances should be about a quarter of the values given in table 3.1 to achieve an overall minimum for the synchronization time.

The system moment of inertia has a significant effect on the optimum damper winding resistance value to achieve synchronous operation after the transient in the shortest period of time. When the inertia of the rotating parts is large compared with the electric power of the generator, the damper winding resistance has a narrow optimal area as can be seen in the figure. When the inertia of the rotating parts is small, the damper winding resistances must be selected high enough to guarantee synchronous operation.

If there is a phase difference between the electromotive force of the generator and the network voltage, large current pulses may occur after the grid connection. Also the amplitude difference between the electromotive force and the network voltage causes a current pulse in the grid connection. The generator needs energy also if the frequency is not correct. The current pulse amplitudes are highly dependent on the subtransient inductance. If the subtransient inductance is very small, very high current pulses may occur. The networks have fault current switches, which can be triggered because of high current pulses in the grid connection. High current pulses can also cause voltage sags if the network is weak. High current pulses mean also high torque components at the time of the grid connection which must be taken into account in the mechanical design. Therefore, accurate enough synchronization equipment is required. The effect of the amplitude difference between the electromotive force of the generator and the grid voltage is shown in Fig. 3.6.

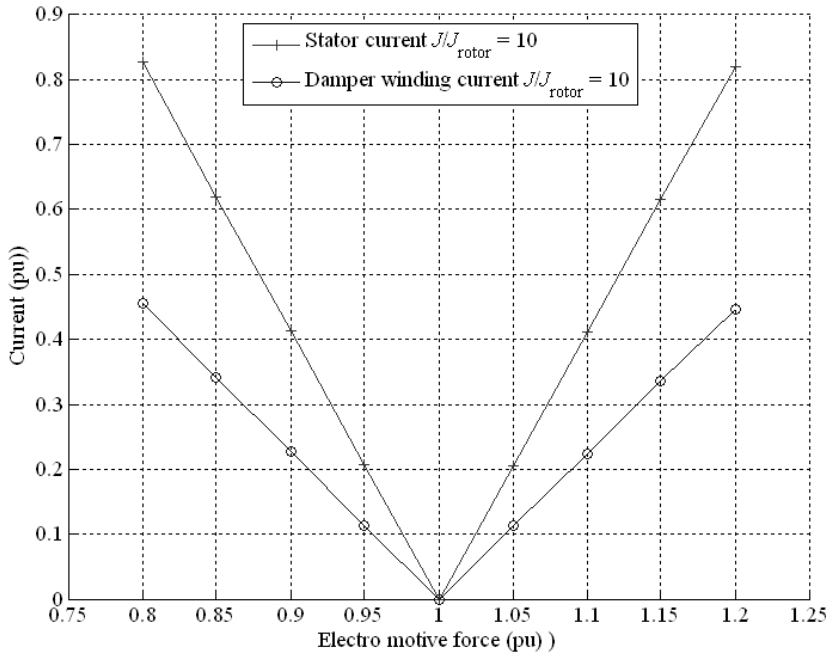

Fig. 3.6. Simulated current pulse in the grid connection as a function of electromotive force of the directly connected permanent magnet generator PMSG in cases where the phases of the grid voltage and the generator voltage are equal. The amplitude difference of E_{PM} and U_s increases the current pulse in the grid connection. The impedance of the network is assumed to be zero.

The effect of the phase difference in the grid connection is shown in Fig. 3.7.

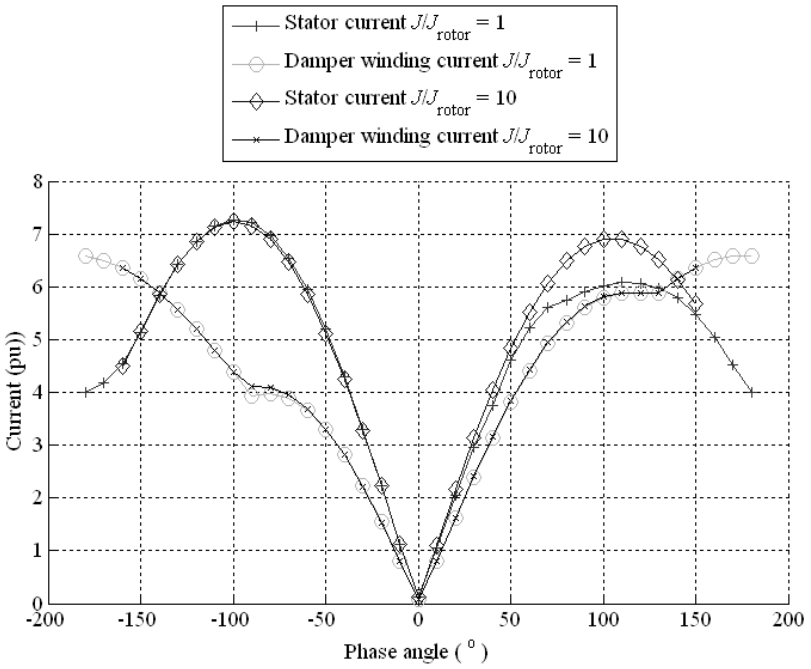

Fig. 3.7. Simulated current pulse in the grid connection as a function of phase difference between the electromotive force of the generator (parameters in Table 3.1) and the network voltage. E_{PM} = 1.04 U_s. The largest current pulse occurs at phase differences ±100°.

It can be seen in Fig. 3.7 that the phase difference between the back-EMF of the generator and the grid voltage rapidly increases the current pulse in the grid connection. According to Helsinki Energy, the guideline for the allowed phase difference is ±10º. At a 10º phase difference, a current pulse of about 1 pu occurs. The largest current pulse occurs at phase differences ±100°. After 100° the load angle slips into another magnetic pole, which takes less energy and current.

The pull-in torque of a permanent magnet synchronous generator is the torque that pulls the connected total inertia into synchronism. The pull-in torque is developed during the transition from the slip speed to the synchronous speed as the generator changes from asynchronous mode to synchronous operation. It is usually the most critical period in the grid connection of a DOL PMSG. Ideally, the torques developed by the damper winding become zero at synchronous speed. In practice, the damper winding filters the slot harmonics, the stator current linkage harmonics and the torque vibrations even at synchronous speed. At the pull-in point only the reluctance torque and the synchronizing torque provided by the permanent magnets are effective. Reluctance torque results from the saliency of the rotor and pulsates at speeds other than the synchronous speed. It also has an influence on the pull-in and pull-out torques, because the rotor with saliency tends to align itself with the stator magnetic field to maintain minimum magnetic reluctance. The synchronous torque represents the total steady-state torque available to drive the load. The load angle at which the machine reaches its maximum torque, that is, the pull-out torque, depends on the saliency of the rotor. Permanent magnet machines provided with damper windings have both synchronous and asynchronous operation modes, and therefore

there are different pull-out torques for the asynchronous operation and for the synchronous operation. For the sake of clarity, they are referred to as the asynchronous pull-out torque and the synchronous pull-out torque, respectively.

The asynchronous performance of the generator (Table 3.1) was analyzed by dropping the rotation speed into 0.8 pu. There is no need for generator to start from this speed. However, during fault conditions the operation speed can drop into deep asynchronous operation unless the safety devices work. For example in small water power plants a wooden log or ice cube could cause a temporary rapid load pulse which may cause reduction of the rotation speed. The performance of the damper winding with lower slip values was simulated to see the effects of the moment of inertia on the synchronization from high slip values, see Figs 3.8 – 3.12.

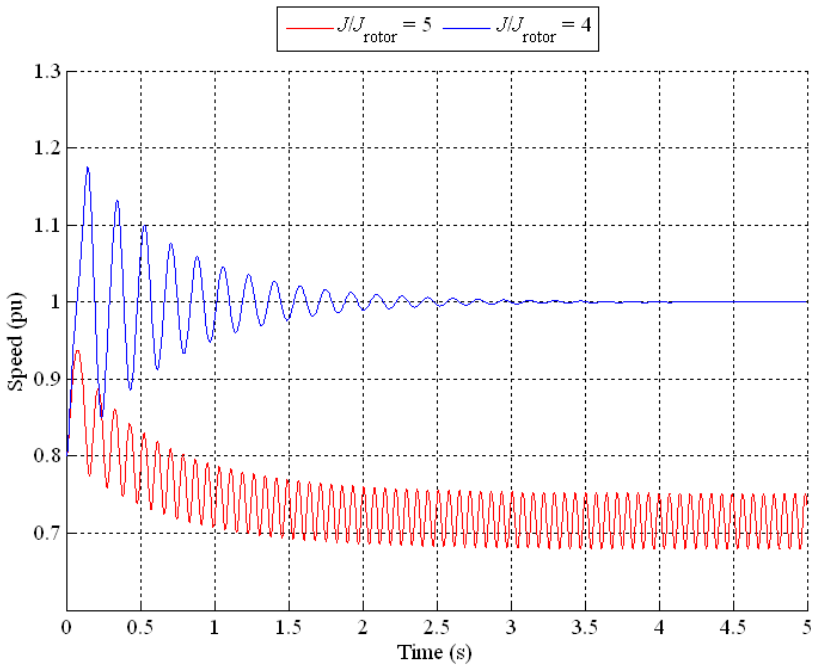

Fig. 3.8 Simulated asynchronous operation of the PMSG (Table 3.1) as a generator dropped from synchronous speed. The load torque is constant, 20 % of the nominal load. The moment of system inertia is compared with the rotor moment of inertia. As it can be seen, the synchronization no longer occurs when the relative inertia is larger than 4.

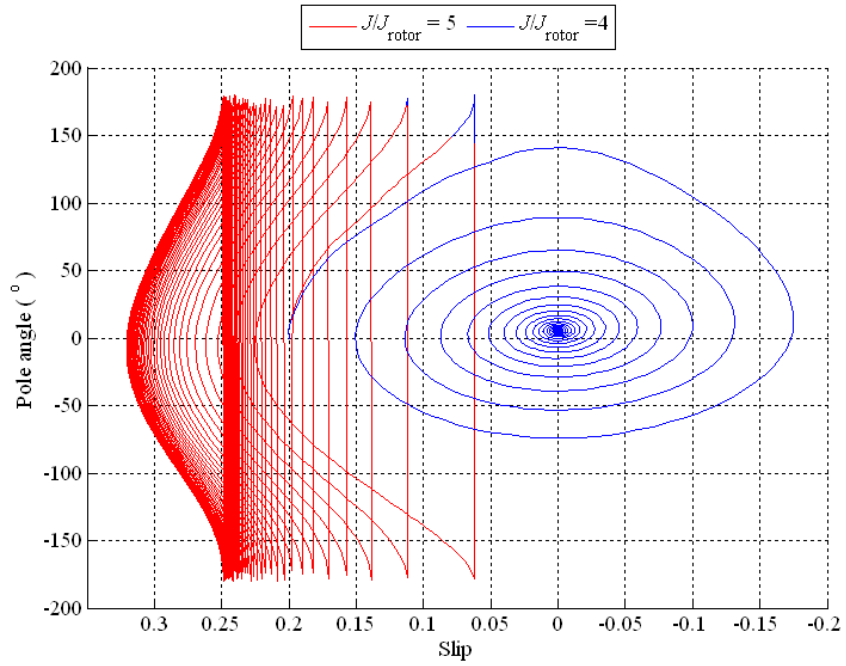

Fig. 3.9 Pole angle of the PMSG (Table 3.1) after the speed has dropped into 0.8 pu (slip s = 0.2). The load torque is 20 % of the nominal value. The generator fails to synchronize when the relative inertia is larger than 4. With relative inertia of 4, the generator starts to synchronize into one pole pair area from the slip s = 0.2.

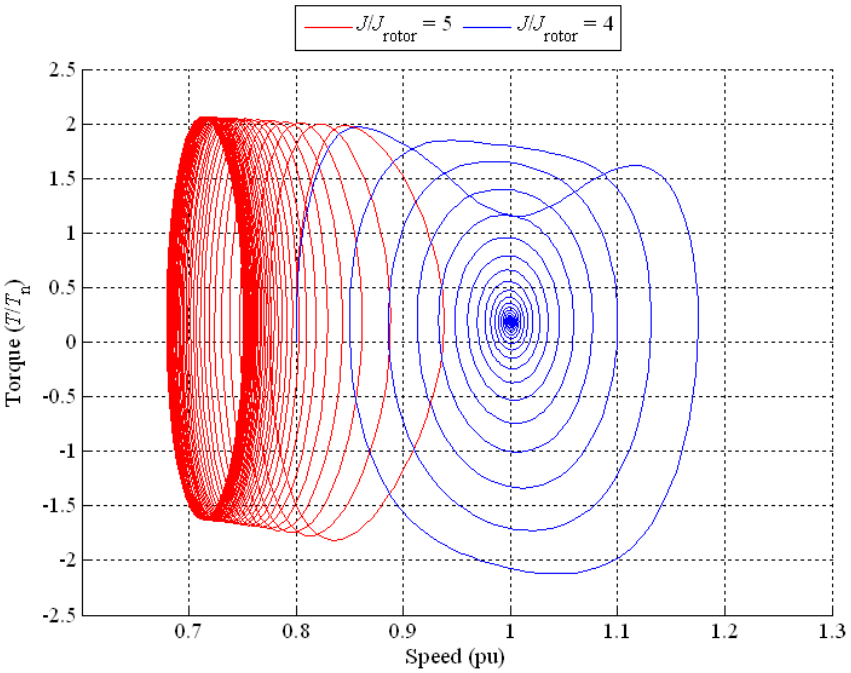

Fig. 3.10 Speed-torque curve from asynchronous state of PMSG (Table 3.1) at speed 0.8 pu. The load torque is 20 % of the nominal value. The moment of inertia ratio J/J_{rotor} = 4 and J/J_{rotor} = 5. The torque pulsates at lower speeds. Near the synchronous speed the rotor tries to synchronize with the stator field. At some point the synchronizing torque of the machines takes control of the asynchronous operation. With a higher moment of inertia ratios, the synchronization fails.

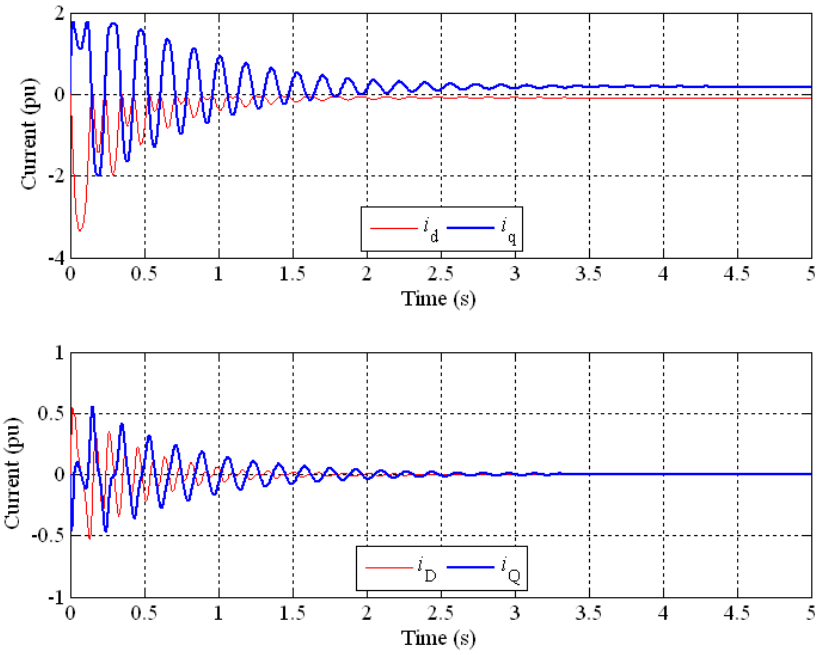

Fig. 3.11. Currents of an PMSG (Table 3.1) beginning from slip s = 0.2. The moment of inertia ratio J/J_{rotor} = 4. Large transient currents exists in asynchronous operation. After 3.5 seconds, the damper winding currents attenuate to zero and the generator operates at synchronous speed with 20 % load torque.

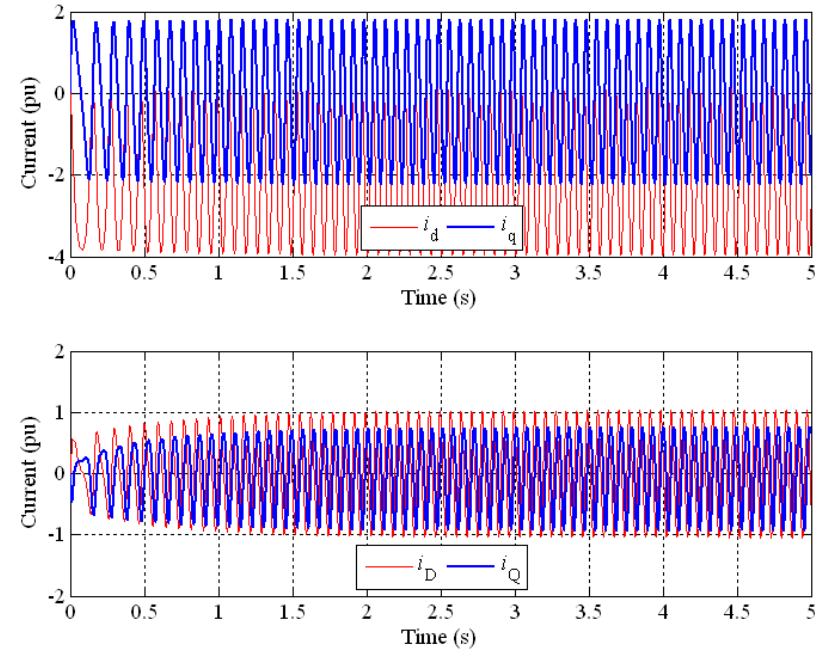

Fig. 3.12 Currents of an PMSG (Table 3.1) beginning from slip s = 0.2. The moment of inertia ratio J/J_{rotor} = 5. The generator fails to synchronize. Large demagnetizing (i_d) currents exists in asynchronous operation.

A simulation model of PMSG for dynamic performance was described. The simulation model was used to examine the parameters of the damper winding and its effects on the dynamic performance. The damper winding should have a small leakage inductance to minimize the oscillation attenuation after transients. The damper winding resistances should be optimized based on the system moment of inertia. Transient performance of PMSG was simulated and analyzed. Asynchronous operation of the permanent magnet synchronous generator is examined in more detail in Chapter 4. Simulation results and analytical calculations are compared with practical experiments in Chapter 5.

4 Design of damper windings for permanent magnet synchronous generators

This chapter focuses on the damper windings. The geometries of the two prototype PMSGs, AFPMSG1 and AFPMSG2, are illustrated. At asynchronous speeds, damper winding produces an accelerating asynchronous torque to reach synchronism. In synchronous operation, the damper winding reduces speed fluctuations. The asynchronous torque is divided into several components, which are discussed in the following. Analytical equations are presented for the calculation of these torque components. Material and geometrical design aspects are discussed. A 3D FEA model of AFPMSG1 is introduced to calculate some of the electrical parameters.

Damper windings are used for several reasons. For synchronous machines, in general, the damper windings provide smooth and stable running characteristics. Even the noise level of the running machine can be reduced, and also the tolerance for pulsating loads improves. The damper winding assists to keep the rotor in synchronism by attenuating the oscillations. In LSPMSMs, the damper windings are essential for starting characteristics, while in DOL PMSGs, the role of the damper windings is emphasized in grid connections and at load transients. The damper winding protects the permanent magnets from demagnetization during asynchronous operation and in the fault conditions.

4.1 Construction topologies of the damper windings

In directly network-operated PMSGs, careful design of damper windings is necessary. The price of the machine must be competitive with traditional generators, which may limit the practical applications of the damper winding structures. Eddy currents in the permanent magnets produce damping effects and thereby also losses, and increase the temperature of the permanent magnets. If the cooling of the rotor is not sufficient, permanent demagnetization of the magnets may occur, especially, if the magnets are embedded under a bandage made of carbon or fibreglass and resin.

The eddy currents in permanent magnets can be reduced with various rotor structures. The permanent magnets can be surrounded by a low-resistivity material, such as copper or aluminium. This material supports the permanent magnets and forms an installation jig. The installation jig forms a coarse squirrel cage as shown in Fig. 4.1.

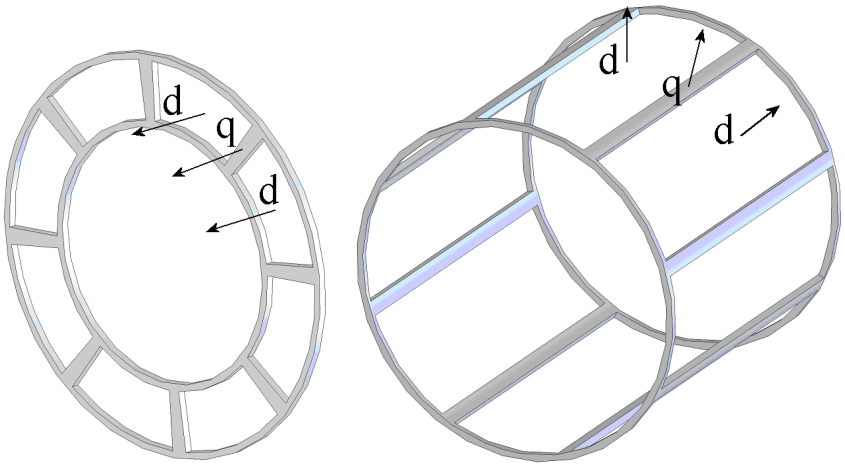

Fig. 4.1 Installation jigs for permanent magnets for a) axial and b) radial flux permanent magnet synchronous machines. Installation jig forms a coarse squirrel cage provided with end rings. Note that in such a case the damper bars surrounding the d-axis are effective but the q-axis damping remains quite ineffective.

To increase the cross-sectional area for the quadrature-axis damper bars, several magnets with the same polarity in the area of one magnetic pole could be used. The space between the magnets can be provided for the damper winding bars. This kind of a structure has been studied to reduce higher space harmonics and to increase the space for the damper windings (Jeon et al. 1999). The permanent magnets can be protected from some of the mechanical damage and eddy currents by installing a plate made of a suitable, usually non-ferrous material, such as aluminium on the rotor surface, Fig. 4.2.

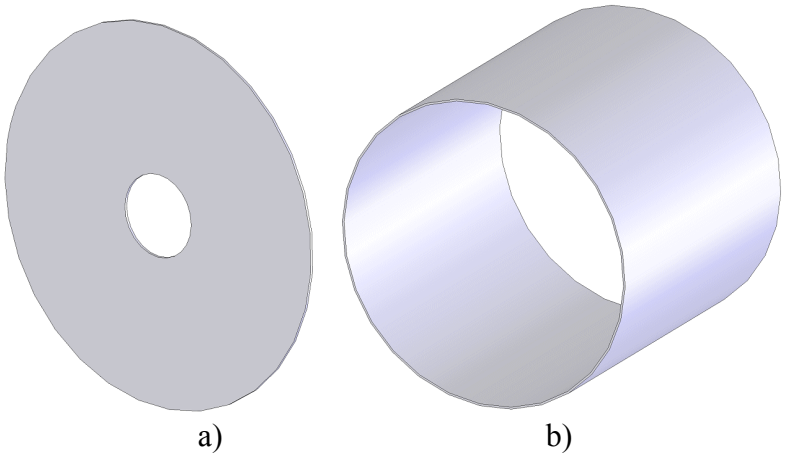

Fig 4.2 Part of damper winding topologies for a) axial and b) radial flux permanent magnet synchronous machines. The damper windings consist of plates installed over the rotor surfaces.

The total damper winding structure illustrated in Figs. 4.1 and 4.2 is a combination of the squirrel cage, the solid materials of the rotor (magnets, non-laminated rotors) and the surface aluminium. The surface aluminium or the installation jig itself is sufficient to protect the permanent magnets from most of the eddy currents.

Therefore, rotor constructions, in which the installation jig or surface plate is non-conductive or does not exist, can be considered.

4.2 Material characteristics of damper windings

There are two values for the resistivity when a material has zero power losses. If the resistivity is zero (superconductive materials) or infinite (perfect insulators), no conducting losses occur. Real materials in normal operating temperatures and pressures do not have such characteristics, but they are not required for damper windings either. Instead, a suitable resistivity may be selected for the material. In the case of permanent magnets, it would be beneficial to have infinite resistivity of the magnet material to prevent eddy current losses in the magnets.

Resistance is the capacity of an electrical circuit to resist the flow of an electric current through it. Resistivity is the measure of a material's resistance to current flow. Some materials are better conductors than others and offer less resistance to the flow of charge. Silver is one of the best conductors, but it is expensive. Copper and aluminium are among the least expensive materials with suitable conducting ability to permit their use in damper windings and armature windings. The conducting ability of a material is often indicated by its resistivity. The resistivity of a material depends on the material's electronic structure and its temperature. For most materials, resistivity increases with increasing temperature. Table 4.1 lists resistivity values for various materials at temperatures of 20 °C.

Table 4.1 Resistivity values of different materials at 20 °C.

Material	Resistivity [Ωm]		Temperature coefficient α	Conductivity σ [10^7Am/V]
Silver	1.59	$\times 10^{-8}$	0.0061	6.29
Copper	1.68	$\times 10^{-8}$	0.0068	5.95
Aluminium	2.65	$\times 10^{-8}$	0.00429	3.77
Tungsten	5.6	$\times 10^{-8}$	0.0045	1.79
Iron	9.71	$\times 10^{-8}$	0.00651	1.03
Platinum	10.6	$\times 10^{-8}$	0.003927	0.943
Manganese	48.2	$\times 10^{-8}$	0.000002	0.207
Lead	22	$\times 10^{-8}$	-	0.45
Mercury	98	$\times 10^{-8}$	0.0009	0.1
Nichrome (Ni,Fe,Cr alloy)	100	$\times 10^{-8}$	0.0004	0.1
Constantan	49	$\times 10^{-8}$	-	0.2
NdFeB	1-3	$\times 10^{-6}$	-	0.05-0.1
Carbon (graphite)	3-60	$\times 10^{-5}$	-0.0005	-
Germanium	1-500	$\times 10^{-3}$	-0.05	-
Silicon	0.1-60	-	-0.07	-
Glass	1-10000	$\times 10^{9}$	-	-
Quartz (fused)	7.5	$\times 10^{17}$	-	-
Hard rubber	1-100	$\times 10^{13}$	-	-

The skin depth of the material defines how deep the magnetic flux can penetrate inside the material. The skin depth depends on the frequency of the penetrating flux. The skin depth is

$$\delta = \sqrt{\frac{2}{\omega\mu\sigma}} = \sqrt{\frac{2}{2\pi f\mu\sigma}}, \tag{4.1}$$

where μ is the permeability, σ is the conductivity and f the frequency. This equation is valid for magnetically linear materials. The skin depths of some materials are illustrated in Fig. 4.3.

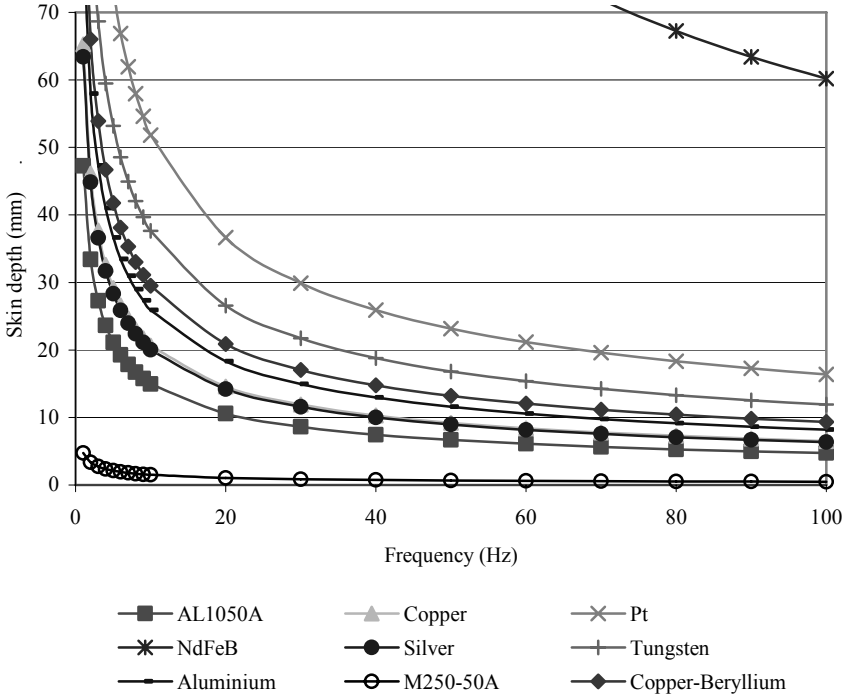

Fig. 4.3 Skin depth of different materials as a function of frequency. The steel lamination M250-50A material is not magnetically linear. Therefore, the evaluation of the skin depth is calculated with fixed relative permeability of $\mu_r = 6600$.

The figure shows that for example aluminium has a skin depth of about 12mm at 50Hz and about 26mm at 10Hz. Most of the operation of the DOL PMSGs takes place close to the synchronous speed and the frequencies seen by the rotor are rather small. Therefore, the flux flows through the whole damper winding and the rotor. The high harmonic content of the air gap flux may cause some shielding effect.

As an example, also the skin depth of an electric steel quality M250-50A is calculated with coarse simplifications by setting the conductivity and the relative permeability of the material constant. As we can see, the depth is low at all frequencies. Consequently, the material has to be used as laminated to be able to use it as a carrier of the AC magnetic flux.

4.3 Limitations for damper winding parameters

In many respects, the selection of the damper winding parameters is a challenging task in the design procedure. The parameters of the damper winding depend on the frequency that the damper winding experiences during transients. The skin effect increases the damper winding resistance as the frequency of the flux through the rotor increases. The decrease of the subtransient inductances as a function of the magnetic field frequency may be explained by eddy currents. As the frequency increases, more eddy currents are induced to the rotor. The eddy currents block the straightforward flow of the magnetic flux through the rotor. Because of the shielding

effect, the flux lines stretch the magneto motive force $\oint \boldsymbol{H} \cdot \mathrm{d}\boldsymbol{l}$ of the circuit and the inductance drops.

The practical damper winding parameters are limited by the available practical material characteristics and by the limited space in the rotor. It is difficult to achieve equal damper winding parameters in direct-axis and quadrature-axis directions with damper winding structures other than a squirrel cage or a solid conducting plate.

4.4 Design of prototype generators

Two prototype permanent magnet synchronous generators, AFPMSG1 and AFPMSG2, were tested. The prototype permanent magnet generator AFPMSG1 (Axial-Flux Permanent-Magnet Synchronous Generator 1) was more carefully studied and analyzed. Another prototype AFPMSG2 was being used for comparison purposes. The rotor constructions in both of these machines were very similar; rotor-surface-mounted permanent magnets with an aluminium jig for positioning the magnets correctly and a surface aluminium plate to protect permanent magnets from eddy currents and mechanical damage. The geometries of the PMSGs are illustrated in Fig. 4.4. The prototype AFPMSG1 is a one-rotor-two stator construction with an aluminium-frame rotor, while the AFPMSG2 is a single- sided construction with a cast-iron rotor yoke. Both the machines have short-pitched stator windings with W/τ_p = 5/6 and q = 2. AFPMSG1 Rotor construction is shown in Fig. 4.5 and AFPMSG2 rotor construction in Fig. 4.6. The main parameters of the prototype machines tested are given in Table 4.2.

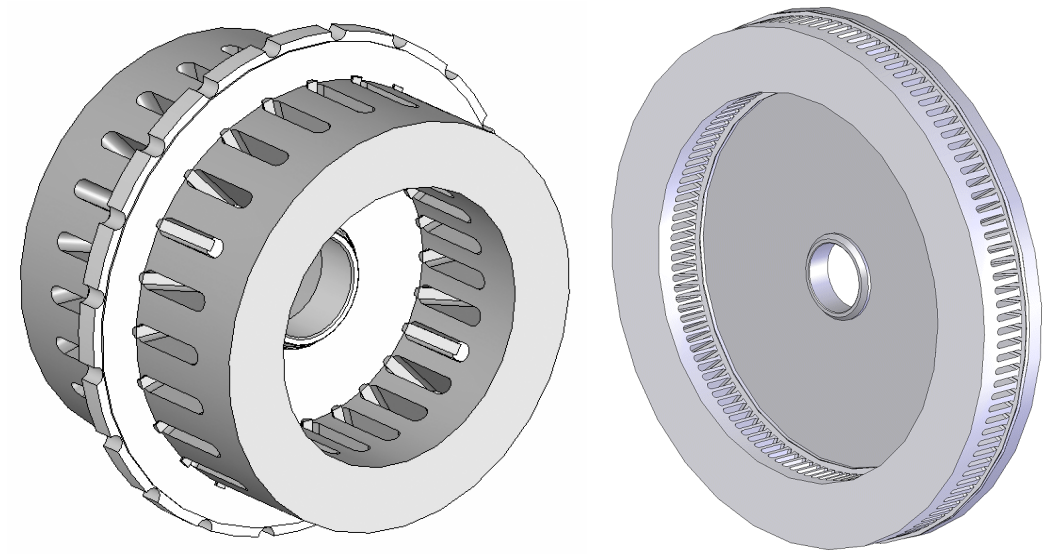

a) b)

Fig. 4.4. Geometry of the 5.6 kVA and 18.3kVA prototype axial flux permanent magnet synchronous generators. a) The generator AFPMSG1 has four magnetic poles. It consists of two stators and one rotor between the stators. b) The geometry of AFPMSG2. The generator has 16 magnetic poles. It consists of one stator and one rotor.

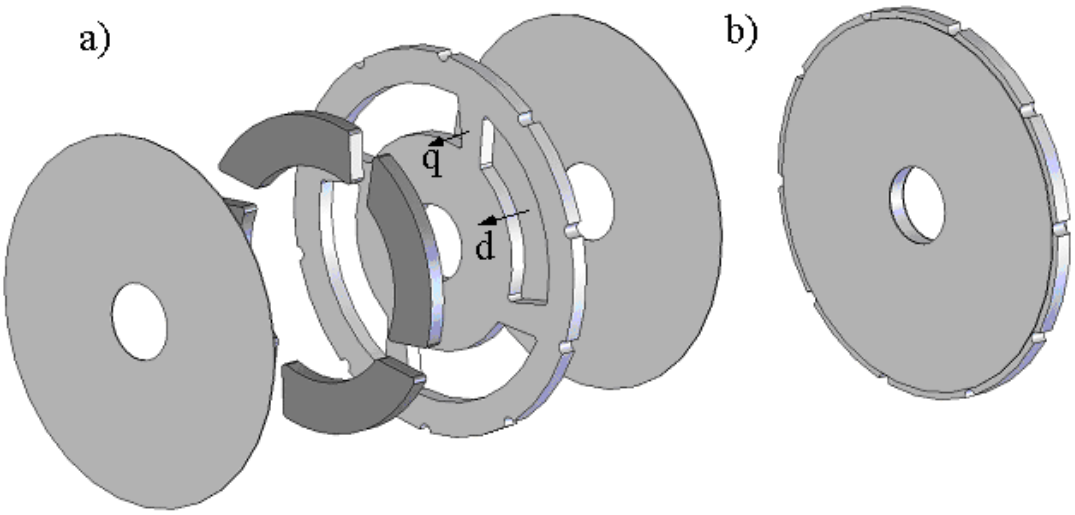

Fig. 4.5 Rotor construction of AFPMSG1. Magnets are surrounded by an aluminium rotor frame called installation jig which aligns the magnets into correct position. Aluminium surface plates are installed on both sides of the disc rotor. a) Exploded view. b) Assembled rotor.

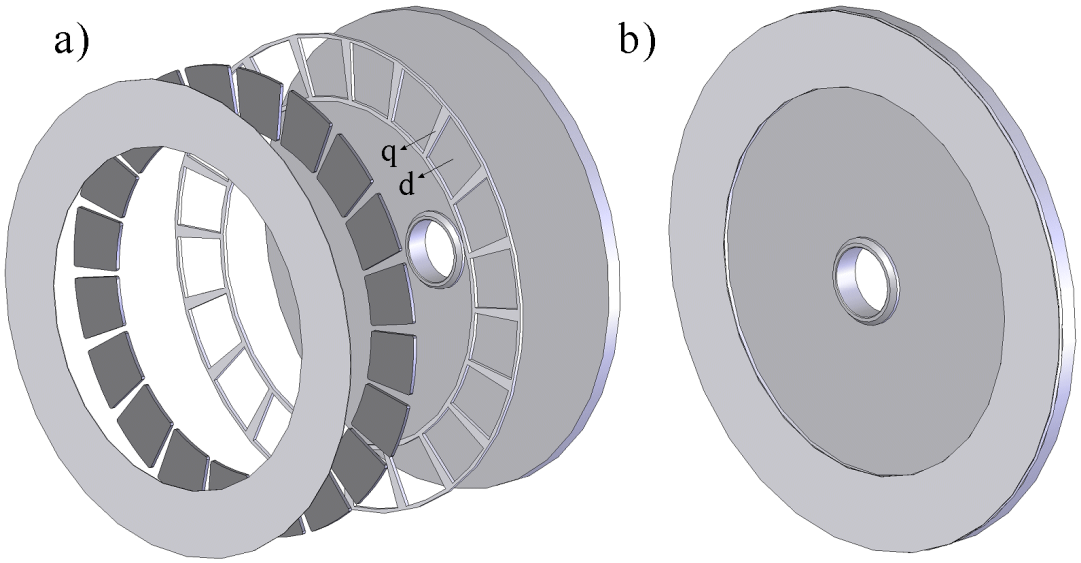

Fig. 4.6 Rotor construction of AFPMSG2. Magnets are surrounded by an aluminium installation jig, which is installed on a cast iron rotor body. An aluminium surface plate is installed over the magnets. a) Exploded view. b) Assembled rotor.

Table 4.2 Main parameters of the two studied prototype permanent magnet synchronous generators AFPMSG1 and AFPMSG2, both provided with damper windings.

		AFPMSG 1		AFPMSG 2	
Parameter	**Symbol**	**Value**	**Per unit value**	**Value**	**Per unit value**
Nominal power	P_n	5200 W		15900 W	
Apparent power	S_n	5600 VA	1	18300 VA	1
Nominal voltage	U_n	400 V		660 V	
Nominal phase voltage	U_{ph}	230 V	1	380 V	1
Nominal current	I_n	8 A	1	16 A	1
Nominal power factor	$\cos\varphi$	0.93	0.93	0.87	0.87
Electromotive force	E	410 V		567 V	
Phase electromotive force	E_{ph}	237 V	1.03	327 V	0.86
Stator resistance	R_s	1.28 Ω	0.044	1,2 Ω	0.051
Direct-axis damper winding resistance	R_D	3.59 Ω	0.124	2.59 Ω	0.109
Quadrature-axis damper winding resistance	R_Q	4.23 Ω	0.147	2.71 Ω	0.114
Number of pole pairs	p	2	2	8	8
Direct and quadrature-axis magnetizing inductance	L_{md}	23 mH	0.251	23.9 mH	0.316
Quadrature-axis magnetizing inductance	L_{mq}	24 mH	0.262	23.9 mH	0.316
Stator leakage inductance	$L_{s\sigma}$	24.3 mH	0.264	15.9 mH	0.210
Direct-axis damper winding leakage inductance	$L_{D\sigma}$	2.09 mH	0.023	4.88 mH	0.065
Quadrature-axis damper winding leakage inductance	$L_{Q\sigma}$	6.82 mH	0.074	6.87 mH	0.091
Damper winding direct-axis open-circuit time constant	T''_{d0}	3.90 ms	1.23	5.99 ms	1.88
Damper winding direct-axis short-circuit time constant	T''_{d}	7.10 ms	2.23	11.94 ms	3.75
Damper winding quadrature-axis open-circuit time constant	T''_{q0}	4.43 ms	1.39	4.20 ms	1.32
Damper winding quadrature-axis short-circuit time constant	T''_{q}	7.14 ms	2.24	7.87 ms	2.47
Nominal load angle	δ	36 °	36 °	18 °	18 °
Nominal torque	T_n	33 Nm	0.929	400 Nm	0.858
Frequency	f	50 Hz	1	50 Hz	1
Rotation speed	n	1500 rpm	1	375 rpm	1
Moment of rotor inertia	J_r	0.026 kgm^2	T_J =36,0	5.47 kgm^2	T_J =144.8
Total moment of system inertia	J_{tot}	0.3334 kgm^2	T_J =461,0	510.5 kgm^2	T_J =13515
Stator lamination outer radius	$R_{s,out}$	110 mm		230 mm	
Stator lamination inner radius	$R_{s,in}$	75 mm		170 mm	
Air gap length	δ_{ag}	2 x 3.5 mm		3 mm	
Rotor PM material		Neorem 495a		Neorem 495a	
Damper construction		Jig + 2 × 1 mm plates (Aluminium)			Jig + 1 mm plate (Aluminium)

4.5 Guidelines for permanent magnet generator damper winding design

According to Vogt (1996) in synchronous generators the cross-sectional area of the damper bars is usually selected to be 20–30 % of the cross-sectional area of the bar of the armature winding. Windings with such a sizing are made of copper. The cross-sectional area of the damper winding short-circuit rings is selected to be approximately 30–50 % of the cross-sectional area of the damper bars per pole. When the damper windings of salient-pole machines are placed in the slots, the slot pitch has to be selected to diverge 10–15 % from the slot pitch of the stator to avoid the pulsation of the flux and noise. To summarize these instructions the amount of bars should be about the same in the rotor and in the stator (10 – 15 % deviation) and the damper bars should have about 20–30% cross sectional area compared to the stator slot copper cross sectional area.

The damper winding constructions of the permanent magnet synchronous generators are proposed to be divided into three categories in this case. The work of this thesis is focused on category 3.

1) Damper bars: traditional design of the squirrel cage.

2) Conducting surface plate(s): surface plate parameter calculation.

3) Combination of the damper cage bars and the conducting surface plate(s): an installation jig and a surface plate, parallel connection of the surface plate and the squirrel cage.

The dimension parameters of the surface plate and damper bars are shown in Fig. 4.7.

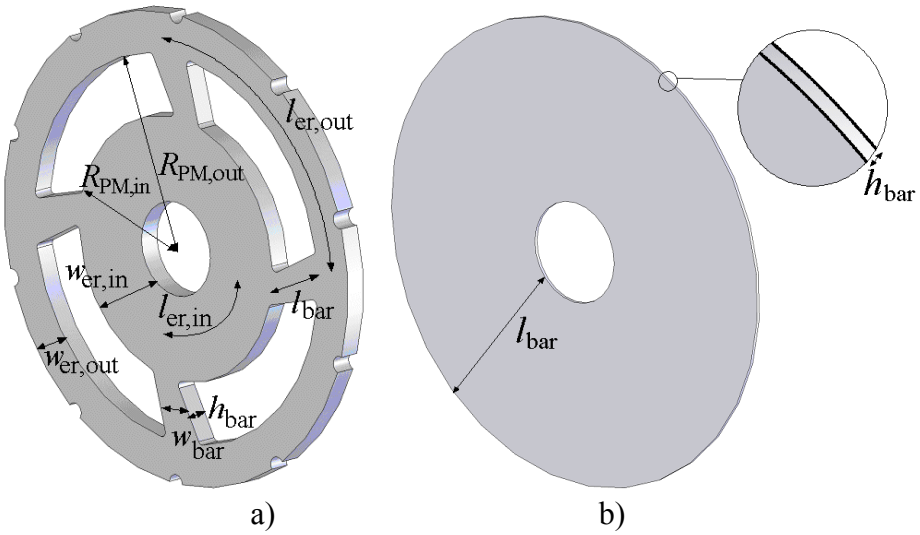

Fig. 4.7 AFPMSG1aluminium damper winding construction. a) damper bars. b) conducting surface plate.

Figure 4.7 indicates that the amount of aluminium in the damper winding is remarkably less than suggested by Vogt (1996). The surface conducting plate, however, increases the amount of conductivity in the rotor and also brings smaller the damper winding resistances. If the damper winding resistance becomes too large the thickness of the surface plates should be increased suitably or the magnets should be divided in several parts and damper bars installed between the magnets.

4.5.1 Damper bars

The parameters of the damper windings consisting of damper bars and end rings can be obtained in the same way as in the induction machines for the squirrel cage. The angular current distribution is approximately the same as would be the case in a conducting surface plate if the cross-sectional areas were the same.

Generally, there has to be at least two conductors in a coil turn at a distance of about 180° from each other. We may thus consider that a single rotor bar comprises half a turn, or $N_\mathrm{r} = ½$. The number of effective coil turns in a stator is $m_\mathrm{s} k_{\mathrm{w1s}} N_\mathrm{s}$ and in the rotor $m_\mathrm{r} k_{\mathrm{w1r}} N_\mathrm{r}$. Here $k_{\mathrm{w1r}} = 1$ and $N_\mathrm{r} = ½$. If the slots of the stator and rotor are skewed with respect to each other, we also have to take the skewing factor k_sq into account. When considering the current linkages of a harmonic ν, the rotor current $I'_{\nu\mathrm{r}}$ referred to the stator and flowing in the stator winding has to produce an equal current linkage as the original rotor current when flowing in the rotor. Thus we may write (Pyrhönen, 2007, lecture material in electrical machines)

$$m_\mathrm{s} N_\mathrm{s} k_{\mathrm{w}\nu\mathrm{s}} I'_{\nu\mathrm{r}} = m_\mathrm{r} N_\mathrm{r} k_{\mathrm{sq}\nu\mathrm{r}} k_{\mathrm{w}\nu\mathrm{r}} I_{\nu\mathrm{r}} . \tag{4.2}$$

The quantities with a prime symbol $'$ are referred to the stator from the rotor. The transformation ratio for the harmonic ν from the rotor to the stator becomes thus

$$K_{\mathrm{rs},\nu} = \frac{I_{\nu\mathrm{r}}}{I'_{\nu\mathrm{r}}} = \frac{m_\mathrm{s} k_{\mathrm{w}\nu\mathrm{s}} N_\mathrm{s}}{m_\mathrm{r} k_{\mathrm{w}\nu\mathrm{r}} k_{\mathrm{sq}\nu\mathrm{r}} N_\mathrm{r}} . \tag{4.3}$$

By applying the above to the cage winding and the fundamental harmonic, we obtain

$$K_{\mathrm{rs},1} = \frac{m_\mathrm{s} k_{\mathrm{w1s}} N_\mathrm{s}}{m_\mathrm{r} k_{\mathrm{w1r}} k_{\mathrm{sq1r}} N_\mathrm{r}} = \frac{m_\mathrm{s} k_{\mathrm{w1s}} N_\mathrm{s}}{Q_\mathrm{r} \cdot 1 \cdot k_{\mathrm{sq1r}} \cdot ½} = \frac{2 m_\mathrm{s} k_{\mathrm{w1s}} N_\mathrm{s}}{Q_\mathrm{r} k_{\mathrm{sq1r}}} . \tag{4.4}$$

If R_r is the resistance of the rotor bar added with the proportion of the short-circuit rings, and I_r is the RMS value of the current of the rotor bar, we obtain, by writing the resistive loss of the rotor equal both in the stator and in the rotor

$$m_\mathrm{s} I'^2_\mathrm{r} R'_\mathrm{r} = Q_\mathrm{r} I^2_\mathrm{r} R_\mathrm{r} . \tag{4.5}$$

The phase resistance of the rotor referred to the stator can now be written as

$$R'_{\mathrm{r}} = \frac{Q_{\mathrm{r}} I_{\mathrm{r}}^2 R_{\mathrm{r}}}{m_{\mathrm{s}} I_{\mathrm{r}}'^2}\,. \tag{4.6}$$

Since

$$\frac{I_{\mathrm{r}}}{I'_{\mathrm{r}}} = K_{\mathrm{rs}}, \tag{4.7}$$

the resistance of the rotor referred to the stator becomes now

$$R'_{\mathrm{r}} = \frac{Q_{\mathrm{r}}}{m_{\mathrm{s}}}\left[\frac{I_{\mathrm{r}}}{I'_{\mathrm{r}}}\right]^2 R_{\mathrm{r}} = \frac{Q_{\mathrm{r}}}{m_{\mathrm{s}}} K_{\mathrm{rs,1}}^2 R_{\mathrm{r}} = \frac{Q_{\mathrm{r}}}{m_{\mathrm{s}}}\left[\frac{2m_{\mathrm{s}} k_{\mathrm{w1s}} N_{\mathrm{s}}}{Q_{\mathrm{r}} k_{\mathrm{sq1r}}}\right]^2 R_{\mathrm{r}} = \frac{4m_{\mathrm{s}}\left(k_{\mathrm{w1s}} N_{\mathrm{s}}\right)^2}{Q_{\mathrm{r}} k_{\mathrm{sq1r}}^2} R_{\mathrm{r}}\,. \tag{4.8}$$

When it is necessary to refer the rotor resistance to the stator, in general, it has to be multiplied with the term

$$\rho_\nu = \frac{m_{\mathrm{s}}}{m_{\mathrm{r}}}\left(\frac{N_{\mathrm{s}} k_{\mathrm{w}\nu\mathrm{s}}}{N_{\mathrm{r}} k_{\mathrm{sq}\nu\mathrm{r}} k_{\mathrm{w}\nu\mathrm{r}}}\right)^2. \tag{4.9}$$

In a squirrel cage damper winding, the above is written in the form

$$\rho_\nu = \frac{4m_{\mathrm{s}}}{Q_{\mathrm{r}}}\left(\frac{N_{\mathrm{s}} k_{\mathrm{w}\nu\mathrm{s}}}{k_{\mathrm{sq}\nu\mathrm{r}}}\right)^2. \tag{4.10}$$

If there is no skewing, we write further

$$\rho_\nu = \frac{4m_{\mathrm{s}}}{Q_{\mathrm{r}}}\left(N_{\mathrm{s}} k_{\mathrm{w}\nu\mathrm{s}}\right)^2. \tag{4.11}$$

The same referring factor is valid also in the referring of the inductances and thereby we get

$$\begin{aligned} R'_{\nu\mathrm{r}} &= \rho_\nu R_{\nu\mathrm{r}} \\ L'_{\nu\mathrm{r}} &= \rho_\nu L_{\nu\mathrm{r}}\,. \end{aligned} \tag{4.12}$$

Here it is worth noticing that in a rotating electrical machine, the referring deviates from the referring in a transformer by the fact that the impedance quantities are not referred directly with the square of the transformation ratio of the current, but we also have to take the ratio of the numbers of phases and winding factors into account.

4.5.2 Conducting surface plate

The conducting surface plate can be divided into infinite amount of bars. The virtual end rings are reduced to zero length. The number of the damper bars will be

subtracted from the rotor resistance equation seen by the stator. The virtual damper bars are assumed to have no skewing.

The resistance of a single bar is

$$R_{\mathrm{bar}} = \frac{l_{\mathrm{bar}}}{\sigma_{\mathrm{Al}} A_{\mathrm{bar}}} = \frac{l_{\mathrm{bar}}}{\sigma_{\mathrm{Al}} w_{\mathrm{bar}} h_{\mathrm{bar}}} \tag{4.13}$$

The width of the bar w_{bar} is infinitely thin. The pole pitch τ_{p} is divided by the number of the virtual damper bars. Thus, the number of the damper bars does no longer appear in the equation. The rotor resistance seen by the stator is

$$\begin{aligned} R'_{\mathrm{r}} &= \frac{4m_{\mathrm{s}}\left(N_{\mathrm{s}} k_{\mathrm{w}\nu s}\right)^2}{Q_{\mathrm{r}}} R_{\mathrm{bar}} = \frac{4m_{\mathrm{s}}\left(N_{\mathrm{s}} k_{\mathrm{w}\nu s}\right)^2}{Q_{\mathrm{r}}} \frac{l_{\mathrm{bar}}}{\sigma_{\mathrm{Al}} \frac{\tau_{\mathrm{p}}}{Q_{\mathrm{r}}} h_{\mathrm{bar}}} = \frac{4m_{\mathrm{s}} l_{\mathrm{bar}}\left(N_{\mathrm{s}} k_{\mathrm{w}\nu s}\right)^2}{\sigma_{\mathrm{Al}} \tau_{\mathrm{p}} h_{\mathrm{bar}}} = \\ &\frac{4m_{\mathrm{s}} l_{\mathrm{bar}}\left(N_{\mathrm{s}} k_{\mathrm{w}\nu s}\right)^2}{\sigma_{\mathrm{Al}} \cdot \frac{2\pi(R_{\mathrm{PM,out}} + R_{\mathrm{PM,in}})}{2 \cdot 2p} \cdot h_{\mathrm{bar}}} = \frac{8pm_{\mathrm{s}} l_{\mathrm{bar}}\left(N_{\mathrm{s}} k_{\mathrm{w}\nu s}\right)^2}{\sigma_{\mathrm{Al}} h_{\mathrm{bar}} \pi(R_{\mathrm{PM,out}} + R_{\mathrm{PM,in}})} \end{aligned} \tag{4.14}$$

4.5.3 Damper bars and conducting surface plate

The rotor bar resistance $R_{\mathrm{r,bar}}$ is calculated from the length of the bar, the cross-sectional area of the bar, and the conductivity of the rotor bar material. For the AFPMSG1, the aluminium installation jig forms a coarse squirrel cage with thick rotor bars connected to the end rings.

The length of the end rings per bar is

$$\begin{aligned} l_{\mathrm{er,in}} &= \frac{2\pi\left(R_{\mathrm{PM,in}} - \frac{w_{\mathrm{er,in}}}{2}\right)}{2p} = \frac{\pi\left(R_{\mathrm{PM,in}} - \frac{w_{\mathrm{er,in}}}{2}\right)}{p} \\ l_{\mathrm{er,out}} &= \frac{2\pi\left(R_{\mathrm{PM,out}} + \frac{w_{\mathrm{er,out}}}{2}\right)}{2p} = \frac{\pi\left(R_{\mathrm{PM,out}} + \frac{w_{\mathrm{er,out}}}{2}\right)}{p} \end{aligned} \tag{4.15}$$

The number of the rotor bars is selected as a number of the spokes in the installation jig. The rotor phase resistance can be calculated when the cross-sectional area of the spoke of the installation jig and the end rings are known.

$$R_{r1} = R_{er,in} + R_{er,out} + R_{bar} = \frac{l_{er,in}}{\sigma_{Al} A_{er,in}} + \frac{l_{er,out}}{\sigma_{Al} A_{er,out}} + \frac{l_{bar}}{\sigma_{Al} A_{bar}}$$
$$= \frac{1}{\sigma_{Al}} \left(\frac{l_{er,in}}{w_{er,in} h_{bar}} + \frac{l_{er,out}}{w_{er,out} h_{bar}} + \frac{l_{bar}}{w_{bar} h_{bar}} \right) \tag{4.16}$$

where w_{bar} is the width of the jig spoke and h_{bar} is the thickness of the installation jig. The spokes of the installation jig are skewed. The skewing factor (Nau 1997) is

$$k_{sqvr} = \frac{\sin\left(\frac{\gamma}{\tau_p} \cdot \frac{\pi}{2} \right)}{\frac{\gamma}{\tau_p} \cdot \frac{\pi}{2}}, \tag{4.17}$$

where γ is the skewing of the magnets. In this case, the skewing is one slot pitch τ_u.

$$k_{sqvr} = \frac{\sin\left(\frac{\gamma}{\tau_p} \cdot \frac{\pi}{2} \right)}{\frac{\gamma}{\tau_p} \cdot \frac{\pi}{2}} = \frac{\sin\left(\frac{\tau_u}{\tau_p} \cdot \frac{\pi}{2} \right)}{\frac{\tau_u}{\tau_p} \cdot \frac{\pi}{2}} \tag{4.18}$$

The damper winding resistance can be referred to the stator

$$R'_{r1} = \frac{4 m_s \left(N_s k_{wvs} \right)^2}{Q_r k_{sqvr}} R_{r1} \tag{4.19}$$

This rotor resistance is in parallel connection with the surface aluminium. The surface aluminium can be divided into an infinite number of bars. The virtual end rings are diminished to zero length. The resistance of the surface plate is

$$R'_{r2} = \frac{8 p m_s l_{bar} \left(N_s k_{wvs} \right)^2}{\sigma_{Al} h_{bar} \pi (R_{PM,out} + R_{PM,in})} \tag{4.20}$$

The total rotor resistance is the parallel connection of these two values

$$R'_r = \frac{R'_{r1} R'_{r2}}{R'_{r1} + R'_{r2}} \tag{4.21}$$

The rotor of the AFPMSG1 has two conducting surface plates. Therefore, another parallel resistance of the surface plate is added to Eq. (4.21).

$$\frac{R'_{r2}\,R'_{r2}}{R'_{r2}+R'_{r2}}=\frac{R'_{r2}}{2}\Rightarrow R'_{r}=\frac{R'_{r1}\,\frac{R'_{r2}}{2}}{R'_{r1}+\frac{R'_{r2}}{2}}=\frac{R'_{r1}\,R'_{r2}}{2R'_{r1}+R'_{r2}} \tag{4.22}$$

The damper winding resistance may be divided equally into d-axis and q-axis components, unless there is better knowledge of the distribution.

$$R_{D}=R_{Q}=\frac{R'_{r}}{\sqrt{2}} \tag{4.23}$$

This method makes coarse assumptions, but the actual analytical modelling of a damper winding of this kind is very complicated. The actual installation jig has damper bars, in which the widths of the bars become larger towards the outer radius of the rotor. Therefore, an average width of the bars was used in the calculations.

4.6 Asynchronous torque components

In grid connections and during the transients the rotation speed is not synchronous. The question is how to determine the sufficient asynchronous pull-out torque compared with the synchronous pull-out torque and the shape of the asynchronous torque to guarantee synchronization in the grid connection. Again, the determination is case specific, and the values are dependent on the load characteristics, the moment of inertia and the synchronization window. The total accelerating torque T_a in the asynchronous operation may be separated into components. T_a consists of the cage torque T_c produced by the damper windings, the braking torque T_b from the permanent magnets and the reluctance torque T_r from the saliency of the rotor ($T_a = T_c + T_r + T_b$). An illustrating example of the different torque components and their behaviour as a function of the slip are shown in Fig. 4.8.

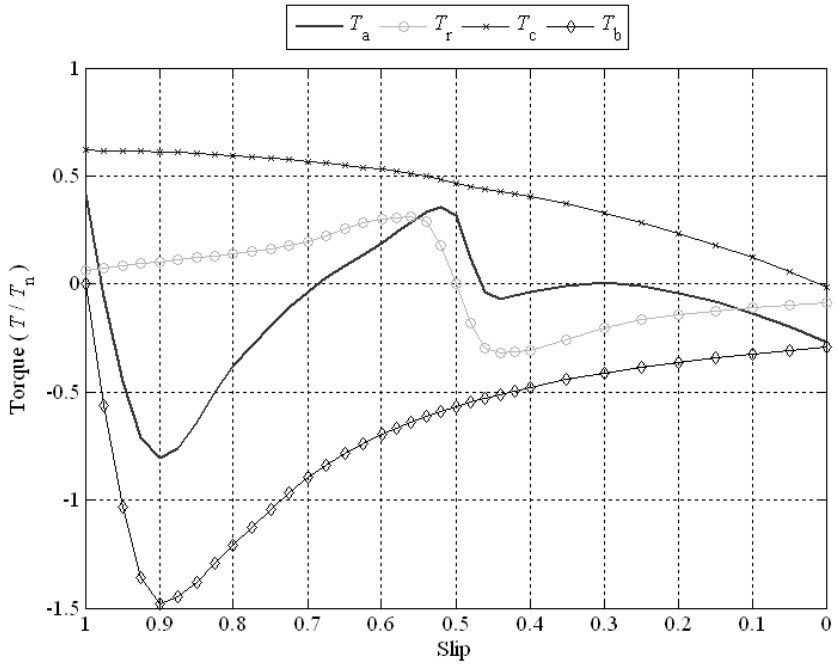

Fig. 4.8. Example of the asynchronous torque components of a fictional salient-pole permanent magnet machine provided with asymmetric damper windings. $E_{PM,pu} = 1.04$, $R_{D,pu} = 0.15$, $R_{Q,pu} = 0.15$, $R_{s,pu} = 0.05$, $L_{D\sigma,pu} = 0.05$, $L_{Q\sigma,pu} = 0.1$, $L_{d,pu} = 0.5$, $L_{q,pu} = 1$. T_c, damper cage torque, T_b, permanent magnet average torque T_r, asynchronous torque caused by the reluctance difference, T_a, accelerating sum torque. The curves indicate the static values of the different torque components.

4.6.1 Braking torque

The permanent magnets produce a pulsating braking torque during the acceleration of the rotor into the synchronous speed. Permanent magnet braking torque T_b in Fig. 4.8 is the average value of the pulsating braking torque. The braking torque of the permanent magnets distorts the synchronization. The asynchronously rotating rotor flux component and the synchronously rotating stator flux component are interacting so that the braking torque includes pulsation because of the asynchronous speed. In principle, the amplitude of the pulsation is the value of the synchronous pull-out torque. The load angle is shifting continuously causing pulsating torque at the frequency of $s \cdot f_s$, shown in Fig. 4.9.

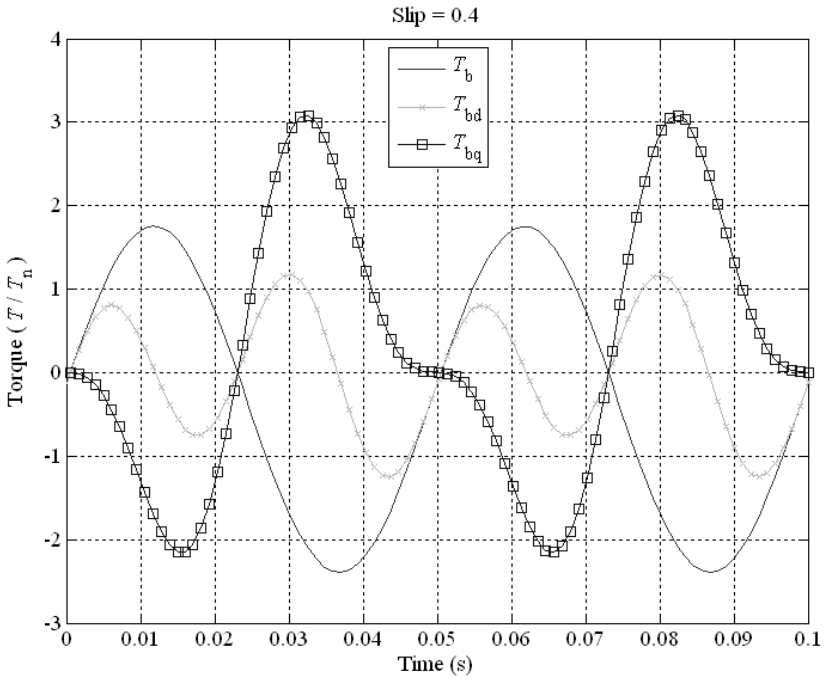

Fig. 4.9 Torque components of the asynchronous permanent magnet braking torque. $E_{PM,pu}$ = 1.04, $R_{s,pu}$ = 0.05, $L_{d,pu}$ = 0.5, $L_{q,pu}$ = 0.5. Supply frequency f_s = 50 Hz. Slip of the rotor s = 0.4. Pulsating braking torque T_b has period 0.05s and thus frequency $s \cdot f_s$ = 20 Hz. $T_b = T_{bd} - T_{bq}$.

When the rotor rotates the magnetic flux generated by the permanent magnets flows through the stator windings and induces voltage components. These voltages are shorted via the network impedance, which is low compared with the impedance of the synchronous machine. These shorted voltages cause currents to the stator windings. The induced currents cause resistive losses in the stator windings and produce the braking torque. The equation for permanent magnet braking torque is derived in Appendix A.1. According to Libert et. al. (2002b), The average of the permanent magnet braking torque is

$$T_b = -3p \cdot \frac{R_s (1-s) E_{PM}^2}{\omega_s} \cdot \frac{R_s^{\,2} + \omega_s^2 L_q^{\,2} (1-s)^2}{\left(R_s^{\,2} + \omega_s^2 L_d L_q (1-s)^2 \right)^2} \propto \frac{E_{PM}^2}{\omega_s^2 L_d L_q}. \tag{4.24}$$

It can be seen in Eq. (4.24) that the amplitude of the electromotive force E_{PM} produced by the permanent magnet significantly increases the braking torque. In line-start machines, the electromotive force is usually rather low in order to achieve line-start capability. This, however, leads to a poor synchronous performance and a poor power factor. PMSGs are usually overexcited, which means a high value of the electromotive force.

The stator resistance does not notably affect the maximum value of the braking torque. However, it has an effect on the total braking torque at different slip values and the slip value of the maximum braking torque. The higher the stator resistance, the lower the slip value of the maximum braking torque. Depending on the stator

resistance and the network impedance, the torque produced by the permanent magnets is very large at low speeds. This is very problematic in LSPMSMs that do not start from zero speed without high resistance damper windings. The performance around the synchronous speed is weak and the motor becomes easily unstable, especially at low operating frequencies. On the contrary, in DOL PMSGs, most of the operation is near by the synchronous operation speed. There is no need for DOL start from zero-speed ability and it is beneficial if the maximum braking torque occurs at low high slip values.

The slip value of the maximum braking torque can be calculated by differentiating Eq (4.24) with respect to the slip.

$$\frac{\mathrm{d}}{\mathrm{d}s}T_{\mathrm{b}}(s)=\frac{3pR_{\mathrm{s}}E_{\mathrm{PM}}^{2}}{\omega_{\mathrm{s}}\left(R_{\mathrm{s}}{}^{2}+\omega_{\mathrm{s}}{}^{2}L_{\mathrm{d}}L_{\mathrm{q}}(1-s)^{2}\right)^{2}}\cdot\Bigg[$$

$$\left(R_{\mathrm{s}}{}^{2}+\omega_{\mathrm{s}}{}^{2}L_{\mathrm{d}}L_{\mathrm{q}}(1-s)^{2}\right)+2(1-s)^{2}\omega_{\mathrm{s}}{}^{2}L_{\mathrm{q}}{}^{2}-\frac{4L_{\mathrm{d}}L_{\mathrm{q}}(1-s)^{2}\left(R_{\mathrm{s}}{}^{2}+\omega_{\mathrm{s}}{}^{2}L_{\mathrm{q}}{}^{2}(1-s)^{2}\right)}{R_{\mathrm{s}}{}^{2}+\omega_{\mathrm{s}}{}^{2}L_{\mathrm{d}}L_{\mathrm{q}}(1-s)^{2}}\Bigg] \tag{4.25}$$

The highest average value of the braking torque is found from the zero crossing value of the Eq (4.25).

$$\frac{\mathrm{d}}{\mathrm{d}s}T_{\mathrm{b}}(s)=0\Leftrightarrow$$

$$s_{\mathrm{peak}}=\frac{2\omega_{\mathrm{s}}L_{\mathrm{q}}{}^{2}L_{\mathrm{d}}\pm\sqrt{-6L_{\mathrm{q}}{}^{2}L_{\mathrm{d}}{}^{2}R_{\mathrm{s}}{}^{2}+6L_{\mathrm{q}}{}^{3}L_{\mathrm{d}}R_{\mathrm{s}}{}^{2}\pm2L_{\mathrm{q}}{}^{2}L_{\mathrm{d}}\sqrt{(9L_{\mathrm{d}}{}^{2}R_{\mathrm{s}}{}^{4}-14L_{\mathrm{q}}L_{\mathrm{d}}+9L_{\mathrm{q}}{}^{2}R_{\mathrm{s}}{}^{4})}}}{2L_{\mathrm{q}}{}^{2}L_{\mathrm{d}}\omega_{\mathrm{s}}} \tag{4.26}$$

The effect of the stator resistance on the shape of the permanent magnet braking torque is illustrated in Fig. 4.10.

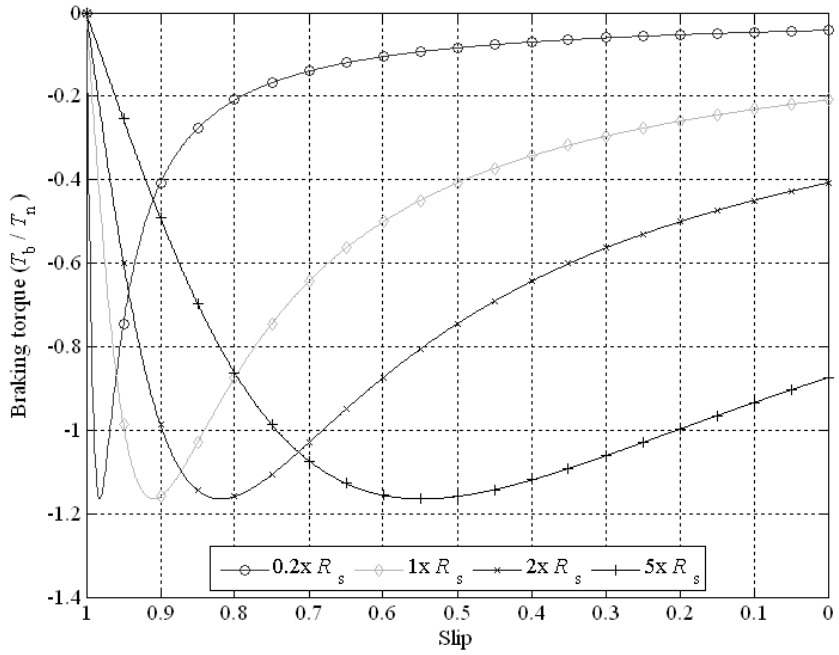

a)

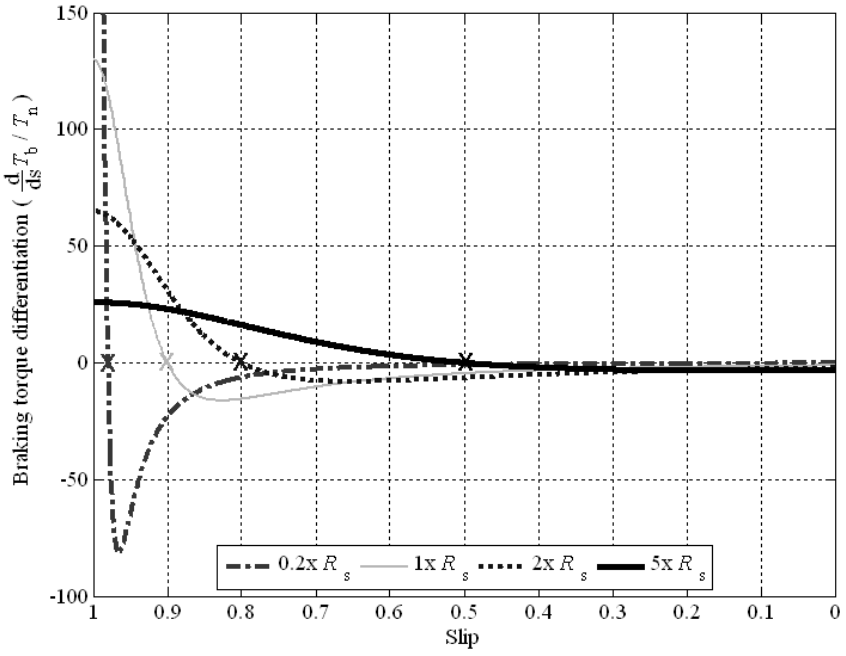

b)

Fig. 4.10. a) Permanent magnet braking torque as a function of slip. $E_{PM,pu}$ = 1.04, $R_{s,pu}$ = 0.05, $L_{D\sigma,pu}$ = 0.05, $L_{d,pu}$ = 0.5, $L_{q,pu}$ = 0.5. The stator resistance R_s has an effect on the slip value of the maximum braking torque. Also the overall braking torque is affected by the stator resistance. The impedance of the network is assumed to be zero. b) Differentiation of the magnet braking torque. The maximum value of the permanent magnet braking torque and the corresponding slip value is found at zero crossing of the curve from Eq. (4.25).

In small PMSGs, the copper losses of the stator resistance are quite high in proportion to the overall losses, and the stator resistance is large. In large generators instead, the stator resistance is usually very small and the maximum value of the permanent magnet braking torque occurs only at high slip values.

4.6.2 Cage torque

In line-start motors, at standstill, the starting torque produced by the damper cage should be high to overcome the permanent magnet braking torque and the load torque. Hence, a high damper resistance is selected. In a DOL PMSG, however, the asynchronous pull-out torque should be close to the zero-slip value to gain good synchronization and good ability to maintain synchronism. Approaches such as double cages or deep bar cages, which are typically used in squirrel cage motors have not been found by the author in DOL PMSGs to enhance the overall performance of the damper winding.

The term ‘cage torque’ comes from the line-start permanent magnet synchronous motors that were designed from induction motors by adding inset permanent magnets in the induction cage rotor. If the rotor is symmetrical, the shape of the cage torque is defined similarly as the cage rotor torque in asynchronous machines by the equation (Engelmann & Middendorf 1995)

$$T_{\mathrm{c}} \approx 3p \frac{U_{\mathrm{s}}^2 \left(\frac{R_{\mathrm{r}}}{s} \right)}{\omega_{\mathrm{s}} \left[\left(R_{\mathrm{s}} + \frac{R_{\mathrm{r}}}{s} \right)^2 + \left(\omega_{\mathrm{s}} L_{\mathrm{s}\sigma} + \omega_{\mathrm{s}} L_{\mathrm{r}\sigma} \right)^2 \right]} \quad . \tag{4.27}$$

The rotor resistance R_{r} is equivalent to the damper winding resistance referred to the stator. The asynchronous pull-out torque of the cage torque can be increased by decreasing the stator and rotor inductances. The slip value of the asynchronous pull-out torque can be determined by the damper winding resistances. The higher the damper winding resistance, the higher the slip value of the asynchronous pull-out torque. The effect of the symmetric damper winding resistance to the slip value of the asynchronous pull-out torque is shown in Fig. 4.11.

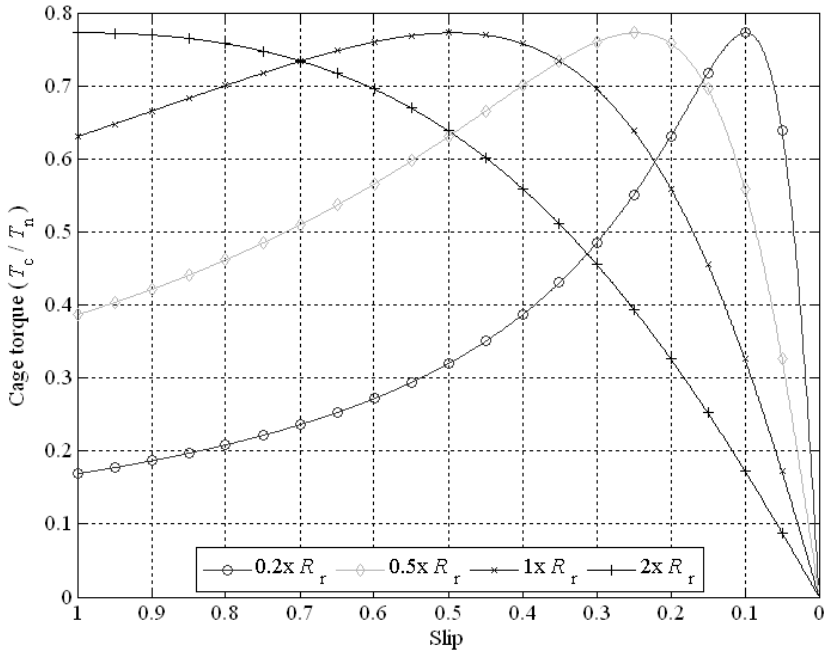

Fig. 4.11. Asynchronous damper cage torque as a function of the slip. $R_{r,pu}$=0.15, $R_{s,pu}$ = 0.05, $L_{r\sigma,pu}$ = 0.07, $L_{s\sigma,pu}$ = 0.25. The damper winding resistance has a remarkable effect on the slip value of the asynchronous pull-out torque.

The actual damper winding parameters of the DOL PMSG may be different in direct and quadrature-axis positions because of the rotor constructions that may have rotor asymmetry due to asymmetrical damper windings or asymmetric magnetizing inductances. In Eq. (4.27) there is only one value for the single-phase equivalent circuit damper-winding-referred resistance. If the damper cage is asymmetric, the cage torque is calculated from the complex equations (Honsinger 1980) by substituting asynchronous current components and conjugate parts of the flux linkages into general torque equation (Appendix A.2).

$$T_{\mathrm{c}} = \frac{1}{2}\frac{3p}{2}\mathrm{Re}\left[\Psi_{\mathrm{dc}}^{*} I_{\mathrm{qc}} - \Psi_{\mathrm{qc}}^{*} I_{\mathrm{dc}}\right], \tag{4.28}$$

The corresponding flux linkages are

$$\begin{cases} \Psi_{\mathrm{dc}} = \dfrac{X_{\mathrm{kd}} I_{\mathrm{dc}}}{\omega} \\ \Psi_{\mathrm{qc}} = \dfrac{X_{\mathrm{kq}} I_{\mathrm{qc}}}{\omega} \end{cases}. \tag{4.29}$$

where current components of the cage torque are

$$\begin{cases} I_{\mathrm{dc}} = \dfrac{U_{\mathrm{ph}}\left(\mathrm{j}R_{\mathrm{s}} + X_{\mathrm{kq}}(1-s)\right)}{R_{\mathrm{s}}^2 + \mathrm{j}sR_{\mathrm{s}}(X_{\mathrm{kd}} + X_{\mathrm{kq}}) + X_{\mathrm{kd}}X_{\mathrm{kq}}(1-s^2)} \\ I_{\mathrm{qc}} = \dfrac{U_{\mathrm{ph}}\left(R_{\mathrm{s}} + \mathrm{j}X_{\mathrm{kd}}(s-1)\right)}{R_{\mathrm{s}}^2 + \mathrm{j}sR_{\mathrm{s}}(X_{\mathrm{kd}} + X_{\mathrm{kq}}) + X_{\mathrm{kd}}X_{\mathrm{kq}}(1-s^2)} \end{cases}, \tag{4.30}$$

where operational reactances X_{kd} and X_{kq} are

$$\begin{cases} X_{\mathrm{kd}} = X_{\mathrm{d}} + \dfrac{s^2 X_{\mathrm{md}}^2}{\mathrm{j}sR_{\mathrm{D}} - s^2\omega_{\mathrm{s}}X_{\mathrm{D}}} \\ X_{\mathrm{kq}} = X_{\mathrm{q}} + \dfrac{s^2 X_{\mathrm{mq}}^2}{\mathrm{j}sR_{\mathrm{Q}} - s^2\omega_{\mathrm{s}}X_{\mathrm{Q}}} \end{cases}. \tag{4.31}$$

The effect of the damper winding resistance asymmetry can be seen around the half speed. According to Schuisky (1949), an inverse component of the rotating magnetic field is also created as a result of the flux pulsation caused by the rotor asymmetry. This pulsation is bound to the rotor. The rotor-bound pulsating magnetic field consists of two opposite rotating fields. The rotor currents have the frequency of $(1 - s)\cdot f_{\mathrm{s}}$. The inverse component of the rotor-bound magnetic field rotates in the opposite direction with the frequency $(1 - 2s)\cdot f_{\mathrm{s}}$. This rotating field changes its direction with respect to the stator at the slip $s = 0.5$, where the net-torque produced by the inverse component part is zero. T_{c} as a function of slip was simulated by the two-axis simulation model presented in Chapter 3. The synchronous inductances in the simulations have the same value in direct-axis and quadrature-axis components, $L_{\mathrm{d}} = L_{\mathrm{q,pu}} = 0.5$. The permanent magnet flux linkage is removed from the simulation. Therefore, only the asymmetry of the damper winding produces torque, shown in Fig. 4.12. Damper winding parameters $L_{\mathrm{D}\sigma,\mathrm{pu}} = 0.05$ and $R_{\mathrm{D,pu}} = 0.15$ are fixed in the simulations.

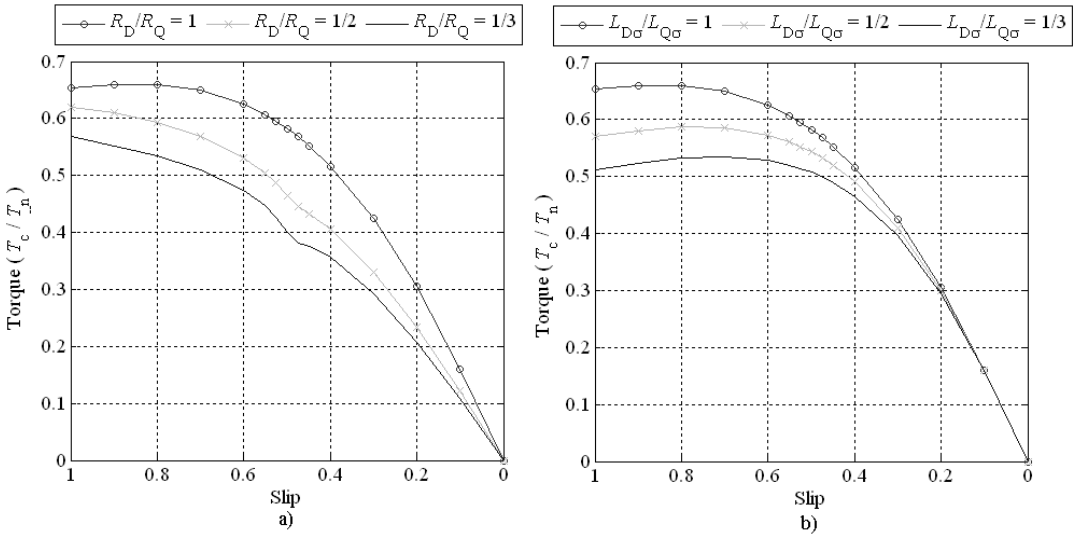

Fig. 4.12 Cage torque as function of slip from two-axis simulation model. a) $R_{D,pu}$ = 0.15, $L_{D\sigma,pu}$ = $L_{Q\sigma,pu}$ = 0.05. Unequal damper winding resistance values cause a notch around s = 0.5. b) $R_{D,pu}$ = $R_{Q,pu}$ = 0.15, $L_{D\sigma,pu}$ = 0.05. Unequal damper winding leakage inductances do not cause notches around s = 0.5.

It was found out by simulations that if the damper winding leakage inductance is asymmetric, it has no similar effect on the cage torque in the half speed area as the asymmetry of the damper winding resistance. This is commonly known as Görges phenomenon (Fišer 1998). Asymmetry is clearly seen in torque components, illustrated in Fig. 4.13.

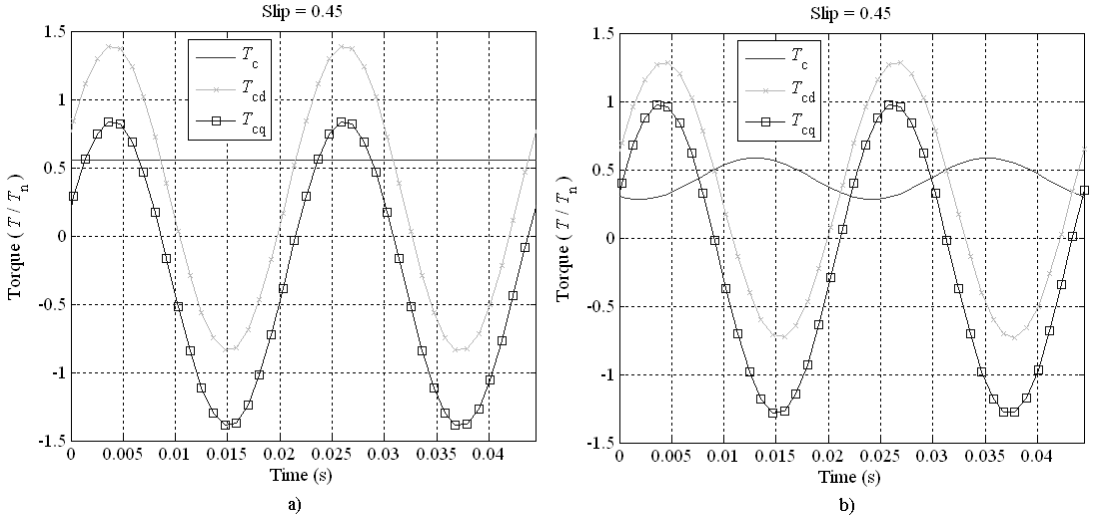

Fig. 4.13. Torque components in the cases of symmetric and asymmetric damper winding resistances. $T_c = T_{cd} - T_{cq}$. $R_{D,pu}$ = 0.15, $R_{s,pu}$ = 0.05, $L_{D\sigma,pu}$ = $L_{Q\sigma,pu}$ = 0.1, $L_{d,pu}$ = $L_{q,pu}$ = 0.5. Slip s = 0.45. a) Symmetric case. b) Asymmetric case. a) $R_{Q,pu}$ = $R_{D,pu}$. b) $R_{Q,pu}$ = $2R_{D,pu}$.

Asymmetry of the damper winding parameters causes a phase shift between direct-axis and quadrature-axis torque components (T_{cd} and T_{cq}), which may be seen as fluctuation of the total cage torque $T_c = T_{cd} - T_{cq}$.

4.6.3 Reluctance torque

If the direct-axis and quadrature-axis synchronous inductances are equal, there is no reluctance torque, as it can be seen in Eq. (2.1). The behaviour of the asynchronous reluctance torque T_r is based on the asymmetry of the synchronous inductances L_d and L_q. T_r as a function of slip was simulated by the simulation model presented in Chapter 3. The damper windings and permanent magnet flux linkage are removed from the simulation. Therefore, only the saliency of the synchronous inductances produces torque, shown in Fig. 4.14. Direct-axis synchronous inductance $L_{d,pu} = 0.5$ is fixed in the simulations.

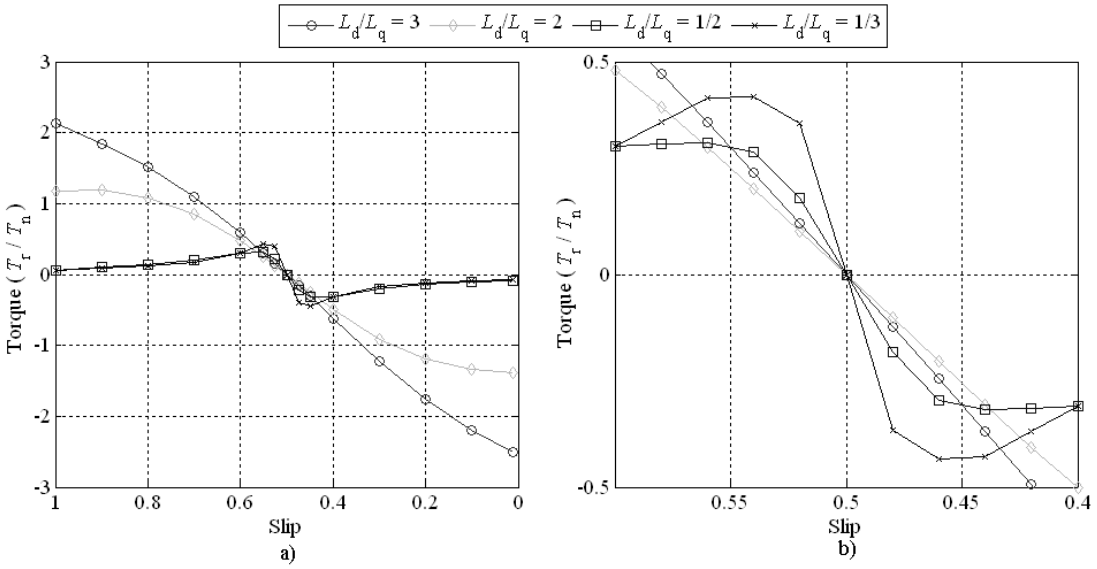

Fig. 4.14. Effects of the reluctance differences on the asynchronous torque component T_r. Direct-axis synchronous inductance $L_{d,pu} = 0.5$ is fixed. The saliency of the rotor reduces the useful asynchronous torque above the slip value $s = 0.5$. a) T_r as a function of slip. b) detail of a).

The amplitude of the pulsating torque component increases as the saliency ratio becomes larger. At asynchronous speed, the difference in direct-axis and quadrature-axis synchronous inductances produces a pulsating reluctance torque having the frequency of $2s \cdot f_s$, shown in Fig. 4.15.

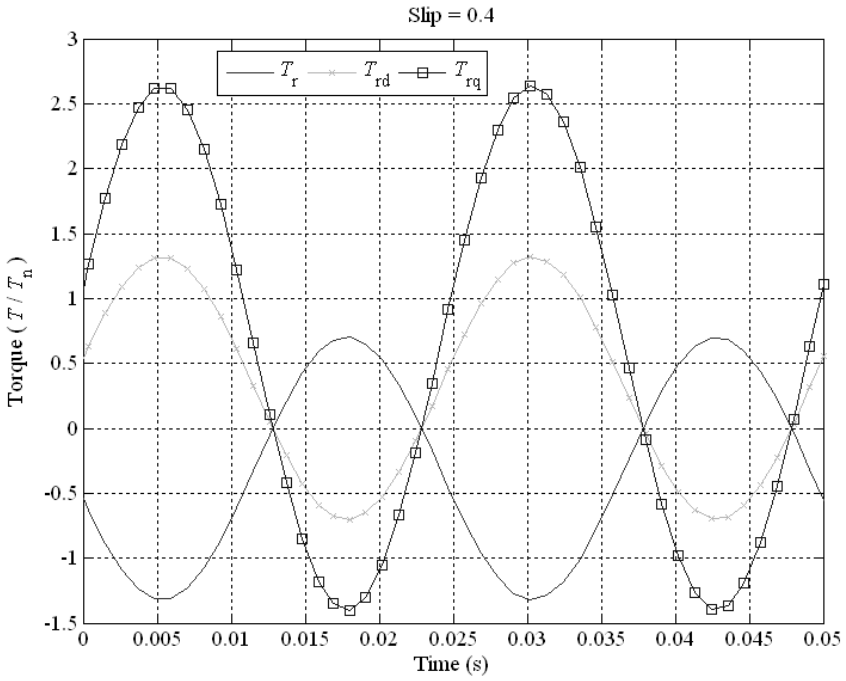

Fig. 4.15 Asynchronous reluctance torque T_r and its components. $T_r = T_{rd} - T_{rq}$. $L_{d,pu} = 0.5$. $L_{q,pu} = 0.25$. Supply frequency $f_s = 50$ Hz. Slip of the rotor $s = 0.4$. Pulsating torque has a period 0.025s, and thus the frequency $2s \cdot f_s = 40$ Hz.

Menzies (1972) has proposed a single equation for the asynchronous torque of line-start synchronous reluctance motors with damper windings.

$$\begin{aligned} T_a &= \frac{3U_s^2\omega_s^3}{D^2}\mathrm{Re}\left[\alpha^2\left(Y_d + Y_q\right) - \alpha R_s\left(2Y_dY_q + Y_d^2 + Y_q^2\right) + R_s^2\left(Y_d^2Y_q + Y_q^2Y_d\right)\right] \\ &= \frac{3U_s^2\omega_s^3}{D^2}\mathrm{Re}\left[\alpha^2\left(Y_d + Y_q\right) - \alpha R_s\left(Y_d + Y_q\right)^2 + R_s^2Y_dY_q\left(Y_d + Y_q\right)\right] \\ &= \frac{3U_s^2\omega_s^3}{D^2}\mathrm{Re}\left[\left(\alpha^2 + R_s^2Y_dY_q\right)\left(Y_d + Y_q\right) - \alpha R_s\left(Y_d + Y_q\right)^2\right] \end{aligned} \tag{4.32}$$

where

$$\alpha = 1 - 2s \tag{4.33}$$

$$\begin{aligned} D &= -\left(R_sY_d + s\right)\left(R_sY_d + s\right)\omega_s^2 + \left(1 - s\right)^2\omega_s^2 \Leftrightarrow \\ D &= \omega_s^2\left(\alpha - R_ss\left(Y_d + Y_q\right) - R_s^2Y_dY_q\right) \end{aligned} \tag{4.34}$$

$$\begin{aligned} Y_d &= \frac{-\mathrm{j}\left(1 + \mathrm{j}s\omega_sT_{d0}''\right)}{\left(1 + \mathrm{j}s\omega_sT_d''\right)X_d} \\ Y_q &= \frac{-\mathrm{j}\left(1 + \mathrm{j}s\omega_sT_{q0}''\right)}{\left(1 + \mathrm{j}s\omega_sT_q''\right)X_q} \end{aligned} \tag{4.35}$$

where the time constants are the same as in Eq. (2.4). The results found by the Honsinger's (1980) Eq. (4.28) seem, however, not to give exactly the same results as the Menzies' (1972) Eq. (4.32). The results from Eqs. (4.28) and (4.32) are compared with the results from the simulation model in Appendix G.

4.6.4 Accelerating torque

An increase in the damper winding resistance degrades the performance by decreasing the average accelerating torque at low slip values. Another option is to alter the inductances of the machine. Based on Eqs. (4.24) and (4.27), only the damper winding leakage inductance should be changed to avoid the increase of the magnet braking torque. The effect of the damper winding resistance and damper winding leakage inductance on the total accelerating torque was shown in Fig. 4.12. The total accelerating torque $T_a = T_b + T_c$ for a non-salient PMSM with symmetrical damper windings is illustrated in Fig. 4.16.

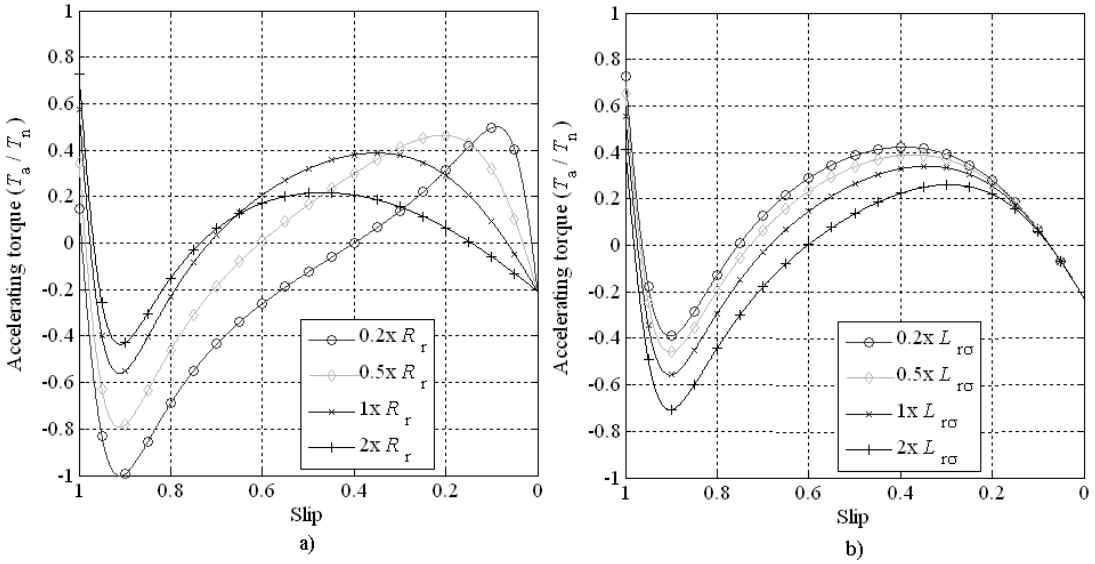

Fig. 4.16. Total accelerating torque. $E_{PM,pu} = 1.04$, $R_{r,pu} = 0.15$, $R_{s,pu} = 0.05$, $L_{r\sigma,pu} = 0.07$, $L_{d,pu} = L_{q,pu} = 0.5$. A low damper winding resistance is needed to be able to synchronize the generator. The damper winding resistance affects mainly the slip value of the asynchronous pull-out torque. However, it has an effect on the total accelerating torque. b) Effect of the damper winding leakage inductance on the accelerating torque T_a.

The accelerating torque increases when the damper winding leakage inductance decreases. Simultaneously, the slip value of the asynchronous pull-out torque increases. It seems that in this case, $L_{r\sigma}$ has not significant effect on the average accelerating torque at low slip values. However, it has a significant effect on the subtransient inductances and dynamic performance of the DOL PMSG near synchronous operation.

The total accelerating torque T_a consists of the cage torque T_c, in which the effects of the permanent magnet braking torque T_b, the reluctance torque T_r and the external load torque T_{load} are taken into account: $T_a = T_c + T_b + T_r + T_{load}$. The permanent

magnet braking torque is always negative, and usually the external load torque is negative. The reluctance torque is positive between $0 \leq s < 0.5$ and negative between $0.5 < s < 1$. The cage torque is always positive.

4.7 Finite element method modelling

Finite element method was used in 3D (three-dimensional) calculations. In 2D FEA, the 3D behaviour of the eddy currents cannot be modelled. In the 2D FEA, it is commonly assumed that the eddy currents flow only in the axial direction of a radial flux machine. This assumption can be made if the damper winding consists of the damper bars equipped with end rings. If there is a solid continuously conducting material, the accuracy of the 2D FEA results should be considered critically. Therefore, the damper windings were analyzed by the 3D FEA. The prototype machines tested are axial flux permanent magnet synchronous machines, and the damper winding is not like a normal squirrel cage with axial current flow. The installation jig of the permanent magnets forms a coarse squirrel cage, but it is electrically connected to the conducting plates on the rotor disc surfaces. Therefore, three-dimensional magnetic field solutions are necessary to take into account the eddy currents in the solid materials. The 3D FEM was used to determine the parameters of the AFPMSG1. Damper winding parameters were obtained by simulating the locked rotor test explained in section 1.7. No-load saturation test and three phase short-circuit test were modelled for the determination of the back-EMF and direct-axis synchronous inductance. Magnetizing inductances were also calculated by the model explained in the following. The no-load saturation test, sudden three-phase short-circuit test and single-phase applied voltage test with a locked rotor were simulated by 3D FEA.

The 3D FEA model includes some simplifications and modifications. The actual stator end windings are not modelled. Only the values of the end winding inductances are included in the circuit model. A thin air layer around magnets is not included in the model. The actual magnets are glued on the surfaces of the rotor. The material properties are fixed at the temperature of 20 ºC. Because of the time-consuming process of the 3D FEA and the limited calculation capacity, the shape of the permanent magnet was modified so that the permanent magnet fits inside one magnetic pole. Otherwise all the four magnetic poles should have been modelled. The actual skewing of the permanent magnet edges is one slot pitch. In the 3D FEA model, the skewing of the magnets is 75% of the slot pitch. Kurronen (2003) has studied in detail the shapes of the axial flux PM machine magnets. The original skewing of the magnets gives a low torque ripple for the machine. The shape of the real rotor geometry is illustrated in Fig. 4.17 and the rotor geometry in the 3D FEA is shown in Fig. 4.18.

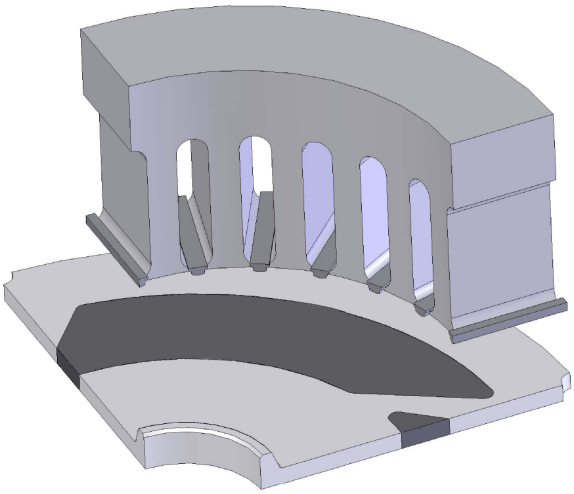

Fig. 4.17. Section view of the real geometry of the AFPMSG1. The edges of the permanent magnets are skewed by one slot pitch to reduce cogging torque and to induce sinusoidal back-emf.

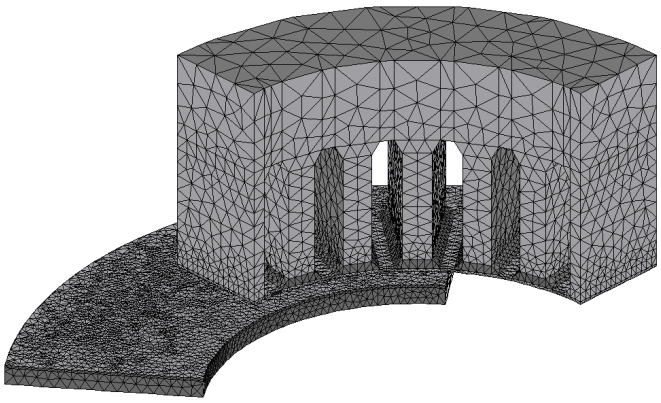

a)

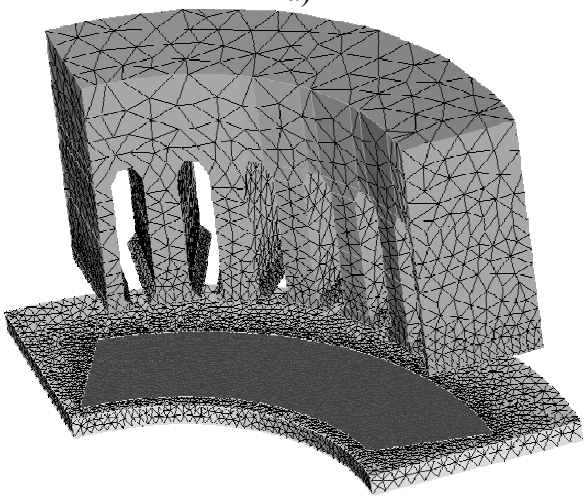

b)

Fig 4.18 Geometry used in the three-dimensional finite element analysis of the AFPMSG1. a) The air gap and the surface aluminium have very dense element networks. b) The shape of the magnet differs from the real geometry to get a reasonable calculation time. The conducting surface plate is not shown in the illustration, and the stator is lifted to show the shape of the permanent magnets.

The size of the 3D FEA model is reduced by introducing an anti-cyclic periodicity on the side surfaces of the domain and symmetry condition in the middle of the rotor. The study domain is a section of a cylinder shown in Fig. 4.19. An infinity box is associated with the study domain. The boundary conditions are set automatically by the program. Dirichlet's boundary condition is set to zero at the outer surface of the cylindrical infinite box. This means that all the magnetic flux flows inside the domain area. Neumann's boundary condition is set in the cross-sectional area of the rotor disc. It is assumed that the flux is normal to the symmetry surface.

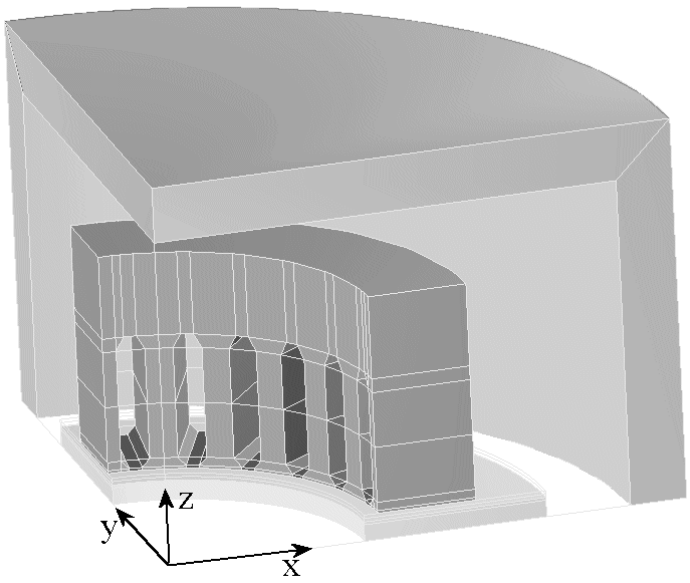

Fig. 4.19 Study domain of the geometry used in the 3D FEA.

The air gap flux density includes the effects of the stator slots and the skewing of the permanent magnets. The flux density concentrates near the tooth tips and drops at the slot openings. The no-load air gap flux density for the geometry studied is illustrated in Fig. 4.20.

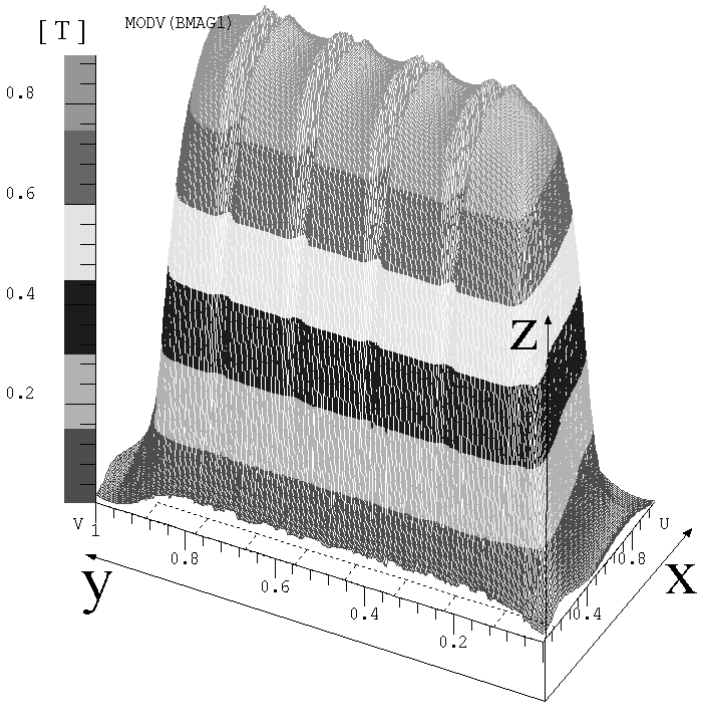

Fig. 4.20. No-load air gap flux density of the AFPMSG1 calculated by the 3D FEA. The coordinates x and y are proportional dimensions. The x-coordinate describes the distance from the inner radius (70 mm) to the outer radius (115 mm) of the 3D FEA air gap plane. The actual dimensions of the magnet inner and outer radius are 75mm and 110mm, respectively. The y-coordinate describes the pole pitch, the proportion 1 being 90 degrees in the geometry. The z-coordinate is the magnitude of the flux density in Teslas.

The stator winding is defined in the circuit models in the 3D FEA in a specific circuit description module. It is a tool for designing electric circuits, and it permits the graphic representation of electric circuit components and electric connections. Some of the electric characteristics of the different components can be defined at this level and represented in the electric circuit diagram. After checking the coherence of the circuit, the electrical scheme is translated into a specific format for use in FLUX2D or FLUX3D (export to FLUX). Circuit model is coupled with 3D geometry. The circuit models used in the simulated tests are shown in Fig. 4.21.

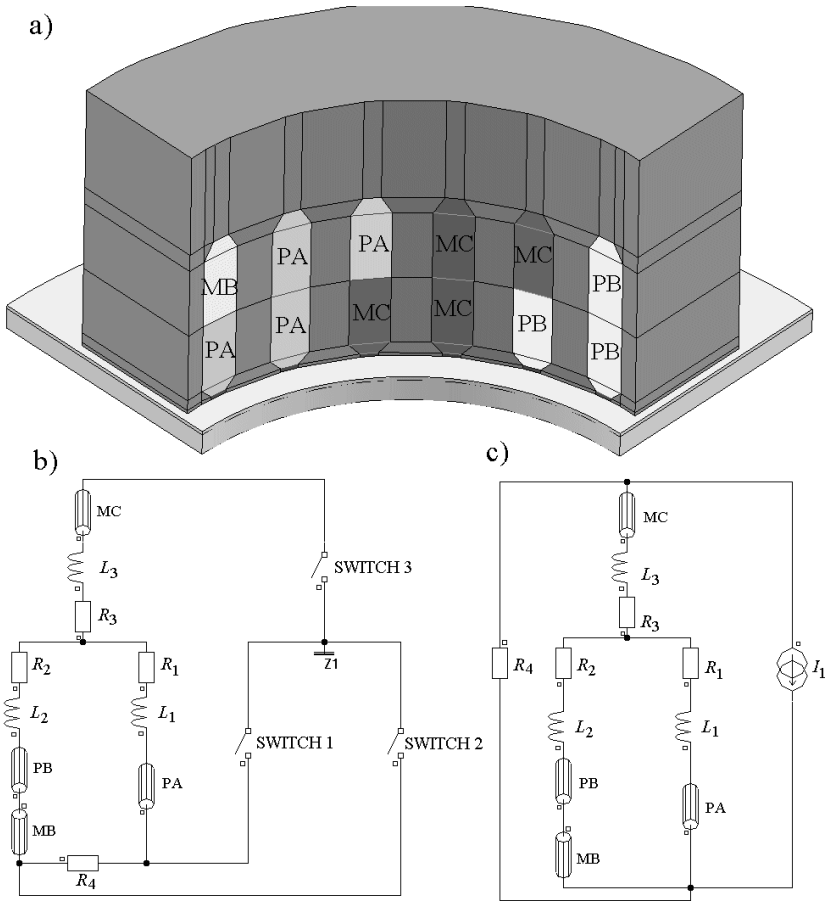

Fig. 4.21 Circuit models used in the 3D FEA calculations. a) 3D FEA geometry that is linked with the circuit model b) Circuit model of three-phase short-circuit test from no-load in generator mode. c) Circuit model of applied voltage test with a locked rotor. The resistance R_4 has an infinite value, and it is used for voltage measurements. $R_{1,2,3}$ are end winding resistances and $L_{1,2,3}$ are end winding leakage inductances. PA, MC, PB and MB are coil conductors; phase A+, phase C-, phase B+ and phase B-, respectively.

The magnetizing inductances of PMSGs may be calculated by the 3D FEM with the help of the armature reaction. If the air gap flux density is known (see Fig. 4.20), the magnetic flux per pole for an axial flux machine can be calculated from the fundamental harmonic components of the flux density:

$$\phi_{\delta 1} = \int_0^{\alpha_p} \int_{R_{in}}^{R_{out}} B_{\delta 1} \mathrm{d}r\mathrm{d}\theta \,, \tag{4.36}$$

where α_p is the pole angle and R_{in} and R_{out} are the inner and outer radii of the stator. In radial flux machines, the radius of the air gap is constant and the shape of the air gap flux density curve remains somewhat same along the axial length of the stator stack. In axial flux machines, the radius of the air gap changes, the air gap flux density curve changes along the stator stack, and single fundamental harmonic component of the flux density cannot be found for the whole pole pitch area. Therefore, an average of several air gap flux density fundamental harmonic

components should be calculated along the radius of the air gap. Equation (4.36) becomes

$$\phi_{\delta 1} = \sum_{k=1}^{N}\sum_{n=1}^{M} B_{\delta 1}(k)\Delta r \Delta\theta$$
$$\Delta r = \frac{r_{\text{out}} - r_{\text{in}}}{M_1}, \quad \Delta\theta = \frac{\alpha_{\text{p}}}{M_2} \tag{4.37}$$

M_1 and M_2 are numbers of discrete measuring points in the directions of the radius and the pole angle respectively. The direct-axis magnetizing inductance can be determined from two separate solutions. First, the magnetic flux is calculated from the air gap flux density created by the permanent magnets. Second, the effect of the armature reaction is added by feeding the phase coils to produce negative current in the direct-axis position. The negative current is demagnetizing the flux in the air gap. The direct-axis magnetizing inductance is determined from the magnetic flux difference $\Delta\phi_\delta$ of these two magnetic flux fundamental wave solutions

$$L_{\text{md}} = \frac{\Delta\psi}{\Delta I} = \frac{m}{2}\frac{k_{\text{w1}} N_{\text{ph}} \Delta\phi_{\delta 1}}{\Delta I_{\text{d}}} \tag{4.38}$$

It is assumed that the permanent magnets in the quadrature-axis are modelled as vacuum, meaning the absence of the permanent magnet material. The quadrature-axis magnetizing inductance is calculated from the flux caused by the stator current only.

$$L_{\text{mq}} = \frac{\psi}{I} = \frac{m}{2}\frac{k_{\text{w1}} N_{\text{ph}} \phi_{\delta 1}}{I_{\text{q}}} \tag{4.39}$$

The amount of the magnetizing stator current affects the saturation and thereby also the values of the magnetizing inductances.

4.8 Summary

Construction topologies of two prototype AFPMSGs were presented. Asynchronous torque components were explained in detail with illustrating figures. The design of damper windings is a challenging task. The parameters of the damper winding depend on the frequency that the damper winding experiences during transients. The skin effect may limit the useful thickness of the damper winding material. The asynchronous operation of DOL PMSG showed that the slip value of the asynchronous pull-out torque depends on the damper winding resistances. There is no need for a line-start ability for DOL PMSGs and therefore, these resistances should be as small as possible to have a high asynchronous torque near synchronous speed. A 3D FEA model was presented to simulate three-phase short-circuit test from no load in the generator mode and to simulate the applied variable frequency voltage test with a locked rotor. Analytical calculation of the damper winding resistance was

also presented. The results from these methods will be compared with the results of the experimental tests in Chapter 5.

5 Experimental results and comparison

In the following, dynamic and steady-state performance of the two prototype generators, AFPMSG1 and AFPMSG2 is tested and the electrical parameters are defined by the experimental tests discussed in the earlier sections. Three-phase short-circuit tests are carried out, explained in sections 2.6.2 and 2.6.5. Also the applied voltage tests with locked rotor are performed (see sections 2.6.3 and 2.6.4). The performances of the damper windings were tested by directly connecting the generators to the grid and by applying load torque steps in motor mode. The AFPMSG1's performance in an island network was tested with various loads. Also the effect of the moment of the system inertia was analyzed with the AFPMSG1. The simulated and analytically calculated results of dynamic and steady-state performance were compared with the practical measurements, including 3D FEA calculations. The test setups for the dynamic and static performance tests of AFPMSG1 are shown in Fig 5.1. The test setup of the applied voltage test with locked rotor is illustrated in Fig. 5.2. The similar setups were implemented also for the AFPMSG2.

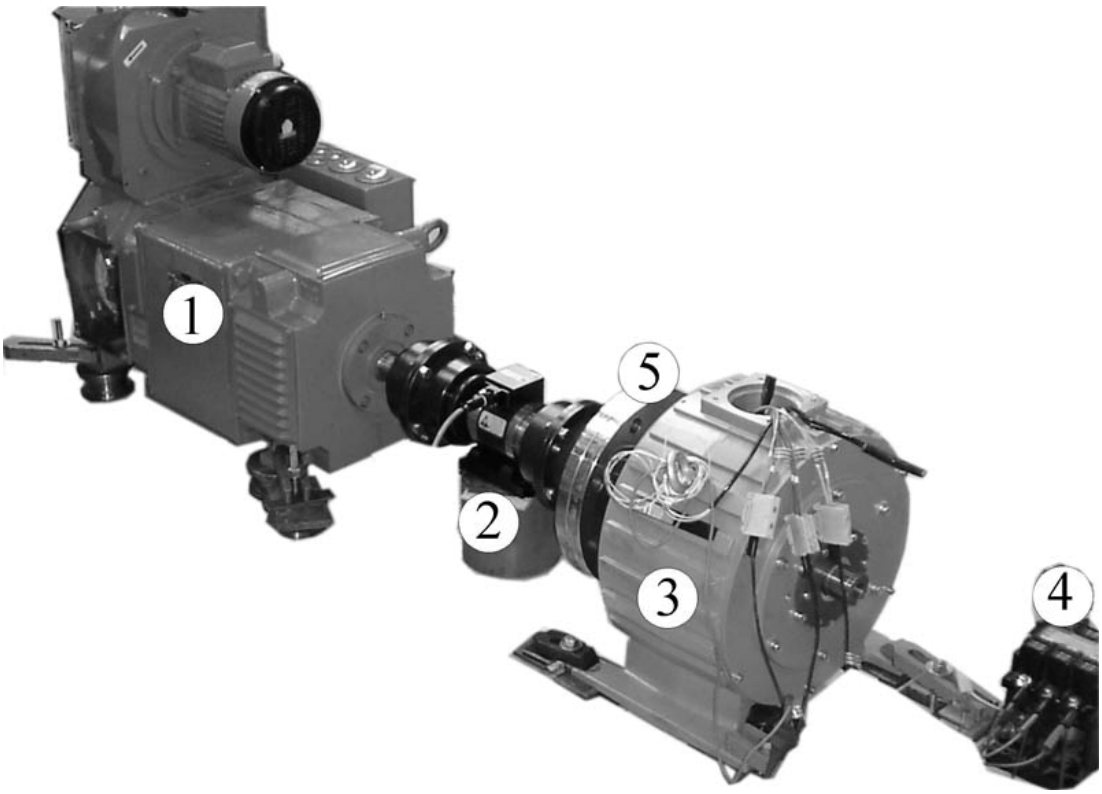

Fig. 5.1 Test setup. 1) A DC machine acts as a prime mover for no-load tests and short-circuit tests. The DC machine acts as a load machine at load torque step tests. 2) Torque transducer for the measurements of rotation speed and torque. 3) The tested prototype AFPMSG1. 4) A contactor is used in the grid connection tests and in three-phase short-circuit tests. 5) Additional discs can be installed to the shaft of the PM machine to vary the value of the rotor inertia.

The locked rotor test illustrated in Fig. 5.2 was used to determine the damper winding parameters. The shaft of the generator was locked mechanically with a

locking arm attached to the rotor shaft. The shaft of the rotor was grounded to avoid possible effects caused by the capacitance between the rotor and the stator. The electricity for the applied voltage test with locked rotor is provided by a three-phase separately excited synchronous generator (SG1). The harmonic content of the voltage is very low and, therefore, this generator is well suited for tests where sinusoidal voltage and adjustable frequency is needed. The generating set consists of the generator, the induction motor IM3 rotating the generator SG1 and the excitation devices of the generator. The induction motor is fed by a frequency converter (FC). The frequency converter is slip-compensated, and thus the induction motor rotates synchronously compared with the reference value of the desired frequency.

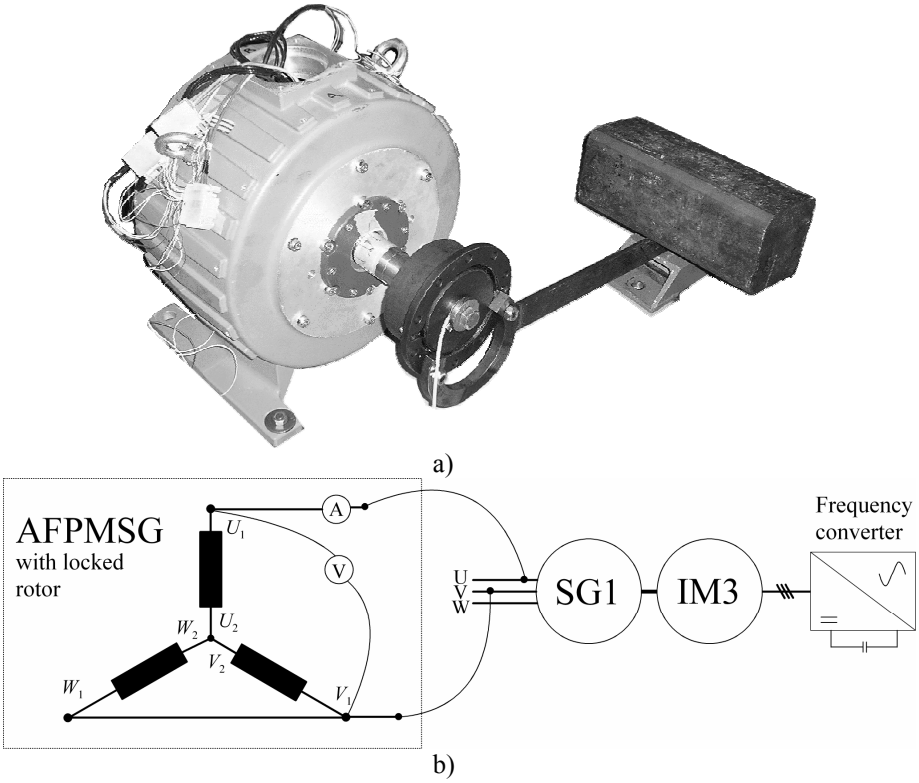

Fig. 5.2 Test setup for the applied single-phase voltage test with locked rotor. a) Mechanical locking of the shaft with a locking arm. b) Electrical connection. Induction motor IM3 is fed by a frequency converter. IM3 is rotating the synchronous generator SG1, which is connected to the AFPMSG tested. The frequency and the voltage of SG1 are adjustable. One of the stator phases of the AFPMSG is connected in series with the two parallel connected phases.

The parameters of the generator SG1 and the induction motor IM1 are given in Table 5.1. Parameters of the investigated AFPMSGs are found in Appendix C.

Table 5.1 Parameters of the induction motor IM3 and the synchronous generator SG1 used in the applied voltage test with locked rotor.

SG1		
S_n	125	kVA
cosφ	0.8	ind
P_n	100	kW
U_n	400	V
I_n	181	A
I_m	7	A
U_m	320	V
n	1500	rpm
η	0.89	
f	50	Hz

IM3		
P_n	55	kW
U_n	380	V
I_n	103	A
n	1475	rpm
f	50	Hz
p	2	

The direct and quadrature-axis positions of the rotor were determined by feeding DC current to turn the rotor in direct-axis position. The next direct-axis position was determined by changing the polarity of the DC current. The quadrature-axis position is in the middle of these two positions.

5.1 Dynamic performance

The damper winding parameters and the moment of inertia were set in the simulations according to Fig. 5.1. In the experimental measurements, the inertia of the rotating parts was tested with three different values (J_{system} = 0.14, J_{system} = 0.2 and J_{system} = 0.334). In the first measurement, a torque step, the magnitude of which was 70 % of the nominal torque, was made at synchronous operation. The same test was repeated in the simulation model. An example of the comparison is illustrated in Fig. 5.3.

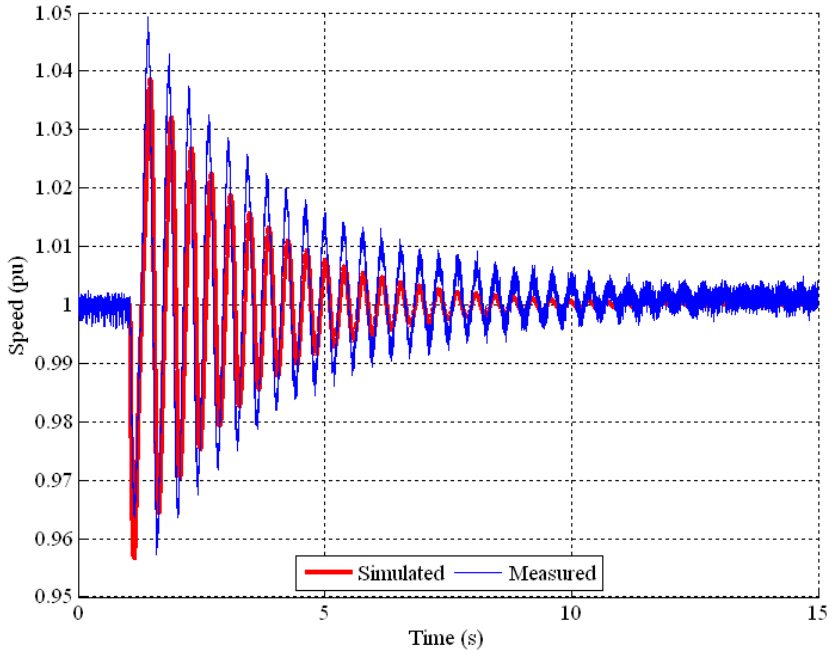

Fig. 5.3 Comparison of the measured and the simulated rotation speed of AFPMSG1 when the load torque step is 70 % of the nominal torque from no load in motor mode. The system moment of inertia $J = 0.334$ kgm^2 ($J/J_{rotor} = 12.28$).

The oscillation frequency of the simulation model has a good correspondence with the measured frequency, but the amplitudes are somewhat different. The amplitude difference of the oscillations comes from the damper winding parameters that are constant in the simulation model. Also, the practical speed measurement includes some noise. In practice, the damper winding parameters depend on the slip and the operating temperature. A larger load torque step, e.g. 80 %, both in the simulation model and practical measurements causes a failure in the synchronization.

The lowest amplitude of the speed oscillation during load transients was achieved by the largest system inertia. Grid connections were made with different initial speeds and phase errors to find out if the PM machine is able to synchronize at a random rotor position and below or over nominal speed. An example of the comparison of the measurements and simulation is shown in Fig. 5.4. The best performance in grid connections was achieved with the lowest inertia. During grid connection, the rotor field tries to align with the stator field. Small inertia is easier to pull into synchronism.

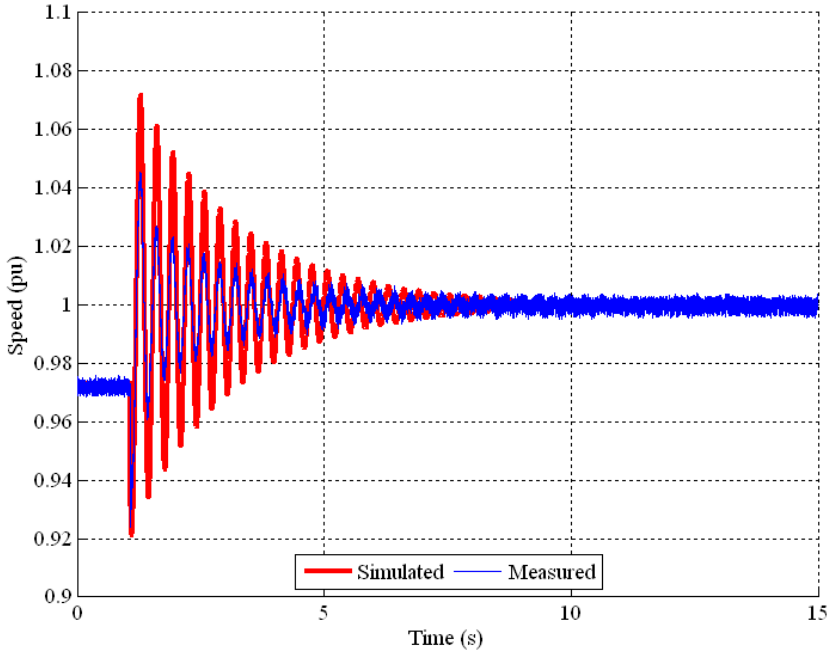

Fig. 5.4 Comparison of the measured and the simulated rotation speed in the grid connection of the generator AFPMSG1. The phase difference between the network voltage and the electromotive force of the PMSG is estimated to be +50 electrical degrees (25 mechanical degrees). Before the grid connection, the speed of the rotor is 1460 rpm (n_{pu} = 0.973). The measured and simulated speed characteristics exhibit a similar behaviour. In the grid connection, the rotor field is ahead, and the stator field tries to align with it.

In practical measurements, the torque limits for the DC motor drive cannot be zero before the grid connection. Otherwise the generator would start loosing speed because of friction from the bearings and drag. This affects the measured speed result in Fig. 5.4.

The performance of the AFPMSG1 was tested in island operation. Both the transient and steady-state operations were tested. Main parameters of the induction motors acting as an inductive load in a microgrid are shown in Table 5.2.

Table 5.2. Main parameters of the induction motors acting as an inductive load in a microgrid.

Load	U_n (V)	I_n (A)	P_n (W)	n (rpm)
Induction motor, IM1	380-440	4.7	2200	3000
Induction motor, IM2	380-440	2	1150	3000

The phase currents, speed, shaft torque and phase voltage were measured at the generator terminals during the loading test. The induction motors IM1 and IM2 were started with the help of the AFPMSG1 that was initially operating in no-load condition. One phase current during the start of the induction motor IM1 is presented in Fig. 5.5.

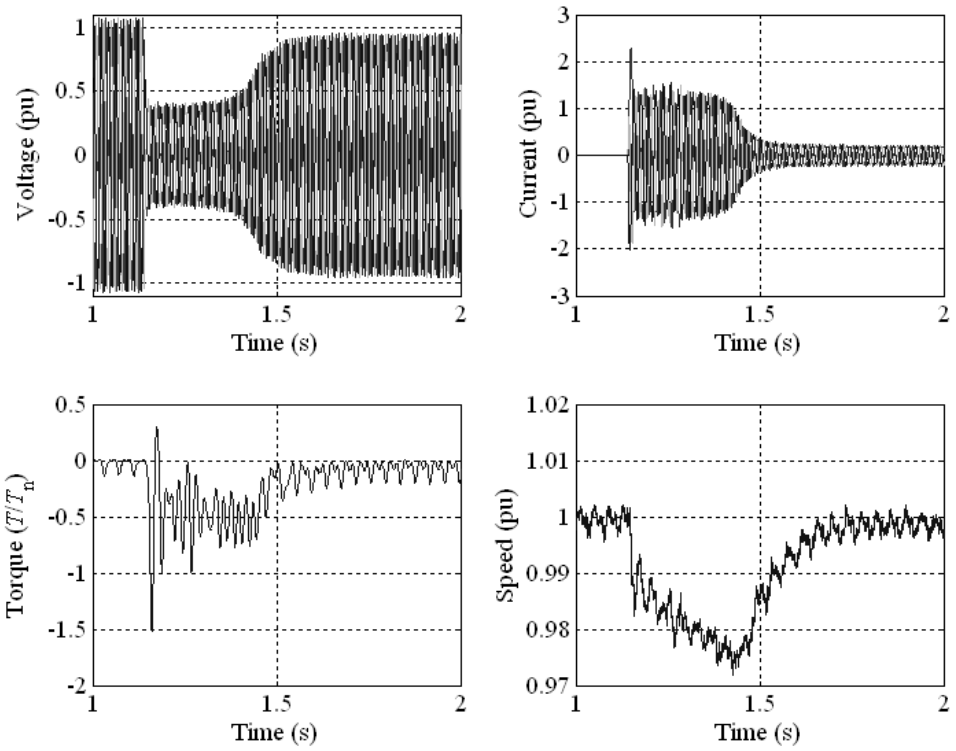

Fig. 5.5 Start of an induction motor IM1 in island operation of the AFPMSG1 from the measurement data. The permanent magnet generator and the induction motor form an isolated microgrid. Only the generator maintains the network voltage level. IM1 is started at time t = 1.15 s. The induction motor reaches its no-load condition at the time t = 1.6 s. A high starting current is taken from the generator. At no-load, the induction motor still takes some current from the system because of the induction motor magnetization and because the system has some friction torque and a fan attached to it.

We can see that the high starting current of the induction motor IM1 causes a large voltage sag. In the no-load condition of the induction motor, the terminal voltage $U_{s,pu}$ = 0.96, while the load current $I_{load,pu}$ = 0.22. With this kind of a generator, a large inductive load is difficult to handle. It may be said that the size of the induction motor was far too large in the test, and therefore the terminal voltage of the permanent magnet generator drops dramatically. The voltage sag is about 60 %. The standards allow 15 % sags for 3 seconds in island operation. The size of the maximum motor to be directly started should be about one fourth compared with the motor used in the test. Also the generator is initially designed to operate as a generator connected in the public electrical network, not in island operation. The operating speed of the permanent magnet synchronous generator was also measured. During the start of the induction machine, high torque is produced by the permanent magnet generator. The prime mover of the generator is not strong enough to hold the speed of the generator constant, which causes an extra 2.5 % decrease of the terminal voltage. Also the frequency drops.

The other induction motor IM2 was connected to the island operating AFPMSG1. The starting time of the IM2 is very long because of the high moment of inertia of the rotor. The phase voltage and the phase current are shown in Fig. 5.6.

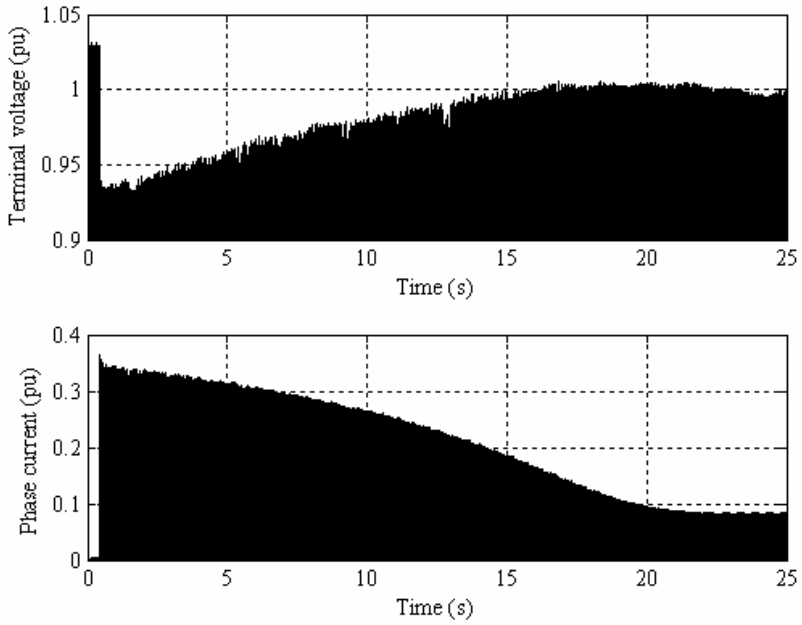

Fig. 5.6 Measured phase voltage and phase current of the generator in per unit values during the start of the induction motor IM2. At start, the terminal voltage of the permanent magnet generator drops into the value of $U_{s,pu} = 0.93$. The induction motor has a large moment of inertia, and it starts slowly. After the start at steady conditions, the terminal voltage stays at the value of $U_{s,pu} = 0.99$. This figure shows that the load is not too large for the generator tested.

The tested induction motor IM2 was not too large for the generator tested. The terminal voltage remained in an acceptable range during the start of the IM2.
The performance of the AFPMSG1 and AFPMSG2 were tested in the grid connection. The phase error and the initial speed of the generators were adjusted. Also the effect of adjusting the grid voltage level was tested. Examples of the grid connections are illustrated in Figs. 5.7 and 5.8.

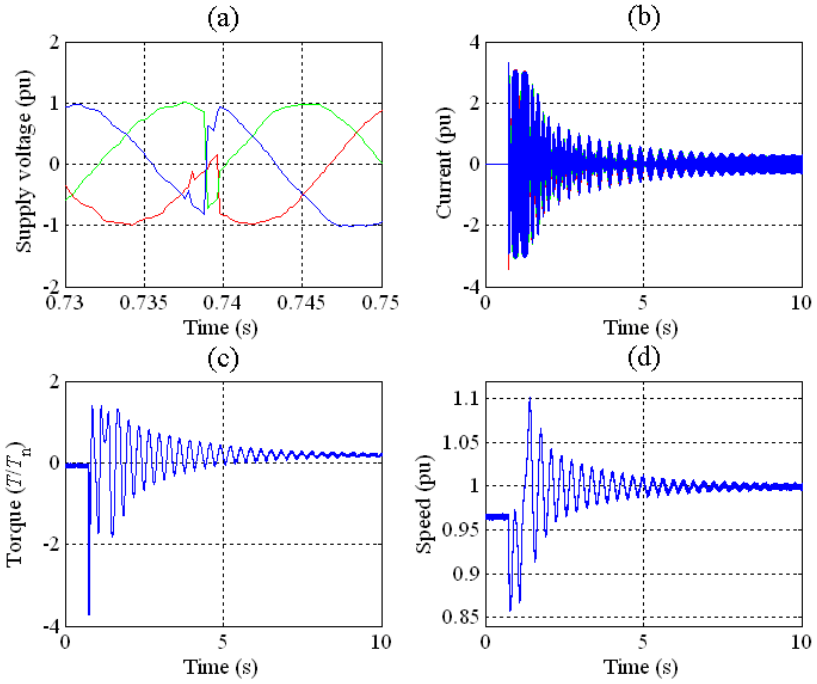

Fig. 5.7 Grid connection of the AFPMSG1 from measured data. The generator is connected to the grid with a large phase difference $\Delta\varphi$= +137° at time t = 0.739. The initial speed before the grid connection is n_{pu} = 0.96. a) The phase difference between the grid and the back-EMF of the generator. b) Transient phase current in the grid connection. c) The shaft torque during synchronization. d) The speed of the generator. The phase difference can be found from supply voltage figure (a). Grid connection occurs at time t = 0.739.

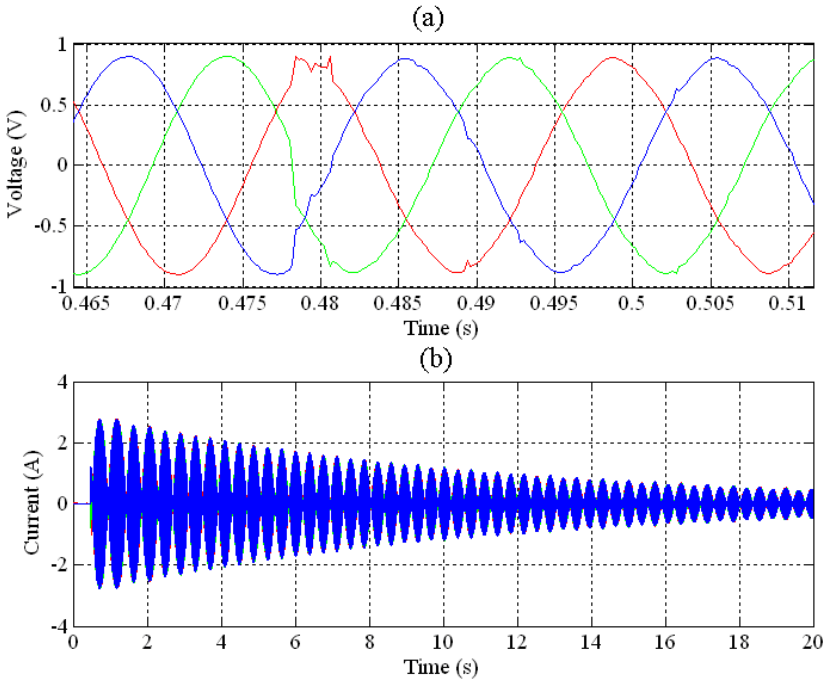

Fig. 5.8. Synchronization of the AFPMSG2 in the grid connection from measured data. a) The phase error $\Delta\varphi$ = 34° at time t = 0.478. b) Phase current during synchronization. The DC machine that acts as a prime mover has a very large moment of inertia. Therefore the synchronization takes a very long time. In this kind of setup the damper winding resistances should be a lot smaller.

Experiments with both machines show that the damper winding resistances are too high. The attenuation of the transients takes too long a time. The machines, however, work satisfactorily and reach synchronism. Comparing tables 3.1 and 4.2 shows that the actual test machine AFPMSG1 has about the same parameters as the simulated machine. The damper winding resistance per-unit values were both 0.15 in the simulated machine and 0.124 and 0.147 in the actual machine. Fig. 3.5 indicates that the damper winding resistances should be about a quarter of 0.15, which is about 0.04.

In the case of AFPMSG2 $R_{D,pu} = 0.109$ and $R_{Q,pu} = 0.114$. Also these seem to be too large, which can be seen in the slow attenuation in Fig 5.8. The transient of this machine takes a longer time because of its larger per-unit inertia. Suitable values according to Fig. 3.5 could again be $R_{D,pu} = 0.04$ and $R_{Q,pu} = 0.04$.

To achieve such values the surface plates should be made thicker or the amount of aluminium should be increased in the damper bars. This is somewhat complicated since increasing the amount of aluminium in the bars should lead to a reduced amount of permanent magnet material, which is not desirable. To maintain the flux created by the magnets they should be selected thicker which is not as effective as using a large permanent magnet surface. Increasing the thickness of the surface plates increases also the magnetic air gap which, again, leads to a reduced magnetizing inductance and a weaker magnetic coupling between the stator and the damper windings. If the best damping properties of a rotor surface magnet permanent magnet machine are desired it may lead to a slightly larger machine dimensioning to get suitable room for the damper windings.

Without additional discs the AFPMSG1 was able to synchronize at any phase difference between the electromotive force of the generator and the grid voltage. The rotation speed with successful synchronization was in the range from 1450 rpm to 1530 rpm. With larger rotor inertias the synchronization became more difficult and did not succeed at large pole angles. This proves that AFPMSG1 reaches easily synchronism if the general regulations concerning PMSG DOL grid connection are fulfilled. In special cases, such as small water power plants, the prime mover is flowing water and therefore the controlling of the speed accurately may be difficult. Grid connection has to be done at asynchronous speed slightly under nominal speed.

As an additional test, the torque at $s = 1$ was measured without the permanent magnets in the rotor. Relative torque of $T/T_n = 0.9$ was measured. In the analytical calculations, the torque $T/T_n = 0.78$ was calculated. At high slip values, the rotor heats up quite rapidly, which increases the torque at $s = 1$ and the comparison becomes rather difficult.

The problem in the grid connection of the AFPMSG2 was the prime mover, DC machine, that had a very large moment of inertia. Therefore the synchronization times were very long and the damper winding was not efficient enough to attenuate oscillations in a reasonable time. The ratio between the rotor and the total system moment of inertia $J/J_{rotor} = 93$. The damper winding resistances of the AFPMSG2 are too large for this kind of a setup. Also the phase error at the beginning of the grid

connection was too large compared with the general requirements for allowed phase error of ±10°. With smaller inertia ratios and phase errors, similar performance compared with AFPMSG1 should be expected.

5.2 Steady-state performance

The generator operations in a rigid network and in island network operation differ from each other. In the rigid network, the terminal voltage is stable and the stator flux linkage is determined by the terminal voltage. The power factor of the generator is defined by the electric load and the electrical parameters of the generator. The steady-state operation of the prototype AFPMSG 1 is described by the phasor diagram in Fig. 5.9.

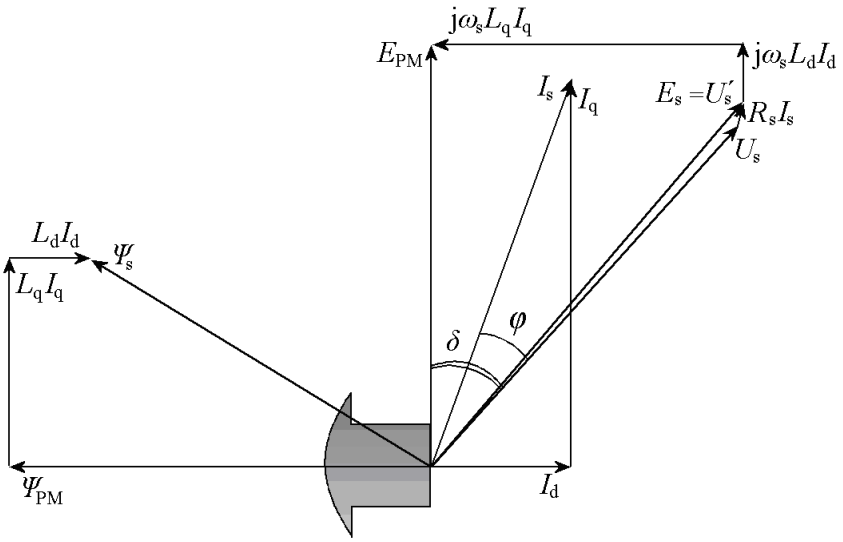

Fig. 5.9. Phasor diagram at infinite bus operation with the nominal load of the prototype axial flux permanent magnet generator AFPMSG1. Because of the rigid network, the terminal voltage does not drop. The power factor of the generator becomes leading, $\cos\varphi = 0.96$.

In island microgrid operation, the terminal voltage is highly dependent on the load and the electrical characteristics of the generator. The power factor of the generator is determined by the circuit elements that define the load. The island network operation of the prototype AFPMSG 1 is shown in Fig. 5.10.

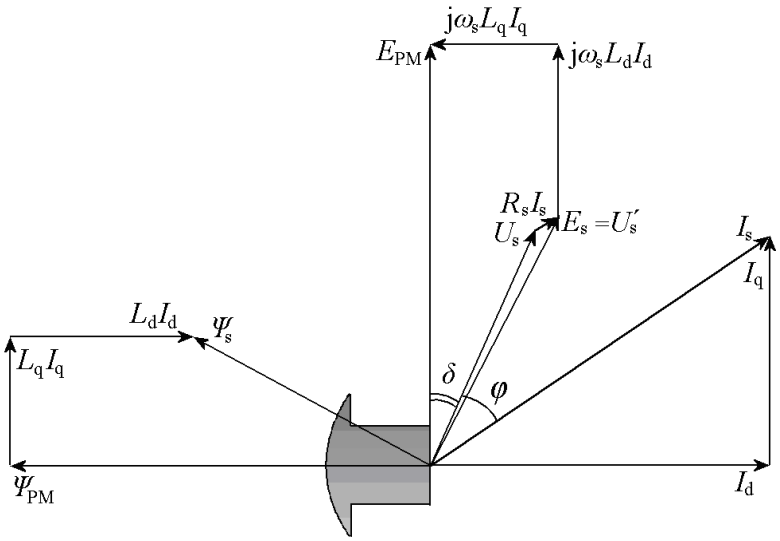

Fig. 5.10. Phasor diagram in island operation in a single-generator grid of AFPMSG1. $I_{s,pu} = 1$. The circuit elements that define the load at the grid define the power factor of the generator. In this figure the nominal load of passive type with a lagging power factor $\cos\varphi = 0.85$ is shown. It may be seen that the terminal voltage drops dramatically. The terminal voltage is only 62 % of the nominal value.

The steady-state performance in island operation of the AFPMSG1 was tested and compared with the analytical results obtained from Eqs. (2.23) and (2.24) with three different power factors. The comparison is shown in Fig. 5.11.

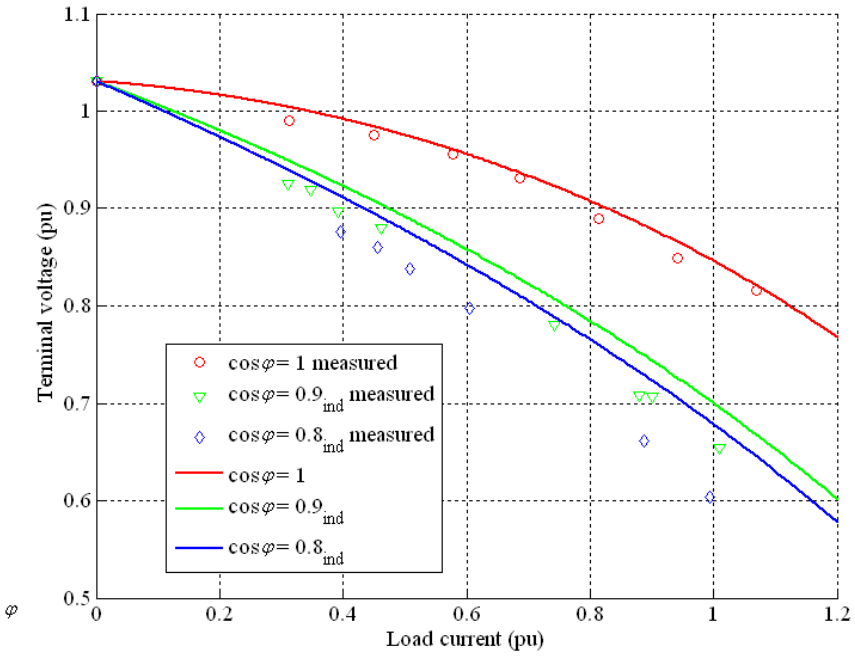

Fig. 5.11 Terminal voltage of the AFPMSG1 in island operation. Based on the practical measurements, for the resistive load, the generator is able to feed $I_{load,pu} = 0.78$ current until the lower limit of 90 % of the nominal terminal voltage is reached. For lagging power factor loads $\cos\varphi = 0.9_{ind}$ and $\cos\varphi = 0.8_{ind}$ the currents are $I_{load,pu} = 0.4$ and $I_{load,pu} = 0.32$, respectively.

5.3 Damper winding parameters

The damper winding parameters were obtained from the applied variable frequency voltage test with the locked rotor in the direct-axis and in the quadrature-axis positions described in section 2.6.3.

The alternating flux through the rotor heats the damper winding. The supply frequency during the tests was varied from 10 Hz to 60 Hz and vice versa from 60 Hz to 10 Hz to see the effect of the temperature build-up and its effects on the results between these two sequences. The damper winding resistances of the AFPMSG1 calculated by the method shown in section 2.6.4 during these two tests are shown in Fig. 5.12.

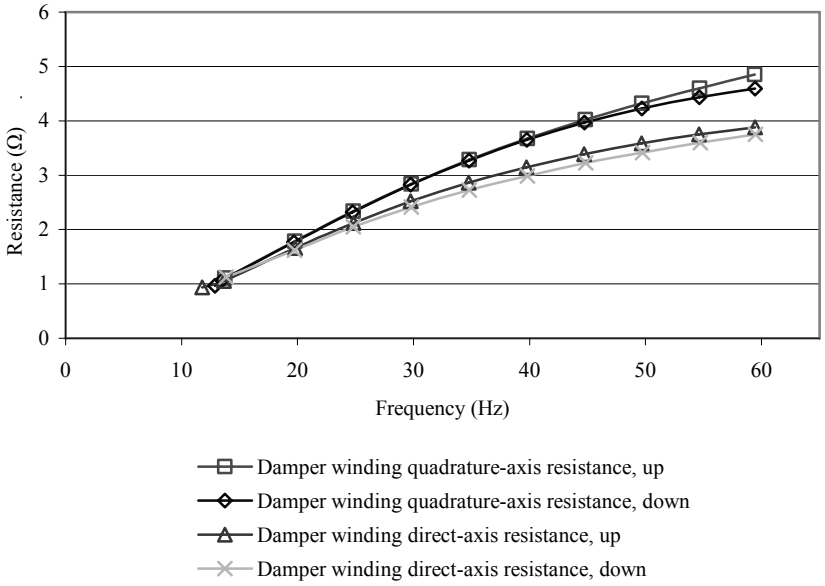

Fig. 5.12 Damper winding resistances of the AFPMSG1. The direct-axis damper winding resistance is smaller because of the rotor structure. The applied voltage in the frequency range was carried out in two ways. At one sequence the frequency was increased by 5Hz steps from a low to a high frequency. The second sequence was carried out vice versa. The effect of the temperature change during the measurements was not significant.

The damper winding quadrature-axis resistance is higher. This is due to smaller conducting cross-sectional area of the damper winding in quadrature-axis. The slip must be taken into account in the asynchronous operation of the PMSGs. The slip-compensated damper winding resistances calculated by Eq. (2.56) for the two tested AFPMSGs are illustrated in Fig. 5.13.

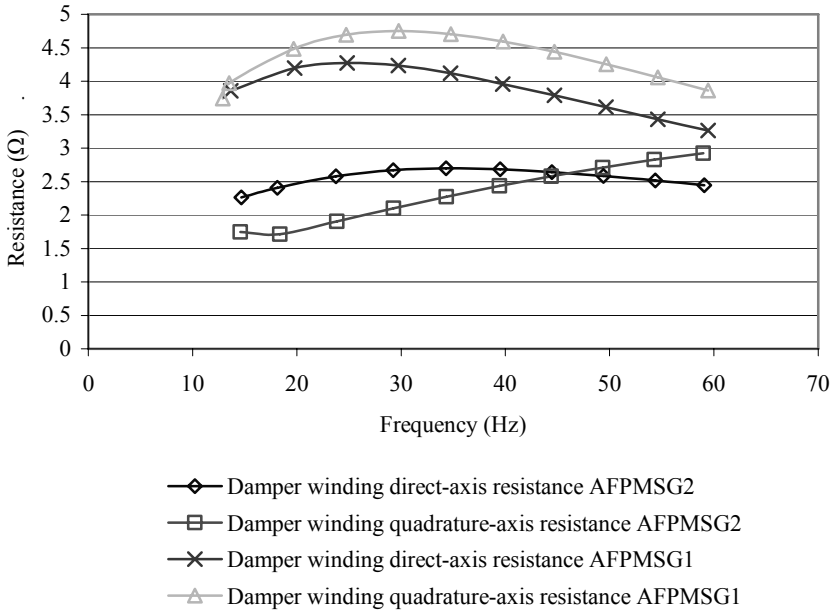

Fig. 5.13 Slip-compensated damper winding resistances of the AFPMSG1 and the AFPMSG2.

The different behaviour of the damper winding resistances in AFPMSG1 and AFPMSG2 results from the different rotor back materials. AFPMSG2 has a cast iron rotor yoke instead of aluminium. The skin depth of iron limits the penetration of the flux as the slip frequency of the rotor increases.

The behaviour of the subtransient inductances as a function of the frequency of the flux flowing through the rotor is shown in Fig. 5.14.

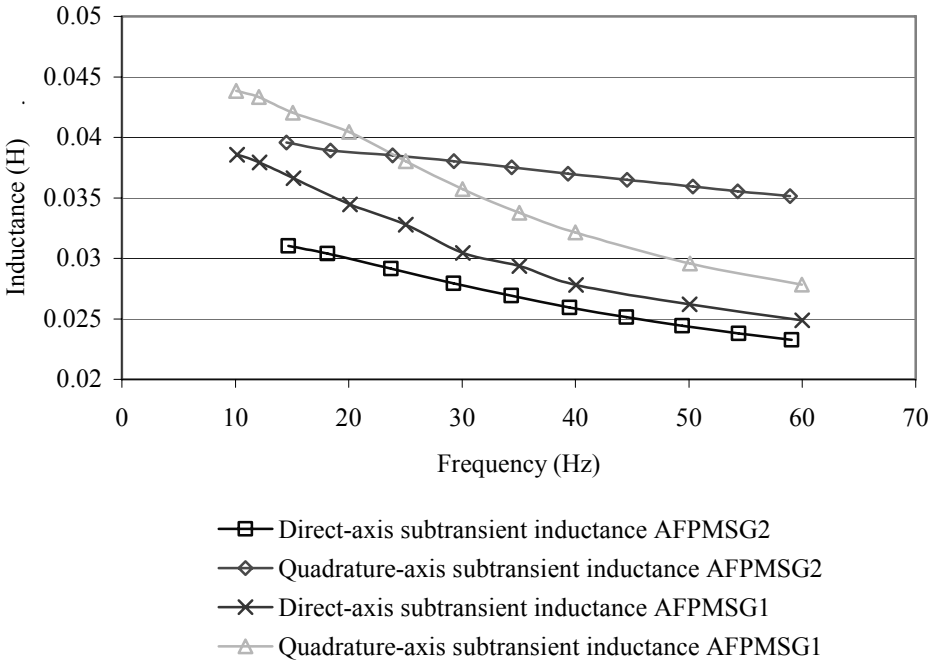

Fig. 5.14 Subtransient inductances for the AFPMSG1 and the AFPMSG2 determined from the locked rotor test and Eq. (2.44).

The behaviour of the damper winding leakage inductances as a function of the frequency of the flux flowing through the rotor is shown in Fig. 5.15.

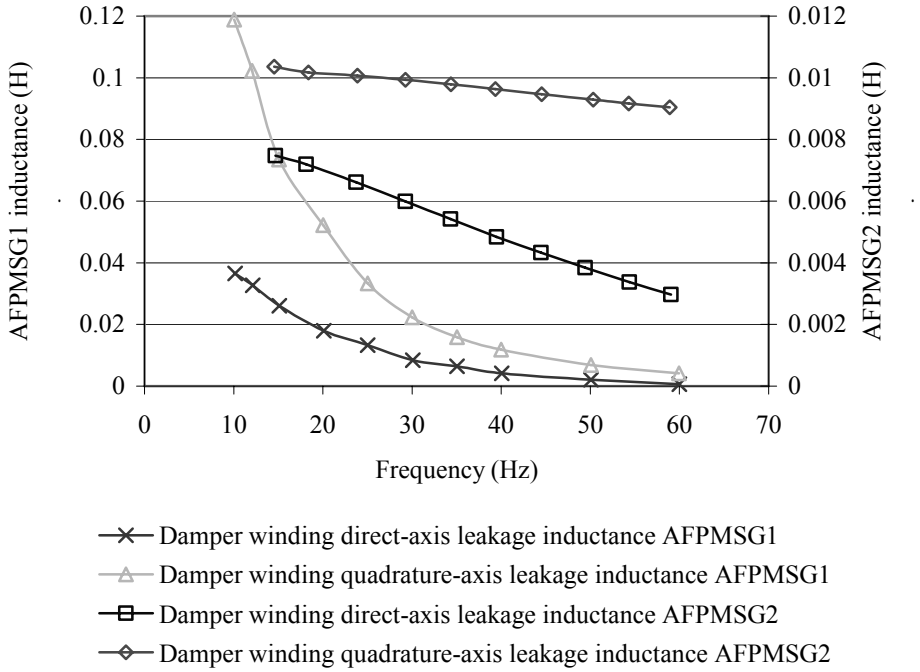

Fig. 5.15 Damper winding leakage inductances of the AFPMSG1 and the AFPMSG2. The damper winding leakage inductances of the AFPMSG2 behave linearly as function of the frequency. The cast iron rotor yoke of the AFPMSG2 gives a small reluctance route to the magnetic flux.

The increasing frequency of the flux flowing through the damper windings induces more and more eddy currents. The eddy currents block the straightforward flow of the flux and the damper winding leakage inductance drops. The subtransient direct-axis inductance results from the applied voltage test with the locked rotor were verified by the three-phase short-circuit test for the AFPMSG1 and AFPMSG2. The measured phase currents during the three-phase short-circuit test are illustrated in Figs. 5.16 and 5.17.

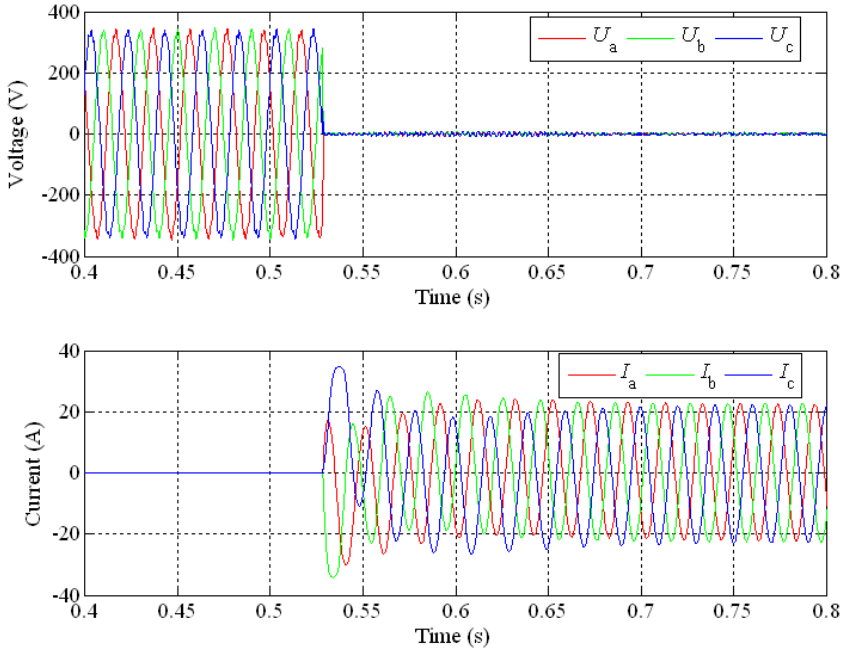

Fig. 5.16 Measured phase currents in a three-phase short-circuit test of the AFPMSG1. The envelope curves of the short-circuit currents were used to calculate the direct-axis subtransient inductance and the direct-axis synchronous inductance. Based on the envelope curves of the short-circuit currents, the subtransient short-circuit current is 1.8 times the sustained short-circuit current. The sustained short-circuit current is 2 times the nominal current of the generator.

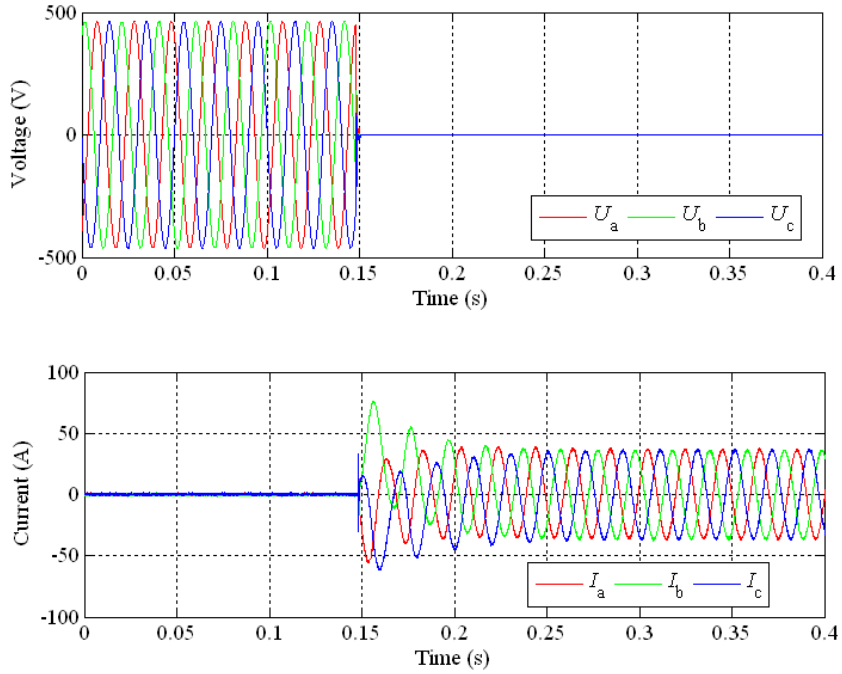

Fig. 5.17 Three-phase short-circuit test from no-load of the AFPMSG2. Based on the envelope curves of the short-circuit currents, the subtransient short-circuit current is 1.75 times the sustained short-circuit current. The sustained short-circuit current is 1.65 times the nominal current of the generator.

The comparison between the results from the three phase short-circuit test and from the applied voltage test with locked rotor and the damper winding resistance for AFPMSG1 calculated from Eqs. (4.15) – (4.23) are shown in Table 5.3.

Table 5.3 Results from three phase short-circuit test, applied voltage test with a locked rotor and analytical equations for damper winding resistances.

Results comparisons for AFPMSG1 and AFPMSG2				
AFPMSG1		**3-phase short-circuit test**	**locked rotor test, 50Hz supply frequency**	**difference**
	L_d [mH]	47.7	-	-
	L''_d [mH]	26.6	26.2	0.4
	L_q [mH]	-	-	-
	L''_q [mH]	-	29.6	-
		analytical calculations	**locked rotor test, 50Hz supply frequency**	
	R_D [Ω]	5.77	3.59	2.18
	R_Q [Ω]	5.77	4.23	1.54

AFPMSG2		**3-phase short-circuit test**	**locked rotor test, 50Hz supply frequency**	**difference**
	L_d [mH]	39.8	-	-
	L''_d [mH]	22.8	24.4	1.4
	L_q [mH]	-	-	-

	L_q'' [mH]	-	35.9	-

There is a good agreement with the results from three-phase short-circuit test and locked rotor test. Both test methods can be considered accurate enough to determine direct-axis subtransient inductance parameters. Analytical calculations introduced in section 4.5.3 give only coarse estimates for the damper winding resistances compared with the results from the measurement data.

5.4 Comparison between finite element analysis results and measurements

The no-load voltage from the 3D FEA is compared with the measured results, Fig. 5.18. The simulated short-circuit currents from 3D FEA are illustrated in Fig. 5.19. As a comparison, measured phase currents in the three-phase short-circuit test are shown in Fig. 5.20.

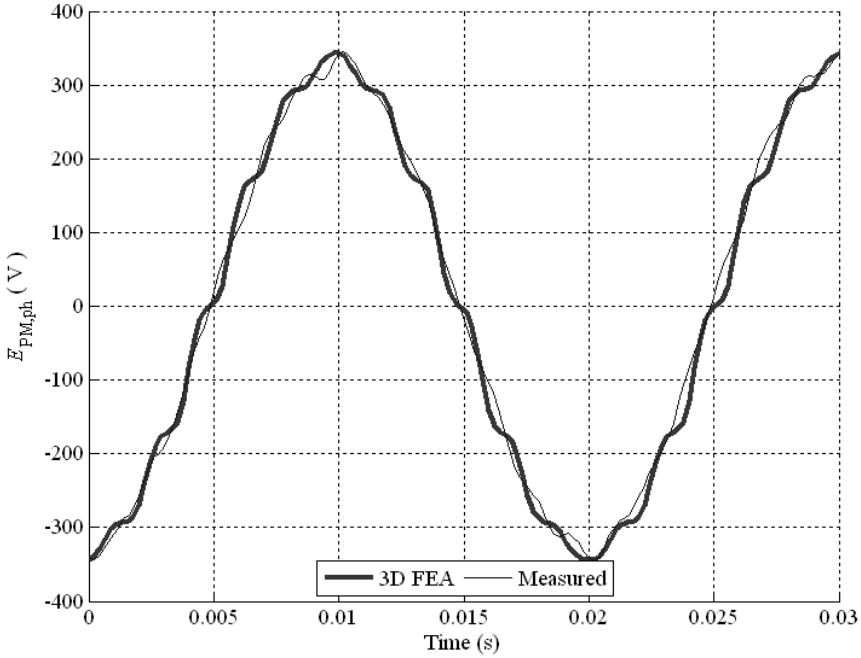

Fig 5.18. Calculated and measured phase electromotive force E_{PM} of the AFPMSG1. The amplitudes between the electromotive forces have sufficient correspondence. The slight difference in the harmonic content comes from the different shapes of the permanent magnets.

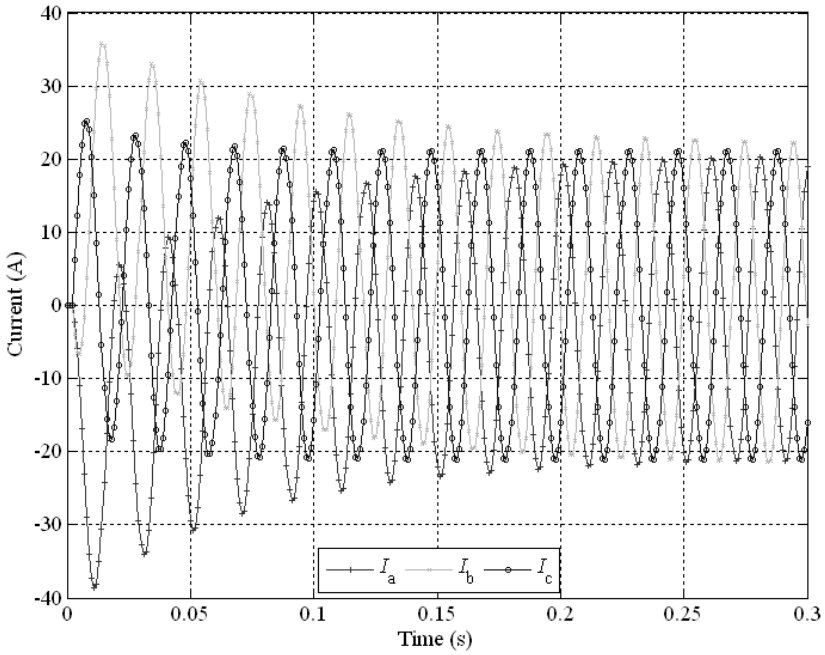

Fig 5.19 Simulated short-circuit currents of the AFPMSG1 by the 3D FEM.

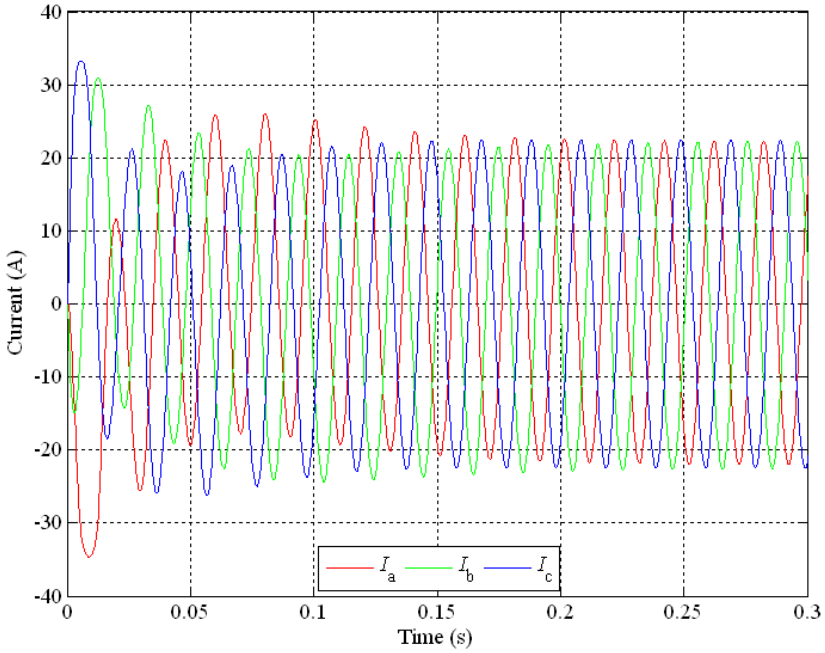

Fig. 5.20 Measured three-phase short circuit currents of the AFPMSG1.

Short-circuit currents from the 3D FEA have a good correspondence with the practical measurements and the 3D FEA model can be used for further analysis of the damper windings. For magnetizing inductance calculations, the pole pitch of AFPMSG1 was divided into 90 radial slices and 1800 points along the pole angle α_p.

90 fundamental harmonic components were calculated from 3D FEA from the inner radius to the outer radius of air gap plane shown in Fig. 4.20.

$$\phi_{\delta 1} = \sum_{k=1}^{N}\sum_{n=1}^{M} B_{\delta 1}(k)\Delta r \Delta\theta$$

$$\Delta r = \frac{r_{\text{out}} - r_{\text{in}}}{N}, \quad \Delta\theta = \frac{\alpha_{\text{p}}}{M} \tag{5.1}$$

$$N = 90, \quad M = 1800, \quad r_{\text{out}} = 115 \ \text{mm}, \quad r_{\text{in}} = 70 \ \text{mm}$$

The magnetizing inductances of the AFPMSG1 calculated by 3D FEM with nominal current according to Eqs. (4.38) and (4.39) are

$$\begin{aligned} L_{\text{md}} &= 0.024 \text{ H} \\ L_{\text{mq}} &= 0.023 \text{ H} \end{aligned} \tag{5.2}$$

The 3D FEA model was used to analyze the effect of the surface plate thickness on the damper winding parameters. The dimension from the magnet surface to the stator was fixed. Only the surface plate thickness and, hence, the physical air gap were adjusted. As an additional test, the conducting installation jig was removed from the 3D FEA model and the thickness of the surface plate was adjusted. Simulated geometries are shown in Fig. 5.21. The measured and the calculated values by the 3D FEA are compared in Figs.5.22 and 5.23.

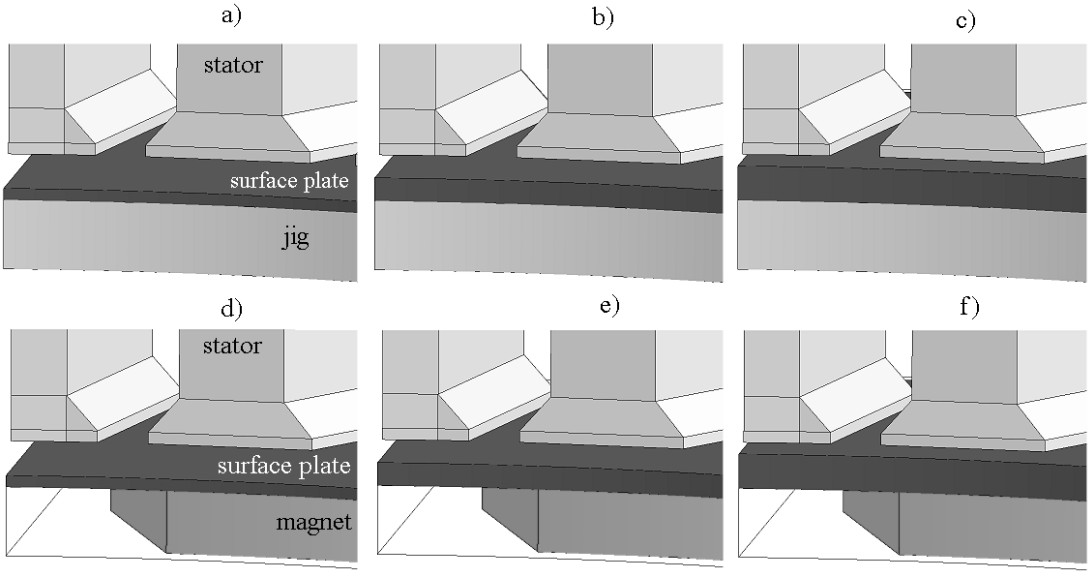

Fig. 5.21 Geometries used in the analysis of the effects of the surface plate thickness on damper winding parameters. The distance from the stator to the magnet surface was fixed. a) Original geometry with 1 mm thick surface plate. b) 2mm surface plate. c) 3 mm surface plate. d)-f) Installation jig was removed and the surface plate thickness was altered from 1 mm to 3 mm.

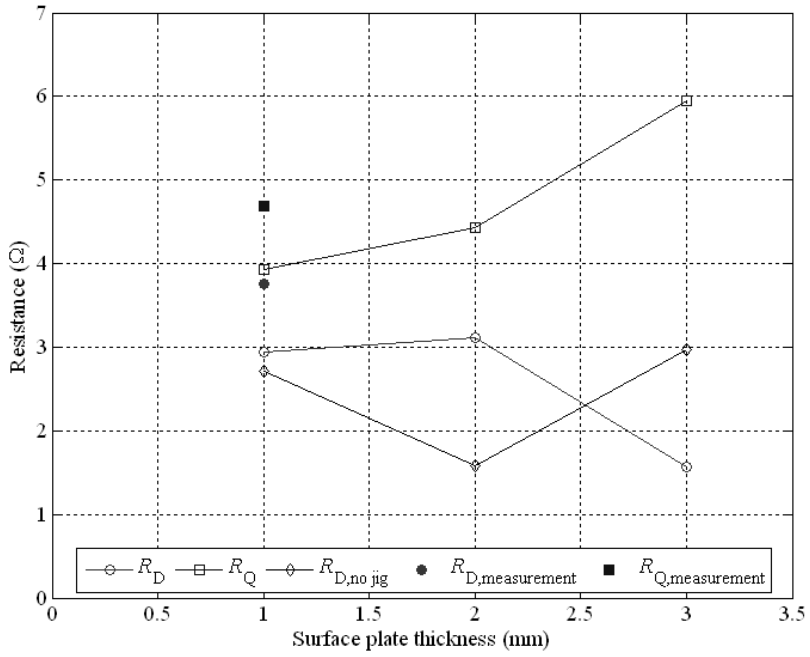

Fig. 5.22 Effect of the damper winding surface plate thickness on the damper winding resistances from the 3D FEA for the AFPMSG1.

The damper winding resistances behave in different ways in the direct- and quadrature-axis positions. According to the 3D FEA, the q-axis resistance increases when the thickness of the surface plate is increased and the d-axis resistance decreases at thick surface plate and thin air gap. The damper winding resistance values obtained from the measurements are larger than the values from the 3D FEA. The geometry used in the 3D FEA has more cross-sectional area of the conducting material in the q-axis direction, which can explain some of the difference. If the installation jig is removed or replaced by a non-conducting material, the d-axis damper winding cross-sectional area decreases. In that case, the conducting damper winding would have equal thicknesses in both d-axis and q-axis directions. Therefore, simulation was performed only in the d-axis direction without the installation jig.

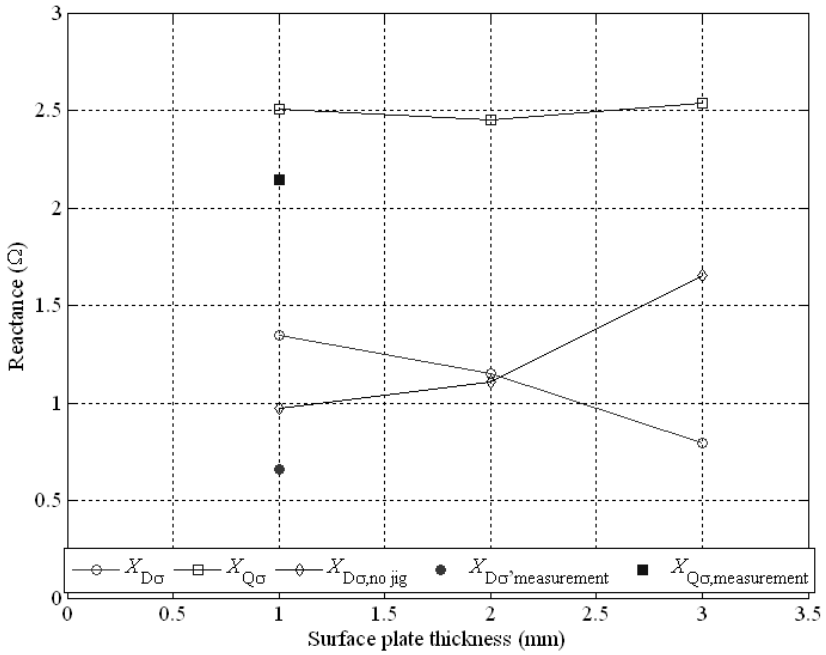

Fig. 5.23 Effect of the damper winding surface plate thickness on the damper winding leakage reactances.

The results from the 3D FEA and analytical calculations were compared with the experimental results. Analytically calculated damper winding resistance was in the same range compared with the measured damper winding resistances. The 3D FEA results had a good agreement with the measurements. The comparisons are shown in Table 5.4

Table 5.4 Comparison of the electrical parameters of AFPMSG1 between 3D FEA and practical measurements.

AFPMSG1 electrical parameter comparison			
Symbol	**Measurements**	**3D FEA**	**difference**
E	410 V	407 V	3 V
E_{ph}	237 V	235 V	2 V
R_D	3.59 Ω	2.95 Ω	0.64 Ω
R_Q	4.23 Ω	3.92 Ω	0.31 Ω
L_{md}	23.4 mH	24.0 mH	0.6 mH
L_{mq}	23.4 mH	23.0 mH	0.4 mH
$L_{Dσ}$	2.09 mH	4.2 mH	2.11 mH
$L_{Qσ}$	6.82 mH	7.96 mH	1.14 mH
τ''_{d0}	3.90 ms	9.6 ms	5.7 ms
τ''_{d}	7.10 ms	5.5 ms	1.6 ms
τ''_{q0}	4.43 ms	7.9 ms	3.47 ms
τ''_{q}	7.14 ms	5.0 ms	2.14 ms

The calculation model in the 3D FEA was used to analyze the effects of the aluminium surface plate thickness of the AFPMSG1 on the damper winding parameters. The calculations showed that in the presence of an installation jig, the asymmetry of the damper winding increases as the surface plate becomes thicker. The physical air gap becomes smaller and the stator harmonics induce more eddy currents into the rotor. The depth of penetration in aluminium and permanent magnets at 50 Hz supply frequency is very large compared with the thickness of the rotor plate. Therefore, the aluminium installation jig for the permanent magnets dominates the operation of the damper winding. The same construction of the rotor without the installation jig was analyzed as a comparison for the effects of the surface plate thickness. The amount of the flux flowing through the damper winding became smaller, which may imply weaker damping properties. It is worth remembering that the cross-sectional area of the surface plate only is notably smaller than the cross-sectional area of the installation jig and the surface plate together. The increased current density and temperature rise in the damper winding should be taken into account. The temperature changes affect also the steady state performance of the PMSGs by changing the flux produced by the magnets and hence, the electromotive force.

The damper winding leakage reactances also behave in different ways in the direct and quadrature-axis directions. The d-axis leakage reactance seems to decrease when the thickness of the surface plate is increased and the q-axis leakage inductance remains at the same level. If the installation jig is removed, the d-axis leakage reactance increases as a function of the surface plate thickness.

The 3D FEA model has fixed temperature (T = 20 ºC), which is not the case in the practical measurements. Therefore, the results are valid only in the specified temperature. The measurements in the test setup shown in Fig. 5.2 were performed in the rotor surface temperature range from 30 to 45 ºC.

When the thickness of the surface plate in the 3D FEA model is increased, the physical air gap gets shorter. The stator slotting increases the harmonic content of the flux that flows through the damper windings. More eddy currents are created and additional heat is produced. This may limit the shortest physical air gap required to avoid overheating of the damper winding plate. The determined damper winding parameters are sensitive to the phase difference of the current and voltage. The phase difference determines the reactive and resistive part of the impedance. Therefore the accuracy of the measuring devices, such as current probes should be carefully taken into account.

5.5 Summary

In this chapter, a comparison between theoretical and experimental results was presented. Grid connection and load transients were tested. The oscillation frequency of the speed after transients had a good correspondence between the simulations and measurements, but due to the fixed parameters of the simulation model, the amplitude of the speed oscillation was somewhat different. The AFPMSG1 is fully functional in the DOL mode in a rigid network. It meets easily the general regulations for a DOL PMSG grid connection. The damper winding parameters as a

function of slip in AFPMSG1 and AFPMSG2 had different characteristics. The rotor body of AFPMSG1 is made of aluminium. Instead, the rotor of AFPMSG2 has a cast iron yoke and an aluminium installation jig for the magnets (see Figs. 4.5 and 4.6). In both cases, the damper winding leakage inductance drops as the frequency of the flux flowing through the damper winding increases. This may naturally help the dynamic performance by allowing more current through smaller inductances. Analytical steady-state results of AFPMSG1 in island operation and also the damper winding parameters from 3D FEA had a good agreement with the results from experimental tests, which implies correctly calculated electrical parameters of the generator.

6 Conclusions

The most relevant scientific contribution of this thesis is the analysis of the design and dimensioning aspects of the DOL PMSGs. In the work, both static and dynamic performance characteristics were analyzed numerically, by simulations and by practical measurements. The objective of the study was to determine the correct damper winding parameters for a direct-on-line non-salient pole axial flux permanent magnet machine. DOL PMSGs have two main requirements. The generator must be capable of synchronization after grid connection and the generator has to maintain synchronous running during electric load variation and other transients.

For DOL PMSG, the following parameter characteristics should be selected:

-Small stator resistance to shift the maximum asynchronous braking torque caused by the permanent magnets into high slip values and to have a low braking torque at low slip values, as shown in Fig. 4.10a. This is difficult to reach in small-scale generators. In large-scale generators, the low slip asynchronous performance is far better because of the far smaller per unit stator resistance.

-Small damper winding resistances to shift the asynchronous pull-out torque into low slip values, as shown in Fig. 4.11. Dynamic stability optimization around synchronous operation requires optimization of the damper winding resistances according to the inertia of the system. The simulations indicated that for each inertia value there is a unique optimum value for the damper winding resistance to reach synchronous operation in the shortest period of time, see Fig. 3.5. Therefore, the dimensioning of the damper winding may be challenging especially in applications where flowing fluids define the system inertia.

-Small damper winding leakage inductances to maximize the asynchronous accelerating torque. $L_{D\sigma}$ and $L_{Q\sigma}$ decrease as the slip increases (see Fig. 4.16). This naturally helps the acceleration of the rotor back into synchronism by allowing higher damper winding currents through smaller inductances.

-Back-EMF and synchronous inductances are limited by the power factor and over voltage and under voltage limits as shown in Fig. 2.18. E_{PM} should be over 1 pu to guarantee a good power factor also in partial loads. It might be beneficial to have larger direct-axis inductance than quadrature-axis inductance in order to produce some reluctance torque. The machine may respond better to the torque changes.

The output power in the island operation mode was compared with the nominal power of the same PMSG in the infinite bus operation. It may be seen that the passive, lagging power factor load that takes a lot of reactive power is problematic for the PMSG, because its E_{PM} cannot be controlled. The demagnetizing armature reaction diminishes the air gap flux linkage remarkably, and consequently, the voltage of the machine drops dramatically. When the load is active as in Figs. 2.14–

2.16, the power of the generator is far better. Therefore, in island operation, the generator size has to be notably larger than in network drive, especially if inductive loads have to be supplied. Otherwise the generator has to be equipped with a static VAr compensator (Fig. 2.26) .

In practice, the values of the damper winding resistances and leakage inductances were measured by applying a voltage test with a locked rotor. To conduct the tests, single-phase AC voltage at different frequencies was applied to the armature windings in the test setups. The corresponding test setup was simulated in 3D FEA. In the practical measurements, it was noticed that the damper winding parameters are dependent on the frequency. Therefore, the exact determination of the damper winding parameters is valid only at the specified frequency. In steady-state operation, the frequency seen by the rotor is zero, and hence most of the transient phenomena in the generator operation appear at low frequencies. In the analytical calculations, the damper winding constructions of the permanent magnet synchronous generators were divided into three categories:

1) Damper bars: traditional design of the squirrel cage.

2) Conducting surface plate(s): surface plate parameter calculation.

3) Combination of the damper cage bars and the conducting surface plate(s): an installation jig and a surface plate, parallel connection of the surface plate and the squirrel cage.

Analytical results, experimental measurement data and 3D FEA results of the damper winding were compared. There was a good correspondence between the results from 3D FEA and experimental data. Analytical calculations gave only coarse estimations.

Experimental tests were compared with the simulation model to verify the correct operation of the simulation model. A good agreement was found between the measurements and simulations.

Among the objectives of the study was to determine if the prototype permanent magnet generators are capable of operating in directly network-connected applications. In rigid network operation, the generators were fully operational. The generators were able to tolerate grid connections and load transients. The transient attenuation times, however were long, which indicates that lower damper winding resistances should be reached. In isolated operation, the terminal voltage drops easily and the maximum loading of the generator had to be limited.

The damper winding proved to be operational for the AFPMSG1. During asynchronous operation, there occur large demagnetizing currents. In the simulations in Chapter 3, the demagnetizing direct-axis current i_d = -4 pu at asynchronous operation, shown in Fig. 3.12. According to Fig. 1.1, the magnetic field strength H_c = −1200kA/m at 60ºC is capable of demagnetizing the permanent magnet material permanently. For AFPMSG1 i_d = -4 pu corresponds to a magnetic field strength of about H_c = -610kA/m. AFPMSG1 is highly tolerant to demagnetizing currents

because of its long air gaps and the nonmagnetic rotor frame. A demagnetizing current i_d = -8 pu would demagnetize the permanent magnets permanently at 60ºC. A current of this magnitude may occur in the grid connection with large phase errors shown in Figs. 3.6 and 5.7. Nevertheless, the duration of the high amplitude demagnetizing current is short and the damper winding protects the permanent magnets.

The moment of inertia of the AFPMSG2 was too large for the damper winding constructed. The performance of the AFPMSG2 could be expected to improve as the moment of inertia would be smaller. The conditions of grid connection of DOL PMSG were selected as follows:

$\Delta U < \pm 8\% U_n$,
$\Delta f < \pm 0.5$ Hz ,
$\Delta \varphi < \pm 10°$.

AFPMSG1 meets these requirements and easily synchronizes to the grid. AFPMSG2 would require less inertia to the system in order to keep synchronization time reasonable. Practical measurements showed that the synchronization of the AFPMSG1 to the grid was successful at any phase difference if the speed error was less than 3% and the total moment of system inertia was 12.28 times or less the moment of the rotor inertia shown in Appendix C.1. When the inertia was increased, the synchronization became more difficult and the phase difference and the speed error had to be limited. Therefore, the generator will easily overcome the synchronization under the conditions of grid connection.

Suggestions for future work

In the future research, a corresponding analysis should be made for a radial flux permanent magnet synchronous generator with a damper cage. A double damper cage could improve the overall performance of the DOL PMSG. This kind of a structure is difficult to construct in axial flux machines. However, in radial flux machines, it could be possible to design a double damper cage that gives a good torque in wide scale of frequencies of the flux flowing through the damper winding. Such damper winding should work efficiently during synchronization and load transients.

The present damper winding structure of the axial flux prototype generators could be improved by increasing the cross-sectional area for the quadrature-axis damper bars e.g. by employing several magnets with the same polarity in the area of one magnetic pole. The space between the magnets would be provided for the damper winding bars, shown in Fig. 6.1.

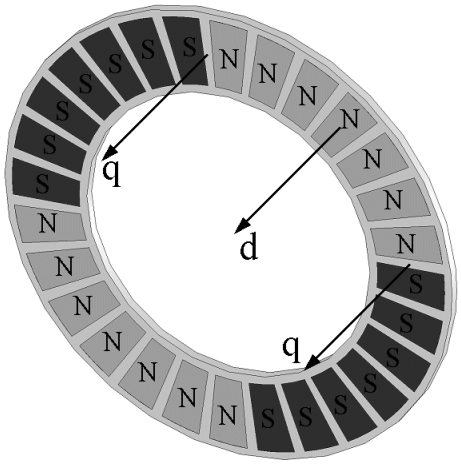

Fig. 6.1 Rotor construction with several magnets with the same polarity in the area of one magnetic pole. dq-axis are denoted by letter d and q. N and S stand for the polarity of the magnets. This kind of an arrangement should provide a lower damper winding resistance and consequently a lower transient attenuation time for the machine.

However, this method may weaken the quality of the electromotive force harmonic content and the amplitude. The effect of the conducting surface plate should also be tested in more detail. The performance of the damper winding with and without the surface plate could be compared.

Another interesting topic is the simulation and analytical analysis of the DOL starting of induction motor in an island-operated PMSG with a parallel active VAr compensator. Tuinman et al. (1998) have presented simulations of a direct-on-line start of a large induction motor connected to a salient pole synchronous generator. Similar analysis could be carried out by replacing the synchronous generator by a PMSG and a VAr compensator.

References

Abdelaziz, M. E. 1982. *Permanent magnet synchronous machines*. Dissertation Nr. 443. École Polytechnique Fédérale de Lausanne.

Arkkio, A. and Westerlund, J. 2000. An electromechanical model for analysing transients in diesel-driven synchronous generators. In *Proceedings of the International Conference on Electrical Machines*, Espoo, Finland, 28–30 August 2000, pp. 878–882.

Bakkermagnetics. 2007. Information sheet for magnetic properties, sintered Neodymium magnets. [online]. [7 May 2007]. Available from: http://www.bakkermagnetics.com

Binns, K.J., Al-Din, M.S.N. and Lisboa, P.J.G. 1992. Use of canned rotors in high-field permanent magnet machines. *IEE Proceedings B*, Volume 139, Issue 5, Sept. 1992. pp. 471–477.

Bödefeld, T. 1943. Die asynchronen und synchronen Drehmomente der Synchronmaschine mit Schenkelpolen und Anlauf- oder Dämpferkäfig. *Elektrotechnik und Maschinenbau*. Jahrgang: 61. pp. 281−286.

Chan, T.F., Yan, L.T. and Lai, L.L. 2004. Performance of a three-phase AC generator with inset NdFeB permanent-magnet rotor. *IEEE Transactions on energy conversion*, Vol 19, No.1 March 2004. pp. 81–87.

Davenport, T. 1837. *Improvement in propelling machinery by magnetism and electro-magnetism.* Patent number: 132.

Deshpande, U.S. 2003. Recent advances in materials for use in permanent magnet machines- a review. In *Proc. IEEE Electric Machines and Drives Conference*, *IEMDC 2003*, Madison, United States, 1–4 June 2003. Vol.1 pp. 509–515.

Engelmann, R.H., Middendorf, W.H.1995. *Handbook of Electric Motors*. Dekker, New York.

Engineering recommendation G.59/1. 1991. *Recommendations for the connection of embedded generating plant to the public electricity suppliers' distribution system*.

European standard EN 50160. 2000. European Committee for Standardization. *Voltage characteristics of electricity supplied by public distribution systems*.

European standard EN 50438, (draft). 2005. *Requirements for the connection of micro-generators in parallel with public low-voltage distribution networks*. 15 August 2005.

Fišer, R. 1998. Study of operational behaviour of induction motor with rotor asymmetry. *Proc. 9th Mediterranean Electrotechnical Conference, MELECON 1998*, Tel-Aviv, Israel. 18–20 May 1998. Vol. 2. pp. 1185–1188.

Foote, C.E.T., Burt, G.M., Elders, I.M. and Ault G.W. 2005. Developing Distributed Generation Penetration Scenarios. *Proc. International Conference on Future Power Systems, FPS 2005*, Amsterdam, The Netherlands. 16–18 November 2005.

General Electric. 2005. *Latest evolution of GE energy wind turbine technology: 2.5 and 3-Megawatt units introduced*. Press release. [online]. [15 December 2006]. Available from:
http://www.gepower.com/about/press/en/2005_press/092005.htm

Honsinger, V.B. 1980. Permanent Magnet Machines: Asynchronous Operation. IEEE Transactions on Power Apparatus and Systems, Vol PAS-99, No.4 July 1980. pp. 1503-1509.

The Institute of Electrical and Electronics Engineers, INC. 1987. STD 86:1987. *IEEE Recommended Practice: Definitions of Basic Per-Unit Quantities for AC Rotating Machines*. New York: The Institute of Electrical and Electronics Engineers.

International Magnetics Association. 2000. MMPA standard No 0100-00. [online]. [29 March 2007]. Available from: http://www.intl-magnetics.org/pdfs/0100-00.pdf.

International standard IEC 60034-2. 1972. Part 2: *Methods for determining losses and efficiency of rotating electrical machinery from tests*.

International standard IEC 60034-4. 1985. Part 4: *Methods for determining synchronous machine quantities from tests.* Second edition.

International standard IEC 61000-3-2. 2001. *Limits for harmonic current emissions (equipment input current ≤ 16 A per phase)*. Edition 2.1.

International standard IEC 61000-3-3. 2002. Part 3-3. *Limits-Limitation of voltage changes, voltage fluctuations and flicker in public low-voltage supply systems, for equipment with rated current ≤ 16 A per phase and not subject to conditional connection*. Edition 1.1.

Jeon W.J, Watanabe H., Nakamoto A., Kamiya Y., Onuki T. 1999. Dynamic Characteristics of Synchronous Motors applying a Plural Sub-magnets Scheme to Rotor.*IEEE Trans. Magn*. vol 35, No.5, September 1999. pp. 3574–3576.

Johnson H.R. 1979. *Permanent magnet motor*. United States Patent No. 4151431.

K&J Magnetics Inc. *Neodymium magnet physical properties datasheet.* [online]. [29 March 2007]. Available from: http://www.kjmagnetics.com/specs.asp.

Kaneko Yuji. 2000. Highest Performance of Nd-Fe-B Magnet Over 55 MGOe. *IEEE Trans. on magnetics*. Vol. 36. No. 5. September 2000, pp. 3275-3278.

Kinnunen, J., Pyrhönen, J., Liukkonen, O. and Kurronen, P. 2006a. Analysis of directly network connected non-salient pole permanent magnet synchronous machines. In *Proc. International Symposium on Industrial Electronics, ISIE 2006*, 9–13 July 2006, Montreal, Canada. pp. 2217–2222.

Kinnunen, J., Pyrhönen, J., Liukkonen, O. and Kurronen, P. 2006b. Design parameters for directly network connected non-salient permanent magnet synchronous generator. In *Proc. International Conference on Electrical Machines, ICEM2006*, 2–5 September 2006, Chania, Greece. Proceedings CD.

Kinnunen J., Pyrhönen J., Liukkonen O., Kurronen P.2007a. Design of Damper Windings for Permanent Magnet Synchronous Machines, paper no. 02-48 on the *International Review of Electrical Engineering, IREE*, issue March 2007. Vol.2. N.2. pp. 260-272.

Kinnunen J., Lipsanen A., Pyrhönen J. 2007b, Permanent Magnet Generator with Active Reactive Power Compensator. *Accepted to be published in International Forum on Systems and Mechatronics, ISFM2007*, 3-6 December 2007, Tainan,Taiwan. In process.

Klempner, G. and Kerszenbaum, I. 2004. *Operation and Maintenance of Large Turbo Generators*. New York: John Wiley & Sons, Inc.

Knight, A.C., McClay, C.I. 2000. The Design of High-Efficiency Line-Start Motors. *IEEE Trans. Ind. Applicat*., vol.36, Nov./Dec. 2000, pp. 1555–1562.

Klöckl, B. 2001. *Measurement Based Parameter Determination of Permanent Magnet Synchronous Machines.* Diploma Thesis, Graz University of Technology.

Kovács, P.K., Rácz, E., *Transient phenomena in electrical machines*, (in German). Verlag der Ungarischen Akademie der Wissenschaften. 1959. Budapest, Amsterdam.

Kral, C. and Haumer, A. 2005. Modelica libraries for dc machines, three phase and polyphase machines, *Proc. 4th International Modelica Conference*, 7–8 March 2005. Hamburg-Harburg, Germany. pp. 549–558.

Kurronen, P. 2003 *Torque vibration model of axial-flux surface-mounted permanent magnet synchronous machine*. Lappeenranta University of Technology. Acta Universitatis Lappeenrantaensis 154.

Laithwaite, E. R. 1992, The influence of Michael Faraday on power engineering, *Power Engineering Journal*, September 1991, Vol. 5, Issue 5, pp.209–219.

Lefevre, L., Soulard, J. and Nee H.-P. 2000, Design Procedure for Line-Start Permanent Magnet Motors, *Proc. IEEE Nordic Workshop on Power and Industrial Electronics, NORPIE 2000*, Aalborg, Denmark, June 2000, pp.261-265.

Libert, F., Soulard, J. and Engström, J. 2002a. *Design of a 4-pole Line Start Permanent Magnet Synchronous Motor*. Royal Institute of Technology, Sweden.

Libert, F., Soulard, J. and Engstrom, J. 2002b. Design of a 4-pole line start permanent magnet synchronous motor. In *Proceedings ICEM 2002*, Brugge, Belgium, August 25–28, 2002. Proceedings CD.

Luukko, J. 2000. *Direct Torque Control of Permanent Magnet Synchronous Machines – Analysis and Implementation*. Dissertation. Acta Universitatis Lappeenrantaensis 97. Lappeenranta University of Technology.

Menzies, R.W. 1972. *Synchronous reluctance motors and method of starting*. US patent. No. 3679924

Merrill, F.W. 1950. *Rotor for dynamoelectrical machines*. US patent No.2525456.

Merrill, F.W. 1954. Permanent magnet excited synchronous motors. *Trans. A.I.E.E.*, Vol. 73, Pt. III, pp.1754–1760.

Miller, T.J.E. 1984. Synchronization of line-start permanent-magnet ac motors. *IEEE Trans. Power Apparatus and Systems*, Vol. PAS-103, No.7, July 1984. pp.1822–1828.

Multibrid. 2006. *Erection of the second M5000 successfully completed.* Press release, [online]. [12 November 2006]. Available from: http://www.multibrid.com/neues/2006_e.html

Nau, S.L., The influence of the skewed rotor slots on the magnetic noise of three-phase induction motors. *Proc. 8th International Conference on Electrical Machines and Drives*, *IEMDC 1997*. Cambridge, UK. 1-3 September 1997. pp. 396-399.

Nabeta, S.I., Foggia, A., Coulomb, J.-L. and Reyne, G. 1997. Finite element analysis of the skin-effect in damper bars of a synchronous machine. *IEEE Transactions on Magnetics*, Volume 33, Issue 2, Part 2, March 1997. pp.2065–2068.

Nee, H.-P., Lefevre, L., Thelin, P. and Soulard, J. 2000. Determination of d and q Reactances of Permanent-Magnet Synchronous Motors Without Measurements of the Rotor Position. *IEEE Trans. Ind. Appl*., Vol.36, No.5, September/October 2000. pp. 1330–1335.

Neorem Magnets Oy. Ruoho, S. 2007a. [Personal communication]. 12 February 2007.

Neorem Magnets Oy. 2007b. NdFeB magnet datasheets. Available from www.neorem.fi [cited October 2007]

Nordel. 1995. *Operational performance specifications for small thermal power units*. Amendment No.1, 1995.

Nordel. 1995. *Operational performance specifications for thermal power units larger than 100 MW*, 1995.

Olivera, T. and Fofana, M. 2003. Maîtrise en Ingénierie, Cours: *Propriétés diélectriques de l'air-6DIG967, HV INSULATORS*, Hiver 2003, Université du Québec à Chicoutimi, pp. 3–4.

Park, R.H., Two-reaction theory of synchronous machines. *AIEE Trans*. 1929.

Parviainen, A. 2005. *Design of axial-flux permanent-magnet low-speed machines and performance comparison between radial-flux and axial-flux machines*. Lappeenranta University of Technology. Acta Universitatis Lappeenrantaensis 208.

Pyrhönen, J. *Lecture notes on the design of electrical machines*. Lappeenranta University of Technology, 2007.

Rahman, M.A. and Zhou P. 1994. Field based analysis of permanent magnet motors, *IEEE Trans. Magn*. Vol.30, No.5, pp. 3664–3667. September 1994. pp. 3664–3667.

Rahman, M.A. and Zhou, P. 1996. Analysis of Brushless Permanent Magnet Synchronous Motors, *IEEE Trans. on Industrial Electronics*, Vol. 43, No.2, April 1996. pp. 256-267.

Richter, R. 1963. *Electrische Machinen. Band II. Synchronmaschinen und Einankerumformer*. Dritte Auflage. Birkhäuser Verlag, Basel und Stuttgart, German.

Sagawa, M., Nagata, H., 1993. Novel Processing Technology for Permanent Magnets. *IEEE Trans. on magnetics*. Vol. 29. No. 6. November 1993. pp. 2747-2751.

Sagawa, M., Fujimuria, S., Yamamoto, H., Matsuura, Y. 1984. Permanent magnet materials based on the rare-earth iron-boron tetragonal compounds (invited). *IEEE Trans. on magnetics*, Vol. MAG-20, No.5, September 1984.

Schuisky, W. 1949. Selbstanlauf eines Synchronmotors. *Archiv für Elektrotechnik*, XXXIX. Band, Heft 10-1950, Hälsingborg, Sweden. pp. 657–667.

Shimmin, D.W., Wang, J., Bennett, N. and Binns, K.J. 1995. Modelling and stability analysis of a permanent-magnet synchronous machine taking into account the effect of cage bars. *IEE Proceedings on Electric Power Applications*, Volume 142, Issue 2, March 1995 pp.137–144.

Shin-Etsu Chemical Co.LTD. Newsarchive. [online]. [2 January 2007]. Available from: http://www.shinetsu.co.jp/e/news/s20060822.shtml.

Siemens AG 2003. *SIEMOSYN motors 1FU8*. Technical data sheet, 09.2003 edition. [online]. [5 August 2006]. Available from: http://www.automation.siemens.com/doconweb/pdf/SINAMICS_0306_E/PFU8.pdf?p=1

Siemens AG 2006a. *Permanent-magnet technology for multi-megawatt wind power plants*. Press release, 19 June, 2006. [online]. [05 August 2006]. Available from: http://www.siemens.com/index.jsp?sdc_p=cfi1075924lmno1217997ps5uz3&sdc_bcpath=1327899.s_5%2C1047890.s_5%2C1176453.s_5%2C&sdc_sid=25068695473&

Siemens AG 2006b . [online]. [15 November 2006]. Available from: http://www.automation.siemens.com/ld/windkraft/html_76/windkraft-ohne1.html

Simond, J.-J., Xuan, M. Tu, Schwery, A. and Regli, P. 2003. Fully automated parameter identification for synchronous machines. *Hydropower & Dams 2003*, Cavtat, Croatia. 17–19 November 2003, pp.1–6.

Slemon, G. R., 1992. *Electric Machines and Drives*. Addison-Wesley, Massachusetts.

Smith, A. and Peralta-Sanchez, E. 2006. Line-Start Permanent-Magnet Chemical Pump Drives. *Proceedings of the International Conference on Electrical Machines*, *ICEM 2006*, Chania, Greece, September 2006. Proceedings CD.

Soulard, J. and Nee, H.P. 2000. Study of the synchronization of line-start permanent magnet synchronous motors. *Proc. Industry Applications Conf. Rec*., Vol.1, 2000, Rome, Italy, 8–12 October 2000, pp. 424–431.

Spooner, E. and Williamson A. C. 1996. Direct coupled, permanent magnet generators for wind turbine applications. *Proceedings of IEE Electric Power Application*, Vol.143, No. 1, Jan. 1996, pp.1–8.

Stephens, C., Kliman, G. and Boyd J. 2000. A Line-Start Permanent Magnet Motor with Gentle Starting Behavior. *IEEE Trans. Ind. Applicat*., Vol. 39, Jul./Aug. 2000, pp. 1021–1030.

Strnat, K., Greinacher, E. and Reinhardt, K. 1971. *Method of increasing the coersive force of pulverized rare earth-cobalt alloys*, Patent number 406391.

Strnat, K.J. The Recent Development of Permanent Magnet Materials Containing Rare Earth Metals. *IEEE Transactions on Magnetics.* Volume: 6, Issue: 2, pp. 182–190, [online]. [3 January 2007]. Available from: http://ieeexplore.ieee.org/xpls/abs_all.jsp?arnumber=1066743

Tuinman, E., Piers, P., de Weerdt, R., Simulation of a ´direct-on-line´start of a large induction motor connected to a salient pole synchronous generator. *International Conference on Simulation ´98*. 30 September-2 October 1998, pp.362-367.

Va Tech Hydro. 2007a. *ECOBulb Turbine Generator* prochure. [online]. [8 April 2007]. Available from: http://www.andritz.com/hydro-media-media-center-compact-hydro-ecobulb_1_.pdf

Va Tech Hydro. 2007b. Johann Hell. [Personal communication]. 24 August 2007.

Vas P. 1998. *Sensorless Vector and Direct Torque Control*. Oxford University Press. USA.

VDN. 2004. *REA* generating plants connected to the high- and extra-high voltage network*. Verband der Netzbetreiber - VDN – e.V. beim VDEW.2004.

Vogt, K. 1996. *Berechnung elektrischer Maschinen*. VCH Verlagsgesellschaft mbH Weinheim.

Westlake, A.J.G., Bumby, J.R. and Spooner, E. 1996. Damping the power angle oscillations of a permanent magnet synchronous generator with particular reference to wind turbine applications. *IEE Proc. Electr. Power Appl.* , Vol 143, No. 3, May 1996. pp. 269–280.

Wärtsilä. Liljenfeldt G. [Personal communication]. 23 May 2005.

Yamamoto, H., Sagawa, M., Fujimura, S. and Matsuura, Y. 1986. *Process for producing magnetic materials*, Patent number: 4601875.

Zhao Qing, An Zhongliang, Tian Lijian, Wu Yanzhong, Tang Renyan, and Yu Shenbo. 2001. Study and design of Large Capacity High Efficiency Permanent Magnet Synchronous Motor. *Electrical Machines and Systems. Proceedings of the Fifth International Conference on Electrical Machines and Systems*. Volume 2, 18–20 August 2001, ShengYang, China. pp. 888–890.

Zhao Qing, Wang Xiulian, Yu Shenbo, Zhang Dong, An Zhongliang and Tang Renyuan. 2003. Study and design for large line-start permanent magnet synchronous motors. *Sixth International Conference on Electrical Machines and Systems ICEMS 2003*. Volume 1, 9–11 November 2003, Beijing, China. pp. 132–133.

APPENDIX A

A.1 Permanent magnet braking torque

Voltage equations in dq-coordinates are

$$u_{\mathrm{d}} = R_{\mathrm{s}} i_{\mathrm{d}} + \frac{\mathrm{d}\psi_{\mathrm{d}}}{\mathrm{d}t} - \omega\psi_{\mathrm{q}} \tag{A.1}$$

$$u_{\mathrm{q}} = R_{\mathrm{s}} i_{\mathrm{q}} + \frac{\mathrm{d}\psi_{\mathrm{q}}}{\mathrm{d}t} + \omega\psi_{\mathrm{d}} \tag{A.2}$$

$$0 = R_{\mathrm{D}} i_{\mathrm{D}} + \frac{\mathrm{d}\psi_{\mathrm{D}}}{\mathrm{d}t} \tag{A.3}$$

$$0 = R_{\mathrm{Q}} i_{\mathrm{Q}} + \frac{\mathrm{d}\psi_{\mathrm{Q}}}{\mathrm{d}t} \tag{A.4}$$

where ω is real electrical angular speed of the rotor. The flux linkages are

$$\psi_{\mathrm{d}} = L_{\mathrm{d}} i_{\mathrm{d}} + L_{\mathrm{md}} i_{\mathrm{D}} + \psi_{\mathrm{PM}} \tag{A.5}$$

$$\psi_{\mathrm{q}} = L_{\mathrm{q}} i_{\mathrm{q}} + L_{\mathrm{mq}} i_{\mathrm{Q}} \tag{A.6}$$

$$\psi_{\mathrm{D}} = L_{\mathrm{md}} i_{\mathrm{d}} + L_{\mathrm{D}} i_{\mathrm{D}} + \psi_{\mathrm{PM}} \tag{A.7}$$

$$\psi_{\mathrm{Q}} = L_{\mathrm{mq}} i_{\mathrm{q}} + L_{\mathrm{Q}} i_{\mathrm{Q}} \tag{A.8}$$

The directions of the voltage components are selected as

$$\begin{aligned} u_{\mathrm{d}} &= i_{\mathrm{q}}\omega L_{\mathrm{q}} - i_{\mathrm{d}} R_{\mathrm{s}} = u_{\mathrm{s}} \sin\delta \\ u_{\mathrm{q}} &= e_{\mathrm{PM}} - i_{\mathrm{d}}\omega L_{\mathrm{d}} - i_{\mathrm{q}} R_{\mathrm{s}} = u_{\mathrm{s}} \cos\delta \end{aligned} \tag{A.9}$$

The load angle is defined as

$$\delta = \omega_{\mathrm{s}} t - \theta_{\mathrm{r}} \tag{A.10}$$

The per unit slip of the machine is

$$s = \frac{\left(\omega_{\mathrm{s}} - \dot{\theta}_{r}\right)}{\omega_{\mathrm{s}}} \tag{A.11}$$

The rotor speed is defined as

$$\dot{\theta}_{\mathrm{r}} = \omega = (1 - s)\omega_{\mathrm{s}} \tag{A.12}$$

The load angle at asynchronous speed becomes

$$\delta = s\omega_{\mathrm{s}} t + \delta_0 \tag{A.13}$$

The rotor speed is assumed to be constant but not necessarily the nominal speed. In the following, differential equations may be solved by use of operational methods. Operational variable is denoted by letter *k*. Diffentiation of Eqs. (A.7) and (A.8) with respect to time gives

$$\begin{aligned} &\frac{\mathrm{d}\psi_{\mathrm{D}}}{\mathrm{d}t} = L_{\mathrm{md}}\frac{\mathrm{d}i_{\mathrm{d}}}{\mathrm{d}t} + L_{\mathrm{D}}\frac{\mathrm{d}i_{\mathrm{D}}}{\mathrm{d}t} + \frac{\mathrm{d}\psi_{\mathrm{PM}}}{\mathrm{d}t} \\ &k = \frac{\mathrm{d}}{\mathrm{d}t}, \quad \frac{\mathrm{d}\psi_{\mathrm{PM}}}{\mathrm{d}t} = 0 \\ &k\psi_{\mathrm{D}} = L_{\mathrm{md}}ki_{\mathrm{d}} + L_{\mathrm{D}}ki_{\mathrm{D}} \end{aligned} \tag{A.14}$$

It is assumed that the flux linkage from permanent magnets is constant and thereby the differentiation of ψ_{PM} with respect to time is zero.

$$\begin{aligned} &\frac{\mathrm{d}\psi_{\mathrm{Q}}}{\mathrm{d}t} = L_{\mathrm{mq}}\frac{\mathrm{d}i_{\mathrm{q}}}{\mathrm{d}t} + L_{\mathrm{Q}}\frac{\mathrm{d}i_{\mathrm{Q}}}{\mathrm{d}t} \\ &k = \frac{\mathrm{d}}{\mathrm{d}t} \\ &k\psi_{\mathrm{Q}} = L_{\mathrm{mq}}ki_{\mathrm{q}} + L_{\mathrm{Q}}ki_{\mathrm{Q}} \end{aligned} \tag{A.15}$$

By substituting Eq. (A.14) into (A.3) the direct-axis damper winding current may be solved.

$$\begin{aligned} &0 = R_{\mathrm{D}}i_{\mathrm{D}} + \frac{\mathrm{d}\psi_{D}}{\mathrm{d}t} = R_{\mathrm{D}}i_{\mathrm{D}} + k\psi_{\mathrm{D}} = R_{\mathrm{D}}i_{\mathrm{D}} + L_{\mathrm{md}}ki_{\mathrm{d}} + L_{\mathrm{D}}ki_{\mathrm{D}} \\ &i_{\mathrm{D}}\left(R_{\mathrm{D}} + kL_{\mathrm{D}}\right) + kL_{\mathrm{md}}i_{\mathrm{d}} = 0 \\ &i_{\mathrm{D}} = \frac{-kL_{\mathrm{md}}i_{\mathrm{d}}}{R_{\mathrm{D}} + kL_{\mathrm{D}}} \end{aligned} \tag{A.16}$$

The quadrature-axis damper winding current is solved the same way by substituting Eq. (A.15) into (A.4).

$$\begin{aligned} &0 = R_{\mathrm{Q}}i_{\mathrm{Q}} + \frac{\mathrm{d}\psi_{Q}}{\mathrm{d}t} = R_{\mathrm{Q}}i_{\mathrm{Q}} + k\psi_{\mathrm{Q}} = R_{\mathrm{Q}}i_{\mathrm{Q}} + L_{\mathrm{mq}}ki_{\mathrm{q}} + L_{\mathrm{Q}}ki_{\mathrm{Q}} \\ &i_{\mathrm{Q}}\left(R_{\mathrm{Q}} + kL_{\mathrm{Q}}\right) + kL_{\mathrm{mq}}i_{\mathrm{q}} = 0 \\ &i_{\mathrm{Q}} = \frac{-kL_{\mathrm{mq}}i_{\mathrm{q}}}{R_{\mathrm{Q}} + kL_{\mathrm{Q}}} \end{aligned} \tag{A.17}$$

By substituting Eq.(A.16) into (A.5) the direct-axis flux linkage becomes

$$\psi_{\mathrm{d}} = L_{\mathrm{d}} i_{\mathrm{d}} + L_{\mathrm{md}}\left(\frac{-kL_{\mathrm{md}} i_{\mathrm{d}}}{R_{\mathrm{D}} + kL_{\mathrm{D}}}\right) + \psi_{\mathrm{PM}} = i_{\mathrm{d}}\left(L_{\mathrm{d}} - \frac{kL_{\mathrm{md}}^2}{R_{\mathrm{D}} + kL_{\mathrm{D}}}\right) + \psi_{\mathrm{PM}}$$

$$\psi_{\mathrm{d}} = L_{\mathrm{kd}} i_{\mathrm{d}} + \psi_{\mathrm{PM}}, \tag{A.18}$$

$$L_{\mathrm{kd}} = L_{\mathrm{d}} - \frac{kL_{\mathrm{md}}^2}{R_{\mathrm{D}} + kL_{\mathrm{D}}}$$

By substituting Eq.(A.17) into (A.6) the quadrature-axis flux linkage becomes

$$\psi_{\mathrm{q}} = L_{\mathrm{q}} i_{\mathrm{q}} + L_{\mathrm{mq}}\left(\frac{-kL_{\mathrm{mq}} i_{\mathrm{q}}}{R_{\mathrm{Q}} + kL_{\mathrm{Q}}}\right) = i_{\mathrm{q}}\left(L_{\mathrm{q}} - \frac{kL_{\mathrm{mq}}^2}{R_{\mathrm{Q}} + kL_{\mathrm{Q}}}\right)$$

$$\psi_{\mathrm{q}} = L_{\mathrm{kq}} i_{\mathrm{q}}, \tag{A.19}$$

$$L_{\mathrm{kq}} = L_{\mathrm{q}} - \frac{kL_{\mathrm{mq}}^2}{R_{\mathrm{Q}} + kL_{\mathrm{Q}}}$$

Now we have a system of equations with operational inductances

$$u_{\mathrm{d}} = R_{\mathrm{s}} i_{\mathrm{d}} + k\psi_{\mathrm{d}} - \omega\psi_{\mathrm{q}} \tag{A.20}$$

$$u_{\mathrm{q}} = R_{\mathrm{s}} i_{\mathrm{q}} + k\psi_{\mathrm{q}} + \omega\psi_{\mathrm{d}} \tag{A.21}$$

$$\psi_{\mathrm{d}} = L_{\mathrm{kd}} i_{\mathrm{d}} + \psi_{\mathrm{PM}} \tag{A.22}$$

$$\psi_{\mathrm{q}} = L_{\mathrm{kq}} i_{\mathrm{q}} \tag{A.23}$$

By substituting Eqs. (A.22) and (A.23) into (A.20) and (A.21) the current components may be solved.

$$\begin{aligned} u_{\mathrm{d}} &= R_{\mathrm{s}} i_{\mathrm{d}} + kL_{\mathrm{kd}} i_{\mathrm{d}} + k\psi_{\mathrm{PM}} - \omega L_{\mathrm{kq}} i_{\mathrm{q}} \\ u_{\mathrm{q}} &= R_{\mathrm{s}} i_{\mathrm{q}} + kL_{\mathrm{kq}} i_{\mathrm{q}} + \omega L_{\mathrm{kd}} i_{\mathrm{d}} + \omega\psi_{\mathrm{PM}} \end{aligned}$$

$$\begin{aligned} i_{\mathrm{d}}(R_{\mathrm{s}} + kL_{\mathrm{kd}}) &= u_{\mathrm{d}} - k\psi_{\mathrm{PM}} + \omega L_{\mathrm{kq}} i_{\mathrm{q}} \\ i_{\mathrm{q}}(R_{\mathrm{s}} + kL_{\mathrm{kq}}) &= u_{\mathrm{q}} - \omega L_{\mathrm{kd}} i_{\mathrm{d}} - \omega\psi_{\mathrm{PM}} \end{aligned} \tag{A.24}$$

$$\begin{cases} i_{\mathrm{d}} = \dfrac{u_{\mathrm{d}} - k\psi_{\mathrm{PM}} + \omega L_{\mathrm{kq}} i_{\mathrm{q}}}{R_{\mathrm{s}} + kL_{\mathrm{kd}}} \\ i_{\mathrm{q}} = \dfrac{u_{\mathrm{q}} - \omega L_{\mathrm{kd}} i_{\mathrm{d}} - \omega\psi_{\mathrm{PM}}}{R_{\mathrm{s}} + kL_{\mathrm{kq}}} \end{cases}$$

Operational reactance and operational impedance are defined as

$$\begin{aligned} X_{\mathrm{kd,q}} &= \omega L_{\mathrm{kd,q}} \\ Z_{\mathrm{kd,q}} &= R_{\mathrm{s}} + kX_{\mathrm{kd,q}} \end{aligned} \tag{A.25}$$

The current components may be solved from the system of equations. Currents become

$$\begin{cases} i_\mathrm{d} = \dfrac{u_\mathrm{d} - k\psi_\mathrm{PM} + \omega L_\mathrm{kq} i_\mathrm{q}}{R_\mathrm{s} + kL_\mathrm{kd}} \\ i_\mathrm{q} = \dfrac{u_\mathrm{q} - \omega L_\mathrm{kd} i_\mathrm{d} - \omega\psi_\mathrm{PM}}{R_\mathrm{s} + kL_\mathrm{kq}} \end{cases} \Leftrightarrow \begin{cases} i_\mathrm{d} = \dfrac{u_\mathrm{d} - k\psi_\mathrm{PM} + X_\mathrm{kq} i_\mathrm{q}}{Z_\mathrm{kd}} \\ i_\mathrm{q} = \dfrac{u_\mathrm{q} - X_\mathrm{kd} i_\mathrm{d} - \omega\psi_\mathrm{PM}}{Z_\mathrm{kq}} \end{cases}$$

$$i_\mathrm{d} = \frac{u_\mathrm{d} - k\psi_\mathrm{PM} + X_\mathrm{kq} \dfrac{u_\mathrm{q} - X_\mathrm{kd} i_\mathrm{d} - \omega\psi_\mathrm{PM}}{Z_\mathrm{kq}}}{Z_\mathrm{kd}} = \frac{u_\mathrm{d} - k\psi_\mathrm{PM}}{Z_\mathrm{kd}} + \frac{X_\mathrm{kq}\left(u_\mathrm{q} - X_\mathrm{kd} i_\mathrm{d} - \omega\psi_\mathrm{PM}\right)}{Z_\mathrm{kd} Z_\mathrm{kq}}$$

$$i_\mathrm{d} = \frac{Z_\mathrm{kq}\left(u_\mathrm{d} - k\psi_\mathrm{PM}\right) + X_\mathrm{kq}\left(u_\mathrm{q} - X_\mathrm{kd} i_\mathrm{d} - \omega\psi_\mathrm{PM}\right)}{Z_\mathrm{kd} Z_\mathrm{kq}}$$

(A.26)

$$i_\mathrm{d}\left(1 + \frac{X_\mathrm{kq} X_\mathrm{kd}}{Z_\mathrm{kd} Z_\mathrm{kq}}\right) = \frac{Z_\mathrm{kq}\left(u_\mathrm{d} - k\psi_\mathrm{PM}\right) + X_\mathrm{kq}\left(u_\mathrm{q} - \omega\psi_\mathrm{PM}\right)}{Z_\mathrm{kd} Z_\mathrm{kq}}$$

$$i_\mathrm{d} = \frac{\dfrac{Z_\mathrm{kq}\left(u_\mathrm{d} - k\psi_\mathrm{PM}\right) + X_\mathrm{kq}\left(u_\mathrm{q} - \omega\psi_\mathrm{PM}\right)}{Z_\mathrm{kd} Z_\mathrm{kq}}}{1 + \dfrac{X_\mathrm{kq} X_\mathrm{kd}}{Z_\mathrm{kd} Z_\mathrm{kq}}}$$

$$i_\mathrm{d} = \frac{\dfrac{Z_\mathrm{kq}\left(u_\mathrm{d} - k\psi_\mathrm{PM}\right) + X_\mathrm{kq}\left(u_\mathrm{q} - \omega\psi_\mathrm{PM}\right)}{Z_\mathrm{kd} Z_\mathrm{kq}}}{\dfrac{Z_\mathrm{kd} Z_\mathrm{kq} + X_\mathrm{kq} X_\mathrm{kd}}{Z_\mathrm{kd} Z_\mathrm{kq}}} = \frac{Z_\mathrm{kq}\left(u_\mathrm{d} - k\psi_\mathrm{PM}\right) + X_\mathrm{kq}\left(u_\mathrm{q} - \omega\psi_\mathrm{PM}\right)}{Z_\mathrm{kd} Z_\mathrm{kq} + X_\mathrm{kq} X_\mathrm{kd}}$$

(A.27)

Now the quadrature-axis current component may be solved

$$i_q = \frac{u_q - \omega L_{kd} i_d - \omega \psi_{PM}}{R_s + kL_{kq}} = \frac{u_q - X_{kd} i_d - \omega \psi_{PM}}{Z_{kq}}$$

$$i_q = \frac{u_q - X_{kd}\left(\frac{Z_{kq}\left(u_d - k\psi_{PM}\right) + X_{kq}\left(u_q - \omega\psi_{PM}\right)}{Z_{kd}Z_{kq} + X_{kq}X_{kd}}\right) - \omega\psi_{PM}}{Z_{kq}}$$

$$i_q = \frac{\frac{u_q\left(Z_{kd}Z_{kq} + X_{kq}X_{kd}\right) - X_{kd}Z_{kq}\left(u_d - k\Psi_{PM}\right) - X_{kd}X_{kq}\left(u_q - \omega\psi_{PM}\right) - \omega\psi_{PM}\left(Z_{kd}Z_{kq} + X_{kq}X_{kd}\right)}{Z_{kd}Z_{kq} + X_{kq}X_{kd}}}{Z_{kq}}$$

$$i_q = \frac{\frac{u_q\left(Z_{kd}Z_{kq}\right) - X_{kd}Z_{kq}\left(u_d - k\psi_{PM}\right) - \omega\psi_{PM}\left(Z_{kd}Z_{kq}\right)}{Z_{kd}Z_{kq} + X_{kq}X_{kd}}}{Z_{kq}} = \frac{u_q Z_{kd} - X_{kd}\left(u_d - k\psi_{PM}\right) - \omega\psi_{PM}Z_{kd}}{Z_{kd}Z_{kq} + X_{kq}X_{kd}}$$

(A.28)

The current components are now

$$\begin{cases} i_d = \dfrac{Z_{kq}\left(u_d - k\psi_{PM}\right) + X_{kq}\left(u_q - \omega\psi_{PM}\right)}{Z_{kd}Z_{kq} + X_{kq}X_{kd}} \\ i_q = \dfrac{u_q Z_{kd} - X_{kd}\left(u_d - k\psi_{PM}\right) - \omega\psi_{PM}Z_{kd}}{Z_{kd}Z_{kq} + X_{kq}X_{kd}} \end{cases} \quad (A.30)$$

At steady state operation, $s = 0$, $\omega = \omega_s$, $k = 0$ and $\omega\psi_{PM} = e_{PM}$. Eq. (A.30) becomes

$$L_{kd} = L_d - \frac{kL_{md}^2}{R_D + kL_D} = L_d$$

$$L_{kq} = L_q - \frac{kL_{mq}^2}{R_Q + kL_Q} = L_q \quad (A.31)$$

$$\begin{cases} i_d = \dfrac{R_s u_d + \omega_s L_q\left(u_q - e_{PM}\right)}{R_s^2 + \omega_s^2 L_q L_d} \\ i_q = \dfrac{u_q R_s - \omega_s L_d u_d - e_{PM}R_s}{R_s^2 + \omega_s^2 L_q L_d} \end{cases}$$

At asynchronous speeds the currents are divided into two modes. One mode comes from the rotor damper windings. Another mode is caused by permanent magnets. Therefore, the asynchronous torque is divided into two components; cage torque and torque caused by permanent magnets. Permanent magnets induce currents in stator windings producing losses and torque with following conditions.

$$u = 0, k = 0 \quad (A.32)$$

Set of equations for permanent magnet braking torque are calculated from Eq. (A.30) for currents and (A.22) and (A.23) for flux linkages with conditions shown in Eq. (A.32). In the following, space vector presentation is used.

$$
\begin{aligned}
&u = 0, \quad k = 0 \\
&\omega\psi_{\mathrm{PM}} = \omega_{\mathrm{s}}(1-s)\psi_{\mathrm{PM}} = e'_{\mathrm{PM}}, \quad e'_{\mathrm{PM}} = (1-s)e_{\mathrm{PM}} \\
&L_{\mathrm{kd}} = L_{\mathrm{d}} - \frac{kL_{\mathrm{md}}^2}{R_{\mathrm{D}} + kL_{\mathrm{D}}} \\
&L_{\mathrm{kq}} = L_{\mathrm{q}} - \frac{kL_{\mathrm{mq}}^2}{R_{\mathrm{Q}} + kL_{\mathrm{Q}}} \\
&X_{\mathrm{kd}} = \omega L_{\mathrm{kd}} = \omega L_{\mathrm{d}} - \frac{\omega k L_{\mathrm{md}}^2}{R_{\mathrm{D}} + kL_{\mathrm{D}}} = \omega_{\mathrm{s}}(1-s)L_{\mathrm{d}} = (1-s)X_{\mathrm{d}} \\
&X_{\mathrm{kq}} = \omega L_{\mathrm{kq}} = \omega L_{\mathrm{q}} - \frac{\omega k L_{\mathrm{mq}}^2}{R_{\mathrm{Q}} + kL_{\mathrm{Q}}} = \omega_{\mathrm{s}}(1-s)L_{\mathrm{q}} = (1-s)X_{\mathrm{q}} \\
&Z_{\mathrm{kd}} = R_{\mathrm{s}} + kX_{\mathrm{kd}} = R_{\mathrm{s}} \\
&Z_{\mathrm{kq}} = R_{\mathrm{s}} + kX_{\mathrm{kq}} = R_{\mathrm{s}}
\end{aligned}
\tag{A.33}
$$

$$
\begin{cases}
i_{\mathrm{d}} = \dfrac{Z_{\mathrm{kq}}(u_{\mathrm{d}} - k\psi_{\mathrm{PM}}) + X_{\mathrm{kq}}(u_{\mathrm{q}} - \omega\psi_{\mathrm{PM}})}{Z_{\mathrm{kd}}Z_{\mathrm{kq}} + X_{\mathrm{kq}}X_{\mathrm{kd}}} = \dfrac{R_{\mathrm{s}}(-k\psi_{\mathrm{PM}}) + X_{\mathrm{kq}}(-e'_{\mathrm{PM,ph}})}{R_{\mathrm{s}}R_{\mathrm{s}} + X_{\mathrm{kq}}X_{\mathrm{kd}}} \\
i_{\mathrm{q}} = \dfrac{u_{\mathrm{q}}Z_{\mathrm{kd}} - X_{\mathrm{kd}}(u_{\mathrm{d}} - k\psi_{\mathrm{PM}}) - \omega\psi_{\mathrm{PM}}Z_{\mathrm{kd}}}{Z_{\mathrm{kd}}Z_{\mathrm{kq}} + X_{\mathrm{kq}}X_{\mathrm{kd}}} = \dfrac{-X_{\mathrm{kd}}(-k\psi_{\mathrm{PM}}) - \omega\psi_{\mathrm{PM}}R_{\mathrm{s}}}{R_{\mathrm{s}}R_{\mathrm{s}} + X_{\mathrm{kq}}X_{\mathrm{kd}}}
\end{cases}
\tag{A.34}
$$

$$
\begin{cases}
i_{\mathrm{d}} = \dfrac{-R_{\mathrm{s}}k\psi_{\mathrm{PM}} - X_{\mathrm{kq}}e'_{\mathrm{PM}}}{R_{\mathrm{s}}^2 + X_{\mathrm{kq}}X_{\mathrm{kd}}} = \dfrac{-X_{\mathrm{q}}(1-s)^2 e_{\mathrm{PM}}}{R_{\mathrm{s}}^2 + X_{\mathrm{q}}X_{\mathrm{d}}(1-s)^2} \\
i_{\mathrm{q}} = \dfrac{-e'_{\mathrm{PM}}R_{\mathrm{s}}}{R_{\mathrm{s}}^2 + X_{\mathrm{kq}}X_{\mathrm{kd}}} = \dfrac{-(1-s)e_{\mathrm{PM}}R_{\mathrm{s}}}{R_{\mathrm{s}}^2 + X_{\mathrm{q}}X_{\mathrm{d}}(1-s)^2}
\end{cases}
$$

The braking torque caused by permanent magnets is solved by substituting currents from Eq. (A.34) to common torque expression in dq-models.

$$\begin{cases} i_{\mathrm{d}} = \dfrac{-X_{\mathrm{q}}(1-s)^2 e_{\mathrm{PM}}}{R_{\mathrm{s}}^2 + X_{\mathrm{q}} X_{\mathrm{d}} (1-s)^2} \\ i_{\mathrm{q}} = \dfrac{-(1-s) e_{\mathrm{PM}} R_{\mathrm{s}}}{R_{\mathrm{s}}^2 + X_{\mathrm{q}} X_{\mathrm{d}} (1-s)^2} \end{cases}$$

$$T_{\mathrm{b}} = \frac{3}{2} p \left[\psi_{\mathrm{PM}} i_{\mathrm{q}} - (L_{\mathrm{q}} - L_{\mathrm{d}}) i_{\mathrm{d}} i_{\mathrm{q}} \right] = \frac{3}{2} p \left[\frac{e_{\mathrm{PM}}}{\omega_{\mathrm{s}}} i_{\mathrm{q}} - (L_{\mathrm{q}} - L_{\mathrm{d}}) i_{\mathrm{d}} i_{\mathrm{q}} \right]$$

$$T_{\mathrm{b}} = \frac{3}{2} p \left[\frac{e_{\mathrm{PM}}}{\omega_{\mathrm{s}}} \left(\frac{-(1-s) e_{\mathrm{PM}} R_{\mathrm{s}}}{R_{\mathrm{s}}^2 + X_{\mathrm{q}} X_{\mathrm{d}} (1-s)^2} \right) - (L_{\mathrm{q}} - L_{\mathrm{d}}) \left(\frac{-X_{\mathrm{q}} (1-s)^2 e_{\mathrm{PM}}}{R_{\mathrm{s}}^2 + X_{\mathrm{q}} X_{\mathrm{d}} (1-s)^2} \right) \left(\frac{-(1-s) e_{\mathrm{PM}} R_{\mathrm{s}}}{R_{\mathrm{s}}^2 + X_{\mathrm{q}} X_{\mathrm{d}} (1-s)^2} \right) \right]$$

(A.35)

By using RMS values, Eq. (A.35) becomes

$$T_{\mathrm{b}} = 3p \left[\frac{E_{\mathrm{PM}}}{\omega_{\mathrm{s}}} \left(\frac{-(1-s) E_{\mathrm{PM}} R_{\mathrm{s}}}{R_{\mathrm{s}}^2 + X_{\mathrm{q}} X_{\mathrm{d}} (1-s)^2} \right) - \left(\frac{X_{\mathrm{q}} - X_{\mathrm{d}}}{\omega_{\mathrm{s}}} \right) \left(\frac{-X_{\mathrm{q}} (1-s)^2 E_{\mathrm{PM}}}{R_{\mathrm{s}}^2 + X_{\mathrm{q}} X_{\mathrm{d}} (1-s)^2} \right) \left(\frac{-(1-s) E_{\mathrm{PM}} R_{\mathrm{s}}}{R_{\mathrm{s}}^2 + X_{\mathrm{q}} X_{\mathrm{d}} (1-s)^2} \right) \right]$$

$$T_{\mathrm{b}} = \frac{3}{\omega_{\mathrm{s}}} p \left[\left(\frac{-(1-s) E_{\mathrm{PM}}^2 R_{\mathrm{s}}}{R_{\mathrm{s}}^2 + X_{\mathrm{q}} X_{\mathrm{d}} (1-s)^2} \right) + (X_{\mathrm{d}} - X_{\mathrm{q}}) \left(\frac{-X_{\mathrm{q}} (1-s)^2 E_{\mathrm{PM}}}{R_{\mathrm{s}}^2 + X_{\mathrm{q}} X_{\mathrm{d}} (1-s)^2} \right) \left(\frac{-(1-s) E_{\mathrm{PM}} R_{\mathrm{s}}}{R_{\mathrm{s}}^2 + X_{\mathrm{q}} X_{\mathrm{d}} (1-s)^2} \right) \right]$$

$$T_{\mathrm{b}} = \frac{3}{\omega_{\mathrm{s}}} p \left[\left(\frac{-(1-s) E_{\mathrm{PM}}^2 R_{\mathrm{s}}}{R_{\mathrm{s}}^2 + X_{\mathrm{q}} X_{\mathrm{d}} (1-s)^2} \right) + \left(\frac{(X_{\mathrm{q}} - X_{\mathrm{d}}) X_{\mathrm{q}} (1-s)^2 E_{\mathrm{PM}}}{R_{\mathrm{s}}^2 + X_{\mathrm{q}} X_{\mathrm{d}} (1-s)^2} \right) \left(\frac{-(1-s) E_{\mathrm{PM}} R_{\mathrm{s}}}{R_{\mathrm{s}}^2 + X_{\mathrm{q}} X_{\mathrm{d}} (1-s)^2} \right) \right]$$

$$T_{\mathrm{b}} = \frac{3}{\omega_{\mathrm{s}}} p \left(E_{\mathrm{PM}} + \frac{(X_{\mathrm{q}} - X_{\mathrm{d}}) X_{\mathrm{q}} (1-s)^2 E_{\mathrm{PM}}}{R_{\mathrm{s}}^2 + X_{\mathrm{q}} X_{\mathrm{d}} (1-s)^2} \right) \left(\frac{-(1-s) E_{\mathrm{PM}} R_{\mathrm{s}}}{R_{\mathrm{s}}^2 + X_{\mathrm{q}} X_{\mathrm{d}} (1-s)^2} \right)$$

$$T_{\mathrm{b}} = -\frac{3}{\omega_{\mathrm{s}}} p \left(E_{\mathrm{PM}} + \frac{(X_{\mathrm{q}}^2 - X_{\mathrm{d}} X_{\mathrm{q}}) (1-s)^2 E_{\mathrm{PM}}}{R_{\mathrm{s}}^2 + X_{\mathrm{q}} X_{\mathrm{d}} (1-s)^2} \right) \left(\frac{(1-s) E_{\mathrm{PM}} R_{\mathrm{s}}}{R_{\mathrm{s}}^2 + X_{\mathrm{q}} X_{\mathrm{d}} (1-s)^2} \right)$$

$$T_{\mathrm{b}} = -\frac{3}{\omega_{\mathrm{s}}} p \left(\frac{\left(\dfrac{R_{\mathrm{s}}^2}{(1-s)^2} + X_{\mathrm{q}} X_{\mathrm{d}} \right) + (X_{\mathrm{q}}^2 - X_{\mathrm{d}} X_{\mathrm{q}})}{\left(\dfrac{R_{\mathrm{s}}^2}{(1-s)^2} + X_{\mathrm{q}} X_{\mathrm{d}} \right)} \right) \left(\frac{(1-s) E_{\mathrm{PM}}^2 R_{\mathrm{s}}}{R_{\mathrm{s}}^2 + X_{\mathrm{q}} X_{\mathrm{d}} (1-s)^2} \right)$$

$$T_{\mathrm{b}} = -\frac{3}{\omega_{\mathrm{s}}} p \left(\frac{R_{\mathrm{s}}^2 + (1-s)^2 X_{\mathrm{q}}^2}{R_{\mathrm{s}}^2 + (1-s)^2 X_{\mathrm{q}} X_{\mathrm{d}}} \right) \left(\frac{(1-s) E_{\mathrm{PM}}^2 R_{\mathrm{s}}}{R_{\mathrm{s}}^2 + X_{\mathrm{q}} X_{\mathrm{d}} (1-s)^2} \right)$$

(A.36)

The derived permanent magnet braking torque is now calculated.

$$T_\mathrm{b} = -\frac{3}{\omega_\mathrm{s}} p \left(\frac{R_\mathrm{s}^2 + (1-s)^2 X_\mathrm{q}^2}{R_\mathrm{s}^2 + (1-s)^2 X_\mathrm{q} X_\mathrm{d}} \right) \left(\frac{(1-s) E_\mathrm{PM}^2 R_\mathrm{s}}{R_\mathrm{s}^2 + X_\mathrm{q} X_\mathrm{d} (1-s)^2} \right)$$

$$T_\mathrm{b} = -\frac{3pR_\mathrm{s}(1-s)E_\mathrm{PM}^2}{\omega_\mathrm{s}} \cdot \frac{R_\mathrm{s}{}^2 + \omega_\mathrm{s}^2 L_\mathrm{q}{}^2 (1-s)^2}{\left(R_\mathrm{s}{}^2 + \omega_\mathrm{s}^2 L_\mathrm{d} L_\mathrm{q} (1-s)^2\right)^2} \propto \frac{E_\mathrm{PM,ph}^2}{\omega^2 L_\mathrm{d} L_\mathrm{q}} \tag{A.37}$$

The maximum value of the T_b is found by differentiating Eq. (A.37) with respect to the slip s by partial differentiation and quotient differentiation.

$$\frac{\mathrm{d}}{\mathrm{d}s} T_\mathrm{b}(s) = \frac{\mathrm{d}}{\mathrm{d}s} \left(-\frac{3pR_\mathrm{s}(1-s)E_\mathrm{PM}^2}{\omega_\mathrm{s}} \cdot \frac{R_\mathrm{s}{}^2 + \omega_\mathrm{s}{}^2 L_\mathrm{q}{}^2 (1-s)^2}{\left(R_\mathrm{s}{}^2 + \omega_\mathrm{s}{}^2 L_\mathrm{d} L_\mathrm{q} (1-s)^2\right)^2} \right) = \frac{\mathrm{d}}{\mathrm{d}s} \left(a_1 \frac{a_2}{a_3} \right)$$

$$a_1 = -\frac{3pR_\mathrm{s}(1-s)E_\mathrm{PM}^2}{\omega_\mathrm{s}}$$

$$a_2 = R_\mathrm{s}{}^2 + \omega_\mathrm{s}{}^2 L_\mathrm{q}{}^2 (1-s)^2$$

$$a_3 = \left(R_\mathrm{s}{}^2 + \omega_\mathrm{s}{}^2 L_\mathrm{d} L_\mathrm{q} (1-s)^2\right)^2 \tag{A.38}$$

$$\frac{\mathrm{d}}{\mathrm{d}s} a_1 = \frac{3pR_\mathrm{s}E_\mathrm{PM}^2}{\omega_\mathrm{s}} \tag{A.39}$$

$$\frac{\mathrm{d}}{\mathrm{d}s} a_2 = \frac{\mathrm{d}}{\mathrm{d}s} R_\mathrm{s}{}^2 + \omega_\mathrm{s}{}^2 L_\mathrm{q}{}^2 (1-s)^2 = -2\omega_\mathrm{s}{}^2 L_\mathrm{q}{}^2 (1-s) \tag{A.40}$$

$$\frac{\mathrm{d}}{\mathrm{d}s} a_3 = \frac{\mathrm{d}}{\mathrm{d}s} \left(R_\mathrm{s}{}^2 + \omega_\mathrm{s}{}^2 L_\mathrm{d} L_\mathrm{q} (1-s)^2\right)^2 = -4\left(R_\mathrm{s}{}^2 + \omega_\mathrm{s}{}^2 L_\mathrm{d} L_\mathrm{q} (1-s)^2\right) \omega_\mathrm{s}{}^2 L_\mathrm{d} L_\mathrm{q} (1-s) \tag{A.40}$$

$$\frac{\mathrm{d}}{\mathrm{d}s} \left(a_1 \frac{a_2}{a_3} \right) = \left(\frac{\mathrm{d}}{\mathrm{d}s} a_1 \right) \frac{a_2}{a_3} + a_1 \left(\frac{\mathrm{d}}{\mathrm{d}s} \frac{a_2}{a_3} \right) = \left(\frac{\mathrm{d}}{\mathrm{d}s} a_1 \right) \frac{a_2}{a_3} + a_1 \frac{\left(\frac{\mathrm{d}}{\mathrm{d}s} a_2 \right) a_3 - a_2 \frac{\mathrm{d}}{\mathrm{d}s} a_3}{a_3^2} \tag{A.41}$$

$$\frac{\mathrm{d}}{\mathrm{d}s} T_\mathrm{b}(s) = \frac{\mathrm{d}}{\mathrm{d}s} \left(a_1 \frac{a_2}{a_3} \right) = \frac{3pR_\mathrm{s}E_\mathrm{PM}^2}{\omega_\mathrm{s}} \frac{R_\mathrm{s}{}^2 + \omega_\mathrm{s}{}^2 L_\mathrm{q}{}^2 (1-s)^2}{\left(R_\mathrm{s}{}^2 + \omega_\mathrm{s}{}^2 L_\mathrm{d} L_\mathrm{q} (1-s)^2\right)^2} + \frac{-3pR_\mathrm{s}(1-s)E_\mathrm{PM}^2}{\omega_\mathrm{s}} \cdot \left\{ \right.$$

$$\left. \frac{\left(-2\omega_\mathrm{s}{}^2 L_\mathrm{q}{}^2 (1-s)\right)\left(R_\mathrm{s}{}^2 + \omega_\mathrm{s}{}^2 L_\mathrm{d} L_\mathrm{q} (1-s)^2\right)^2 - \left(R_\mathrm{s}{}^2 + \omega_\mathrm{s}{}^2 L_\mathrm{q}{}^2 (1-s)^2\right)\left(-4\left(R_\mathrm{s}{}^2 + \omega_\mathrm{s}{}^2 L_\mathrm{d} L_\mathrm{q} (1-s)^2\right) \omega_\mathrm{s}{}^2 L_\mathrm{d} L_\mathrm{q} (1-s)\right)}{\left(\left(R_\mathrm{s}{}^2 + \omega_\mathrm{s}{}^2 L_\mathrm{d} L_\mathrm{q} (1-s)^2\right)^2\right)^2} \right\} \tag{A.42}$$

$$\frac{\mathrm{d}}{\mathrm{d}s}T_{\mathrm{b}}(s)=\frac{\mathrm{d}}{\mathrm{d}s}\left(a_1\frac{a_2}{a_3}\right)=\frac{3pR_{\mathrm{s}}E_{\mathrm{PM}}^2}{\omega_{\mathrm{s}}}\frac{{R_{\mathrm{s}}}^2+{\omega_{\mathrm{s}}}^2{L_{\mathrm{q}}}^2(1-s)^2}{\left({R_{\mathrm{s}}}^2+{\omega_{\mathrm{s}}}^2L_{\mathrm{d}}L_{\mathrm{q}}(1-s)^2\right)^2}+\frac{-3pR_{\mathrm{s}}(1-s)E_{\mathrm{PM}}^2}{\omega_{\mathrm{s}}}\cdot\left\{\right.$$
$$\left.\frac{\left(-2{\omega_{\mathrm{s}}}^2{L_{\mathrm{q}}}^2(1-s)\right)\left({R_{\mathrm{s}}}^2+{\omega_{\mathrm{s}}}^2L_{\mathrm{d}}L_{\mathrm{q}}(1-s)^2\right)^2-\left({R_{\mathrm{s}}}^2+{\omega_{\mathrm{s}}}^2{L_{\mathrm{q}}}^2(1-s)^2\right)\left(-4\left({R_{\mathrm{s}}}^2+{\omega_{\mathrm{s}}}^2L_{\mathrm{d}}L_{\mathrm{q}}(1-s)^2\right){\omega_{\mathrm{s}}}^2L_{\mathrm{d}}L_{\mathrm{q}}(1-s)\right)}{\left(\left({R_{\mathrm{s}}}^2+{\omega_{\mathrm{s}}}^2L_{\mathrm{d}}L_{\mathrm{q}}(1-s)^2\right)^2\right)^2}\right\}$$

(A.43)

After a series of manipulations Eq. (A.43) becomes

$$\frac{\mathrm{d}}{\mathrm{d}s}T_{\mathrm{b}}(s)=\frac{3pR_{\mathrm{s}}E_{\mathrm{PM}}^2}{\omega_{\mathrm{s}}\left({R_{\mathrm{s}}}^2+{\omega_{\mathrm{s}}}^2L_{\mathrm{d}}L_{\mathrm{q}}(1-s)^2\right)^2}\cdot\left[\right.$$
$$\left.\left({R_{\mathrm{s}}}^2+{\omega_{\mathrm{s}}}^2L_{\mathrm{d}}L_{\mathrm{q}}(1-s)^2\right)+2(1-s)^2{\omega_{\mathrm{s}}}^2{L_{\mathrm{q}}}^2-\frac{4L_{\mathrm{d}}L_{\mathrm{q}}(1-s)^2\left({R_{\mathrm{s}}}^2+{\omega_{\mathrm{s}}}^2{L_{\mathrm{q}}}^2(1-s)^2\right)}{{R_{\mathrm{s}}}^2+{\omega_{\mathrm{s}}}^2L_{\mathrm{d}}L_{\mathrm{q}}(1-s)^2}\right] \tag{A.44}$$

The slip value of the maximum braking torque is found by solving the zero crossings of Eq. (A.44).

$$\frac{\mathrm{d}}{\mathrm{d}s}T_{\mathrm{b}}(s)=0\Leftrightarrow$$
$$s_{\mathrm{peak}}=\frac{2\omega_{\mathrm{s}}{L_{\mathrm{q}}}^2L_{\mathrm{d}}\pm\sqrt{-6{L_{\mathrm{q}}}^2{L_{\mathrm{d}}}^2{R_{\mathrm{s}}}^2+6{L_{\mathrm{q}}}^3L_{\mathrm{d}}{R_{\mathrm{s}}}^2\pm2{L_{\mathrm{q}}}^2L_{\mathrm{d}}\sqrt{(9{L_{\mathrm{d}}}^2{R_{\mathrm{s}}}^4-14L_{\mathrm{q}}L_{\mathrm{d}}+9{L_{\mathrm{q}}}^2{R_{\mathrm{s}}}^4)}}}{2{L_{\mathrm{q}}}^2L_{\mathrm{d}}\omega_{\mathrm{s}}} \tag{A.45}$$

A.2 Cage torque

In cage torque mode, a set of dq-currents caused by applied voltage is selected. The following conditions are set for the determination of the current components.

$$k=js\omega,\quad \omega=(1-s)\omega_{\mathrm{s}},\quad e'_{\mathrm{PM}}=0,\quad u_{\mathrm{d}}=\mathrm{j}u_{\mathrm{s}},\quad u_{\mathrm{q}}=u_{\mathrm{s}}$$
$$Z_{\mathrm{kd}}=R_{\mathrm{s}}+\mathrm{j}s\omega X_{\mathrm{kd}}=R_{\mathrm{s}}+\mathrm{j}s(1-s)\omega_{\mathrm{s}}X_{\mathrm{kd}}$$
$$Z_{\mathrm{kq}}=R_{\mathrm{s}}+\mathrm{j}s\omega X_{\mathrm{kq}}=R_{\mathrm{s}}+\mathrm{j}s(1-s)\omega_{\mathrm{s}}X_{\mathrm{kq}}$$
$$L_{\mathrm{kd}}=L_{\mathrm{d}}-\frac{kL_{\mathrm{md}}^2}{R_{\mathrm{D}}+kL_{\mathrm{D}}}$$
$$L_{\mathrm{kq}}=L_{\mathrm{q}}-\frac{kL_{\mathrm{mq}}^2}{R_{\mathrm{Q}}+kL_{\mathrm{Q}}}$$
$$X_{\mathrm{kd}}=\omega L_{\mathrm{kd}}=\omega L_{\mathrm{d}}-\frac{\mathrm{j}s\omega L_{\mathrm{md}}^2}{R_{\mathrm{D}}+\mathrm{j}s\omega L_{\mathrm{D}}}=(1-s)\omega_{\mathrm{s}}L_{\mathrm{d}}-\frac{\mathrm{j}s(1-s)\omega_{\mathrm{s}}L_{\mathrm{md}}^2}{R_{\mathrm{D}}+\mathrm{j}s(1-s)\omega_{\mathrm{s}}L_{\mathrm{D}}}=(1-s)\left(X_{\mathrm{d}}+\frac{sX_{\mathrm{md}}^2}{\omega_{\mathrm{s}}(\mathrm{j}R_{\mathrm{D}}-sX_{\mathrm{D}})}\right)$$
$$X_{\mathrm{kq}}=\omega L_{\mathrm{kq}}=\omega L_{\mathrm{q}}-\frac{\mathrm{j}s\omega L_{\mathrm{mq}}^2}{R_{\mathrm{Q}}+\mathrm{j}s\omega L_{\mathrm{Q}}}=(1-s)\left(X_{\mathrm{q}}+\frac{sX_{\mathrm{mq}}^2}{\omega_{\mathrm{s}}(\mathrm{j}R_{\mathrm{Q}}-sX_{\mathrm{Q}})}\right) \tag{A.46}$$

From Eq. (A.30) the following can be derived

$$\begin{cases} i_{\mathrm{d}} = \dfrac{Z_{\mathrm{kq}}\left(u_{\mathrm{d}} - k\psi_{\mathrm{PM}}\right) + X_{\mathrm{kq}}\left(u_{\mathrm{q}} - \omega\psi_{\mathrm{PM}}\right)}{Z_{\mathrm{kd}}Z_{\mathrm{kq}} + X_{\mathrm{kq}}X_{\mathrm{kd}}} = \dfrac{\left(R_{\mathrm{s}} + \mathrm{j}s\omega X_{\mathrm{kq}}\right)\left(u_{\mathrm{d}} - \mathrm{j}s\omega\psi_{\mathrm{PM}}\right) + X_{\mathrm{kq}}\left(u_{\mathrm{q}} - \omega\psi_{\mathrm{PM}}\right)}{Z_{\mathrm{kd}}Z_{\mathrm{kq}} + X_{\mathrm{kq}}X_{\mathrm{kd}}} \\ i_{\mathrm{q}} = \dfrac{u_{\mathrm{q}}Z_{\mathrm{kd}} - X_{\mathrm{kd}}\left(u_{\mathrm{d}} - k\psi_{\mathrm{PM}}\right) - \omega\psi_{\mathrm{PM}}Z_{\mathrm{kd}}}{Z_{\mathrm{kd}}Z_{\mathrm{kq}} + X_{\mathrm{kq}}X_{\mathrm{kd}}} = \dfrac{u_{\mathrm{q}}\left(R_{\mathrm{s}} + \mathrm{j}s\omega X_{\mathrm{kd}}\right) - X_{\mathrm{kd}}\left(u_{\mathrm{d}} - \mathrm{j}s\omega\psi_{\mathrm{PM}}\right) - \omega\psi_{\mathrm{PM}}Z_{\mathrm{kd}}}{Z_{\mathrm{kd}}Z_{\mathrm{kq}} + X_{\mathrm{kq}}X_{\mathrm{kd}}} \end{cases}$$

$$\begin{cases} i_{\mathrm{d}} = \dfrac{\left(R_{\mathrm{s}} + \mathrm{j}s\omega X_{\mathrm{kq}}\right)\left(u_{\mathrm{d}} - \mathrm{j}se'_{\mathrm{PM}}\right) + X_{\mathrm{kq}}\left(u_{\mathrm{q}} - e'_{\mathrm{PM}}\right)}{Z_{\mathrm{kd}}Z_{\mathrm{kq}} + X_{\mathrm{kq}}X_{\mathrm{kd}}} = \dfrac{\left(R_{\mathrm{s}} + \mathrm{j}s\omega X_{\mathrm{kq}}\right)u_{\mathrm{d}} + X_{\mathrm{kq}}u_{\mathrm{q}}}{Z_{\mathrm{kd}}Z_{\mathrm{kq}} + X_{\mathrm{kq}}X_{\mathrm{kd}}} \\ i_{\mathrm{q}} = \dfrac{u_{\mathrm{q}}\left(R_{\mathrm{s}} + \mathrm{j}s\omega X_{\mathrm{kd}}\right) - X_{\mathrm{kd}}\left(u_{\mathrm{d}} - jse'_{\mathrm{PM}}\right) - e'_{\mathrm{PM}}Z_{\mathrm{kd}}}{Z_{\mathrm{kd}}Z_{\mathrm{kq}} + X_{\mathrm{kq}}X_{\mathrm{kd}}} = \dfrac{u_{\mathrm{q}}\left(R_{\mathrm{s}} + \mathrm{j}s\omega X_{\mathrm{kd}}\right) - X_{\mathrm{kd}}u_{\mathrm{d}}}{Z_{\mathrm{kd}}Z_{\mathrm{kq}} + X_{\mathrm{kq}}X_{\mathrm{kd}}} \end{cases}$$

(A.47)

$$Z_{\mathrm{kd}} = R_{\mathrm{s}} + \mathrm{j}s\omega X_{\mathrm{kd}} = R_{\mathrm{s}} + \mathrm{j}s\left(1-s\right)\omega_{\mathrm{s}}X_{\mathrm{kd}}$$

$$Z_{\mathrm{kq}} = R_{\mathrm{s}} + \mathrm{j}s\omega X_{\mathrm{kq}} = R_{\mathrm{s}} + \mathrm{j}s\left(1-s\right)\omega_{\mathrm{s}}X_{\mathrm{kq}}$$

$$\begin{cases} i_{\mathrm{d}} = \dfrac{\left(R_{\mathrm{s}} + \mathrm{j}s\omega X_{\mathrm{kq}}\right)\mathrm{j}u_{\mathrm{s}} + X_{\mathrm{kq}}u_{\mathrm{s}}}{\left(R_{\mathrm{s}} + \mathrm{j}s\omega X_{\mathrm{kd}}\right)\left(R_{\mathrm{s}} + \mathrm{j}s\omega X_{\mathrm{kq}}\right) + X_{\mathrm{kd}}X_{\mathrm{kq}}} = \dfrac{u_{\mathrm{s}}\left(\mathrm{j}R_{\mathrm{s}} - s\left(1-s\right)\omega_{\mathrm{s}}X_{\mathrm{kq}} + X_{\mathrm{kq}}\right)}{R_{\mathrm{s}}^2 + \mathrm{j}s\omega R_{\mathrm{s}}\left(X_{\mathrm{kd}} + X_{\mathrm{kq}}\right) + X_{\mathrm{kd}}X_{\mathrm{kq}}} \\ i_{\mathrm{q}} = \dfrac{u_{\mathrm{s}}\left(R_{\mathrm{s}} + \mathrm{j}s\omega X_{\mathrm{kd}}\right) - X_{\mathrm{kd}}\mathrm{j}u_{\mathrm{s}}}{\left(R_{\mathrm{s}} + \mathrm{j}s\omega X_{\mathrm{kd}}\right)\left(R_{\mathrm{s}} + \mathrm{j}s\omega X_{\mathrm{kq}}\right) + X_{\mathrm{kd}}X_{\mathrm{kq}}} = \dfrac{u_{\mathrm{s}}\left(R_{\mathrm{s}} + \mathrm{j}X_{\mathrm{kd}}\left(s\left(1-s\right)\omega_{\mathrm{s}} - 1\right)\right)}{R_{\mathrm{s}}^2 + \mathrm{j}s\omega R_{\mathrm{s}}\left(X_{\mathrm{kd}} + X_{\mathrm{kq}}\right) + X_{\mathrm{kd}}X_{\mathrm{kq}}} \end{cases}$$

$$\begin{cases} i_{\mathrm{d}} = \dfrac{u_{\mathrm{s}}\left(\mathrm{j}R_{\mathrm{s}} + X_{\mathrm{kq}}\left(s\left(s-1\right)\omega_{\mathrm{s}} + 1\right)\right)}{R_{\mathrm{s}}^2 + \mathrm{j}s\left(1-s\right)\omega_{\mathrm{s}}R_{\mathrm{s}}\left(X_{\mathrm{kd}} + X_{\mathrm{kq}}\right) + X_{\mathrm{kd}}X_{\mathrm{kq}}} \\ i_{\mathrm{q}} = \dfrac{u_{\mathrm{s}}\left(R_{\mathrm{s}} + \mathrm{j}X_{\mathrm{kd}}\left(s\left(1-s\right)\omega_{\mathrm{s}} - 1\right)\right)}{R_{\mathrm{s}}^2 + \mathrm{j}s\left(1-s\right)\omega_{\mathrm{s}}R_{\mathrm{s}}\left(X_{\mathrm{kd}} + X_{\mathrm{kq}}\right) + X_{\mathrm{kd}}X_{\mathrm{kq}}} \end{cases}$$

(A.48)

The flux linkages are now calculated by substituting currents from Eq. (A.48) into(A.22) and (A.23) with the conditions shown in Eq. (A.46)

$$\begin{aligned} &\psi_{\mathrm{d}} = L_{\mathrm{kd}}i_{\mathrm{d}} = \frac{X_{\mathrm{kd}}i_{\mathrm{d}}}{\omega_{\mathrm{s}}} = \\ &\frac{1}{\omega_{\mathrm{s}}}\left(1-s\right)\left(X_{\mathrm{d}} + \frac{sX_{\mathrm{md}}^2}{\mathrm{j}R_{\mathrm{D}} - sX_{\mathrm{D}}}\right)\cdot\frac{u_{\mathrm{s}}\left(\mathrm{j}R_{\mathrm{s}} + X_{\mathrm{kq}}\left(s\left(s-1\right)\omega_{\mathrm{s}} + 1\right)\right)}{R_{\mathrm{s}}^2 + \mathrm{j}s\left(1-s\right)\omega_{\mathrm{s}}R_{\mathrm{s}}\left(X_{\mathrm{kd}} + X_{\mathrm{kq}}\right) + X_{\mathrm{kd}}X_{\mathrm{kq}}} \\ &\psi_{\mathrm{q}} = L_{\mathrm{kq}}i_{\mathrm{q}} = \frac{X_{\mathrm{kq}}i_{\mathrm{q}}}{\omega} = \\ &\frac{1}{\omega}\left(1-s\right)\left(X_{\mathrm{q}} + \frac{sX_{\mathrm{mq}}^2}{\mathrm{j}R_{\mathrm{Q}} - sX_{\mathrm{Q}}}\right)\cdot\frac{u_{\mathrm{s}}\left(R_{\mathrm{s}} + \mathrm{j}X_{\mathrm{kd}}\left(s\left(1-s\right)\omega_{\mathrm{s}} - 1\right)\right)}{R_{\mathrm{s}}^2 + \mathrm{j}s\left(1-s\right)\omega_{\mathrm{s}}R_{\mathrm{s}}\left(X_{\mathrm{kd}} + X_{\mathrm{kq}}\right) + X_{\mathrm{kd}}X_{\mathrm{kq}}} \end{aligned} \tag{A.49}$$

The asynchronous cage torque is calculated from the complex equations (Honsinger 1980) by substituting currents from Eq. (A.48) and conjugate parts of the flux linkages from Eq. (A.49).

$$T_\mathrm{c} = \frac{1}{2}\frac{3p}{2}\mathrm{Re}\left[\psi_\mathrm{d}^* i_\mathrm{q} - \psi_\mathrm{q}^* i_\mathrm{d}\right] \tag{A.50}$$

If the damper winding is symmetric, the asynchronous cage torque may be calculated with the following equation

$$T_\mathrm{c} \approx \frac{3U_\mathrm{s}^2\left(\frac{R_\mathrm{r}}{s}\right)}{\frac{\omega_\mathrm{s}}{p}\left[\left(R_\mathrm{s}+\frac{R_\mathrm{r}}{s}\right)^2 + \left(\omega_\mathrm{s}L_{\mathrm{s}\sigma} + \omega_\mathrm{s}L_{\mathrm{r}\sigma}\right)^2\right]} \tag{A.51}$$

The asynchronous pull-out torque of the cage torque is found by differentiating Eq. (A.51) with respect to the slip s.

$$\frac{\mathrm{d}}{\mathrm{d}s}T_\mathrm{c}(s) = \frac{\mathrm{d}}{\mathrm{d}s}\frac{3U_\mathrm{s}^2\left(\frac{R_\mathrm{r}}{s}\right)}{\frac{\omega_\mathrm{s}}{p}\left[\left(R_\mathrm{s}+\frac{R_\mathrm{r}}{s}\right)^2 + \left(\omega_\mathrm{s}L_{\mathrm{s}\sigma} + \omega_\mathrm{s}L_{\mathrm{r}\sigma}\right)^2\right]} = \frac{-3U_\mathrm{s}^2\frac{R_\mathrm{r}}{s^2}}{\frac{\omega_\mathrm{s}}{p}\left[\left(R_\mathrm{s}+\frac{R_\mathrm{r}}{s}\right)^2 + \left(\omega_\mathrm{s}L_{\mathrm{s}\sigma} + \omega_\mathrm{s}L_{\mathrm{r}\sigma}\right)^2\right]} + \frac{6U_\mathrm{s}^2\frac{R_\mathrm{r}^2}{s^3}}{\frac{\omega_\mathrm{s}}{p}\left[\left(R_\mathrm{s}+\frac{R_\mathrm{r}}{s}\right)^2 + \left(\omega_\mathrm{s}L_{\mathrm{s}\sigma} + \omega_\mathrm{s}L_{\mathrm{r}\sigma}\right)^2\right]}\left(R_\mathrm{s}+\frac{R_\mathrm{r}}{s}\right) \tag{A.52}$$

The slip value of the maximum cage torque is found by solving the zero crossings of Eq. (A.52).

$$\frac{\mathrm{d}}{\mathrm{d}s} T_{\mathrm{c}}(s) = 0$$

$$\Leftrightarrow \frac{-3U_{\mathrm{ph}}^2 \frac{R_{\mathrm{r}}}{s^2}}{\frac{\omega_{\mathrm{s}}}{p}\left[\left(R_{\mathrm{s}} + \frac{R_{\mathrm{r}}}{s}\right)^2 + \left(\omega_{\mathrm{s}} L_{\mathrm{s}\sigma} + \omega_{\mathrm{s}} L_{\mathrm{r}\sigma}\right)^2\right]} + \frac{6U_{\mathrm{ph}}^2 \frac{R_{\mathrm{r}}^2}{s^3}}{\frac{\omega_{\mathrm{s}}}{p}\left[\left(R_{\mathrm{s}} + \frac{R_{\mathrm{r}}}{s}\right)^2 + \left(\omega_{\mathrm{s}} L_{\mathrm{s}\sigma} + \omega_{\mathrm{s}} L_{\mathrm{r}\sigma}\right)^2\right]}\left(R_{\mathrm{s}} + \frac{R_{\mathrm{r}}}{s}\right) = 0$$

$$\Leftrightarrow \frac{-\frac{1}{s^2} + 2\frac{R_{\mathrm{r}}}{s^3}\left(R_{\mathrm{s}} + \frac{R_{\mathrm{r}}}{s}\right)}{\left(R_{\mathrm{s}} + \frac{R_{\mathrm{r}}}{s}\right)^2 + \left(\omega_{\mathrm{s}} L_{\mathrm{s}\sigma} + \omega_{\mathrm{s}} L_{\mathrm{r}\sigma}\right)^2} = 0 \Leftrightarrow \frac{\frac{1}{s^2}\left(-1 + 2\frac{R_{\mathrm{r}} R_{\mathrm{s}}}{s} + 2\frac{R_{\mathrm{r}}^2}{s^2}\right)}{\left(R_{\mathrm{s}} + \frac{R_{\mathrm{r}}}{s}\right)^2 + \left(\omega_{\mathrm{s}} L_{\mathrm{s}\sigma} + \omega_{\mathrm{s}} L_{\mathrm{r}\sigma}\right)^2} = 0$$

$$\Leftrightarrow s_{\mathrm{pull-out}} = R_{\mathrm{r}}\left(R_{\mathrm{s}} \pm \sqrt{2 + R_{\mathrm{s}}^2}\right) \tag{A.53}$$

According to Engelmann & Middendorf (1995)

$$s_{\mathrm{pull-out}} = \pm \frac{R_{\mathrm{r}}}{R_{\mathrm{s}}^2 + \left(\omega_{\mathrm{s}} L_{\mathrm{s}\sigma} + \omega_{\mathrm{s}} L_{\mathrm{r}\sigma}\right)^2} \tag{A.54}$$

APPENDIX B

B.1 Terminal voltage in island operation

The direct and the quadrature-axis parts of the terminal voltage are:

$$\begin{aligned} U_\mathrm{d} &= I_\mathrm{q}\omega_\mathrm{s}L_\mathrm{q} - I_\mathrm{d}R_\mathrm{s} = U_\mathrm{s}\sin\delta \\ U_\mathrm{q} &= E_\mathrm{PM} - I_\mathrm{d}\omega_\mathrm{s}L_\mathrm{d} - I_\mathrm{q}R_\mathrm{s} = U_\mathrm{s}\cos\delta \end{aligned} \tag{B.1}$$

The current components are

$$\begin{aligned} I_\mathrm{d} &= I_\mathrm{s}\sin(\delta+\varphi) \\ I_\mathrm{q} &= I_\mathrm{s}\cos(\delta+\varphi) \end{aligned} \tag{B.2}$$

The line voltage depends on the load characteristics:

$$\underline{U}_\mathrm{s} = \underline{Z}\underline{I}_\mathrm{s},\ \underline{Z} = Z\angle\varphi\ . \tag{B.3}$$

By substituting Eq. (B.1) into Eq. (B.2):

$$U_\mathrm{d} = -U_\mathrm{s}\sin\delta = \omega_\mathrm{s}L_\mathrm{q}I_\mathrm{s}\cos(\delta+\varphi) - R_\mathrm{s}I_\mathrm{s}\sin(\delta+\varphi)\ . \tag{B.4}$$

By substituting Eq. (B.3) into Eq.(B.4) and converting the sums of the sine and cosine functions

$$\begin{aligned} ZI_\mathrm{s}\sin\delta &= \omega_\mathrm{s}L_\mathrm{q}I_\mathrm{s}(\cos\delta\cos\varphi - \sin\delta\sin\varphi) - R_\mathrm{s}I_\mathrm{s}(\sin\delta\cos\varphi + \cos\delta\sin\varphi) \\ Z\sin\delta &= \omega_\mathrm{s}L_\mathrm{q}(\cos\delta\cos\varphi - \sin\delta\sin\varphi) - R_\mathrm{s}(\sin\delta\cos\varphi + \cos\delta\sin\varphi) \\ Z\tan\delta &= \omega_\mathrm{s}L_\mathrm{q}\cos\varphi - \omega_\mathrm{s}L_\mathrm{q}\tan\delta\sin\varphi - R_\mathrm{s}\tan\delta\cos\varphi - R_\mathrm{s}\sin\varphi \end{aligned} \tag{B.5}$$

The load angle can be calculated:

$$\begin{aligned} \tan\delta(Z + \omega L_\mathrm{q}\sin\varphi + R_\mathrm{s}\cos\varphi) &= \omega_\mathrm{s}L_\mathrm{q}\cos\varphi - R_\mathrm{s}\sin\varphi \\ \delta &= \tan^{-1}\left(\frac{\omega_\mathrm{s}L_\mathrm{q}\cos\varphi - R_\mathrm{s}\sin\varphi}{Z + \omega_\mathrm{s}L_\mathrm{q}\sin\varphi + R_\mathrm{s}\cos\varphi}\right) \end{aligned} \tag{B.6}$$

When the load power factor is known the load current and the terminal voltage can be calculated.

$$\tan\delta(Z + \omega_\mathrm{s}L_\mathrm{q}\sin\varphi + R_\mathrm{s}\cos\varphi) = \omega_\mathrm{s}L_\mathrm{q}\cos\varphi - R_\mathrm{s}\sin\varphi \tag{B.7}$$

$$\tan\delta = \frac{\omega_s L_q \cos\varphi - R_s \sin\varphi}{Z + \omega_s L_q \sin\varphi + R_s \cos\varphi} = \frac{\sin\delta}{\cos\delta} \Rightarrow$$
$$\cos\delta = \frac{Z\sin\delta + \omega_s L_q \sin\varphi\sin\delta + R_s \cos\varphi\sin\delta}{\omega_s L_q \cos\varphi - R_s \sin\varphi} \tag{B.8}$$

Eq. (B.8) is substituted into Eq. (B.1)

$$U_q = U_s \cos\delta = E_{PM} - X_d I \sin(\delta+\varphi) - R_s I \cos(\delta+\varphi) \tag{B.9}$$

$$U_s \frac{Z\sin\delta + \omega_s L_q \sin\varphi\sin\delta + R_s \cos\varphi\sin\delta}{\omega_s L_q \cos\varphi - R_s \sin\varphi}$$
$$= E_{PM} - X_d \frac{U_s}{Z}\sin(\delta+\varphi) - R_s \frac{U_s}{Z}\cos(\delta+\varphi)$$
$$U_s\left(\frac{Z\sin\delta + \omega_s L_q \sin\varphi\sin\delta + R_s \cos\varphi\sin\delta}{\omega_s L_q \cos\varphi - R_s \sin\varphi} + \frac{X_d}{Z}\sin(\delta+\varphi) + \frac{R_s}{Z}\cos(\delta+\varphi)\right) = E_{PM}$$
$$U_s = \frac{E_{PM}}{\frac{Z\sin\delta + \omega_s L_q \sin\varphi\sin\delta + R_s \cos\varphi\sin\delta}{\omega_s L_q \cos\varphi - R_s \sin\varphi} + \frac{X_d}{Z}\sin(\delta+\varphi) + \frac{R_s}{Z}\cos(\delta+\varphi)}$$
$$U_s = \frac{E_{PM} Z}{\frac{Z^2\sin\delta + Z\omega_s L_q \sin\varphi\sin\delta + ZR_s \cos\varphi\sin\delta}{\omega_s L_q \cos\varphi - R_s \sin\varphi} + X_d \sin(\delta+\varphi) + R_s \cos(\delta+\varphi)}$$
$$U_s = \frac{E_{PM} Z}{\frac{Z^2\sin\delta + Z(\omega_s L_q \sin\varphi\sin\delta + R_s \cos\varphi\sin\delta)}{\omega_s L_q \cos\varphi - R_s \sin\varphi} + X_d \sin(\delta+\varphi) + R_s \cos(\delta+\varphi)} \tag{B.10}$$

The reactance is defined by the product of the angular frequency and inductance.

$$X = \omega_s L \tag{B.11}$$

By substituting Eq. (B.11) into Eq. (B.10)

$$U_s = \frac{E_{PM} Z}{\frac{Z^2\sin\delta + Z\sin\delta(\omega_s L_q \sin\varphi + R_s \cos\varphi)}{\omega_s L_q \cos\varphi - R_s \sin\varphi} + \omega_s L_d \sin(\delta+\varphi) + R_s \cos(\delta+\varphi)} \tag{B.12}$$

The corresponding load current is

$$\underline{I} = \frac{\underline{U}_\mathrm{s}}{\underline{Z}} \quad .$$

(B.13)

$$I = \frac{E_\mathrm{PM}}{\dfrac{Z^2 \sin\delta + Z\sin\delta\left(\omega_\mathrm{s} L_\mathrm{q} \sin\varphi + R_\mathrm{s}\cos\varphi\right)}{\omega_\mathrm{s} L_\mathrm{q}\cos\varphi - R_\mathrm{s}\sin\varphi} + \omega_\mathrm{s} L_\mathrm{d}\sin(\delta+\varphi) + R_\mathrm{s}\cos(\delta+\varphi)}$$

(B.14)

B.2 Power equation in island operation

The power of the isolated generator is defined as

$$P = 3U_\mathrm{s} I\cos\varphi = \frac{3U_\mathrm{s}^2\cos\varphi}{Z}$$

(B.15)

By substituting the terminal voltage in Eq. (B.10) into Eq. (B.15), the power of the generator becomes

$$P = \frac{3\left(\dfrac{E_\mathrm{PM} Z}{\dfrac{Z^2\sin\delta + Z\sin\delta\left(\omega_\mathrm{s} L_\mathrm{q}\sin\varphi + R_\mathrm{s}\cos\varphi\right)}{\omega_\mathrm{s} L_\mathrm{q}\cos\varphi - R_\mathrm{s}\sin\varphi} + \omega_\mathrm{s} L_\mathrm{d}\sin(\delta+\varphi) + R_\mathrm{s}\cos(\delta+\varphi)}\right)^2\cos\varphi}{Z}$$

$$P = \frac{3E_\mathrm{PM}^2 Z\cos\varphi}{\left(\dfrac{Z^2\sin\delta + Z\sin\delta\left(\omega_\mathrm{s} L_\mathrm{q}\sin\varphi + R_\mathrm{s}\cos\varphi\right)}{\omega_\mathrm{s} L_\mathrm{q}\cos\varphi - R_\mathrm{s}\sin\varphi} + \omega_\mathrm{s} L_\mathrm{d}\sin(\delta+\varphi) + R_\mathrm{s}\cos(\delta+\varphi)\right)^2}$$

(B.16)

B.3 Current components of a permanent magnet generator in rigid network

Voltage equation for permanent magnet synchronous generator are

$$\begin{aligned} U_\mathrm{d} &= I_\mathrm{q}\omega_\mathrm{s} L_\mathrm{q} - I_\mathrm{d} R_\mathrm{sd} = U_\mathrm{s}\sin\delta \\ U_\mathrm{q} &= E_\mathrm{PM} - I_\mathrm{d}\omega_\mathrm{s} L_\mathrm{d} - I_\mathrm{q} R_\mathrm{s} = U_\mathrm{s}\cos\delta \end{aligned}$$

(B.17)

Solving current components gives

$$\begin{cases} I_{\mathrm{d}} = \dfrac{E_{\mathrm{PM}} - U_{\mathrm{s}}\cos\delta - R_{\mathrm{s}} I_{\mathrm{q}}}{\omega_{\mathrm{s}} L_{\mathrm{d}}} \\ I_{\mathrm{q}} = \dfrac{U_{\mathrm{s}}\sin\delta + R_{\mathrm{s}} I_{\mathrm{d}}}{\omega_{\mathrm{s}} L_{\mathrm{q}}} \end{cases} \tag{B.18}$$

By substituting q-axis current into d-axis current in Eq. (B.18), the d-axis current may be solved.

$$\begin{aligned} I_{\mathrm{d}} &= \frac{E_{\mathrm{PM}} - U_{\mathrm{s}}\cos\delta - R_{\mathrm{s}}\dfrac{U_{\mathrm{s}}\sin\delta + R_{\mathrm{s}} I_{\mathrm{d}}}{\omega_{\mathrm{s}} L_{\mathrm{q}}}}{\omega_{\mathrm{s}} L_{\mathrm{d}}} \\ I_{\mathrm{d}} &= \frac{E_{\mathrm{PM}} - U_{\mathrm{s}}\cos\delta}{\omega_{\mathrm{s}} L_{\mathrm{d}}} - \frac{R_{\mathrm{s}} U_{\mathrm{s}}\sin\delta}{\omega_{\mathrm{s}} L_{\mathrm{d}}\omega_{\mathrm{s}} L_{\mathrm{q}}} - \frac{R_{\mathrm{s}}^2 I_{\mathrm{d}}}{\omega_{\mathrm{s}} L_{\mathrm{d}}\omega_{\mathrm{s}} L_{\mathrm{q}}} \\ I_{\mathrm{d}}\left(1 + \frac{R_{\mathrm{s}}^2}{\omega_{\mathrm{s}} L_{\mathrm{d}}\omega_{\mathrm{s}} L_{\mathrm{q}}}\right) &= \frac{E_{\mathrm{PM}} - U_{\mathrm{s}}\cos\delta}{\omega_{\mathrm{s}} L_{\mathrm{d}}} - \frac{R_{\mathrm{s}} U_{\mathrm{s}}\sin\delta}{\omega_{\mathrm{s}} L_{\mathrm{d}}\omega_{\mathrm{s}} L_{\mathrm{q}}} \\ I_{\mathrm{d}} &= \frac{\dfrac{E_{\mathrm{PM}} - U_{\mathrm{s}}\cos\delta}{\omega_{\mathrm{s}} L_{\mathrm{d}}} - \dfrac{R_{\mathrm{s}} U_{\mathrm{s}}\sin\delta}{\omega_{\mathrm{s}} L_{\mathrm{d}}\omega_{\mathrm{s}} L_{\mathrm{q}}}}{1 + \dfrac{R_{\mathrm{s}}^2}{\omega_{\mathrm{s}} L_{\mathrm{d}}\omega_{\mathrm{s}} L_{\mathrm{q}}}} = \frac{\dfrac{E_{\mathrm{PM}} - U_{\mathrm{s}}\cos\delta}{\omega_{\mathrm{s}} L_{\mathrm{d}}} - \dfrac{R_{\mathrm{s}} U_{\mathrm{s}}\sin\delta}{\omega_{\mathrm{s}} L_{\mathrm{d}}\omega_{\mathrm{s}} L_{\mathrm{q}}}}{\dfrac{\omega_{\mathrm{s}} L_{\mathrm{d}}\omega_{\mathrm{s}} L_{\mathrm{q}} + R_{\mathrm{s}}^2}{\omega_{\mathrm{s}} L_{\mathrm{d}}\omega_{\mathrm{s}} L_{\mathrm{q}}}} \\ I_{\mathrm{d}} &= \frac{\omega_{\mathrm{s}} L_{\mathrm{d}}\omega_{\mathrm{s}} L_{\mathrm{q}}\dfrac{E_{\mathrm{PM}} - U_{\mathrm{s}}\cos\delta}{\omega_{\mathrm{s}} L_{\mathrm{d}}} - \omega_{\mathrm{s}} L_{\mathrm{d}}\omega_{\mathrm{s}} L_{\mathrm{q}}\dfrac{R_{\mathrm{s}} U_{\mathrm{s}}\sin\delta}{\omega_{\mathrm{s}} L_{\mathrm{d}}\omega_{\mathrm{s}} L_{\mathrm{q}}}}{\omega_{\mathrm{s}} L_{\mathrm{d}}\omega_{\mathrm{s}} L_{\mathrm{q}} + R_{\mathrm{s}}^2} \\ I_{\mathrm{d}} &= \frac{\omega_{\mathrm{s}} L_{\mathrm{q}}\left(E_{\mathrm{PM}} - U_{\mathrm{s}}\cos\delta\right) - R_{\mathrm{s}} U_{\mathrm{s}}\sin\delta}{\omega_{\mathrm{s}} L_{\mathrm{d}}\omega_{\mathrm{s}} L_{\mathrm{q}} + R_{\mathrm{s}}^2} \end{aligned} \tag{B.19}$$

Now we have to substitute the solved d-axis current into q-axis equation.

$$
\begin{cases} I_{\mathrm{d}} = \dfrac{\omega_{\mathrm{s}} L_{\mathrm{q}} \left(E_{\mathrm{PM}} - U_{\mathrm{s}} \cos\delta \right) - R_{\mathrm{s}} U_{\mathrm{s}} \sin\delta}{\omega_{\mathrm{s}} L_{\mathrm{d}} \omega_{\mathrm{s}} L_{\mathrm{q}} + R_{\mathrm{s}}^2} \\ I_{\mathrm{q}} = \dfrac{R_{\mathrm{s}} I_{\mathrm{d}} + U_{\mathrm{s}} \sin\delta}{\omega_{\mathrm{s}} L_{\mathrm{q}}} \end{cases}
$$

$$
I_{\mathrm{q}} = \frac{R_{\mathrm{s}} \dfrac{\omega_{\mathrm{s}} L_{\mathrm{q}} \left(E_{\mathrm{PM}} - U_{\mathrm{s}} \cos\delta \right) - R_{\mathrm{s}} U_{\mathrm{s}} \sin\delta}{\omega_{\mathrm{s}} L_{\mathrm{d}} \omega_{\mathrm{s}} L_{\mathrm{q}} + R_{\mathrm{s}}^2} + U_{\mathrm{s}} \sin\delta}{\omega_{\mathrm{s}} L_{\mathrm{q}}}
$$

$$
I_{\mathrm{q}} = \frac{\dfrac{R_{\mathrm{s}} \omega_{\mathrm{s}} L_{\mathrm{q}} \left(E_{\mathrm{PM}} - U_{\mathrm{s}} \cos\delta \right) - R_{\mathrm{s}}^2 U_{\mathrm{s}} \sin\delta + \left(\omega_{\mathrm{s}} L_{\mathrm{d}} \omega_{\mathrm{s}} L_{\mathrm{q}} + R_{\mathrm{s}}^2 \right) U_{\mathrm{s}} \sin\delta}{\omega_{\mathrm{s}} L_{\mathrm{d}} \omega_{\mathrm{s}} L_{\mathrm{q}} + R_{\mathrm{s}}^2}}{\omega_{\mathrm{s}} L_{\mathrm{q}}}
$$

$$
I_{\mathrm{q}} = \frac{\dfrac{R_{\mathrm{s}} \omega_{\mathrm{s}} L_{\mathrm{q}} \left(E_{\mathrm{PM}} - U_{\mathrm{s}} \cos\delta \right) + \omega_{\mathrm{s}} L_{\mathrm{d}} \omega_{\mathrm{s}} L_{\mathrm{q}} U_{\mathrm{s}} \sin\delta}{\omega_{\mathrm{s}} L_{\mathrm{d}} \omega_{\mathrm{s}} L_{\mathrm{q}} + R_{\mathrm{s}}^2}}{\omega_{\mathrm{s}} L_{\mathrm{q}}} \tag{B.20}
$$

$$
I_{\mathrm{q}} = \frac{R_{\mathrm{s}} \left(E_{\mathrm{PM}} - U_{\mathrm{s}} \cos\delta \right) + \omega_{\mathrm{s}} L_{\mathrm{d}} U_{\mathrm{s}} \sin\delta}{\omega_{\mathrm{s}} L_{\mathrm{d}} \omega_{\mathrm{s}} L_{\mathrm{q}} + R_{\mathrm{s}}^2}
$$

$$
I_{\mathrm{q}} = \frac{R_{\mathrm{s}} \left(E_{\mathrm{PM}} - U_{\mathrm{s}} \cos\delta \right) + \omega_{\mathrm{s}} L_{\mathrm{d}} U_{\mathrm{s}} \sin\delta}{R_{\mathrm{s}}^2 + \omega_{\mathrm{s}}^2 L_{\mathrm{d}} L_{\mathrm{q}}}
$$

Now we have solved current components in dq-coordinates

$$
\begin{cases} I_{\mathrm{d}} = \dfrac{\omega_{\mathrm{s}} L_{\mathrm{q}} \left(E_{\mathrm{PM}} - U_{\mathrm{s}} \cos\delta \right) - R_{\mathrm{s}} U_{\mathrm{s}} \sin\delta}{\omega_{\mathrm{s}} L_{\mathrm{d}} \omega_{\mathrm{s}} L_{\mathrm{q}} + R_{\mathrm{s}}^2} \\ I_{\mathrm{q}} = \dfrac{R_{\mathrm{s}} \left(E_{\mathrm{PM}} - U_{\mathrm{s}} \cos\delta \right) + \omega_{\mathrm{s}} L_{\mathrm{d}} U_{\mathrm{s}} \sin\delta}{\omega_{\mathrm{s}} L_{\mathrm{d}} \omega_{\mathrm{s}} L_{\mathrm{q}} + R_{\mathrm{s}}^2} \end{cases} \tag{B.21}
$$

APPENDIX C

C.1 Parameters of the permanent magnet synchronous generators

		AFPMSG 1		AFPMSG 2	
Parameter	**Symbol**	**Value**	**pu value**	**Value**	**pu value**
Nominal power	P_n	5200 W		15900 W	
Apparent power	S_n	5600 VA	1	18300 VA	1
Nominal voltage	U_n	400 V		660 V	
Nominal phase voltage	U_{ph}	230 V	1	380 V	1
Nominal current	I_n	8 A	1	16 A	1
Nominal power factor	$\cos\varphi$	0.93	0.93	0.87	0.87
Electromotive force	E	410 V		567 V	
Phase electromotive force	E_{ph}	237 V	1.03	327 V	0.86
Stator resistance	R_s	1.28 Ω	0.044	1.2 Ω	0.051
Direct-axis damper winding resistance	R_D	3.59 Ω	0.124	2.59 Ω	0.109
Quadrature-axis damper winding resistance	R_Q	4.23 Ω	0.147	2.71 Ω	0.114
Number of pole pairs	p	2	2	8	8
Direct and quadrature-axis magnetizing inductance	$L_{md,q}$	23.4 mH	0.255	23.9 mH	0.316
Stator leakage inductance	$L_{s\sigma}$	24.3 mH	0.264	15.9 mH	0.210
Direct-axis damper winding leakage inductance	$L_{D\sigma}$	2.09 mH	0.023	4.88 mH	0.065
Quadrature-axis damper winding leakage inductance	$L_{Q\sigma}$	6.82 mH	0.074	6.87 mH	0.091
Damper winding direct-axis open-circuit time constant	T''_{d0}	3.90 ms		5.99 ms	
Damper winding direct-axis short-circuit time constant	T''_d	7.10 ms		11.94 ms	
Damper winding quadrature-axis open-circuit time constant	T''_{q0}	4.43 ms		4.20 ms	
Damper winding quadrature-axis short-circuit time constant	T''_q	7.14 ms		7.87ms	
Nominal load angle	δ	36 °	36 °	18 °	18 °
Nominal torque	T_n	33 Nm	0.929	400 Nm	0.858
Frequency	f	50 Hz	1	50 Hz	1
Rotation speed	n	1500 rpm	1	375 rpm	1
Moment of rotor inertia	J_r	0.026 kgm^2	T_J =36.0	5.47 kgm^2	T_J=144.8
Total moment of system inertia	J_{tot}	0.3334 kgm^2	T_J =461.0	510kgm^2	T_J=13515
Stator lamination outer radius	$R_{s,out}$	110 mm		230 mm	
Stator lamination inner radius	$R_{s,in}$	75 mm		170 mm	
Air gap length	δ_{ag}	3.5 mm		3 mm	
Rotor PM material		Neorem 495a		Neorem 495a	
Damper construction		Jig + 2x1 mm plates Aluminium			Jig + 1 mm plate Aluminium

C.2 Auxiliary electrical machines used in the laboratory tests

Table C.1. Main parameters of the induction motors acting as an inductive load for AFPMSG1 in a microgrid.

Load	U_n (V)	I_n (A)	P_n (W)	n (rpm)
Induction motor, IM1	380-440	4,7	2200	3000
Induction motor, IM2	380-440	2	1150	3000

Table C.2 Parameters of the induction motor IM3 and the synchronous generator SG1 used in the applied voltage test with a locked rotor for AFPMSG1 and AFPMSG2.

SG1		
S_n	125	kVA
cosφ	0.8	ind
P_n	100	kW
U_n	400	V
I_n	181	A
I_m	7	A
U_m	320	V
n	1500	rpm
η	0.89	
f	50	Hz

IM3		
P_n	100	kW
U_n	380	V
I_n	103	A
n	1475	rpm
f	50	Hz
p	2	

APPENDIX D

D.1 Current and voltage space vectors in a two-axis simulation model

The phase currents i_a, i_b and i_c of the stator form a space vector defined as

$$\boldsymbol{i}_s = i_a e^{j0} + i_b e^{j\frac{2\pi}{3}} + i_c e^{j\frac{4\pi}{3}} \tag{D.1}$$

The length of the space vector is 1.5 times the peak value of the sinusoidal phase current. In the case of synchronous machine the space vector current is normally reduced by the factor 2/3 to use directly the parameters of the equivalent circuit model of the electrical machine. The voltage space vector $\boldsymbol{u}_s$ and the flux linkage space vector $\boldsymbol{\psi}_s$ are defined in the same way. Now, the reduced current, voltage, and flux linkage space vectors are written as

$$\begin{aligned}
\boldsymbol{i}_s &= \frac{2}{3}\left(i_a e^{j0} + i_b e^{j\frac{2\pi}{3}} + i_c e^{j\frac{4\pi}{3}} \right) \\
\boldsymbol{u}_s &= \frac{2}{3}\left(u_a e^{j0} + u_b e^{j\frac{2\pi}{3}} + u_c e^{j\frac{4\pi}{3}} \right) \\
\boldsymbol{\psi}_s &= \frac{2}{3}\left(\psi_a e^{j0} + \psi_b e^{j\frac{2\pi}{3}} + \psi_c e^{j\frac{4\pi}{3}} \right)
\end{aligned} \tag{D.2}$$

Knowing that

$$e^{j\theta} = \cos\theta + j\sin\theta, \tag{D.3}$$

the three phase current components can be presented in a stator-oriented two-axis form with the components i_x and i_y.

$$\begin{aligned}
&\boldsymbol{i}_s = \frac{2}{3}\left(i_a e^{j0} + i_b e^{j\frac{2\pi}{3}} + i_c e^{j\frac{4\pi}{3}} \right) = \\
&\frac{2}{3} i_a + i_b\left(\cos\frac{2\pi}{3} + j\sin\frac{2\pi}{3} \right) + i_c\left(\cos\frac{4\pi}{3} + j\sin\frac{4\pi}{3} \right) \\
&i_x = \mathrm{Re}(\boldsymbol{i}_s), i_y = \mathrm{Im}(\boldsymbol{i}_s) \\
&i_x = \frac{2}{3}\left(i_a + i_b\cos\frac{2\pi}{3} + i_c\cos\frac{4\pi}{3} \right) = \frac{2}{3} i_a - \frac{1}{3}(i_b + i_c) \\
&i_y = \frac{2}{3}\left(i_b\sin\frac{2\pi}{3} + i_c\sin\frac{4\pi}{3} \right) = \frac{1}{\sqrt{3}}(i_b - i_c)
\end{aligned} \tag{D.4}$$

In a rotor-oriented coordinate system, the transformation from xy-coordinates to dq-coordinates produces the current components i_d and i_q.

$$i_s^{dq} = i_d + \mathrm{j}i_q = \left(i_x + \mathrm{j}i_y\right)e^{-\mathrm{j}\theta_r}$$

$$\begin{aligned} i_d &= \mathrm{Re}\left(i_s^{dq}\right), i_q = \mathrm{Im}\left(i_s^{dq}\right) \\ i_d &= i_x \cos\theta_r + i_y \sin\theta_r \\ i_q &= -i_x \sin\theta_r + i_y \cos\theta_r \end{aligned} \qquad \text{(D.5)}$$

The voltage and flux linkage components u_d, u_q, ψ_d, and ψ_q are defined in the same way.

APPENDIX E

E.1 Analytical calculation of the damper winding resistance for AFPMSG1

The length of the end ring of the installation jig is

$$l_{\mathrm{er,in}} = \frac{2\pi\left(R_{\mathrm{PM,in}} - \frac{w_{\mathrm{er,in}}}{2}\right)}{2p} = \frac{\pi\left(R_{\mathrm{PM,in}} - \frac{w_{\mathrm{er,in}}}{2}\right)}{p}$$

$$= \frac{\pi\left(0.075\mathrm{m} - \frac{0.04\mathrm{m}}{2}\right)}{2} = 0.086\mathrm{m}$$

$$l_{\mathrm{er,out}} = \frac{2\pi\left(R_{\mathrm{PM,out}} + \frac{w_{\mathrm{er,out}}}{2}\right)}{2p} = \frac{\pi\left(R_{\mathrm{PM,out}} + \frac{w_{\mathrm{er,out}}}{2}\right)}{p} \quad \text{(E.1)}$$

$$= \frac{\pi\left(0.11\mathrm{m} + \frac{0.025\mathrm{m}}{2}\right)}{2} = 0.192\mathrm{m}$$

Rotor damper bar resistance is

$$R_{\mathrm{r1}} = R_{\mathrm{er,in}} + R_{\mathrm{er,out}} + R_{\mathrm{bar}} = \frac{l_{\mathrm{er,in}}}{\sigma_{\mathrm{Al}} A_{\mathrm{er,in}}} + \frac{l_{\mathrm{er,out}}}{\sigma_{\mathrm{Al}} A_{\mathrm{er,out}}} + \frac{l_{\mathrm{bar}}}{\sigma_{\mathrm{Al}} A_{\mathrm{bar}}}$$

$$R_{\mathrm{r1}} = \frac{1}{\sigma_{\mathrm{Al}}}\left(\frac{l_{\mathrm{er,in}}}{w_{\mathrm{er,in}} h_{\mathrm{er}}} + \frac{l_{\mathrm{er,out}}}{w_{\mathrm{er,out}} h_{\mathrm{er}}} + \frac{l_{\mathrm{bar}}}{w_{\mathrm{bar}} h_{\mathrm{bar}}}\right)$$

$$R_{\mathrm{r1}} = \frac{1}{\frac{1}{2.65\cdot 10^{-8}\,\Omega\mathrm{m}}}\left(\frac{0.086\mathrm{m}}{0.04\mathrm{m}\cdot 0.006\mathrm{m}} + \frac{0.192\mathrm{m}}{0.025\mathrm{m}\cdot 0.006\mathrm{m}} + \frac{0.042\mathrm{m}}{0.011\mathrm{m}\cdot 0.006\mathrm{m}}\right) \quad \text{(E.2)}$$

$$R_{\mathrm{r1}} = 6.04\cdot 10^{-5}\,\Omega$$

Skewing of the damper bars is one slot pitch

$$k_{\mathrm{sqvr}} = \frac{\sin\left(\frac{\gamma}{\tau_{\mathrm{p}}}\cdot\frac{\pi}{2}\right)}{\frac{\gamma}{\tau_{\mathrm{p}}}\cdot\frac{\pi}{2}} = \frac{\sin\left(\frac{\tau_{\mathrm{u}}}{\tau_{\mathrm{p}}}\cdot\frac{\pi}{2}\right)}{\frac{\tau_{\mathrm{u}}}{\tau_{\mathrm{p}}}\cdot\frac{\pi}{2}} = \frac{\sin\left(\frac{1}{6}\cdot\frac{\pi}{2}\right)}{\frac{1}{6}\cdot\frac{\pi}{2}} = \frac{\sin\left(\frac{\pi}{12}\right)}{\frac{\pi}{12}} = 0.9886 \quad \text{(E.3)}$$

Installation jig resistance referred to stator is

$$R_{r1}^{'} = \frac{4m_s\left(N_s k_{ws}\right)^2}{Q_r k_{sqir}} R_r = \frac{4 \cdot 3 \cdot \left(0.933 \cdot 512\right)^2}{4 \cdot 0.9886} 6.04 \cdot 10^{-5} = 41.83\Omega \quad \text{(E.4)}$$

Resistance of the conducting surface plate is estimated by dividing the surface plate into infinite amount of bars.

$$\begin{aligned} R_{r2}^{'} &= \frac{8pm_s l_{bar}\left(N_s k_{ws}\right)^2}{\sigma_{Al} h_{bar} \pi (R_{PM,out} + R_{PM,in})} \\ R_{r2}^{'} &= \frac{8 \cdot 2 \cdot 3 \cdot 0.042 \cdot (0.933 \cdot 512)^2}{\frac{1}{2.56 \cdot 10^{-8}} \cdot 0.001 \cdot \pi (0.11 + 0.075)} = 20.26\Omega \end{aligned} \quad \text{(E.5)}$$

The damper winding consists of parallel connection of two surface plates and one installation jig.

$$R_r^{'} = \frac{R_{r1}^{'} R_{r2}^{'}}{2R_{r1}^{'} + R_{r2}^{'}} = \frac{41.83 \cdot 20.26}{2 \cdot 41.83 + 20.26} = 8.15\Omega \quad \text{(E.6)}$$

The damper winding resistance may be divided equally into d-axis and q-axis components

$$R_D = R_Q = \frac{R_r^{'}}{\sqrt{2}} = \frac{8.15\Omega}{\sqrt{2}} = 5.77\Omega \quad \text{(E.7)}$$

APPENDIX F

F.1 Asynchronous cage torque comparison

Three methods to calculate asynchronous cage torque is presented. Menzies (1972) and Honsinger (1980) have analytical equations to calculate the asynchronous cage torque. Simulation model is using two-axis space vectors. Fig. F.1 shows the comparison of asynchronous cage torque curves.

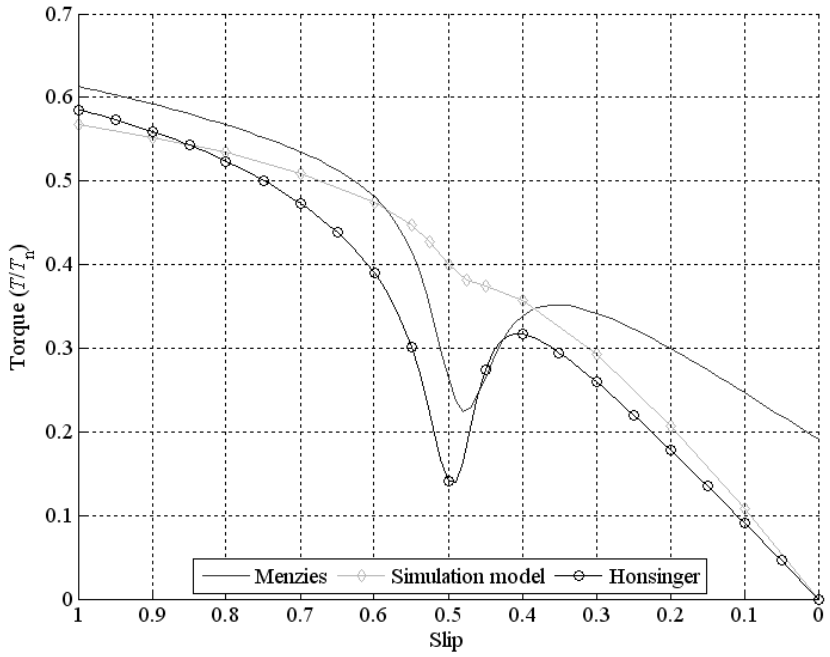

Fig. F.1 Comparison of asynchronous cage torques for PMSG with asymmetric damper windings. $R_{D,pu} = 0.15$, $R_{Q,pu} = 3\ R_{D,pu}$, $L_{D\sigma,pu} = L_{Q\sigma,pu} = 0.05$, $R_{s,pu} = 0.05$, $L_{d,pu} = L_{q,pu} = 0.5$

ACTA UNIVERSITATIS LAPPEENRANTAENSIS

236. DUFVA, KARI. Development of finite elements for large deformation analysis of multibody systems. 2006. Diss.

237. RITVANEN, JOUNI. Experimental insights into deformation dynamics and intermittency in rapid granular shear flows. 2006. Diss.

238. KERKKÄNEN, KIMMO. Dynamic analysis of belt-drives using the absolute nodal coordinate formulation. 2006. Diss.

239. ELFVENGREN, KALLE. Group support system for managing the front end of innovation: case applications in business-to-business enterprises. 2006. Diss.

240. IKONEN, LEENA. Distance transforms on gray-level surfaces. 2006. Diss.

241. TENHUNEN, JARKKO. Johdon laskentatoimi kärkiyritysverkostoissa. Soveltamismahdollisuudet ja yritysten tarpeet. 2006. Diss.

242. KEMPPINEN, JUKKA. Digitaaliongelma. Kirjoitus oikeudesta ja ympäristöstä. 2006.

243. PÖLLÄNEN, KATI. Monitoring of crystallization processes by using infrared spectroscopy and multivariate methods. 2006. Diss.

244. AARNIO, TEIJA. Challenges in packaging waste management: A case study in the fast food industry. 2006. Diss.

245. PANAPANAAN, VIRGILIO M. Exploration of the social dimension of corporate responsibility in a welfare state. 2006. Diss.

246. HEINOLA, JANNE-MATTI. Relative permittivity and loss tangent measurements of PWB materials using ring resonator structures. 2006. Diss.

247. SALMELA, NINA. Washing and dewatering of different starches in pressure filters. 2006. Diss.

248. SISSONEN, HELI. Information sharing in R&D collaboration – context-dependency and means of governance. 2006. Diss.

249. PURANEN, JUSSI. Induction motor versus permanent magnet synchronous motor in motion control applications: a comparative study. 2006. Diss.

250. PERÄLÄ, KARI. Kassanhallintakäytännöt Suomen kunnissa. 2006. Diss.

251. POUTIAINEN, ILKKA. A modified structural stress method for fatigue assessment of welded structures. 2006. Diss.

252. LIHAVAINEN, VELI-MATTI. A novel approach for assessing the fatigue strength of ultrasonic impact treated welded structures. 2006. Diss.

253. TANG, JIN. Computational analysis and optimization of real gas flow in small centrifugal compressors. 2006. Diss.

254. VEHVILÄINEN, JUHA. Procurement in project implementation. 2006. Diss.

255. MIROLA, TUULI. Impacts of the European integration and the European Union membership on Finnish export industries – Perceptions of export business managers. 2006. Diss.

256. RAUMA, KIMMO. FPGA-based control design for power electronic applications. 2006. Diss.

257. HIRVONEN, MARKUS. On the analysis and control of a linear synchronous servomotor with a flexible load. 2006. Diss.

258. LIU, JUNHONG. On the differential evolution algorithm and its application to training radial basis function networks. 2006. Diss.

259. LAITINEN, RISTO. Development of LC-MS and extraction methods for the analyses of AKD, ASA, and rosin sizes in paper products. 2006. Diss.

260. KUISMA, PETRI. Seinärakenteen infrapunakontrastin pienentäminen käyttäen ilmajäähdytystä ja säteilysuojausta. 2007. Diss.

261. ELLONEN, HANNA-KAISA. Exploring the strategic impact of technological change – studies on the role of Internet in magazine publishing. 2007. Diss.

262. SOININEN, AURA. Patents in the information and communications technology sector – development trends, problem areas and pressures for change. 2007. Diss.

263. MATTILA, MERITA. Value processing in organizations – individual perceptions in three case companies. 2007. Diss.

264. VARTIAINEN, JARKKO. Measuring irregularities and surface defects from printed patterns. 2007. Diss.

265. VIRKKI-HATAKKA. TERHI. Novel tools for changing chemical engineering practice. 2007. Diss.

266. SEKKI, ANTTI. Successful new venturing process implemented by the founding entrepreneur: A case of Finnish sawmill industry. 2007. Diss.

267. TURKAMA, PETRA. Maximizing benefits in information technology outsourcing. 2007. Diss.

268. BUTYLINA, SVETLANA. Effect of physico-chemical conditions and operating parameters on flux and retention of different components in ultrafiltration and nanofiltration fractionation of sweet whey. 2007. Diss.

269. YOUSEFI, HASSAN. On modelling, system identification and control of servo-systems with a flexible load. 2007. Diss.

270. QU, HAIYAN. Towards desired crystalline product properties: In-situ monitoring of batch crystallization. 2007. Diss.

271. JUSSILA, IIRO. Omistajuus asiakasomisteisissa osuuskunnissa. 2007. Diss.

272. 5th Workshop on Applications of Wireless Communications. Edited by Jouni Ikonen, Matti Juutilainen and Jari Porras. 2007.

273. 11th NOLAMP Conference in Laser Processing of Materials Lappeenranta, August 20-22, 2007. Ed. by Veli Kujanpää and Antti Salminen. 2007.

274. 3rd JOIN Conference Lappeenranta, August 21-24, 2007. International Conference on Total Welding Management in Industrial Applications. Ed. by Jukka Martikainen. 2007.

275. SOUKKA, RISTO. Applying the principles of life cycle assessment and costing in process modeling to examine profit-making capability. 2007. Diss.

276. TAIPALE, OSSI. Observations on software testing practice. 2007. Diss.

277. SAKSA, JUHA-MATTI. Organisaatiokenttä vai paikallisyhteisö: OP-ryhmän strategiat institutionaalisten ja kilpailullisten paineiden ristitulessa. 2007. Diss.

278. NEDEOGLO, NATALIA. Investigation of interaction between native and impurity defects in ZnSe. 2007. Diss.

279. KÄRKKÄINEN, ANTTI. Dynamic simulations of rotors during drop on retainer bearings. 2007. Diss.